Developing *in vitro* models of traumatic injury for neural tissue engineering applications

Jessica Patricia Wiseman

Thesis submitted for Doctor of Philosophy in Neuroscience

March 2023

Keele University

ABSTRACT

Penetrating traumatic brain injury (pTBI) and spinal cord injury (SCI) cause significant neurological damage and debilitation. The management of these central nervous system (CNS) injuries is largely supportive, with no clinically available regenerative therapies. Regeneration is difficult to achieve because of the inhibitory microenvironment in CNS injury sites. Researchers are constantly developing and testing new therapies to aid regeneration of neural tissue, however, these are heavily reliant on live animal experimentation. There is an urgent need for clinically predictive, *in vitro* models of neurological injury which satisfy requirements such as: mimicry of complex neural architecture, patho-mimicry, high throughput and facile technical procedures, and being in line with the Reduction, Replacement and Refinement of animal experimentation.

Two important approaches for regeneration of damaged CNS tissue are biomaterial application and electrical stimulation (ES) therapy. This thesis aims to develop and evaluate novel *in vitro* models of CNS injury for evaluation of biomaterial and ES therapy. The thesis goals were to: i) compare and contrast an ex vivo (organotypic) model of SCI and TBI with implantation of a neurosurgical grade scaffold (DuraGen™); ii) develop a technical method for a 2D and 3D culture model of cortical injury, and iii) establish a platform for electrophysiological studies of the injury environment using multi-electrode arrays (MEAs). Pathological responses such as glial scarring (astrogliosis), microglial activation and neuronal outgrowth were assessed.

I provide evidence that these newly developed models replicate key pathological features of injury, and can be reliably used for assessment of regenerative therapies, including neural cell responses to biomaterial implantation, and for interfacing with bioelectronic recording/stimulation systems.

Table of Contents

LIST OF FIGURES AND TABLES

LIST OF ABBREVIATIONS

CNS – Central nervous system

SCI – Spinal cord injury

TBI – Traumatic brain injury

pTBI – Penetrating traumatic brain injury

PNS – Peripheral nervous system

ECM – Extracellular matrix

TEM – Transmission electron microscopy

AIS – American spinal injury impairment scale

DVT – Deep vein thrombosis

CSF – Cerebral spinal fluid

MAG – Myelin associated glycoprotein

GFAP – Glial fibrillary acidic protein

CSPG – Chondroitin sulfate proteoglycan

OPC – Oligodendrocyte precursor cells

BBB – Blood brain barrier

DG - DuraGen™

DIV – Days *in vitro*

TEM – Transmission electron microscopy

MSCs/NSCs/ESCs–
Mesenchymal/Neural/Embryonic stem cells

OESs – Olfactory ensheathing cells

ES – Electrical stimulation

2D – Two dimensional

3D – Three dimensional

DC – Direct current

AC – Alternating current

OFS – Oscillating field stimulation

OTS – Organotypic slice

scOSC – Spinal cord organotypic slice culture

bOSC – Brain organotypic slice culture

FDA – Food and drug administration

BDNF – Brain derived neurotrophic factor

MEA – Multi electrode array

ASDR – Array-wide spike detection rate

DPL – Days post lesion

ACKNOWLEDGMENTS

1 Chapter 1: General introduction

1.1 Introduction summary

This thesis aimed to develop new *in vitro* models of CNS injury and evaluate their use for assessment of regenerative approaches. To achieve this, I compare and contrast: ex vivo models of SCI and TBI, 2D and 3D cortical cell cultures, with implantation of a neurosurgical grade scaffold (DuraGen™) or nanomaterial application. Additionally, I aimed to develop a robust system evaluating electrical stimulation using the 2D *in vitro* injury model. As this was a proof of concept, initial data focused on recording activity in the model rather than stimulation studies. Please note, however, that the platform was developed with the eventual aim of delivering ES therapy.

This introduction covers an overview of central nervous system anatomy and the pathological characteristics of injury. Current therapeutic interventions and potential experimental therapeutic approaches will be reviewed, along with the major therapeutic targets of CNS injury repair. Modelling the human CNS and the injury mechanisms through *in vivo* animal and *in vitro* models will be discussed, with specific focus on the 3Rs principles (Replacement, Reduction and Refinement) of animals in research through various *in vitro* modelling systems. Additionally, two therapeutic approaches of most interest to this thesis, namely biomaterial implantation and electrical stimulation, will be explained, and their current limitations highlighted. Lastly, the objectives of the experimental chapters will be outlined.

1.2 An overview of injury to the central nervous system

1.2.1 Socioeconomic impact of the injury to the central nervous system

In the UK it is estimated that ~1200 individuals suffer from spinal cord injuries from traumatic events per year, with an annual incidence of 16 new cases per million population (McDaid et al., 2019). While across the globe between 250,000 to 500,000 people suffer spinal cord injury every year (AANS, 2020). On average within the UK, this has a healthcare cost of 1.12 million per SCI case, which varies depending on the case injury grade (Vella et al., 2017). SCI in relation to age has a bimodal graphical distribution, where peaks occur in young adulthood and then again, in later life, yet injury continues to be predominantly sustained by men (AANS, 2020).

Globally, traumatic brain injury (TBI), affects close to 10 million people per year. In England and Wales, around 1.4 million patients per year are admitted to hospital with TBI. It is the most common cause of death for individuals under 40, and this is similar to the USA, where TBI is the leading cause of death in patients under 44 (Bloom et al., 2021; Lawrence et al., 2016). However, TBI remains a significant cause of mortality and morbidity, for all age groups. In the US, the total annual direct cost of TBI management is approximately 48 billion dollars. Both injury to the spinal cord and the brain result in many functional detriments and a poor quality of life, which leads to many years of necessary care and medical treatment that have profound socioeconomic impacts (McDaid et al., 2019; Vella et al., 2017).

1.2.2 Anatomy of the brain and spinal cord

The nervous system is divided into the central nervous system (CNS) consisting of the brain and spinal cord, and the peripheral nervous system (PNS), which is comprised of cranial nerves and spinal nerves that project between the spine and the body. The brain is split into four individual interlinking regions: the cerebrum, the diencephalon, the cerebellum, and the brain stem (midbrain, pons and medulla), whereas the spinal cord is one distinct structure (Kandel et al., 2000). The spinal cord extends caudally as a continuation of the medulla oblongata of the brain, the cord tapers off around vertebral level L2 (second lumbar vertebrae) to form the cauda equina (a collection of spinal nerves) (**figure 1.1**). The length of the spinal cord is divided into four regions: cervical, thoracic, lumbar and sacral. This is further divided into 31 pairs of spinal nerves which carry information to the body: eight cervical, twelve thoracic, five lumbar, five sacral, one coccygeal, at each segment a dorsal nerve root and ventral nerve root emerge at either side. Dorsal (afferent) nerves transmit sensory information to the brain, while ventral (efferent) nerves serve to output motor function. Additionally, there are twelve pairs of cranial nerves that also relay information to the body. Damage to the spinal cord does not affect pathways that are controlled by the cranial nerves. i.e. parasympathetic system (Sofroniew and Vinters, 2010; Mctigue et al., 2008; Purves et al., 2018).

Both the brain and the spinal cord are protected by the meningeal layers: the pia mater (the inner most layer), the arachnoid and the dura mater (the outermost layer). Offering a more mechanical protection, the brain is surrounded by the skull, while vertebral bones enclose the cord. The CNS tissue is comprised of grey matter, which consists predominantly of cell bodies, dendrites and synaptic interactions, and white matter comprising of ascending and descending neuronal myelinated tracts or interneurons (Seabrook et al., 2006).
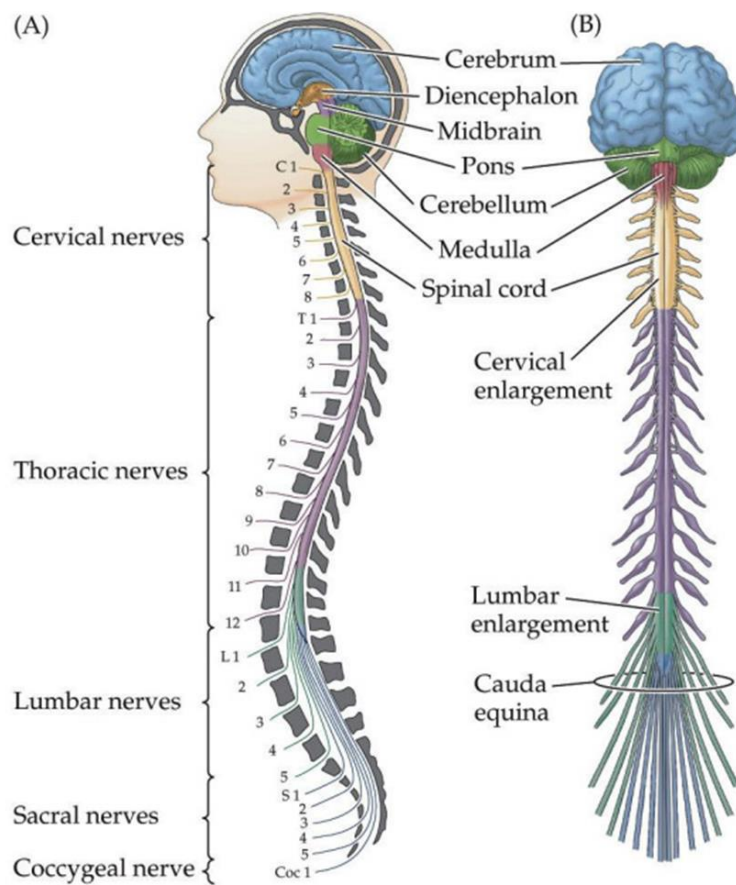
Figure 1.1 The subdivisions and components of the central nervous system. (Figure taken from Purves et al., Neuroscience, 6th edition, 2018)

The spinal cord is a complex network of pathways that relay information and instruction. Distinct anatomical pathways i.e. neuronal tracts within the cord are accountable for the transmission of precise information for specific functions. Neural tracts are commonly grouped according to their origin, projection and purpose. The first part of the name reflects tract origin and second part its termination. The ascending spinothalamic tract is responsible for transmission of information involved in the sensory

pathways: relaying information for pain, temperature, and touch. The spinocerebellar tract (ascending) relays other sensory information like proprioception. However, the descending tracts transmit motor information such as, the corticospinal tract which is associated with skilled voluntary movement, and the vestibulospinal tract mediating balance and posture. Ascending tracts carry sensory information from body to brain and descending tracts transmit involuntary and voluntary motor information. Sensory pathways from the body are carried by first-order neurons. First-order neurons either terminate in the ipsilateral dorsal horn of the spinal cord in the region at the entry level, or the axon continues up the spinal cord and terminates within the ipsilateral medulla oblongata (**figure 1.2**). First-order neuron cell bodies reside in the dorsal root/cranial ganglion. The terminating first order neuron then forms a synapse with a second-order neuron. Following synapse formation, second order neurons cross over the spinal cord midline in a process termed decussation and ascend to the thalamus. These decussations associate one side of the brain to the contralateral side of the body. Lastly, the second order neuron synapses with a third-order neuron within the thalamus which can then project to various ipsilateral areas of grey matter within the brain (Kandel et al., 200; Nieuwhuys et al., 2014; Kuhlenbeck et al., 1967). This mechanism has particular significance when considering a partial/one sided spinal cord injury, for example, the ipsilateral or contralateral effect of a left sided spinal cord injury will depend on whether the point of decussation is above or below the injury (**figure 1.2**).

The brain constitutes 2% of an adult's body weight and requires 15% of the blood within the body. The cerebrum encompasses interconnected complex areas named lobes or cortices that have varying functions. For example, vision is dependent on the functioning of the occipital lobe, temporal lobe is dedicated to hearing and the frontal lobe controls movement and coordination. The limbic system within the diencephalon has significant importance in short term memory, emotions and behaviour; this includes the amygdala, thalamus, hippocampus and the cingulate gyrus (Ludwig et al., 2021).
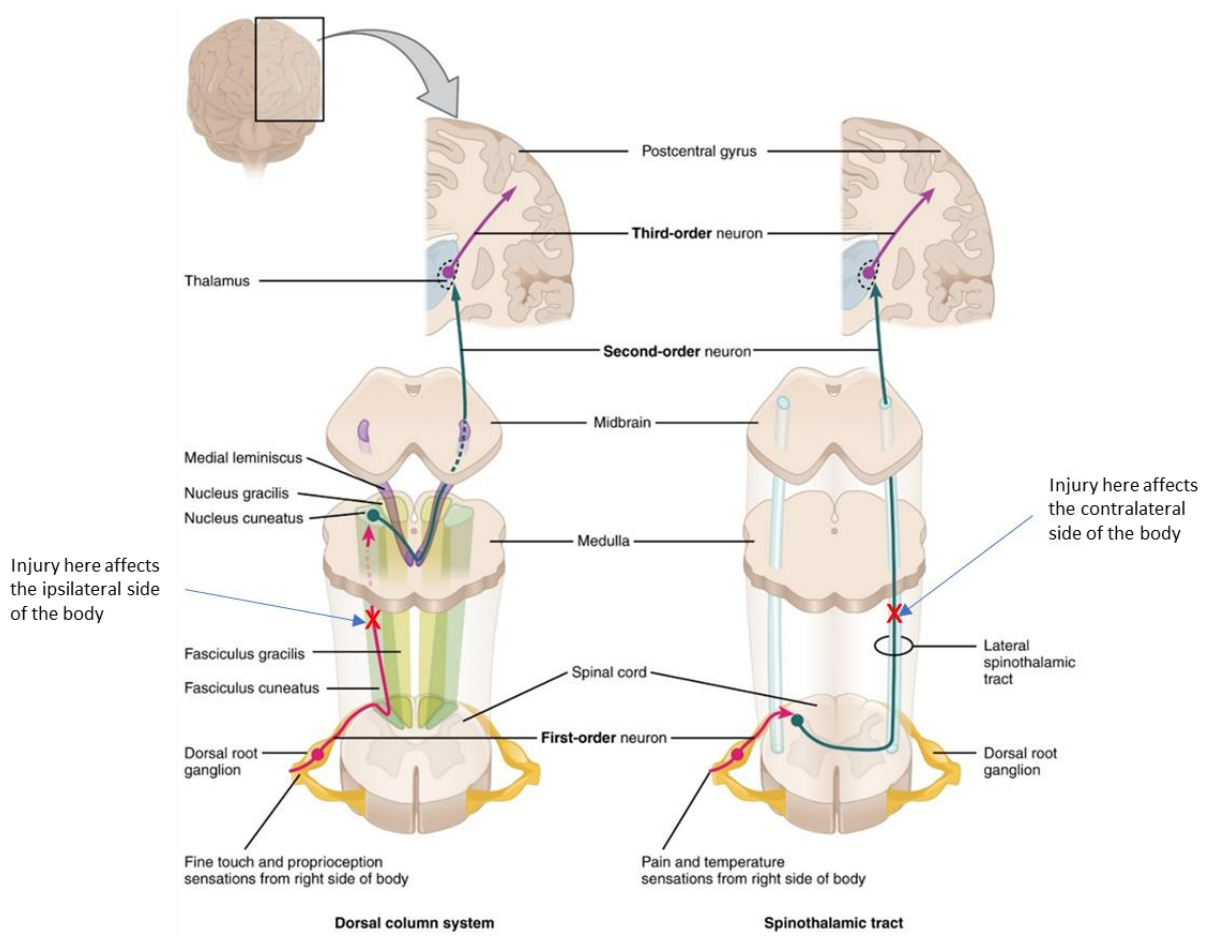
Figure 1.2. Ascending sensory pathways of the spinal cord and the potential effect of a one-sided injury.
(Figure adapted from Biga et al, Anatomy and Physiology, 2019)

The CNS is composed of multiple cell types that mediate these specialised functions. The major functional element of the nervous system are the **neurons** which transmit information along their axon to neighbouring cells in the form of electrical signals and are said to make up ~40% of the brain (Kuhlenbeck et al., 1967). Information between neuronal synapses is mediated via neurotransmitters and distinct neurotransmitters are released by certain neurons for diverse purposes. Glutamate is the major excitatory neurotransmitter in the CNS and is commonly associated with cognition, learning and memory and additionally regulates brain development (Hyman et al., 2005). Neurons are supported by the neuroglial cells (astrocytes, oligodendrocytes, and microglia) which collectively are the most abundant cells of the CNS. Their main functions are to act as a structural and chemical support system to allow efficient transmission of electrical signals and control tissue homeostasis (Gerard, 1993). Glial

cells and neuronal cells are said to have an approximately a 1:1 ratio within the CNS, however there is some controversy on this fact (Herculano-ouzel, 2012).

Astrocytes: are "stellate" cells with many fine processes from a central body. Astrocytes are the major glial cell type, and studies have found the astrocyte proportions varies from 20-40% dependING on the anatomical region (Bartheld et al., 2016). Astrocytes have a key role in CNS development and the formation of synapses; they secrete a variety of neurotrophic growth factors and inhibitory molecules mediating axon growth cone guidance. Astrocytes are crucial in neurotransmitter metabolism and regulating extracellular ionic levels and pH. Additionally, they maintain the integrity and homeostasis of the blood brain barrier (BBB) and blood flow through the brain and spinal cord (Bayraktar et al., 2015). Further, astrocytes are involved in the clearance of aberrant axons and neuronal cells during development. Specifically, astrocytes stimulate neurons selected for removal to upregulate the complement protein c1q, following which microglial cells recognise this tag and phagocytose these cells. Lastly, they have a major role in scarring/repair processes in CNS damage (Sofroniew and Vinters, 2010).

Oligodendrocytes: are predominantly found in the white matter and are responsible for producing the myelin sheath surrounding axons (Hofmann et al., 2017). The sheath extends from the cell soma and wraps spirally around the axon via a thin projection. This mostly insulates the axon excluding small gaps between consecutive myelin sheaths (nodes of Ranvier) and enhances the propagation rate of action potentials. One oligodendrocyte cell can myelinate as many as 30-50 separate axons (McTigue et al., 2008). In addition to the conduction of electrical signals, oligodendrocytes can provide trophic support and regulate neuronal microenvironments (Baumen and Pham-Dinh, 2001).

Oligodendrocyte precursor cells (OPCs): reside throughout the grey and white matter of the CNS (contributing to ~8% of CNS cells) (Ning and Leung, 2015). Although these cells are the progenitor cell for oligodendrocytes and a major contributor to myelination, OPCs are a distinct glial cell type with various functions within the developing and adult CNS. Though their role as progenitors is well

understood, their additional capacities remain relatively undetermined. As well as replenishing oligodendrocyte populations, OPCs have also been said to have regulatory roles with postsynaptic neurons. Additionally, OPCs support integrity of the BBB, modulate neuroinflammation and have been shown to form synapses with neurons (Baumen and Pham-Dinh, 2001; Akay and Aurrey et al., 2021).

Microglia: are the resident immune cell of the CNS, and tissue trauma results in their rapid activation during which they clear the injury site from debris and insults. Microglia contribute to around 20% of all the glial cells within the adult CNS parenchyma (~8% of all cells) (Bartheld et al., 2016). In healthy tissues, M0 microglia continuously scan their environment for damage associated molecular patterns (DAMPS) or pathogen associated molecular patterns (PAMPS) (Lam et al., 2017). They have crucial roles of removal of metabolites and clearing cellular debris resulting from programmed cell death. In addition, microglia are involved in CNS homeostasis through mediating neuronal expansion and differentiation and influencing the establishment and maintenance of synaptic connections (Ginhoux and Prinz, 2015).

1.2.3 CNS injury manifestations and mechanisms

The brain and spinal cord hold vital functional importance and are essential for humans/animals to interact with their environment and survive. Ultimately, the incapacity for the CNS to undergo significant intrinsic repair following neurological injury results in serious devastating injuries.

SCI: SCI can be classified as either non-traumatic (internal spinal cord compressions i.e. from disc prolapse or cysts) or traumatic injuries (blunt trauma or penetrating injury) (Lee and Thumbikat, 2015). Traumatic incidents are a main cause of spinal cord injuries (90%), with motor vehicle accidents being over 30%, and of these cases 80% are males (WHO, 2013). SCI is also common in falls, sporting accidents and violence (gunshot/stab wounds). Symptoms of SCI may include partial or complete loss of motor and sensory functions of the arms, legs and/or body. The severity of the clinical features of SCI are dependent on tissue damage location. The most debilitating injuries are those that occur at the cervical

level and result in the complete paralysis of all four limbs, quadriplegia (Papa et al., 2020). Traumatic tissue damage events can arise through external forces of separate mechanisms. Mechanism of these physical forces can vary and is a key determinant of injury severity, these include: laceration from external objects or broken bones, distraction/stretching/tearing from spinal column dislocations or fractures, or prolonged compression incidents. SCI is classified through the American spinal injury impairment scale (AIS). This is a guide to determine the level of injury and therefore predict a possible recovery. SCI is classified as complete if there is no motor or sensory function below the injury, and incomplete with some preservations of tissue. Injury has three subsets: i) sensory function preserved but no motor function, ii) motor function preserved with little muscle function, and iii) motor function is preserved with good muscle function (Patek and Stewart, 2020; Roberts et al., 2017). In addition to muscle paralysis, SCI has many other debilitating injury outcomes, these include reduced pulmonary function, deep vein thrombosis (DVT), stroke, lack of bowl and bladder control, pressure ulcers, sexual dysfunction/impairment of fertility, long term pain, obesity, diabetes and cognitive decline (Ahuja et al. 2017).

TBI: TBI can be generally grouped into two distinct aetiologies; penetrating TBI where an external object or skull bone penetrates the brain tissue, or closed TBI resulting from an injury to the head without a dural breach. Penetrating traumatic brain injury (pTBI) is the most incapacitating mechanism of injury, with 70-90% of patients dying prior to hospital admission and half of those admitted to hospital die in the emergency department (Hyder et al., 2007). pTBI survivors live with severe debilitation in cognition and movement. pTBI is particularly prevalent in civilians living in areas with high incidence in violence and in military personnel. In military populations, injuries are caused by gunshot wounds and shrapnel from explosive devices that pierce the skull. Traffick accidents and major falls can also cause skull rupture and penetration through the brain tissue (Wyck and Grant, 2015). TBI is categorised into three distinct categories: mild, moderate and severe. Mild is the most common of three representing 75-85% of all TBI. However, pTBI most often is classified as a severe TBI where patients have prolonged loss of

consciousness, inability to speak or open eyes and present major motor and cognitive deficits (Vella et a., 2017).

1.2.4 Pathomechanism of traumatic penetrating injuries in the CNS

Both SCI and TBI have similar injury mechanisms, and can be categorised into primary (instantaneous), secondary (minutes to weeks post-injury) and chronic phases (months or years post injury) (Oyinbo, 2011). Primary injury mechanisms occur immediately as a result of the physical force of injury and the mechanical disruption of tissue. In particular, this includes rupturing of neuronal tracts and neuronal networks (Kamber et al., 2009). The primary event initiates the pathobiological cascade of secondary phase events which is there to essentially protect the uninjured tissue, but can in turn exacerbate neurological deficits and injury outcomes. Within seconds at the injury epicentre cellular necrosis, haemorrhage, glutamate release and cytokine upregulation occur. Following this, other mechanisms unfold i.e. ionic dysregulation, glutaminergic excitotoxicity, ischemia and potential oedema (Papa et al., 2020). Neurological injury quickly induces activation of resident astrocytes and microglia, which migrate and proliferate into the injury site (Karve et al., 2016). Additionally (as a result of the disruption of blood vessels); blood borne inflammatory cells such as macrophages, T-cells and neutrophils also infiltrate the injury site. These cells release pro-inflammatory cytokines such as (tumour necrosis factor) TNF-alpha, interleukin (IL)-1alpha, and these cytokines are elevated for up to 4 days post initial injury. In contrast, M2-like macrophages produce pro-regenerative cytokines like IL-10. This robust neuroinflammatory response enhances other secondary injury mechanisms (Cheriyan et al., 2014). Furthermore, hyperglycaemia occurs following a loss of ionic homeostasis, which activates calcium-dependent ion channels leading to mitochondrial dysfunction and subsequent apoptotic cell death. Inflammation and apoptosis at the tissue damage site promotes the formation of a cystic cavity containing cerebral spinal fluid (CSF). Oligodendrocytes proximal and distal to the lesion epicentre are prone to apoptotic cell death, initiating the demyelination of preserved axons. Additionally, oligodendrocyte necrosis at the epicentre releases myelin debris into the microenvironment, some of these breakdown products i.e.

myelin associated glycoprotein (MAG), oligodendrocyte myelin glycoprotein and Nogo-A, are potent inhibitors of axonal growth contributing to a regeneration-inhibitory environment (Sofroniew and Vinters, 2010); this also leads to further myelin breakdown disseminating outwards from the injury epicentre. Furthermore, reactive state astrocytes at the damage site periphery undergo cell body hypertrophy, enhanced proliferation, and a pronounced upregulation of their cytoplasmic protein glial fibrillary acidic protein (GFAP) (Karve et al 2016). These astrocytes then knit together to form the glial scar. This formation of the glial scar is a physical and biochemical barrier composed primarily of a dense interconnected network of astrocytes and the glial scar proteins they secrete (i.e chondroitin sulfate proteoglycan (CSPG)) (Kline et al., 2016) and is inhibitory to regeneration (Fitch and Silver, 2008). A primary purpose for this activation is to wall off the areas of damage (as shown in **figure 1.3**) to protect the fragile yet intact spinal cord and brain tissue from further damage (Myer et al., 2006). Lastly, injury induces oligodendrocyte precursor cells (OPCs) and pericytes to migrate and proliferate within the injury epicentre contributing to the glial scar (Moeendarbary et al., 2017).

1.2.5 Role of microglia within CNS tissue and injury

Resident quiescent 'resting' (M0) microglia of the brain and spinal cord tissues present a distinct ramified morphology; multiple branches extending from a central cell body (**figure 1.4**). Trauma to the CNS tissue and the induction of a neuroinflammatory response promotes a shift from resting M0 microglia to amoeboid 'activated' microglial (M1). Microglia lose their extensive processed cytoplasm and become amoeboid or bushy in morphology **(figure 1.4**), which transforms microglia into a highly motile phagocytic cell for migration and phagocytosis. These are morphologically similar to macrophages and monocytes (Kawabori and Yenari, 2015). Reactive microglia migrate and proliferate into the lesion epicentre and primarily phagocytose damaged cells and cellular debris. While the clearance of cellular debris prevents debris-mediated tissue degeneration, the release of the pro-inflammatory cytokines (TNF-α and IL-1α) along with protease enzymes and reactive oxygen species (ROS) can exacerbate injury (Zanier et al., 2015).
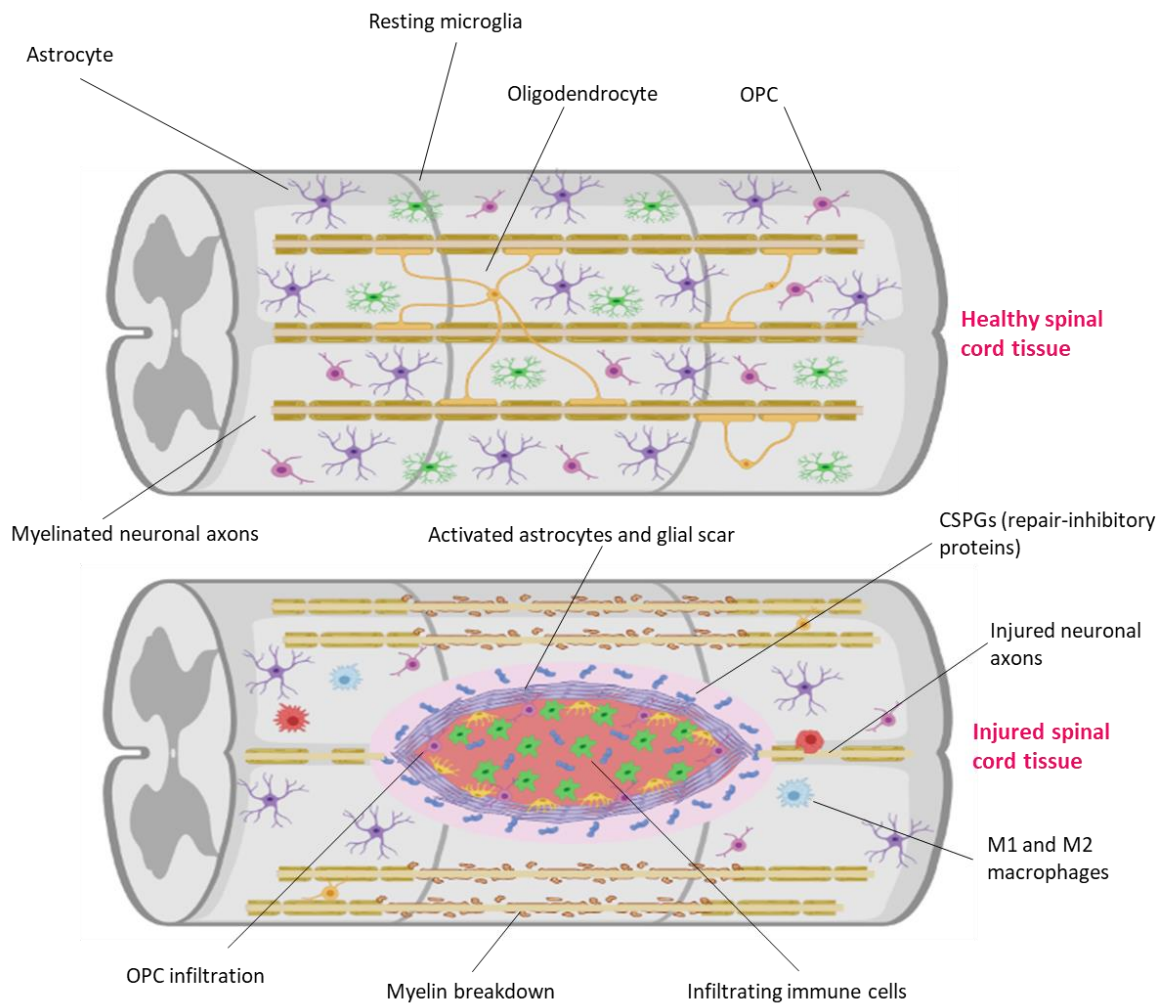
Figure 1.3. Schematic representation of the cellular composition in healthy CNS tissue versus tissue upon traumatic injury. After a traumatic injury event, the tissue is mechanically disrupted and a cystic cavity forms at the lesion core. In response to initial injury, damage-induced cell necrosis and cytokine release, microglia, astrocytes and OPCs are recruited to the injury site. Microglia release further cytokines and engulf debris created from injury. Astrocytes undergo astrogliosis (a reactive and proliferative state) and form a dense interconnect glial scar around the lesion periphery. Astrocytes also secrete CSPGs to reinforce the glial scar. As a result of tissue damage, myelin breakdown occurs within the surrounding tissues which in turn causes axonal degeneration. Created with BioRender.com.
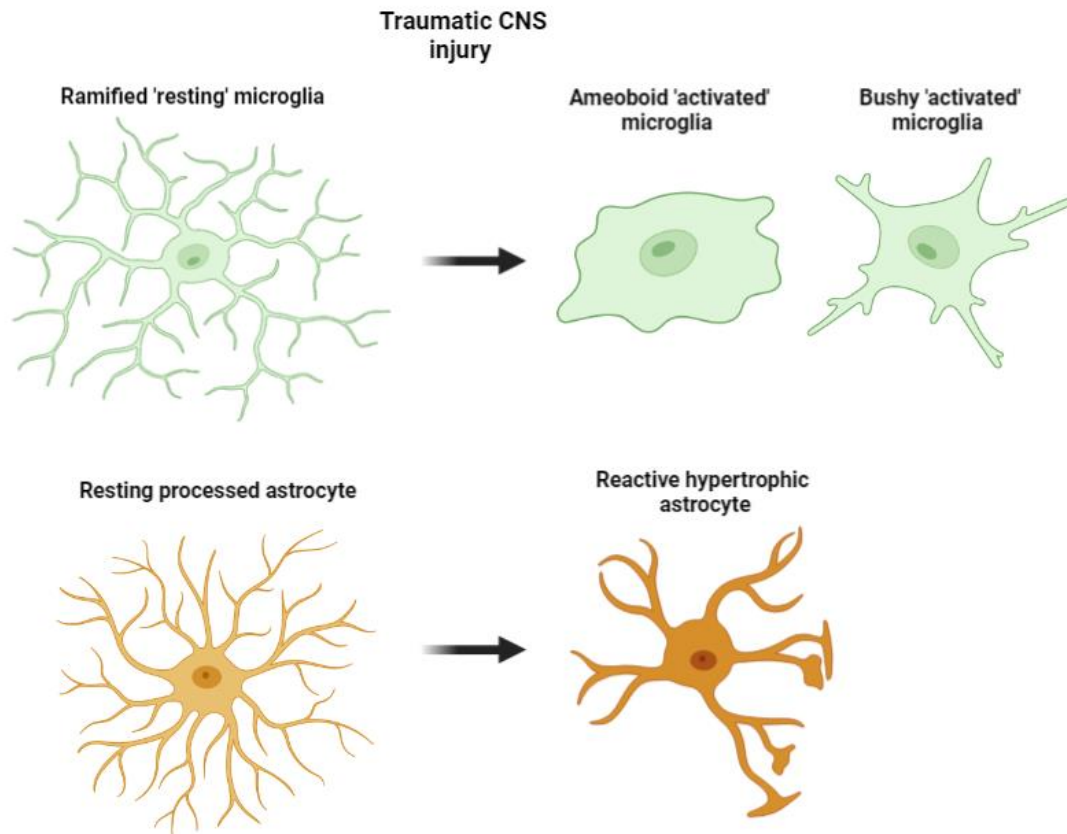
Figure 1.4. A schematic representation showing the morphological shift that microglia and astrocytes undergo in response the CNS trauma *in vivo*. Created with BioRender.com.

Alternatively, activated microglia can have a neuroprotective effect, and these are termed M2 microglia. Neuroprotection is defined as the mitigation and modulation of secondary phase damage through secretion of neurotrophic factors (Assinck et al., 2017). These microglia can promote regeneration within the CNS by initiating neurogenesis and oligodendrogenesis (Cargill et al., 2012). Miron et al (2013) demonstrated that M1 microglia "switch" to M2 microglia during remyelination (oligodendrogenesis), which were observed to enhance oligodendrocyte differentiation, thus providing evidence that M2 microglia may also have a pro-neuroregenerative role (Miron et al., 2013).

1.2.6 Astrocytes modulate homeostasis and neuroinflammation within the CNS

Astrocytes are key mediators of neuroinflammation (Columbo and Farina, 2016). Injury-activated astrocytes can secrete a variety of cytokines and chemokines, which can recruit more immune

cells/astrocytes/OPCs to the lesion epicentre. Quiescent astrocytes in healthy physiological conditions have a stellate morphology with many long thin projections from a central cell body (**figure 1.4**). However, under stress or injury conditions transform to a reactive proliferative phenotype known as astrogliosis (**figure 1.4**), which contributes to the glial scar. The upregulation of GFAP depends on the nature of the injury, the time after injury and the distance from the damage site (Becerra-Calixto and Cardona-Gomez, 2017). In addition to upregulated GFAP expression, activated astrocytes secrete CSPGs which reinforce the glial scar. Generally, these are extracellular matrix (ECM) components however CSPGs like brevican and phosphacan are expressed largely in the glial scar and contribute to the axon growth-inhibitory environment. The glial scar is not only composed of astrocytes, but OPCs microglia, and macrophages are spatially intermingled with other reactive glia at the injury border (Bradbury and Burnside, 2019). The lesion core predominantly consists of NG2+ OPCs, fibroblasts/pericytes and microglia/macrophages. The outer layer surrounding the lesion core is defined by reactive hypertrophic astrocytes (Mohn and Koob, 2015). Although reactive astrocytes are seen as a barrier to neuronal regeneration after injury, it is considered that astrogliosis has a neuroprotective mechanism by providing factors that promote cell survival against further injury and degeneration (Mohn and Koob, 2015). Importantly, preventing the formation of the glial scar impacts negatively on wound-healing as ultimately this response prevents further damage to the surrounding tissues (Bradbury and Burnside, 2019).

1.2.7 Neuronal roles and responses to injury

Upon injury neurons are ruptured creating an immediate influx of extracellular Ca^{2+} which in turn triggers the severed end of the axons to reseal and form large, swollen endings generically called 'retraction bulbs' (Kamber et al., 2009). Following injury to the CNS, injured axons fail to regenerate and rebuild functional connections with their original targets resulting in permanent disabilities. By contrast, injury to the peripheral nerves is followed by regeneration and considerable recovery of sensory and motor functions (Mahar and Cavalli, 2018). Intriguingly, Richardson et al demonstrated that adult CNS

neurons do have the potential to regenerate within a PNS environment indicating the post-injury microenvironment may be determining factor of neuronal regeneration rather than the neurons themselves (Richardson et al., 1980).

Upon injury neurons can be pulled, stretched and torn, and this causes many neuronal membranes to rupture around the injury epicentre leading to axonal die back and cell death. This is a process named Wallerian degeneration which begins at the injury epicentre and proceeds in a direction away from the site of injury. This active process results in fragmentation and disintegration of the axon, which is eventually removed by macrophages and microglia (Mahar and Cavalli, 2018). Neuronal regeneration occurs via one of two mechanisms, either the regrowth of the injured neural tracts or the intrinsic recruitment of neural stem cell to repopulate the lost neurons. Both these mechanisms could represent therapeutic targets to promote regeneration after injury.

1.2.8 Oligodendroglial response to CNS injury

Oligodendrocyte loss at the injury site results in the demyelination of axons and the release of regeneration-inhibitory myelin products. This death of oligodendrocytes also triggers the recruitment and migration of quiescent populations of NG2+ OPCs (Baumen and Pham-Dinh, 2001). Oligodendrocytes are postmitotic cells so loss of these within the acute phase following injury is dependent on the process of oligodendrogenesis driven by OPC differentiation to oligodendrocytes. Morphologically, OPCs have a small cell body and multiple processes, while activated migrating OPCs adopt a bipolar migratory morphology. OPCs react rapidly to injuries and proliferate at a high rate accumulating around the injury site where they can differentiate into myelin forming cells (Ning and Leung, 2015). OPCs develop into oligodendrocytes or astrocytes under specific conditions but predominantly function as regenerating oligodendrocyte populations after demyelination. Overall, the proliferation rate of OPCs significantly increases by the first day after injury and remains elevated for the following week (Ning and Leung, 2015). Studies employing stab wound injuries to the spinal cord

and the brain cortex found a large increase in NG2+ glial at the injury site by 2 days after injury (Rabchevsky et al., 2007; Hampton et al., 2004).

1.2.9 Current and future therapies for CNS injury

In summary, the barrier to CNS regeneration is the potent inhibitory microenvironment surrounding the lesion epicentre which includes: i. glial scar, ii. myelin breakdown products, iii. pro-inflammatory cytokines, iv. limited sprouting and plasticity of adult CNS neurons, v. cystic injury cavity and vi. neuronal dieback and demyelination in surrounding tissues.

Current treatment for CNS injuries first, before any long-term treatment is applied, concentrate on immobilising the spinal cord or brain, especially in the case of cervical damage. Blood pressure must be kept stable and surgical decompression of the brain or spinal cord is required in order to allow blood flood and avoid ischemia (Ahuja et al., 2017). Following this, drug administration together with rehabilitation are the main treatment approaches. Currently the drugs administered to patients aim to stabilise the lesion area and prevent further damage to proximal spinal or brain tissue. The most common drug prescribed for TBI and SCI management is methylprednisolone, a glucocorticoid that enhances anti-inflammatory cytokine release and promotes cell survival (Ahuja et al., 2017; Sloka and Stefanelli, 2005). Although methylprednisolone is widely prescribed, animal studies have shown mixed results for recovery. A 2009 systemic review showed 58% of animal studies exhibit no advantages in recovery with only 34% showing beneficial effects (Akhtar et al., 2009). Other prescribed drugs include minocycline (which is typically an antibiotic), has shown a tendency to promote recovery; by inhibiting microglial activation, and release of pro-inflammatory factors (Seabrook et al 2006). Minocycline administration via an intraperitoneal injection every day for 28 days after injury in mice reduced lesion size and enhanced hind limb function (Wells et al 2003). A recent study shows that minocycline administration has potent neuroprotective effects (Shultz and Zhong, 2017). Yet a clinical phase 2 study lacked statistical significance of patient improvement after spinal cord injury (Casha et al., 2012). In

combination with drug administration, the post-operative rehabilitation aims to guide and reteach patients any functionality they have lost if possible and help restore patients to daily life.

At present there is no effective clinical therapeutic approach targeting neural tissue regeneration following SCI or TBI (Mothe et al 2012). Functional restoration post severe CNS injury is considered one of the most challenging issues in clinical research. There are five major therapeutic goals that a treatment should ideally target for the most promising therapeutic intervention (**figure 1.5**): i) bridging of the cystic cavity ii) prevention of the astrocytic scar iii) enhancement of axonal outgrowth iv) remyelination of regenerated axons and vi) reduction of inflammation. To address these major therapeutic goals a multitude of strategies are currently under investigation within neuro-regenerative research (highlighted in **figure 1.5**) (Papa et al., 2020; Vella et al., 2017; Ahuja et al., 2017). Due to the complexity of injury and the multifaceted patho-mechanisms as previously described, it is more than likely that a combinatorial approach of two or more of these strategies working in tandem will be necessary for the repair and regeneration of CNS injury. Alone these therapies will not be able to target all the 5 therapeutic goals that are required for functional restoration of traumatic injury.

1.2.9.1 Neuroregenerative pharmacological therapies

One strategy is to block regenerative-inhibitory molecules through the administration of specific synthesis-/activity-inhibitors and (in theory), encourage the intrinsic fibre outgrowth of severed axons. In particular, CSPG inhibitors have shown some enhancement of the growth of neurons *in vitro* and the remyelination of axons (Monnier et al., 2003; Keough et al., 2016). Use of the enzyme chondroitinase ABC (ChABC) has led to a reduction in CSPGs in spinal injured animals with a significant improvement of function (Bradbury & Carter, 2010). Furthermore, blocking the activity of Nogo-A (myelin breakdown product) by treatment of anti-Nogo-A induced innervation of denervated brain stem and spinal cord *in vivo* for rats and macaque monkeys with acute SCI. These studies were taken to clinical trials and reported success in phase 1 clinical trials; however no further advances were achieved (Zorner and Schwab, 2010). Other pharmacological approaches such as the administration of neurotrophic factors

to the injury site have been shown to be effective in promoting axonal outgrowth from the lesion edge. These function by enhancing neuronal survival, proliferation, axon growth and synaptic plasticity. For example, administration of brain derived neurotrophic factor (BDNF) into the lesion area limits neuronal damage and promotes the regeneration of injured neurons after SCI (Koda et al. 2004).
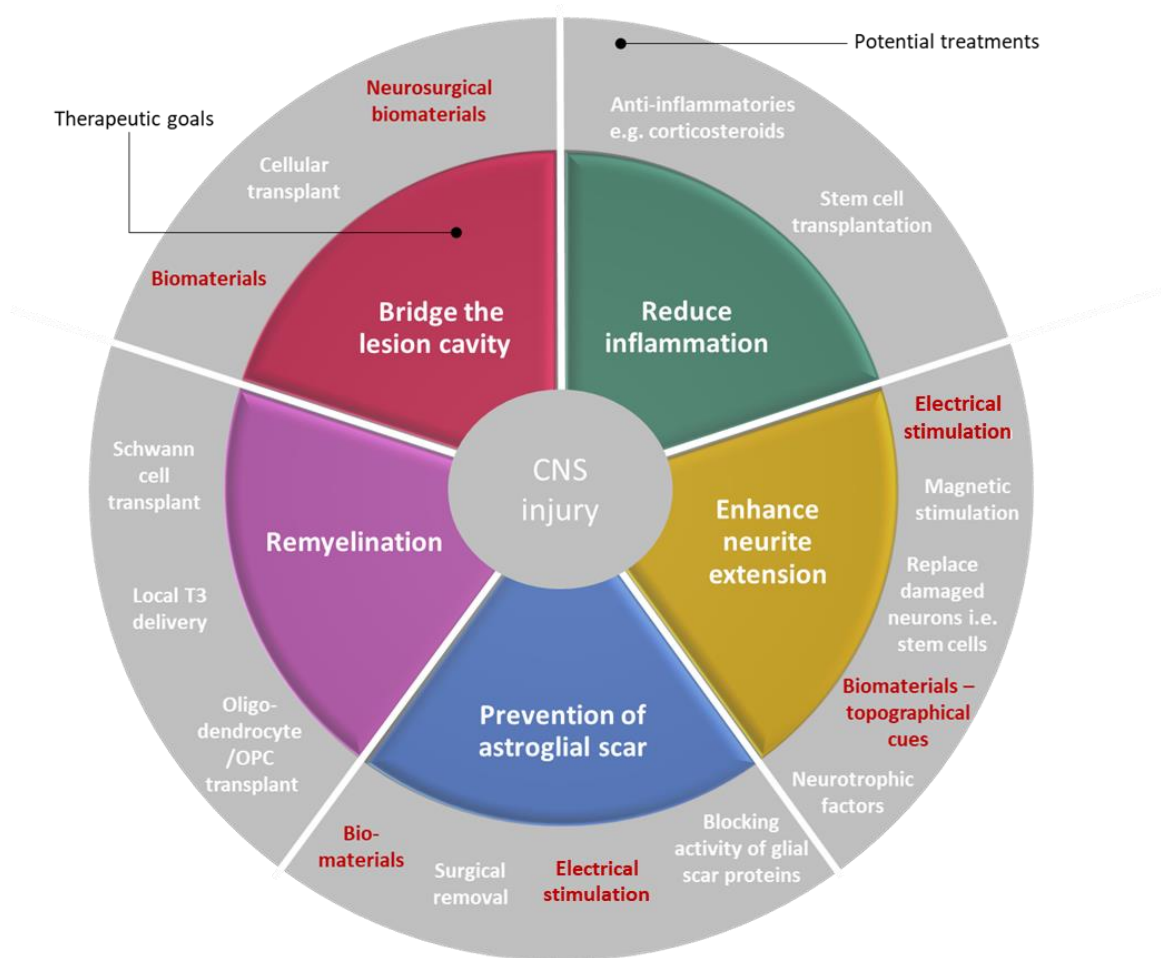
Figure 1.5: Wheel schematic to illustrate the 5 major therapeutic goals for CNS repair, clinically relevant treatment strategies and the necessity for a combinatorial approach. The strategies of focus in this thesis are highlighted in red. Created with Powerpoint.

1.2.9.2 Non-pharmacological regeneration strategies

A popular therapeutic strategy for CNS injury is cell or stem cell therapy, involving the transplantation of the exogenous cells to replenish neural cells lost through initial trauma and to encourage

regeneration. Transplantation of various cells into the trauma site has also shown to provide trophic support, regenerate neural circuits, remyelinate axons and modulate the inflammatory response. Numerous animal studies have demonstrated benefits of a range of transplanted cell types, including mesenchymal stem cells (MSCs), neural stem cells (NCSs), embryonic stem cells (ESCs), oligodendrocyte precursor cells (OPCs), Schwann cells and olfactory ensheathing cells (OESCs) (Ahuja et al, 2017; Assinck et al., 2017).

Specifically, MSCs have intrinsic neurotrophic and neuroprotective properties (Hasan et al. 2017). Neurotrophic factors can be separated into three categories: neurotrophins, neuropoietic cytokines, and the glial cell derived neurotrophic factor (GDNF) protein family. Neurotrophins i.e., nerve growth factor (NGF), brain-derived neurotrophic factor (BDNF) or neurotrophin-3 (NT-3), influence cell survival and neuronal differentiation. GDNFs secreted by glial cells often play roles in neuronal survival, in particular provide trophic support to dopaminergic, sympathetic and spinal motor neurons (Kotliarova & Sidorova, 2021). Lastly, neuropoietic cytokines, like interleukin-6 (IL-6) and IL-11, have been associated with the mediation of the immune response, neural cell differentiation and neurite outgrowth (Boyd & Gordon, 2003). Schwann cells transplanted into the lesioned CNS have been correlated with improved remyelination (Biernaskie et al., 2007). OECs are found in the nasal mucosa and ensheath olfactory neurons (like Schwann cells), phagocytose debris and release neurotrophic factors (Ahuja et al., 2017b). Injection of OECs into CNS injury has also resulted in increased axonal regeneration and subsequent locomotor improvement recovery (Ramón-Cueto et al., 2000). Furthermore, NSCs can be harvested from embryonic tissue or from the subventricular zone or central canal in adults and can differentiate into neurons, astrocytes and oligodendrocytes. Therefore, they can provide an ideal cellular replacement strategy for the loss within injury. Implantation of NSCs into the lesioned spinal cord has resulted in axonal regeneration and formation of new synapses between grafted cells and host tissue (Ahuja et al., 2020).

Despite the positive outcomes of exogenous cell transplants, injected cells into injury sites have low viability rates and disperse away from the area of interest, which has prevented their progression to clinical trials. An approach to maximise treatment effect and enhance the lifespan of these transplant cells is for them to be encapsulated and protected via a fibrous biomaterial scaffold in a combinatorial approach. In addition to this, regeneration is often hindered by presence of a cystic cavity and biomaterials have emerged to recapitulate the architecture of the ECM and to fill these defects (Li et al., 2016). Several biomaterials have been shown effective in animal models of CNS injury, and as the technology evolves it shows great promise to not only fill defects but to promote regeneration, reduce inhibitory barriers and efficiently deliver molecules or cells to the injury site (Hlavac et al., 2020). Biomaterial scaffold treatment as a clinically relevant regenerative therapeutic approach will be discussed in more detail later.

While biomaterial scaffolds represent the macroscale cellular support, materials on the nanometer scale (i.e. nanotechnology) have been tested, and interestingly these can provide control and manipulation over biological processes allowing such treatments to be delivered directly to damaged cells. Nanoparticles that are between 1 to 100 nano-meters in size and can be classified into different classes based on their properties, shapes and sizes. Magnetic nanoparticles (MNPs) possess a unique physical property in which they can be controlled via magnetic stimulation. This property makes them an attractive and versatile therapeutic approach within neuro regenerative research. From magnetic resonance imagining (MRI) and tracking transplant cells to the potential to influence cellular differentiation mechanisms, MNPs have been well documented in CNS research (Sanot er al., 2012; Jain et al., 2008;). Lastly, electrical stimulation (ES) is another promising strategy in which cellular responses to injury can be mediated and specific regenerative parameters can be enhanced. This will be discussed further later in this thesis.

1.3 Appropriate modelling of neurological injury for the therapeutic development

1.3.1 Live animal experimentation and the necessity for alternate injury models

Research into development of therapeutic approaches for traumatic CNS injuries is heavily reliant on live animal models, to assess injury mechanisms and efficacy of possible treatments. Though SCI and TBI have been studied in a range of species including rats, mice, rabbits, cats, dogs, zebra fish, sheep, pigs and non-human primates; mice and rat models predominantly feature in the pre-clinical literature. Many external force injury devices/procedures have been established within live rodent models to mimic injury mechanisms observed within humans; these include fluid percussion, contusion (via weight drop), compression, dislocation, ballistic (gunshot), penetrating injury (trans/hemi-section) and blast injuries (Kumaria et al., 2017; Alhoseini et al., 2017; Xiong et al., 2013; Marklund et al., 2016; Lilley et al., 2020).

Several ethical and practical drawbacks are associated with live animal experimentation. Firstly, in an attempt to mimic the clinical features of SCI or TBI, highly invasive injuries are created in the spinal cord or brain *in vivo*. Injuries can have serious direct and indirect adverse effects on biological functionality, in addition to the model-dependant motor/sensory or cognitive disorders, animals can suffer from bladder dysfunction, surgery-associated infections and other health complications demanding rigorous post-operative monitoring of the animals. These require extensive post-operative care from specialist staff with high financial costs (Morrison et al. 1998; Krassioukov et al. 2002). In addition, application of a therapeutic approach usually requires a second operative procedure i.e. implantation of scaffolds or electrical stimulation devices pre/post injury. These procedures can require high technical expertise and the process can be very time consuming, with significant inter-animal variation (Talac et al. 2004). Further to this a large number of animals are required for these studies in order to yield statistical validity, which increases cost and contributes to ethical issues with the use of animals (Daviaud et al. 2013). A significant concern of such studies is that the data produced in animal models are not reliable

in predicting true human outcomes, reflected in phase II clinical trial failure (around 79%). Overall animal experimentation is a controversial area of research for the public and scientists, with public approval for this research declining from 75% (2010) to 51% (2017) (Tickle et al., 2022).

The development and advancement of *in vitro* models for SCI and TBI have also been in great demand for understanding the underlying cellular, structural and biochemical mechanisms of the brain/spinal cord development and the pathophysiology of injury. This information is an essential and complementary step towards CNS regeneration. The techniques that enable the *in vitro* manipulation of injury-modelling systems include approaches such as isolation of 'pure' neural cell cultures, mixed neural cell culture, neural stem cell cultures, 3D neural tissue constructs, neural organoids, organ-on-a-chip and ex vivo organotypic tissue sections through organ dissection (Slovinska et al 2016; Cheriyan et al., 2014; Jgamadze et al., 2020, Humpel, 2015; Morrison et al., 2011; Wu et al., 2021).

1.3.2 3 R principles of animal research

The 3 R's principles (Reduction, Replacement and Refinement) of animal research is an initiative to alleviate unnecessary suffering and increase research dedicated to the development of suitable *in vitro* tissue models. This framework was developed over 50 years ago for performing more humane animal research. This aims to: find adequate alternatives to avoid or Replace animal models, Reduce and minimise the number of animals used per experiment and Refine experimental procedures to guarantee animal welfare and minimise suffering (actions to address these targets are highlighted in **figure 1.5**) (Lilley et al., 2020) (Russel and Bruch, 1959) (NC3Rs, 2022). Although *in vitro* models cannot replace animal models (particularly for pre-clinical experimentation), they can be very valuable when utilised within early-stage therapeutic testing and development. Accordingly, the development of new alternative efficient *in vitro* methods to study neurotrauma is imperative to supplement unnecessary animal experimentation. It is important to note that *in vitro* models are not exempt from ethical drawbacks but undoubtedly present significantly fewer ethical issues (Kumaria, 2017).

Modelling TBI and SCI *in vitro*: *In vitro* models of TBI and SCI can play a primary role in establishing and testing therapeutic hypotheses in isolation. Such modelling systems can permit tighter experimental control, a reduction in confounding variables and therefore leads to a higher experimental reliability. In addition, *in vitro* assessment of CNS trauma poses significantly fewer ethical issues (i.e. the harvesting of tissues or cells from animals), is more cost effective, and offers a high-throughput platform with the capabilities to screen multiple agents simultaneously or develop multimodal therapeutics. These models offer a snapshot of the complex endogenous pathomechanisms whereby many important conclusions can be drawn. **However, it is important to understand that brain or spinal cord injury cannot be modelled in their entirety through *in vitro* models alone.** For a therapeutic strategy to reach human clinical trials, a successful 'preclinical study' must be demonstrated. Preclinical road maps include safety and efficacy assessment within animal models, thus translation of putative therapeutics means animal models cannot be entirely removed. Efficient *in vitro* models for therapeutic CNS screening have the potential to identify experimental flaws and remove ineffective strategies before application to animal models, subsequently this will reduce *in vivo* failure rate during developmental phases of therapies. To emphasise, *in vitro* models used in parallel with *in vivo* models to further understand CNS pathophysiology is an ideal strategy towards the 3Rs and reducing the unnecessary use of animals.
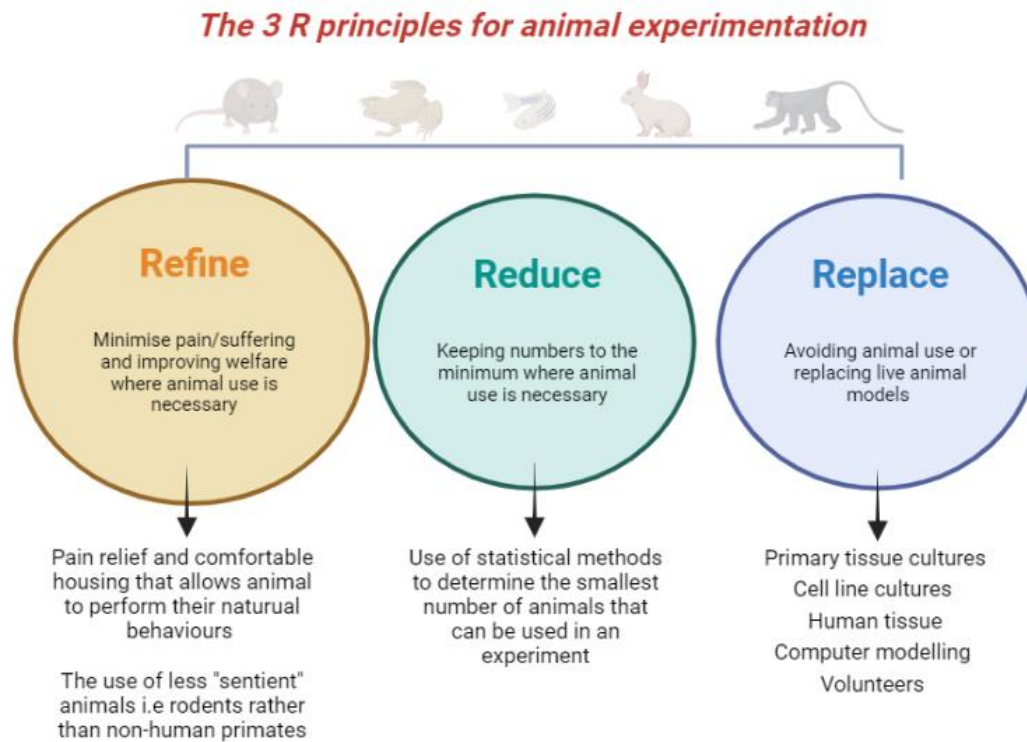
Figure 1.6 Schematic representation of the 3R principles and possible actions to consider. Created with BioRender.com.

1.3.3 *In vitro* models of neural tissue

In vitro models range in complexity from the simplest, two-dimensional (2-D) monolayer cell cultures to the highly complex three-dimensional (3-D) organotypic slice or organoid cultures. An overview of possible *in vitro* models for modelling the central nervous system tissue and pathology is highlighted in **table 1.1**. Different *in vitro* models have specific associated features which determine their research utility i.e. pathological relevance, technical difficulty and the ease of maintenance.

1.3.3.1 Complex models

The most complex *in vitro* models are considered to mimic multiple features of CNS physiology and the patho-mechanisms of injury with comparable response to native dynamics (Wu et al, 2021; Solvinska et al., 2016). A complex model such as ex vivo organotypic tissue slices of the brain or spinal cord have

the potential to bridge the existing gap between *in vivo* experimentation and *in vitro* isolated neural cell culture models.

Organotypic slice (OTS) cultures: represent a transitional system that preserves the original tissue, and its inherent structural architecture, therefore combines characteristics of *in vivo* and the *in vitro* cell culture models. Whole organs are dissected i.e. the brain or spinal cord and the tissue is cut into slices using a tissue chopper or vibratome (without any cellular dissociation), and the thickness of slices vary depending on experiment (Gahwiler, 1981). There are two methods of achieving organotypic culture. The first developed was the roller-tube culture, where slices are embedded into a collagen/plasma matrix on glass coverslips and then placed into culture tubes with growth medium which undergo a continuous slow rotating action. This rotation permits the oxygenation of the slice by generating an alternating liquid-gas interface. Via this method, slices can be cultured for several weeks (Gahwiler, 1981). The second technique (and now the most common technique for neurological OTS culture), involves a semi-porous membrane supporting the tissue slice above the growth medium creating an air-medium interface. The medium below the membrane allows for appropriate nutrient absorption, facilitated via capillary action and oxygenation is permitted from above the slice (Stoppini et al. 1991; Gahwiler et al. 1997). An advantage of this interface membrane method is that the medium does not submerge the OTS permitting therapeutic agents, materials, stimuli or mechanical injury to be applied directly to the slice at any stage of culture. Before simulating an impact injury upon these slices, time is required after initial culture to allow for slices to adapt to the culturing conditions, attach to the membrane and mature. This period of time can vary, some groups advise 12-14 days (Adamchik et al. 2000) others have said less than a week for efficient attachment/stabilisation (Krassioukov et al. 2002; Sypecka et al. 2015). There are currently established OTS models for both spinal cord and brain derived tissues from species including mouse, rats, rabbits (Savas et al. 2001), human (Jeong et al. 2011).

Ex vivo tissues in culture retain their native tissue cytoarchitecture and structures, including white and grey matter, neuronal tracts and the central canal. In addition, they continue to develop and mature

within culture. In terms of mechanisms for modelling injury, manipulation of the slices is more straightforward with no requirement for the invasive procedures or ethical issues associated with *in vivo* injury models. Various types of injury can be introduced in the slices; ischemic injury (involves a depletion of oxygen) (Li et al., 2016), injury through over exposure of glutamate (Dorset et al., 2017), LPS-induced neuroinflammation (Lutz et al 2015), or traumatic injury (involving damage from an external force). Traumatic external force mechanisms include: i) weight drop mechanisms mimicking contusion injuries (Adamchik et al., 2000; Krassioukov et al., 2002; Pansamooz et al., 2019), ii) stretch mechanisms (Morrison et al., 2000; Morrison et al., 2006; Di Pietro et al., 2013), iii) a compressed-air driven shock tube (Campos-Pires et al., 2018), iv) a focal injury can be induced through dropping a metal stylus under stereomicroscopic control (Krings et al., 2016) or, v) through transecting lesion models where a doubled bladed scalpel is used to dissect the organotypic tissue (Weightman et al., 2014; Guijarro-Belmar et al., 2019).

Implantation of biomaterial or electrical devices is simpler in organotypic slices compared with *in vivo* as there is no further animal surgery or risk of infection from secondary procedures and arduous physiological monitoring. OTS offer a moderate throughput platform to simultaneously monitor parameters of neural regeneration (i.e. nerve fibre outgrowth, glial scar formation, remyelination, and immune cell activation) in response to various injury mechanism and therapeutic approaches.

It is important to note that most successful organotypic slice models are generated with immature tissue from early postnatal animals, due to having more plasticity and resilience than adult tissue (Finley et al. 2004). Majority of traumatic injuries to the CNS will occur at adult age so younger tissue is a limitation when considering translational therapy assessment. Brain and spinal cord slices however, have been cultured successfully from weeks to several months (Ostergaard et al., 1990; Marksteiner and Humpel, 2008; Sypecka et al., 2015), to increase tissue age before injury.

In recent years, there has been increasing attention to human organotypic tissue cultures, however for CNS tissues an efficient, well characterised human injury model is yet to be developed. Human *in vitro*

organotypic spinal cord and brain models are extremely rare. In 2010, a human spinal cord model derived from adult autopsy tissue (with no injury mechanism), was reported (Jeong et al., 2011). One group has developed an organotypic model that facilitated *in vitro* culture of human adult brain tissue for up to 3-4 weeks. This was achieved with tissue of human origin obtained during operations from patients with focal epilepsies (Eugene et al. 2014). Long-term adult human brain slice culture has also been achieved in 2019 (Schwarz et al., 2019). In 2020, Lin et al., achieved the first human SCI/TBI organotypic model through culture of human foetal brain stem and spinal cord slices. This tissue was harvested from pregnancy donors within the first trimester and a weight drop injury mechanism was performed on transverse slices (Lin et al., 2020). Nevertheless, due to the ambiguity of human OTS cultures and the extensive use of rodents for *in vivo* therapeutic testing, rodent organotypic modelling systems are the most suitable replacement for screening novel pharmacological tools and potential regenerative therapies prior to preclinical testing.

In general, there are several major advantages of organotypic models compared to *in vivo* studies: i) slicing an organ can produce multiple repeats in form of separate tissues slices so less animals are required ii) slices can be cultured at several ages of tissues iii) can be achieved with several species (including human foetal donors), iv) many tissues types could be cultured from one animal (i.e. brain and spinal cord simultaneously), v) models can also be made from transgenic animals and vi) they offer the facile nature *in vitro* manipulation and maintenance (Jeong et al., 2011; Duff et al., 2002 ; Weightman et al., 2014 ; Daviaud et al., 2013).

1.3.3.2   Other complex models for modelling brain and spinal cord injury

Alternatively, for spinal cord tissues, a lot of attention has been paid to the efficient derivation of spinal cord motor neurons from human pluripotent stem cells (hPSCs). These focused on the ventral- and dorsalisation of motor neuron progenitor cells (Amoroso et al.,2013; Du et al., 2015; Maury et al., 2015). However, these cellular culture methods can only contribute in a limited way in the attempt to mimic SCI *in vitro*, as they do not replicate the dynamic multicellular interactions observed *in vivo*. There has also been a large focus on human iPSCs to reproduce the various neuronal types of the brain in 2D *in*

vitro culture. These neuronal cells have been combined with microfluidic culturing systems to generate brain-on-a-chip modelling systems resembling tissue-like physiology (Bang et al., 2019). These systems however are low throughput with limitations to their scalability and lack cellular maturity within the models. Peter Lolskill and his team developed an organ-on-disc technology allowing the parallel generation of multiple 3D tissues in pump-free perfusion system. This centrifugal generation of several 3D constructs in unison requires minimal manual handling, is high throughput and is a promising enabling platform technology (Schneider et al., 2020). Despite this promising organ-on-disc platform technology, it is yet to be successfully adapted to the parallel production of 3D brain-like tissues.

Human cell-derived CNS organoids are another complex *in vitro* modelling contender, which have the potential for molecular and structural mimicry of the brain and spinal cord and to mimic injury pathology. CNS organoids are stem-cell-derived self-organising suspension cultures with major neural cell types (excluding microglia) and cytoarchitectures recapitulating developing tissues (Jgamadze et al., 2020). Self-organising approaches allow for the formation of a "mini-brain" displaying multiple regions of neural tissue comparable to that of the human brain (Qian et al., 2016). Brain-like organoid structures are more commonly documented within the literature, but spinal cord organoids appear more difficult to achieve. Reported in 2020 was the first and only detailed description of a spinal cord organoid; providing initial evidence of the possible structures that can be produced via the dorsal- and ventral-isation of embryoid bodies (Ogura et al., 2018). Currently, this does not recapitulate all the domains extending from ventral to dorsal, and the tissue generated is very immature -this will require substantial development for injury modelling. Following this, the concept of organoid "assembloids" was developed in a recent report, another valuable discovery for SCI modelling. This is the fusion of separate organoid types to generate a more complex system. For example, the dorsal, ventral and intermediate segments of the spinal cord could be assembled from separate organoids, generating tissue that will appropriately mimic spinal cord cellular diversity and cytoarchitecture (Birey et al., 2017). However, again this requires significant development and cannot immediately resolve any current matters concerning the reduction or replacement of live animal modelling for spinal cord injury.

Self-patterned organoids are individually inconsistent, and lack the immune component, yet the model does allow inter-regional interactions (Lancaster et al. 2013). In terms of recapitulating traumatic injury, organoid techniques do not provide an accessible platform for physical manipulation due to their free floating nature, making it challenging to recreate this sort of injury. One group in 2020 developed a mechanism of traumatic brain injury to brain organoids through high-intensity focused ultrasound (Lai et al., 2020). Despite this, traumatic injury mechanisms are rare within CNS organoids and therefore are not ideal for pre-animal CNS injury testing without significant development.

As an alternative to organoids/organ-on-a-chip models, hydrogels are excellent candidates to mimic the ECM soft tissues and have emerged for the development of 3D CNS-like tissue models. Hydrogels can be modulated to match the endogenous tissue stiffness of the brain or spinal cord which can shift dependant on area (3-10 kPa) (Juge et al., 2016) and change upon injury. Prager at el., 2020 demonstrated an efficient method to match collagen hydrogel stiffness to the measurable stiffness of an injured canine spinal cord. Cell encapsulating hydrogels have the potential to be high-throughput modelling systems with technical ease whilst offering complex *in vivo*-like cellular dynamics. This will be discussed further in chapter 4.

1.3.3.3   Simplistic models: Neurological cell culture models

Neural cell cultures can be generated from immortalised cell-lines, stem cell lines, primary cultures from dissociated tissue or stem cells isolated from primary tissue.

Immortalised cell-based models: can be desirable due to their high-throughput and facile culture properties. Nevertheless, the indefinite propagation property of these cell lines make them resistant to death and unreliable in mimicking pathophysiological mechanisms, additionally they are at high risk of cryptic contaminations such as mycoplasma (Gordon et al, 2013; Carter and Shieh, 2015; Vagaska et al., 2020). Clonal cells like this differ genetically and phenotypically from their endogenous counterparts showing altered morphology over time, which causes an undesirable heterogeneity throughout these

models (Ulrich et al., 2001). Cell lines are most often pure cell cultures and these lack the intercellular communication required for recapitulating the *in vivo* milieu.

Stem cell lines: multiple neural cell generation through embryonic stem cells (ESCs), neural stem cells (NSCs) and induced pluripotent stem cells (iPSCs) are common within the literature. These cells can be of human origin rather than animal which is a key advantage of such stem cell lines; the potential for a more human specific response is seen as a major approach to bridge the gap between translating preclinical studies to successful human clinical trials. Human neural stem cells are derived originally from foetal brain. iPSCs however originate from adult cells that are genetically reprogrammed into a pluripotent state through the addition of certain factors. Then both are expanded into cell lines which have the capacity to proliferate extensively *in vitro*. Though iPSCs can be patient specific and retain genetic identity for disease modelling, they are demanding to maintain in culture and have long differentiation protocols (Pistollato et al., 2017, Tukker et al., 2018). As injury modelling systems do not necessarily require patient specific genetic identities and iPSCs do not produce superior mixed cultures

In vitro models	Description	Advantages	Disadvantages	References
3D 'organotypic' slices	Ex vivo brain tissue slices	-Retain *in vivo* cytoarchitecture -Retain major brain cell types (including microglia) -Ease of mechanical manipulation -Moderate difficulty to induce mechanical injury -Can be interfaced with biomaterials -Display complex injury responses -Adaptable for excitotoxicity/hypoxia studies	-Moderate throughput -Can be technically difficult to isolate and maintain slices -Requires more animals versus other *in vitro* models	(Morrison et al., 2000) (Di Pietro et al., 2012) (Bar-Kochba et al., 2016) (Campos-Pires et al., 2018) (Krings et al., 2016) (Ucar et al., 2021)
3D Organoids	Stem-cell derived self-organising suspension cultures forming brain-like spheroids (iPSC origin)	-Cytoarchitecture recapitulates developing tissues -Can be human / patient specific -Closely simulate *in vivo* cellular communication -Adaptable for excitotoxicity studies -Ideal for disease and development studies	-Moderate throughput -Little uniformity between aggregates -Largely immature in cellular development -Long culture periods -Few injury systems reported -Lack vascular and immune components -Problematic for mechanical manipulation due to free floating nature -Spheroid centres can become hypoxic due to lack of nutrient access -Difficult cellular analysis -Complicated for biomaterial interfacing	(Jgamadze et al., 2020) (Ogura et al., 2018) (Birey et al., 2017) (Ramirez et al., 2021)
Brain-on-a-chip	Microfluidic culture systems of 3D iPSC derived cultures	-Tissue-like physiology -Perfusion system of 3D tissue -Adaptable for disease/toxicity mechanisms -Axonal strain injury attempted	-Low throughput -Scalability limitations -Lack immune and vascular components -Lack cellular maturity -Difficulty with mechanical injury induction -Difficulty with biomaterial interfacing	(Bang et al., 2019) (Dolle et al., 2014)

3D hydrogel constructs	Cells encapsulated within a 3D matrix	-3D architecture resembling tissue-like environment -Physiologically relevant cellular morphology -Simple maintenance -Moderate to high-throughput -Moderate technical difficulty for injury mechanisms -Biomaterial interfacing feasible	-Difficult analysis of 3D environment -Can lack complexity if not multicellular constructs i.e., lack immune component if cells are NSC derived -Not currently documented with all the major cell types of primary brain cell dissociates -Lack vascular component (but feasible with tissue engineered blood vessels)	(Raimondi et al., 2020) (Antoni et al., 2015) (Haycock, 2010)
2D primary multicellular models	Complex multicellular cultures of brain dissociates	-Can encompass major brain cell types (including microglia and neurons) -Simple injury mechanisms -High throughput -Low technical difficulty -Simple maintenance and analysis -Biomaterial interfacing feasible	-2D environment (*Cells undergo artificial responses to adapt to the flat, stiff surface of 2D cultures systems) -Lack vascular component	(Goshi et al., 2020) (Kumaria, 2017) (Basit et al., 2021)
Primary neural stem cell cultures	Cultures of differentiated stem cells isolated from neurogenic regions e.g. subventricular zone (SVZ)	-High throughput -Low technical difficulty -Multicellular cultures -Simple injury manipulation -Biomaterial interfacing feasible	-Lack immune component -Moderate length differentiation protocols -2D environment * -Preferential differentiation to astrocytes -Lack immune and vascular components	(Vagaska et al., 2020) (Mogas et al., 2021) (Barbora et al., 2020) (Goa et al., 2013)
Induced pluripotent stem cells (iPSCS)	Stem cells genetically reprogrammed from adult cells	-Indefinite propagation -Can be of human origin -Patient specific (retain genetic identity) -Low technical difficulty -Beneficial for patient specific disease modelling -Biomaterial interfacing feasible	-Moderate throughput (long differentiation protocols) -Differ genetically/phenotypically from endogenous counterparts – altered morphology -Heterogeneity of cells -Resistant to cell death -Risk of mycoplasma contamination -2D environment *	(Pistollato et al., 2017) (Tukker et al., 2018) (Ulrich et al., 2001) (Kang et al., 2017)

			-Biomaterial-injury interface not reported -Lack immune and vascular components	
2D primary pure cell cultures	Primary cultures from brain dissociates; purified through sequential shaking or specific media components	-High throughput -Low technical difficulty -Useful to study specific cell responses -Simple injury mechanisms -Biomaterial interfacing feasible	-Overly simplistic model of the brain -2D environment * -Absence of multicellular interactions -Lack vascular and immune component (if not 'pure' microglial cultures)	(Chen et al., 2007) (Vellis and Cole, 2011) (Geddes et al, 2003)
Cell lines: Pure cells, NSCs/ ESCs (neural/ embryonic stem cells)	Immortalised cell lines	-Indefinite propagation -High throughput -Facile -Can be of human origin -Biomaterial interfacing feasible -Simple injury mechanisms	-Genetically and phenotypically differ from endogenous counterparts -High risk of mycoplasma contamination -Cellular heterogeneity -Resistant to cell death -2D environment * -Lack immune and vascular components	(Gordon et al., 2013) (Carter and Shieh, 2015) (Tapia & Scholar, 2016)

Table 1.1: Possible *in vitro* systems for modelling CNS tissue, traumatic injury mechanisms and biomaterial interventions- advantages and disadvantages, arranged from highest complexity to least complexity. Highlighted in green are models of interest within this thesis. Mechanical injury includes – stretch, weight drop and penetrating injuries. *Cells undergo artificial responses to adapt to the flat, stiff surface of 2D cultures systems.

to NSCs, the use of iPSCs over NSCs does not seem appropriate. Again, like immortalised cell-lines these stem cell lines have altered genetic profiles.

To eliminate these concerns, **primary stem cell cultures** can be derived from NSC cultures or mixed brain cultures which are routinely produced from directly dissociating embryonic or post-natal rodent tissue. Primary NSC (isolated from the subventricular zone or the subgranular zone) cultures generate mixed cultures of neurons, astrocytes, oligodendrocytes and OPCs. These multicellular cultures can efficiently mimic some of the features within neural injury, however inevitably they lack one major component, namely the immune cell. Neural stem cells cannot differentiate into microglia as they are of haematopoietic lineage (Vagaksa et al., 2020). In previous years, the role of microglia within the CNS was generally believed to be no more than the removal of dead cells through phagocytosis (Feng et al., 2011). Now increasing evidence has indicated a much higher level of function and importance in the development and maintenance of other cell types. Microglial presence is highly important when aiming to recapitulate endogenous pathophysiology of the CNS as they are necessary in neural cell homeostasis, and lead the neuroinflammatory response (Gu et al., 2011). Understanding microglial responses whilst interacting with other neural cell types is paramount for establishing therapeutic agents (Goshi et al., 2020). Therefore, neural stem cell cultures may not be ideal when modelling injury, considering neuroinflammation is a predominant mechanism of tissue damage (this applies to any model which lacks the immune cell component). Furthermore, in some cases post-natal NSC cultures particularly from the sub ventricular zone preferentially differentiate into astrocytes (Mogas et al., 2021), and this attribute may not be helpful when attempting to achieve a complete multicellular neural model with a large neuronal network.

Over the years **"pure" primary cell cultures, mixed glial models or neuron-glial models** have been used widely as neural disease and injury platforms for drug and therapeutic testing (Malon et al., 2016; Ioannou et al., 2019; Goshi et al., 2020; Lam et al., 2017). Primary mixed cell cultures are generally derived from rodent isolated cortical, hippocampal, or spinal cord tissue dissociates. In particular, the

mixed glial model established in 1980 by Mcarthy and De Vellis has previously been reported in over 2,500 research papers for pharmacological, molecular and biochemical studies (Vellis and Cole, 2011), and more specifically it has been used to understand: the pathophysiology of CNS injury (Koss et al., 2017;), responses to biomaterial implantation (Basit et al., 2021) and for bioscreening of nanomaterials (Jenkins et al., 2016). This mixed glial model with the application of a chemically defined medium has an inherent capacity to promote the generation of the three major glial cells: microglia, OPCs and astrocytes, typically derived from rat post-natal (P0-P3) cortical tissue. This forms a stratified culture of; an astrocytic bed layer, while microglia and OPCs tend to dwell at the surface (McCarthy and De Vellis, 1980). Although mixed glial models are robust and reproducible with a broad applicability within the neuro-regenerative field, it nevertheless fails to replicate the neuronal element of central nervous system tissue (Basit et al., 2021). The lack of the neuronal component means axotomy and neuronal mediated responses cannot be mimicked or investigated, including interactions with various cell types, hence this is a major disadvantage for modelling injury.

Neuron-glial models have been developed however these have been more challenging and typically use embryonic tissue over postnatal to produce more versatile cultures. Embryonic tissues are less vulnerable to damage during the dissociation process. (Sciarretta and Minichiello, 2010). Isolating embryonic tissue for primary culture is not only more technically challenging, but the whole litter and the mother must be sacrificed (removing her from the breeding pool), this is a major ethical disadvantage when considering the 3Rs principles for neural tissue models. In contrast, post-natal models do not always require the whole litter, and the mother is used for further breeding purposes. Generating an efficient neuron-glial culture to model injury will be discussed further in chapter 4.

In vitro 2D culture injury mechanisms: Previously, researchers have lesioned (scratched) confluent cultures of 'pure' astrocytes (Nishio et al., 2005; Etienne-Manneville et al., 2006; Gao et al., 2013), mixed-glial cultures (Basit et al., 2021) and neuro-glial cultures (Goshi et al., 2020), these have shown TBI patho-mimicry of reactive gliosis at the lesion edge. Additionally, neuronal networks have been

subject to lesion studies to achieve axonal transection/regeneration assessment (Chuckowree and Vickers, 2003; Kang et al., 2021). Alternatively, neuroinflammatory responses can be stimulated by lipopolysaccharide (LPS) exposure, glutamate-induced excitotoxicity (Goshi, et al., 2020) or oxygen glucose deprivation (Salvador et al., 2015).

1.4 Hydrogel biomaterials as treatment for SCI and TBI

1.4.1 Why are hydrogels important as a therapeutic strategy?

Hydrogels are a three-dimensional network of hydrophilic polymers that comprise of up to 90% water and can be synthesised from natural or synthetic polymers. The high-water content gives hydrogels a cohesive yet malleable tissue-like quality ideal for imitating extra-cellular matrix (ECM). This makes them favourable for transplantation into the soft tissues on the CNS as they can be conveniently placed and integrated, matching the endogenous mechanical properties and conforming to the defect shape (Ucar and Humpel, 2018). Materials regularly used as regenerative scaffolds include natural polymers, synthetic polymers, biodegradable polymers or functionalised polymers (with immobilised proteins or functional groups). Naturally occurring scaffold materials (i.e., collagen, hyaluronan, fibrin, and glycosaminoglycans) are favoured due to their biocompatibility properties, essential when considering implantation into patients for tissue regeneration (Glowaki et al. 2008; Li and Dai, 2018). Assessment of biocompatibility involves two schools of thought. Firstly, biomaterial transplants should be minimally immunogenic, and consequently do not stimulate an adaptive or innate immune response. Secondly, hydrogels support the growth and survival of host cells and should not be cytotoxic (Aurand et al., 2012). If possible, the material would have an anti-inflammatory/pro repair capacity. Collagen type-1, as the most abundant and ubiquitous molecule within the ECM, is a particularly attractive component of hydrogels and has shown efficient integration within the host tissue and the support/growth of neural cells (Kornev et al., 2018).

Furthermore, the 3D nature of hydrogels offers a multitude of benefits i.e., can fill the injury cavity, offers a structural support to the surrounding tissues, encompass topographies for cellular guidance, and in combinatorial therapies can be utilised as a vehicle for the delivery of transplant cells to the injury site and offer a trophic microenvironment through biomolecule delivery (Aurand et al., 2012; Kornev et al., 2018). All these factors aim to promote a pro-regenerative environment at the injury site for transplant cells and/or recruited endogenous cells to repopulate and regenerate the injured tissue. Transplanting stem cells into the injury site for neural regeneration is a very popular and promising

strategy. However, when injecting pro-regenerative cells into injury sites without a supporting biomaterial scaffold, cells can be disseminated through the surrounding area. Hence, a combinatorial approach where a biomaterial encapsulates the transplant cells is a necessity when considering a cell transplantation therapy for TBI/SCI (Oliveira et al., 2018; Kornev et al., 2018; Adil et al., 2017), this highlights the necessity for developing the most competent biomaterials.

Biomaterials can be developed and fine-tuned to enhance their efficacy, including: pore size for appropriate cellular ingrowth and nutrient delivery, the stiffness modulus for matching to CNS physiology and degradation rate/degradation products for biocompatibility,.

The nature and architecture of collagen hydrogels can be manipulated to have a desired geometry, and the addition of topographical cues into scaffold designs aids contact guidance and can elicit more physiologically relevant cellular behaviours and phenotypes (Shuo et al., 2019). However, one of the major advantages hydrogels offer is their tuneable stiffness. Designing hydrogels of a particular stiffness through determining its Young's modulus (measurement of elasticity) is a major advantage for tissue or cellular specific survival. For example, biomaterial transplantation for bone regeneration would require stiff materials with a high modulus compared to that of the central nervous system, hence hydrogels can be tailored towards the region of transplantation. Survival and differentiation of particular cell types is promoted by various modulus values: NCS differentiating into neurons, astrocytes and oligodendrocytes is favoured in 'soft' constructs ($0.1 - 1$ kPa), and interestingly NSCs preferentially differentiate to neurons in softer substrates (around 500 Pa) whereas harder substrates promotes astrocytic differentiation (5 kPa) (Banerjee et al., 2009; Zimmerman, 2019). Others have shown that oligodendrocytes and astrocytes prefer a rigidity of 6.5 kPa (Lourenco et al., 2016). Interestingly, MSCs will develop neurogenic cells when cultured at 0.1-1 kPa yet produce myocytes or osteogenic phenotypes at stiffnesses between 8-17 kPa and 25-40 kPa respectively. ESCs have been shown preferentially differentiate into mature neurons at a 2kPa substrate (Farrukh et al., 2018). It is also important to note that once you seed cells or cells migrate into your hydrogel this will alter the stiffness modulus of the material (usually this increases).

Once the scaffold has served its purpose it must be biodegradable, and degradation products must be non-immunogenic and non-toxic to the microenvironment hence another reason why collagen is ideal candidate. It is also important that the biomaterial degradation rate is in line with the time scales for axon growth and tissue regeneration to support full recovery of the tissue before the scaffold is degraded (Macaya & Spector, 2012). Post-implantation, hydrogels that completely degrade before tissue regeneration can leave cavities in the reparative tissue (Park et al., 2019). Biomaterial degradation is usually mediated through an inherent time dependency degradation, yet it can be

regulated through a designed "smart release" of its contents. This rate must be established prior to use as a transplant therapy, and imaging these properties *in vivo* has significant challenges without sacrificing the animal an ideal *in vitro* testing model would be required (Oliviera et a., 2018; Park et al., 2019).

Finally, some hydrogels have ability to polymerise in situ in the case of an injection-based system rather an implantation. Injectable hydrogels provide a minimally invasive alternative where the injury cavity can be filled and the gelation process takes process at physiological temperatures (Haines-Butternick et al., 2007). These are very important candidates for less invasive biomaterial therapies, however for the purpose of this thesis we concentrate on implantable hydrogels.

1.4.2 Biomaterials for regenerative neurology

Regenerative scaffolds have been employed in a range of *in vivo* models of CNS injury for developmental testing (highlighted in **table 1.2)** (Sugai et al., 2015; Breen et al., 2016; Han et al., 2015; Yeh et al., 2020; Joosten et al., 1995; Renault-Mihata et al., 2011; Chen et al., 2019), yet interfacing with *in vitro* injury models is rarely reported (Weightman et al., 2014, Basit et al., 2021, Guijarro-Belmar et al., 2019). Collagen hydrogels have been observed to influence some of the major therapeutic goals essential for tissue regeneration and functional repair i.e. reduction of glial scarring, enhancing neurite outgrowth, and attenuate inflammation (Sugai et al., 2015; Breen et al., 2016; Han et al., 2015).

Glial scar reduction may require an attenuation of astrocytic activation combined with the migration of astrocytes away from the injury margins (Renault-Mihata et al, 2011). For example, a collagen hydrogel implanted into mouse SCI which incorporated an astrocytic migration factor, induced an increased astrocytic migration away from the lesion border. Interestingly, the enhanced astrocytic migration reduced glial scarring, demonstrated a simultaneous reduction in neuroinflammation and promoted overall recovery (Renault-Mihata et al, 2011). Other groups have also demonstrated these benefits of biomaterial-mediated astrocyte ingrowth away from the lesion border (Khaing et al. 2014; Joosten et al. 1995). Furthermore, astrocytes have a valuable potential of providing a framework that can facilitate necessary axonal guidance and growth (Sofroniew and Vinters, 2010). Previously an *in vitro* study of a

collagen scaffold with aligned astrocytes directly correlated to enhanced neurite extension. The improvement of neurite outgrowth is lost when there are no astrocytes within the system, suggesting that the presence of astrocytes provides trophic support in neurites outgrowth (East et al. 2010). Furthermore, matching the mechanical properties of the soft neural tissue is highly important for cellular integration of astrocytes and extension of neurites (Macaya et al. 2012). Implantation of a collagen gel into an *in vivo* rat SCI model demonstrated that CST (cortico-spinal tract) neurons were extending into the graft in concurrence with this an extensive astroglial ingrowth. In parallel, a collagen gel of increased stiffness was investigated, and this inhibited the astroglial-material integration and no regrowth of CST fibres was observed (Joosten et al., 1995).

Material	Animal model	Type of injury	Outcome	Functional recovery Motor Sensory		Reference
Collagen	Mouse	Transection	Connection of neural stumps within spinal cord, differentiation of transplanted cells	No	NM	Sugai et al. (2015)
	Rat	Hemisection	Reduction in glial scar and collagen deposition, increase of neurons	Yes	NM	Breen et al. (2016)
	Canine	Transection	Behavioural recovery, glial scar prevention and enhanced axon regeneration	Yes	Yes	Han et al. (2015)
Fibrin	Rat	Transection	Reduced cavity area and enhanced tissue retention	Yes	NM	Mukhamedshina et al. (2018)
Hyaluronan	Rat	Transection	Inhibits inflammation and reduced glial scar formation	Yes	NM	Li et al. (2017)
Alginate	Mouse	Hemisection	Stimulates neurite growth	NM	NM	Forton et al. (2016)
	Rat	Transection	Enhanced growth of neurons	Yes	NM	Jiao et al. (2017)

Table 1.2. Natural regenerative biomaterials for CNS injury *in vivo*. Yes: improvement in function; No: no improvement in function NM: no improvement mentioned.

Successful pre-clinical animal experimentation of biomaterial implantation has led to clinical trials for the treatment of spinal cord injury, these include: a collagen scaffold functionalised with BDNF and human umbilical cord mesenchymal stem cells (hUC-MSCs) (Li et al. 2017), a collagen scaffold embedded with patient derived olfactory ensheathing cells (Tabakow et al., 2014), an acellular synthetic scaffold (Kim et al., 2021). Additionally, a clinical trial investigating a combinatorial therapy of functional collagen scaffold transplantation in conjunction with an epidural electrical stimulation is currently running (http://clinicaltrials.gov). At present, there has been no scaffold therapies in clinical trials for pTBI and the existing clinical trials for SCI biomaterial therapy are still in progress. Many scaffolds with separate mechanical strength, porosity, biodegradability and spatial structure have been advanced though SCI and TBI repair in animal models. Even though therapeutic outcomes are beneficial, globally no commercial biomaterial has yet been approved for treating patients with SCI or TBI, and currently available scaffolds are routinely rejected for human treatment, presenting a major barrier to therapeutic translation, and overwhelming use of animal models for biomaterial testing (Ucar and Humpel, 2018; Prestwhich et al. 2012).

1.5 Electrical stimulation as a therapeutic approach for SCI and TBI

1.5.1 Scientific rationale for use of electric fields in brain and spinal cord regeneration

The presence of endogenous electrical fields and its crucial purpose in facilitating neural tissue development and polarisation, has encouraged exploration of electrical stimulation (ES) on neuronal growth and orientation in 2D, 3D and *in vivo* models (Borgens et al 1981; Patel and Poo, 1982; Tang-Schomer et al. 2018; Yang et al. 2019; Alexander et al. 2006; Yao et al. 2008; Al-Majed et al. 2000; Udina et al. 2008; Carmel et al. 2014). Original *in vivo* studies that applied direct current (DC) electrical fields to Xenopus neurons demonstrated preferential sprouting of neurons towards the cathode, whilst simultaneously retracting fibres away from the anode. At the same time astrocytes were found to have preferential alignment and migration towards the anode (Patel and Poo 1982; Borgens et al., 1981;

Borgens et al., 1986). The two-way projection required for injury repairs posed an interesting problem since the DC-induced axon growth is unidirectional towards the cathode and a retraction from the anode. However, this phenomenon was partially resolved through the observation that the rate of axon growth towards the cathode is faster than the retraction from the anode (Bacova et al., 2019). Therefore, with application of an oscillating electrical field stimulation (OFS) or alternating current (AC) (alternation of the anode and cathode polarity) growth of neurons can be encourage from either side of the lesion still with a lower rate of retraction (Tang-Schomer et al. 2018; Yang et al. 2019). These initial in vitro experiments showed that the polarity reversal had two effects promoting axonal regeneration: a) it encouraged a bidirectional outgrowth and b) the reversal neutralised the electrochemical by-product that usually accumulates at the electrodes.

Paper and reference	Model/ cellular response	*In vivo*/vitro	Technique/Parameters	Result	Publisher
Error! Reference source not found. (Zang et al., 2018)	Astroglial scar	*In vivo* Rat	-Weight drop SCI -8 weeks -OFS -600uV/mm	-OFS decreased glial scar	Biological information and biomedical engineering
Electric field-induced astrocyte alignment directs neurite outgrowth (Alexander et al., 2008)	Primary astrocytes and dorsal root ganglia neurons	*In vitro*	-EF chambers -10mV/mm > 500mVmm -DC -24hrs astrocytes - add neurons then 48hrs +/- ES	-Astrocytes alone aligned after 24 w/o reapplication alignment is not sustained -Neurons aligning with astrocytes was enhanced with reapplied field	Neuron Glia Biology
Error! Reference source not found. (Yang et al., 2019)	Primary astrocytes human adult brain	*In vitro*	-EF chamber -40-300mV/mm -4h timepoint	-Highest migration 300mV/mm -Elongated morphology perpendicular to EF	Experimental cell research
Error! Reference source not found. (Yao et al., 2008)	Hippocampal neurons	*In vitro*	-EF chamber salt bridges -50-300mV/mm -EF 1h then polarity reversed 1h -8 hour stim	-Cathodal migration -120mv/mm + striking cathodal migration	Journal of Cell Physiology
Error! Reference source not found. (Tang-Schomer, 2018)	Dissociated cortical neurons	3D *in vitro* model	-Silk protein scaffold -ES via embedded gold wires - 80mv/mm at 0.5hz-2khz -Stimulated at 3 DIV -Timepoints – 24h, 48h + 4d	-0.5-20Hz promote axon growth -2Hz most significant -Perpendicular orientation -Significant outgrowth found at 24hr+	Brain research

Error! Reference source not found. (Zhang et al., 2018)	Primary cortical neurons	*In vitro* 3D collagen gel	-Conductive polymer -ES 8h per day for 3 days -1.25/0.75 mA/cm2 -100µs pulses 20µs interphase 250Hz (biphasic)	-Enhanced neurite outgrowth -Enhanced synaptogenesis -Neural cell aggregation	Scientific reports
Epidural oscillating field stimulation as an effective therapeutic approach in combination therapy for spinal cord injury (Bacova et al., 2019)	Compression SCI in rats	*In vivo*	-OFS 15-minute reverse polarity -50uA -4-week stimulation	-Reduced astrogliosis -Increased numbers of neurofilaments -Reduced inflammation	Journal of neuroscience methods
Error! Reference source not found. (Koppes et al., 2014)	Peripheral – dorsal root ganglion cells	*In vitro* 2D	-ES chamber -DC ES 8 hours at 50mV/mm 1mA	-ES enhances neurite outgrowth by 32% -126% increase with ES plus aligned fibres -Field polarity had no influence of directionality of neurite	Journal of neural engineering
Error! Reference source not found. (Jack et al., 2018)	Neuronal outgrowth	*In vivo* adult rat cervical SCI	-Cortical ES -20Hz or 333 Hz (pulse width 0.2ms) -Incomplete transection	-Significantly enhanced axon collateral sprouting with ES -No difference in regeneration between ES groups -Increased dieback with low ES	Journal of neuroscience research
Error! Reference source not found. (Carmel et al., 2010)	Functional recovery and neuronal outgrowth	*In vivo* rat	-Incomplete transection -Cortical ES -0.2ms, 333Hz, 1.1-1.8mA -6h ES period for 10 days	-ES restored skilled locomotion -ES promoted outgrowth of CST axons to impaired side	Journal of neuroscience

Table 1.3. Summary of a range of *In vitro* CNS models that has been used for the assessment of electrical stimulation

Borgens et al. went on to establish that an electric field that switched polarity every 15 minutes applied to naturally injured paraplegic dogs with SCI significantly improved the locomotor outcomes post implantation. The stimulation delivered for 3, 6 or 15 weeks at 200 µA resulted in a significant improvement of the neurological scores by 6 months (Borgens et al. 1993). Other promising OFS canine SCI trials were also carried out by Shapiro et al. (2005). This saw an improvement in locomotor function from a low frequency, slowly oscillating electric field. Additionally, other *in vivo* studies on SCI and TBI have similarly highlighted a positive influence of OFS on axon growth, locomotor function, cognitive function (Al-Majed et al. 2000; Udina et al. 2008; Carmel et al. 2014) and glial scar reduction (Zhang et al., 2018). These indicate that ES mechanisms must have a pro-regenerative effect, possibly through an enhanced growth of regenerating axons thus promoting the formation of new connections, and through astrocytic migration away from the lesion site for glial scar reduction. Although *in vitro* models have also shown enhanced outgrowth through OFS stimulation in primary neuronal cultures (Koppes et al., 2014; Yao et al., 2008), **these mechanisms have not yet been confirmed through *in vitro* neural injury systems**.

Following the initial pre-clinical canine studies, the separate teams of Borgens and Sharpiro began OFS experimentation in human clinical trials under very similar criteria. Patients received initial surgical intervention which included decompression, then OFS devices were implanted 18 days after initial injury through a second surgery. Electrodes emitted 200µA of stimulation and polarity reversed every 15 minutes. Patients were shown to have a significantly improved recovery with the OFS treatment (assessed through ASIA scoring system). Surprisingly, despite the positive outcome the technology has remained relatively dormant since then without explanation (Jianming 2019). Furthermore, ES has been applied for the treatment of cognitive and consciousness disorders post mild TBI, this is known as "deep brain stimulation", this also has demonstrated significant functional recovery in patients and *in vivo* models over the past years (Schiff et al., 2007; Kundu et al., 2018). ES as a regenerative therapy for cases of severe TBI with penetrating injuries has not been well documented.

furthermore, more recent *in vitro* studies have assessed the behaviour of axon growth in a 3D brain-like tissue model with AC stimulation. The brain tissue model is likened to a donut shape where the central core is acellular, and under electrical stimulation axons were stimulated to grow into the central core of the scaffold. 24 hours after stimulation, neurite growth preferentially aligned perpendicular to the orientation of the electrical current axis. Interestingly, through 3D neurite tracing, this group established that 200-2000Hz significantly inhibited axon outgrowth in contrast to enhanced outgrowth with stimulation at 0.5-20Hz. 2Hz exhibited the strongest effect of statistical significance for axonal growth into the central core after 4 days of continuous AC stimulation (Tang-Schomer et al. 2018). These are interesting findings that can benefit towards establishing the correct parameters for an injury environment, yet as neurons are intact in this model this could differ appropriate parameters could differ somewhat.

Electrical stimulation is thought to enhance the expression of the neurotrophic growth BDNF (Al-Majed et al. 2008) and this expression could be correlated with its potential in enhancing neuronal outgrowth. BDNF has the ability to protect injured neurons post PNS injury and enhance regeneration by promoting neurite outgrowth, re-myelination and projection mapping. Mice deficient in BDNF receptor treated with ES failed to present any regeneration, compared to the nondeficient mice (Wenjin et al. 2011), which confirms the fundamental prominence of BDNF function for regeneration with ES. A system that promotes optimal BDNF expression through ES could be a successful approach. In addition to axonal fibre outgrowth, applied electrical fields have been recognised as guidance cues for migrating neurons, where hippocampal neurons have been shown to migrate towards the cathode. In development, axonal outgrowth is influenced via other neuronal bodies, so this alignment of neuronal bodies has potential *in vivo* to guide regenerating neurons. In respect to an injury environment ES-directed neuronal guidance could be beneficial as this has the potential to align transplant cells while enhancing endogenous outgrowth (Yao et al. 2008).

Similar to neurons, astrocytes have also shown distinctive responses to applied electric fields, which includes migration towards the anode (opposite to neurons) (as mentioned previously), an elongated cellular morphology and a perpendicular orientation to the electric current. More importantly, ES can induce astrocyte migration and alignment, and this could essentially support and direct neurite growth or induce astrocytic migration away from the active injury site (Yang et al 2019; Alexander et al 2006) or this could be important to promote reactive astrocytic migration away from the lesion site in order to reduce glial scarring. Oscillating field stimulation (OFS) implemented into a CNS weight drop injury model illustrated that GFAP fluorescence intensity in the control groups (laminectomy and weight drop injury) exhibited significantly higher expression of GFAP compared with the OFS treated group (laminectomy, weight drop injury and OFS). This indicates that there may be a correlation with the application of an electrical field and the reduction of the glial scarring. This could be through 2 mechanisms: a) the applied electrical field reduced GFAP expression inducing astrocytes into a less-reactive state or b) the ES has promoted migration of reactive astrocytes away from the lesion where they in turn become less reactive. This group supported their findings via western blotting expression analysis of certain astrocytic markers; GFAP, Neurocan and PCNA. Neurocan is a CSPG primarily produced reactive astrocytes and within the glial scar (McKeon et al. 1991). PCNA is a reliable marker for proliferating cells, and in this study it was used to investigate astroglial proliferation, however this protein is not unique to proliferating astrocytes. PCNA, Neurocan and GFAP followed a similar pattern of statistical analysis, with OFS treated groups displayed significantly lower levels of all these proteins in comparison to the injury only group. This suggests that OFS application reduced the proliferation and reduced the glial scar proteins that are usually upregulated in injury (Yang et al 2019). In parallel, a second report of an *in vivo* CNS model showed that OFS significantly reduced the area of the injury cavity and cavity perimeter of injury. In this study the field was applied parallel to the spinal cord at 0.6mV/mm where polarity was reversed every 15 minutes (Zhang et al., 2018). It is possible that ES stimulation may have a multitude of effects of astrocytes at the lesion site, including inducing migration away from the epicentre, mediating the upregulation of GFAP in activated astrocytes and an inhibition

of the proliferation of astrocytes (all these can exacerbate injury if not controlled). There have been a range of parameters used for electrical stimulation of the CNS *in vitro* and *in vivo* and these are described in the **table 1.3**.

1.5.2 The need for *in vitro* electrical interfacing systems

Currently there are major limitations with evaluation of electrical stimulation for regenerative studies. Firstly, development of ES parameters and understanding the direct mechanism on the CNS parenchyma is difficult to achieve *in vivo,* yet in vivo models are most commonly used to test ES therapies. Since *in vivo* modelling systems are highly complex and observing the effects of ES is not straightforward, many timepoints and techniques would be required to achieve suitable assessment. Additionally, appropriate ES parameters for injury environments are not yet widely understood hence these require a diverse investigation. Together, this means many animals would be required for this kind of development study *in vivo*. Sacrificing this many animals for a multitude of parameters it not considered ethical and hence an alternative method is essential. Secondly, most *in vitro* studies of electrical stimulation of neural cells are employed to a non-injury environment, therefor not appropriately modelling the response of injury-activate cells to the stimulus. Unfortunately, interfacing electrical recording/stimulation systems with *in vitro* traumatic injury modelling systems for the CNS has rarely been reported. An ideal scenario would incorporate an understanding of the underlying electrophysiological signature of the injury environment in combination with a subsequent investigation into the influence of an electrical stimulus. This thesis will aim to look at an in vitro stimulation and recording system in which the injury environment can be assessed pre and post stimulation, with the eventual aim to establish the correct stimulation parameters for regeneration of injured neural tissue.

1.5.3 Methods for electrical interfacing *in vitro*

Electrical stimulation parameters applied to cell or slice cultures of the CNS generally range from 10-400µA of current strength with stimulation periods of 10-90 minutes over various days *in vitro* (Euskirchen et al., 2021). The most widely used method for electrical stimulation *in vitro* is through direct coupling of singular electrode probes. Direct coupling involves two electrodes (anode and cathode) that are inserted directly into the culture medium at apposing ends (**figure 1.6 A**). Here the electrical current is carried through the culture media and the electrical field generated passes over the cells within the culture. However, contact with the medium can lead to temperature rises, pH changes and generation of harmful by products when applied for long periods of time (Chen et al., 2019). Alternatively electrical stimulation chambers can be used, generally with a top lid consisting of platinum electrodes and a 6-well culture plate wells beneath that are simultaneously stimulated (**figure 1.6 B**). This essentially creates the same electric field current between the anode and cathode as the direct coupling method. Both these systems however only produce direct current stimulation. Alternating the polarity of the electrodes i.e., reversing the anode and cathode can generate an oscillating field stimulation (OFS) or an alternating current (AC) (Mobini et al., 2018). This system can be effective for the stimulation of cells however they do not give information on any basal electrical activity of the cultures and the activity responses to stimulation.

Alternatively, multi-electrode array (MEA) systems are another method for stimulating cells or tissue *in vitro*, this involves an array of microscopic electrodes distributed over a small surface area which can record from and directly stimulate the cells/tissue juxtaposing the electrode. Micro-electrode electrical stimulations have been widely consolidated for use in studying neuronal networks, treating brain diseases and somatosensory dysfunction (Kumar et al., 2016; Benabid et al., 2009; Fan et al., 2019). This *in vitro* technology enables the exploration of multiple parameters in varying voltages and frequencies to electrically stimulate neurons in 2D/3D cultures or slices. More recently, a wireless OFS communication device has been designed specific for *in vivo* use. This integrates microelectronics into a low-power circuit, and generates a current of 200µA per electrode whilst simultaneously monitoring

the current output (Jianming, 2019). As MEAs can simultaneously record electrically signals this is an attractive platform for understanding the injury environment.

Nevertheless, *in vitro* MEA systems are not yet employed for regenerative purposes and currently there appear to be no reports on interfacing *in vitro* neural injury models with MEAs to either: i) study the electrophysiology of the injury environment or ii) to study a potential electrical stimulation therapy. This particular research gap leads on to last objective of this thesis.
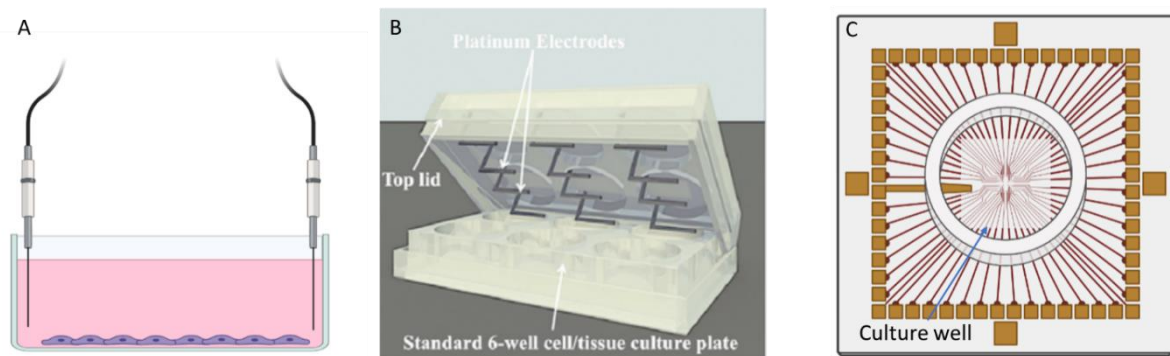
Figure 1.6: Separate methods for electrical interfacing *in vitro*. A directional coupling. **B** electrostimulation chamber. **C** multi-electrode arrays. A and C created with BioRender.com. B adapted from Mobini et al., 2018)

1.6 Knowledge gaps and thesis objectives

In summary, the extensive use of live animal models in CNS regenerative research and tissue engineering, particularly in transecting spinal cord injury and penetrating traumatic brain injury (as described) necessitates for the development of effective *in vitro* neurological injury models. Unlike *in vivo* testing, these models can ethically allow for the high-throughput developmental optimisation necessary for various therapeutic strategies, specifically biomaterial assessment and establishing parameters for electrical stimulation. As many *in vitro* models are overly simplistic (i.e. mono and co-cellular cultures) this thesis aims to develop and test more complex *in vitro* models of injury, to generate a multidimensional cellular response. The developed models will be used for biomaterial testing and interfacing with bioelectronic systems (MEAs). We set out to investigate biomaterial and

electrostimulation therapy independently will the eventual aim to apply these as a combinatorial therapy to boost regeneration efficacy.

The thesis objectives are:

1) To model traumatic brain and spinal cord injury in organotypic slice cultures and test implantation of a surgical grade matrix (DuraGen™) in these models (**chapter 3**).

2) To develop an *in vitro* 2D multicellular neural injury model of cortical dissociated cells, and refine this into a 3D injury model encapsulating cells in a biomimetic substrate (**chapter 4**).

3) To interface the injury model developed in chapter 4 with MEAs and establish a proof-of-concept for MEA-induced electrical stimulation (**chapter 5**).

2 Chapter 2: Methodology

2.1 Reagents

Slice and cellular culture: Millicell culture inserts (PICM0RG50) and Omnipore™ (JHWP04700) membranes were from Millipore (Watford, UK). Needles (21 gauge) were obtained from BD Biosciences (Oxford, UK). Disposable scalpels and size 15 surgical blades were obtained from Swann-Morton (Sheffield, UK). Cell culture grade plastics were purchased from Fisher Scientific (Loughborough, UK). Media components were from Thermo Fisher Scientific (Loughborough, UK), and Sigma-Aldrich (Dorset, UK). Primary cell culture and slice culture media components included Dulbecco's Modified Eagle Medium (Fisher 41966029), Neurobasal-A Medium (Fisher 11540366), minimum essential medium (MEM) (Invitrogen 42360-024), Earle's Balanced Salt Solution (EBSS) (Invitrogen 24010-043), heat-inactivated horse serum (HS) (BioSera S0910-500), Foetal bovine serum (FBS) (Fisher 11573397), HEPES (BioSera L0180-100), D-glucose, penicillin-streptomycin solution (Fisher 11528876), B27 supplement (Fisher VX17504044), sodium pyruvate (Fisher 11360070) and glutaMAX-I (Fisher 35050061). Neurosurgical biomaterial DuraGen Plus™ was from Integra LifeSciences (New Jersey, USA). The Mcllwain tissue chopper was from The Mickle laboratory engineering co. Ltd (Guilford, UK). Paraformaldehyde (PFA) was from Thermo Fisher Scientific (Loughborough, UK).

Collagen gels: To generate collagen gels rat tail collagen type 1 (Sigma-Aldrich), 10x MEMα (Gibco), acetic acid and sodium hydroxide (Sigma Aldrich) were used. Live dead assay: Ethidium homodimer (Sigma E1903), Calcein AM (VWR 89139-470).

Antibodies: Primary antibodies were rabbit anti-β-tubulin (Tuj-1) (BioLegend 801202) (1:500), goat anti-ionized calcium binding adaptor molecule 1 (Iba1) (Abcam ab5076) (1:200), rabbit anti-glial fibrillary acidic protein (GFAP) (BioLegend 644702) (1:500), mouse anti-neuronal glial antigen2 (NG2) (Abcam ab275024) (1:200), rat anti-myelin basic protein (MBP) (BioRad 160223) (1:200). A summary of the antibody targets are given in Table 1. Fluorescein isothiocyanate (FITC) and cy-3 conjugated secondary antibodies were from Jackson Immunoresearch Laboratories Ltd (Westgrove, PA, USA). Vectashield

mounting medium with 4,6-diamidino-2-phenylindole (DAPI) was from Vector Laboratories (Peterborough, UK).

Antigen	Description and cellular target
GFAP	Cytoskeletal protein in astrocytes
Tuj-1	Major constituent of microtubules in neurons
Iba1	Microglia-specific calcium-binding protein
Ng2	Integral membrane chondroitin sulfate proteoglycan found on (OPCs)
MBP	Main component of myelin generated by oligodendrocytes

Table 2.1. Immunostaining antibody targets and their cellular function.

2.2 Generating brain and spinal cord organotypic slices, introducing injury and implantation of DuraGen™

Brain and spinal cord slice culture and lesioning methods were adapted from Weightman et al., 2014. Spinal cord organotypic slice cultures and brain organotypic slice cultures are named scOSCs and bOSCs respectively for the purpose of this report.

2.2.1 Brain and spinal cord dissection from P1-P4 mice.

The care and procedures involving the mice were in accordance with the Animals Act of 1986 (Scientific procedures UK) and with the local ethics committee approval. Mouse pups (BALB-CJ) (litters ranged from 8-12 pups) aged postnatal day 1-4 (P1-P4) were administered with pentobarbital, then decapitated once unresponsive to a hindfoot pinch.

For brain dissection the skull was revealed via an incision through the skin from neck to nose using dissection scissors. Next a central incision through the skull bone (very soft at this age) from the back of the skull to nose was made using micro-dissecting Vannas spring scissors. Lateral incisions were made from the central incision to create flaps in the skull. Using the spatula, the skull bone flaps were lifted, and the brain was removed carefully ensuring no damage to the brain tissue. The brain tissue was immediately placed in slicing medium (Earle's Balanced Salt Solution (EBSS) buffered with 2.5% of 1M HEPES) on ice.

For spinal cord dissection, an incision into the skin was made using dissection scissors up the dorsal midline and through the dorsal neck muscles, the skin flaps and neck muscles were retracted to expose the spinal column. Next, a midline incision was made down the length of the spinal vertebrae via fine micro-dissecting Vannas spring scissors (ensuring the spinal cord tissue was not damaged). To completely reveal the spinal cord, the vertebrae were pushed back at either side of the column using the back of the closed fine dissecting scissors. A scalpel blade was run down either side of the spinal cord to release any peripheral nerve connections from the central spinal cord. An incision was made at the start of the thoracic region (with small Vannas scissors) then the spinal cord released of any connections. Following this, the length of spinal cord from the thoracolumbar region was removed using a small spatula and immediately placed in slicing medium on ice (**figure 2.1 1**).

2.2.2 Generating organotypic brain and spinal cord tissue slices.

The spinal cord was transferred to the chopping plate of a pre-set McIlwain Tissue Chopper and sliced longitudinally along the parasagittal plane (**figure. 2.1 2**) at 350µm thickness. The brain was cut down the sagittal midline with a scalpel and sliced with the tissue chopper along the coronal plane (**figure. 2.1 2**) (350µm thickness). The brain and spinal cord slices were immediately placed in fresh slicing medium and kept on ice for 90 minutes. At 90-minutes, slices were transferred to pre-cut Omnipore 'confetti' membranes, resting on Millicell culture insert membranes inside small round petri dishes (one slice per confetti, three confettis per insert) with culture medium (50% minimum essential medium (MEM), 25% heat-inactivated horse serum, 25% EBSS and supplemented with 36mM D-glucose, 0.5% pen/strep). A wide-bore plastic Pasteur pipette (trimmed down for brain slices) was used to facilitate the transferring of a slice to the membrane, and any excess slicing medium was removed through a narrow bore Pasteur pipette. The pre-cut confetti for each slice allows manoeuvrability of individual slices (**figure. 2.1 3**). This set up generates an air-medium interface between the culture medium and the humidified atmosphere; the medium provides adequate nutrition to the tissue slice through capillary action whilst the air regulates appropriate gaseous exchange throughout the slice. Slices were

cultured for up to 18 days, 5 small petri dishes were placed inside a large square petri dish for ease of transportation and improved sterility, these were incubated at 37°C, 5% C02. Following 4 days *in vitro* (DIV) a transecting lesion was introduced to mimic traumatic neurological injury. Every two days a 50% medium change was carried out.

2.2.3 Introducing a transecting lesion to the organotypic slices.

A double-bladed scalpel tool was assembled with a distance between each blade of 300μm, meaning a reproducible lesion size of approximately 300μm would be produced when introducing the transection injury to the bOSCs and scOSCs. Lesions were made perpendicular to the length of the slice and carried out under a dissection microscope in sterile conditions (**figure 2.1 3**). The lesion tool was used primarily to mark out the lesion margins and if it was difficult to cut (usually the case with the scOSCs) a scalpel would be used along the same lines to cut the tissue efficiently. The waste tissue from the injury was removed and any debris was cleared via the aspirator with a fine nozzle to leave a clean transecting lesion.

2.2.4 Introducing DuraGen™ scaffold into the lesion site.

Once the bOSCs and scOSCs were generated and the injury introduced, DuraGen™ was implanted within an hour of lesioning. DuraGen™ is a porous substrate which absorbs medium and swells in size, therefore application of the material to the tissue slice lesion is only carried when the material has been soaked in medium (more details on DuraGen™ is found in the chapter specific introduction for these experiments chapter 3). DuraGen™ is supplied sterile and to prepare DuraGen™ for implantation, a small section (~ 5mm x 5mm) was cut from the DuraGen™ sheet provided with a scalpel. This was then transferred to the pre-set tissue chopper under sterile conditions with a small drop of medium and then sliced at 250μm thickness (**figure 2.1 4**) (thickness optimised within our laboratory by Finch et al., 2020). One sheet was then transferred back to tissue chopper and chopped to a 300μm width (approximate lesion distance). In preparation for lesion width variations (smaller or larger than 300μm) the material was also cut at varying diameters. The sliced material was then transferred to a small petri dish of

media, sealed with parafilm, and kept at 4°C until further use. Post-injury the DuraGen™ material was implanted within one hour of injury, and this procedure was carried out under a dissection microscope in sterile conditions (**figure 2.1 5**). As the transection length can vary, particularly between spinal cord and brain slices, DuraGen™ was cut to size with a scalpel to match the length of the injury area. Both injury only and injury + DuraGen™ (DG) slices were maintained in the same conditions throughout.

Note: for the assessment of microglial morphology, the DuraGen™ was additionally sliced at a 150-200µm thickness. When immunostaining for microglial markers it was established that thinner material allowed for optimal visualisation of the microglia.
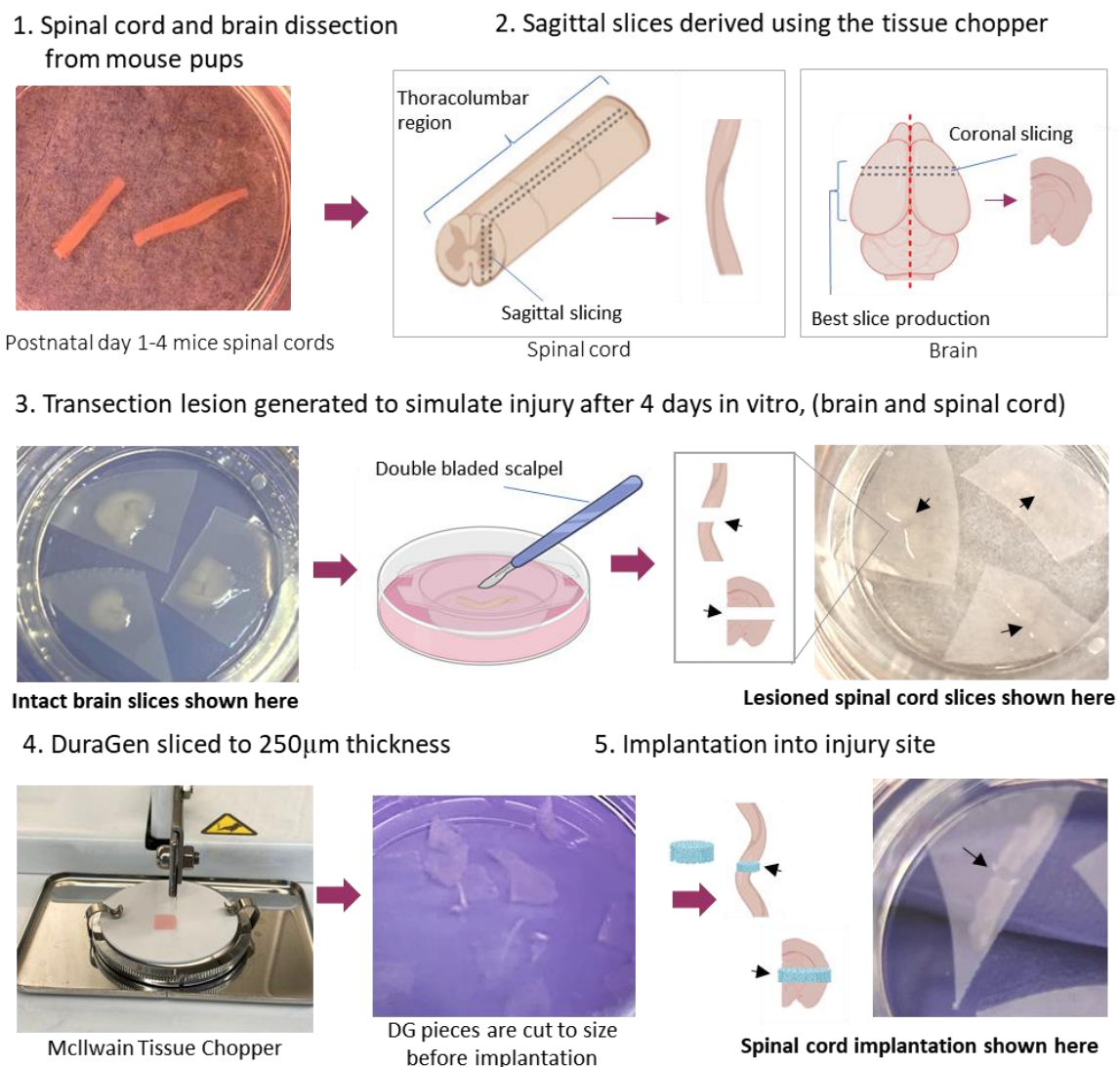
Figure 2.1: Schematic representation of experimental process from mouse spinal cord/brain slice culture and the implantation of DuraGen™

2.3 Slice viability and assessing cellular responses via immunocytochemistry

2.3.1 Viability assessment

Prior to fixation, live/dead assays were carried out at 5DIV, 11DIV, 18DIV, 7DPL and 14DPL, which involved submerging the slices in a solution diluted in the normal culture medium of 3µl/mL ethidium homodimer to label dead cells and 1µl/mL of Calcein AM to label live cells for 40 minutes at 37°C. Slices were then mounted on a glass slide with DAPI mounting medium for imaging. Fluorescence micrographs of live/dead staining were captured with consistent exposure settings.

2.3.2 Fixation and immunocytochemistry for slice cultures

At appropriate times point post lesioning (4, 7 or 14 days), slices were fixed with 4% paraformaldehyde (PFA) in PBS for 1hr. After fixation slices were washed with PBS 3 times and incubated with blocking buffer (5% normal donkey serum and 0.3% Triton-X-100 in PBS) at room temperature (RT) for 1 hour. Following this, samples were incubated with the appropriate primary antibodies diluted in blocking buffer overnight at 4°C: Tuj-1 (1:500), GFAP (1:500), Iba1 (1:200). Slices were washed 3 times with PBS, 5 minutes per wash, and incubated with the appropriate secondary antibodies diluted in blocking buffer (1:200) for 4 hours at RT (or overnight at 4°C) in dark conditions. Subsequently, slices were washed 3 times with PBS (5min/wash) and mounted on glass slides with Vectashield mounting medium (containing DAPI for the nuclear stain). Mounts were sealed with varnish and allowed to dry before imaging. Images of spinal cord and brain organotypic slices with or without implanted DuraGen™ were taken under a fluorescence microscope (Leica DMC 2500 LED) equipped with a CCD camera (DFC350 FX). The software used for imaging was Leica Application Suite X v.1 (2017).

2.3.3 Transmission electron microscopy (TEM)

2.3.3.1 Sample preparation

Transmission electron microscopy (TEM) was carried out to visualise the tissue responses to DuraGen™ at high resolution. TEM utilises energetic electrons to provide biological ultrastructural information with

a maximum resolution of 2 nm allowing magnifications beyond light microscopy (90X − 500,000X magnification). Slice preparation for TEM required multiple steps over a 2-week period. The samples were pre-fixed with 2.5% glutaraldehyde in 0.1M sodium cacodylate (CAC), after 1 hour this was removed then washed with 1% sodium cacodylate 3 times. The fixed samples were incubated in osmium tetroxide (OsO4), a post-fixative, for 1 hour (tissue samples become blackened) and then washed with dH2O 3 times. The next process was sample dehydration, wherein water is completely removed from the samples using a series of increasing concentrations of alcohol: the sample was placed in 70% ethanol for 10 minutes, 90% for 10 minutes, 100% ethanol for 15 minutes, then lastly 100% dry ethanol for 15 minutes. Following this, samples were infiltrated with a series of Spurr resin concentrations. Firstly a 1:1 concentration of resin:dry absolute ethanol was added to the sample for 1 hour. Next 3:1 resin:propylene oxide dilution was added overnight. The following day the sample was placed in pure resin 3 times for 2 hours (*fresh resin each time). Following the resin infiltration steps the tissue samples were ready for embedding. Each sample was placed into a planchette mould and pure resin was added to fill the mould, these were then placed into a 60˚C oven for 2 days to polymerise the resin.

2.3.3.2   TEM sample trimming

Post-polymerisation of the resin the sample was removed from the planchette and was then ready for trimming and section cutting. The hardened block was trimmed to the area of interest using a saw and further trimmed to have a small cutting face in the shape of a trapezoid (figure 2.2b) via a razor blade. Final trimmings were made using the precision controls of ultramicrotome (figure 2.2a) and a glass knife (figure 2.2d). The width of the trapezoid should be around the $\frac{1}{5}$ - $\frac{1}{4}$ of the knife edge length.

2.3.3.3   Glass knife production

A glass knife was made from a strip of glass using a specific manual glass knife generator (**figure 2.2 C**). Firstly, a line was scored in parallel to the glass edge, generating a square shape, then the glass was snapped to produce a glass square. Following this, the glass square was repositioned, scored diagonally,

and snapped again producing a diagonal fracture and 2 triangular glass knifes. The knifes edges were examined for quality: edge imperfections or knicks. The sharpest edge of the knives are parallel to stress line before it begins the downward arc (**figure 2.2 D**), the far-right corner here would be avoided. Of the two knives generated by the bisecting square, one was commonly of better quality than the other. New glass knifes may be required often to ensure a smooth cutting edge; the cutting action itself can results in knife edge imperfections, these can lead the scratch lines on the cutting face of the sample, which ideally would be avoided.
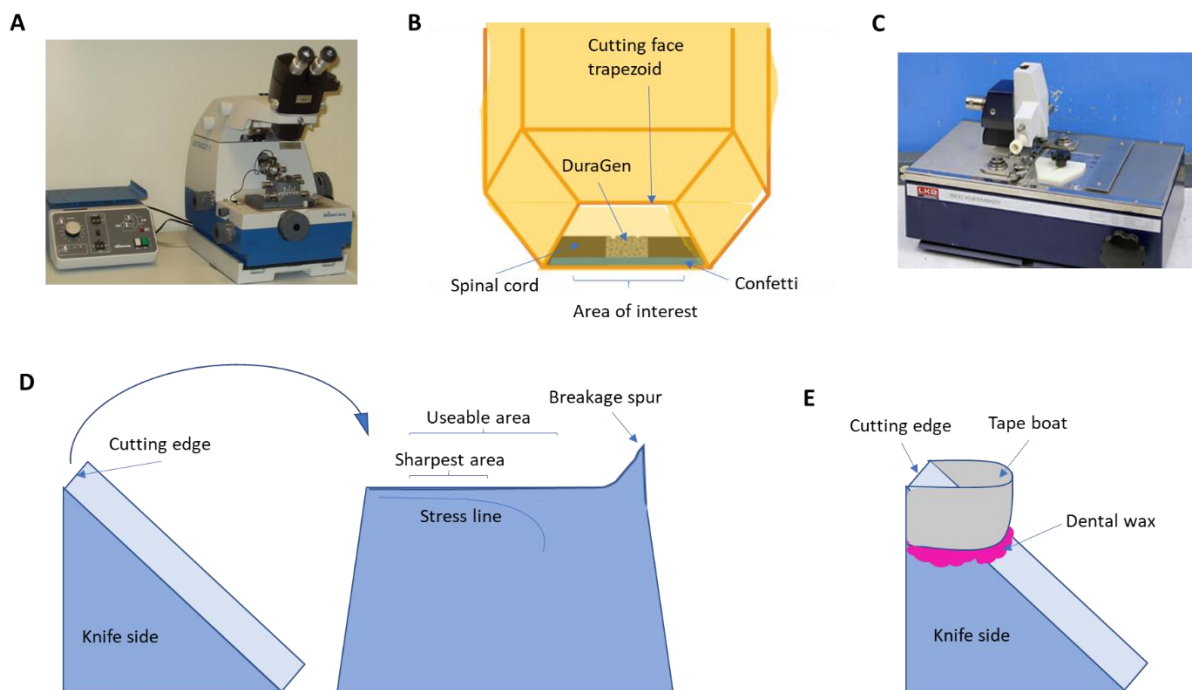
Figure 2.2: Equipment images and diagrams to aid the explanation of TEM techniques. **A** image of a ultramicrotome. **B** diagram of the cross section of the area of interest on the trapezoid face cut with the razor blade under the ultramicrotome. **C** the glass knife generator. **D** diagram of the glass knife produced and identifying the best cutting area. **E** demonstrates how to assemble the tape water boat for collecting ultra-thin sections.

2.3.3.4 Sample sectioning

The glass knife was inserted into the ultramicrotome and the sample was cut until the appropriate cross section of the sample was exposed. The area of interest in the tissue sample was firstly identified via survey sections. A survey section of 1 µm was cut and transferred to a drop of water on a glass slice

using fine forceps. By waving the glass slide over a flame the water evaporated leaving the section, then a drop of toluidine blue stain was added to the section, gently warmed for a few seconds over the flame and then washed off thoroughly to reveal the tissue components. The survey sections were examined under a light microscope to locate area of interest and check preservation of the tissue. Survey sections were too large and thick to use under electron microscopy.

The block was then retrimmed suitably, and ultrathin sections (<90 nm) were cut. The glass knife can be replaced with a diamond knife which makes cutting of the ultrathin sections easier. However, these are expensive and easily damaged (within this experiment glass knifes were used throughout). Next a water bath was made on the glass knife (using tape and hot wax to seal) **(figure 2.2 E)** and filled with water. The ultrathin sections floated onto the water as they leave the knife edge. Compressions in the sections were removed by using chloroform vapour. Sections have certain colours that relate to their thickness, only silver to gold sections are suitable for electron microscopy (<90 nm).

2.3.3.5   Staining the sample sections for TEM

Once silver and gold sections were generated, they were ready to be collected onto a copper alloy support grid 3mm in diameter. The grid was lowered into the water bath and the ultrathin tissue sections were picked up. This was then dried ready for staining. To stain the samples, the grid was lowered into a drop of uranyl acetate (2% saturated UA in 70% alcohol) solution for 10 minutes, dipped into 3 pots dH_2O 10 times each pot. Next, the grids were lowered into a drop of lead citrate (0.4g lead citrate in 10ml dH_20 and 500 ⃝L of 4N NaOH, centrifuged and supernatant used) for 15 minutes and washed again by 10 dips in 3 pots of dH_2O and left to dry. The samples were now ready for viewing under the electron microscope. These heavy metals dyes enhance the contrast between cellular compartments. The regions within the sample with heavy metals deposits deflect the electron beam, and thus scattered so that the intensity is reduced, giving a 'shadow' view. These dark areas are referred to as being electron dense. Areas of the sample lacking heavy metals allow electrons to pass through to the phosphor screen where they activate the emission of visible light to different intensities.

2.3.3.6 How to use the transmission electron microscope

The TEM is a complex and delicate machine and must be treated with care and precise operation. Electron columns are vacuums and entry of air molecules disturbs the functioning of the TEM due to interference with the electron beam. Firstly, to remove the specimen holder, it must be twisted through a series of vacuum locks. The copper grid with stained tissue section was then placed onto the specimen holder and clasped tight. The holder was twisted back through the series of vacuum locks ensuring no air enters the vacuum. Once in position the electron beam and filament were turned on. The electron gun at the top of the TEM emits electrons which travel down the vacuum tube, the TEM employs electromagnetic lenes which focus the electrons into a fine beam. The copper grid was easily located as this is a large electron dense area, through finer tweaking the tissue sample could be identified. Magnification, aperture, focus, intensity and grid location was operated through a control panel connected to the microscope. The camera was placed (Megaview III camera system) in field and an image was produced through the analysis software (Olympus) and modified by navigating the control panel.

2.3.3.7 Troubleshooting TEM procedure

Throughout this whole process a couple of issues were encountered, and below are some suggested troubleshooting steps for the future.

Problem 1: the resin within the sample underneath the confetti began to break down during sectioning. Following trimming down of the resin-embedded sample for ultramicrotomy, the confetti (on which the slice sits on) span the whole distance of the cross-section (figure 2.3). The confetti itself was more resistant to the permeation of the resin, as the connections were weak this resulted in the lower section of resin underneath the confetti (**figure 2.3**) breaking away when sectioning the sample. The breaking away of this area of resin caused the tissue sections to tear and damaged the area of interest.

Problem 2: When placing the ultrathin sections over the copper grids it resulted in severe tearing and folding of the section causing major difficulties in imaging the area of interest (**figure 2.4**). This process

was carried out over 30 times and each time presented the same problem. It is evident from the images in **figure 2.4** that the confetti were torn on every occasion, this in turn may have weakened the structural integrity of the section, particularly near the area of interest. Nearly all sections, apart from a select few (shown below), were completely torn over the area of interest.

Resolution 1: To avoid the breaking away of the resin two possible approaches could be attempted. I) Prior to the embedding of the sample the confetti should be cut down to the size of the spinal cord area required, this will avoid the resin spanning the width of the trimmed sample. II) Additionally, when embedding the tissue sample, next time I would add the sample to the resin solution as appose to adding the resin to sample in the mould. This could avoid the sample resting at the bottom of resin mould and give an even level of resin surrounding the sample (**figure 2.3**). Both these factors could improve section resilience.

Resolution 2: Another possible drawback could be that samples were being sectioned with a glass knife rather than a diamond knife. The use of a glass knife may have resulted of more striations on the sections surface, weakening its structural integrity and causing tears. Unfortunately, in my time at the TEM unit there was no expert available in person (only virtually) so the diamond knives could not be used.
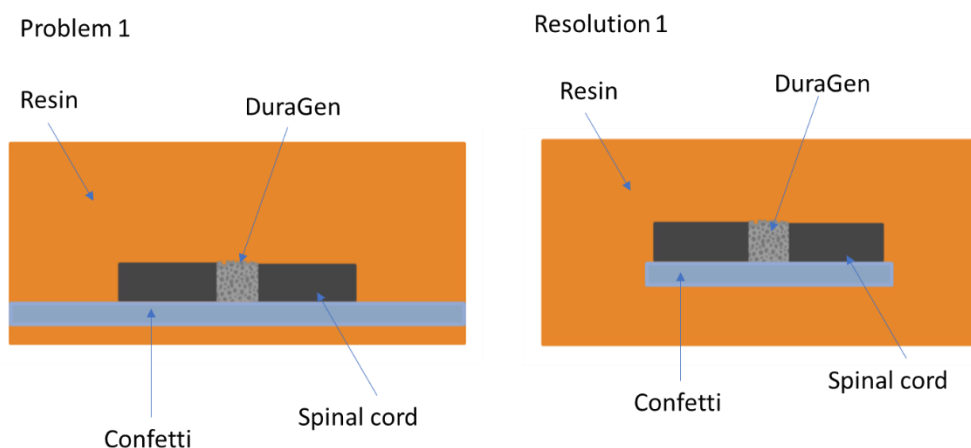
Figure 2.3. Diagram of the cross-section view generated from sectioning the resin-embedded sample. Problem 1: confetti spanning the distance of the resin and the sample was suspended at bottom of the resin. Resolution 1: trim the confetti to the size of the area of interest and suspend the sample in the centre of the resin mould.
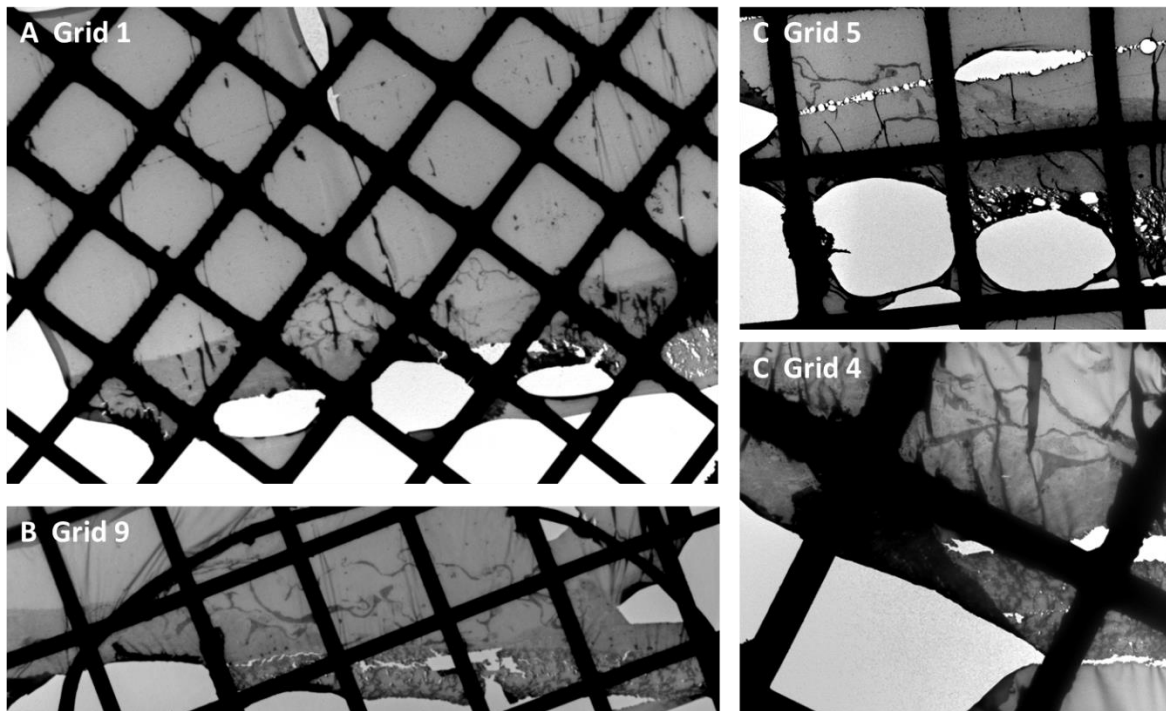
Figure 2.4. Low magnification TEM images of ultrathin sample sections over the copper grid. The area of interest (the material-slice interface) is shown on these images. Confetti underneath the tissue slice is evidently tearing and weakening the section.

2.3.4 Determination of lesion edges and the material boundaries under fluorescent microscopy

DAPI nuclear staining helped to determine the lesion edges when DG was implanted. The nuclei within the original slice are more densely populated compared to that within the DG implant, this demonstrated a clear lesion boundary (**figure 2.5 A**). DuraGen™ within the injury site was highly populated with nuclei (mostly GFAP negative nuclei in this case). In contrast, the areas without DuraGen™ often present little or no nuclei (i.e the upper right area **figure 2.5 B** to the side of the tissue slice). This clear disparity in nuclear density helps to distinguish the boundaries of the DuraGen™ (**figure 2.5**). Additionally, DuraGen™ produces a slight auto-fluorescent haze when visualised under the fluorescent microscope, this can be detected through different fields of view.
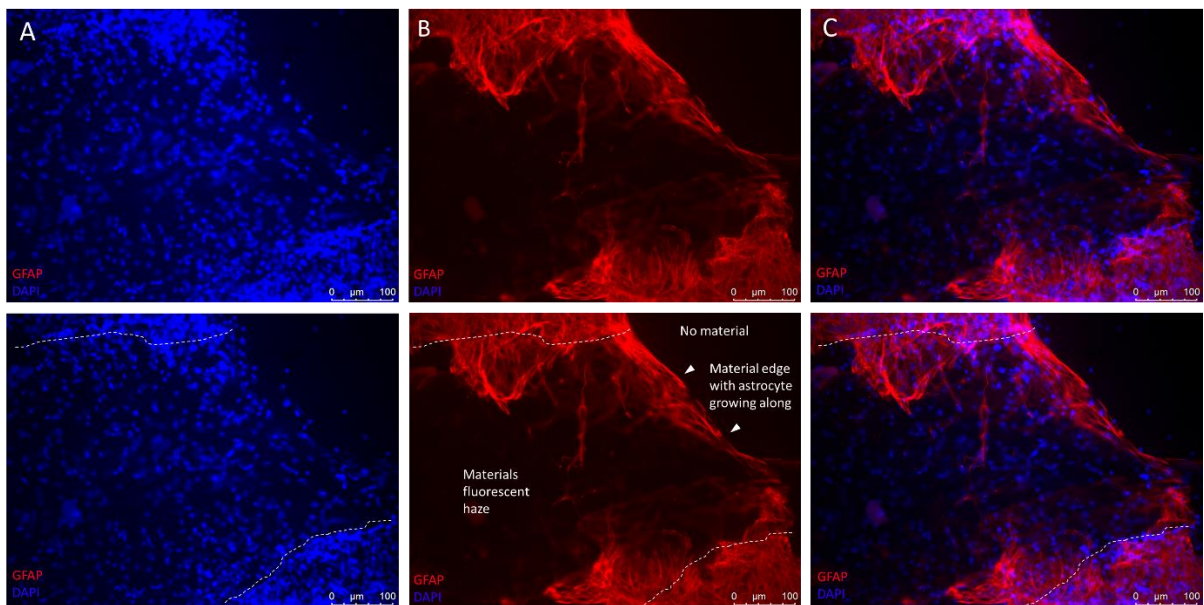
Figure 2.5: Determining the lesion margins and the boundaries of the DuraGen™. Top row shows the un-modified images. The bottom row shows how the lesion margins and DuraGen™ boundaries were determined. **A-B** Lesion margins (white dotted lines) were defined by very densely populated areas of nuclei compared to the nuclei within the DG. DG itself exhibited a slight fluorescent haze (shown in A and B) and was highly populated by nuclei compared the surrounding area (shown in A) and this helps to distinguish the outer boundaries of the material. In B the outer boundary of the material was easily defined by the growth of astrocytic processes along it. **C** merged image demonstrates how the edge of the mate rial (and nuclei) line up with the extended astrocytic processes.

2.3.5 Astrocyte reactivity analysis

Determining the most effective method for GFAP expression analysis at the lesion margins proved difficult for DuraGen™ implanted slices. For injury only slices this was slightly less complicated; as a defined astrocytic lesion edge would be produced at the original injury site, this could easily be determined as 0µm into the slice. However, ingrowth of astrocytes into the implanted DuraGen™ meant the lesion edge became a rough astrocytic edge which was no longer in line with the original incision margins. Due to uneven growth of astrocytes into the material, there were areas of no tissue which could skew the results if not avoided in GFAP measurements. Considering this, 7 requirements were set out to yield the most efficient analysis technique and data representation:

i)	Incorporate the ingrowing astrocytes into quantifiable measurements: the astrocytic edge.

ii)	Define an assumed injured baseline of GFAP optical density as a comparative control i.e., astrocytes at 400-500μm from lesion edge within the slice.

iii)	Avoid holes or areas with no astrocytes i.e., lines of measurements used rather than boxed areas.

iv)	Unbiased measurements (random yet follow a certain rule) i.e., parallel line measurements using overlaid grid for interval guidance.

v)	Use an appropriate independent variable i.e., plotting distance at appropriate intervals from astrocytic edge.

vi)	Plot a fold change within each data set to account for interslice variability.

vii)	Incorporate a system to compensate the autofluorescence of the material.

Images were captured with a Leica DMC2500 LED microscope at constant exposure throughout the experiments for reproducible data analysis. For GFAP quantification all images were converted to greyscale (8-bit) and inverted on image J (**figure 2.6B**). Quantification of GFAP was achieved via evaluating the optical density profile from the lesion margins towards the centre of the slice, up to 500μm in, each at 100μm intervals. This was done by drawing multiple parallel lines from the astrocytic edge at intervals determined by a standardised overlayed grid (**figure 2.6B**), the same angled lines were used throughout analysis. Images were taken at 10x magnification to observe the whole lesion edge. Through ImageJ micrographs of GFAP stained spinal cord and brain slices were converted to 8-bit type, inverted and the programme was calibrated to calculate global optical density (OD) (the protocol for OD analysis is adapted from Weightman et al., 2014). Following this, a grid was laid over the image to give the measurement intervals. Parallel lines were drawn from where the grid lines first meet the astrocytic edge and 500μm into the slice, these were angled in two directions to encompass a more robust analysis of the change in GFAP OD at the lesion edge (**figure 2.6C**). Measurements of GFAP

optical density at 400-500µm with the slice were assumed as the baseline astrocytes. A background OD was calculated by measure the OD of an area with no tissue, this was subtracted from the OD values from the same image to give a true OD. ODs were averaged and a fold change was calculated at each 100µm interval from the astrocytic edge.

A

Material

Activated intra-matrices astrocytes

Slicing-induced glial scarring

Baseline GFAP expression of astrocytes within slice

B

C

1. Following this gridline - the point at which you first meet the astrocytic edge is the start of the OD density measurement

2. Do this with every vertical grid line taking parallel lines from the astrocytic edge i.e. all parallel yellow lines

3.Do the same process going backwards i.e green parallel lines

** Avoid lines going though tissue gaps
* In this case move over the parallel line until it avoids the tissue gap

** Avoid lines that go through large part or end in the glia scar at the slice edge

Figure 2.6. The process of quantification of GFAP optical density from the astrocytic edge and into the slice. (a) A diagram of injury + DuraGen™ spinal cord slice astrocytic response. (b) An example of an GFAP stained injury + DuraGen™ image converted to an inverted 8-bit image type on ImageJ (lines represent where optical density (OD) measurements were taken). (c) Explains the quantification technique process once the grid was overlaid. Values generated by Image-J were extracted into excel, and a fold change for each data set plotted. The same method was used with injury-only tissue slices.

2.3.6 Neuronal outgrowth analysis

Neurite outgrowth from the lesion edge ± DuraGen™ was evaluated through TUJ-1 immunostaining. Neurite length was not measurable due the density of neurites and untraceable neurite outgrowth patterns. Therefore, to quantify neuronal outgrowth from the lesion margins, TUJ-1 positive neurites that had extended into the lesion area ± implanted material, were counted via the line crossing method (**figure 2.7**). Fluorescent micrographs were imported over to ImageJ and the 12 equal lines were placed over the lesion area (as shown below), this is a standardised grid function within imageJ. At any point a neurite passes across the overlay line this was counted as 1 unit (one neurite can cross multiple grid lines). An average number of axons crossings was calculated over 4 biological repeats. This method is adapted from previous neurite analysis carried out by various members of the Laboratory.

2.3.7 Microglial infiltration analysis

Quantification of microglial cell number within the injury site ± DG was achieved via counting the number Iba1 positive cells with a given area. Five randomly located fields of view within the lesion area with and without DuraGen™ implantation were taken at 40x magnification to give these values. An average value was generated per slice, then averages per experiment were plotted and statistically analysed for 4, 7 and 14 days post lesioning.
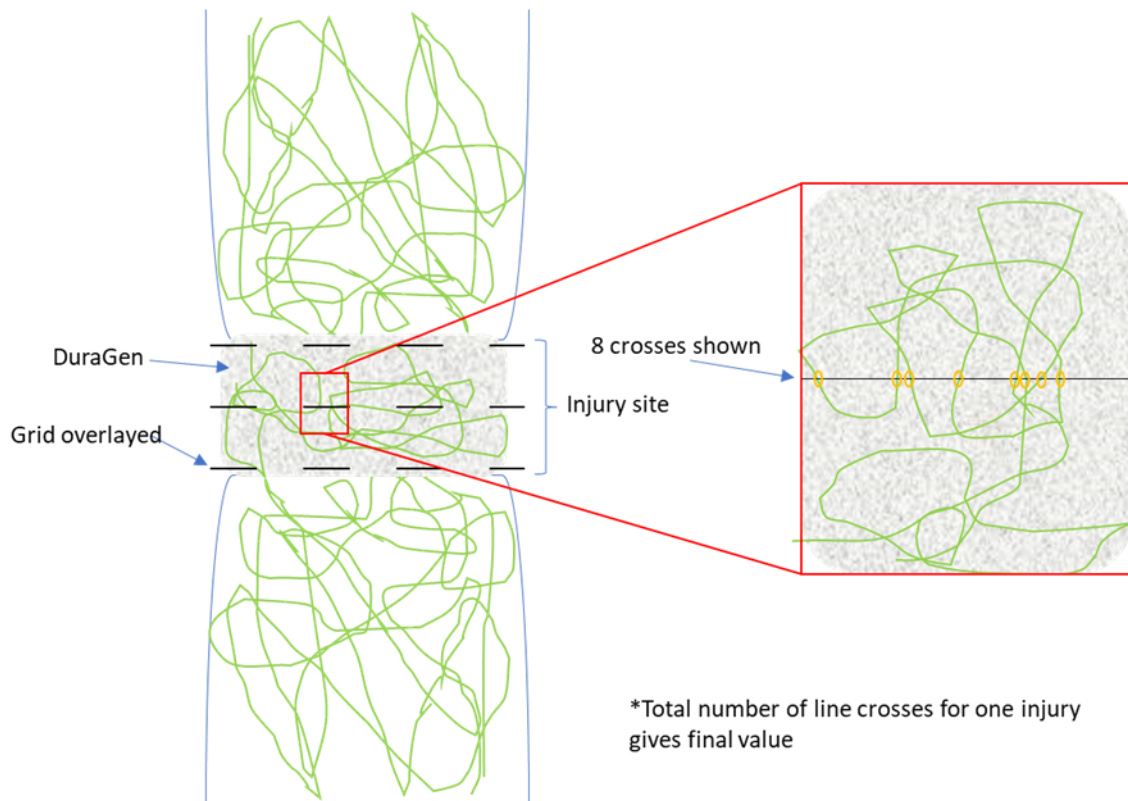
Figure 2.7: Quantification of neuronal outgrowth via the line crossing method. This process was applied to fluorescent micrographs of TUJ-1 staining at the lesion site ± DuraGen^TM.

2.3.8 Microglial characterisation

Microglia morphology was characterised by a cell roundness index (CRI) (adapted from Fujita et al., 1996). This can quantitatively describe the effect of the biomaterial on the morphology of the resident microglia, to determine their possible reactive state. Iba1 immunolabeled micrographs were imported into ImageJ. The relevant scale was set globally, and the freehand drawing tool function selected. Each Iba1+ cell within the lesion area was traced around and measured. Recorded measurements from each traced cell provides cell perimeter, area values. These values were then plugged into the equation for CRI. CRI = (4*3.142*area)/perimeter^2), here the value of 1 denotes a complete circle, and towards 0 is ramified (**figure 2.8**).

Cell roundedness index

CRI: 0.90   CRI: 0.65

CRI: 0.42   CRI: 0.26   CRI: 0.15

CRI: 0.10   CRI: 0.05
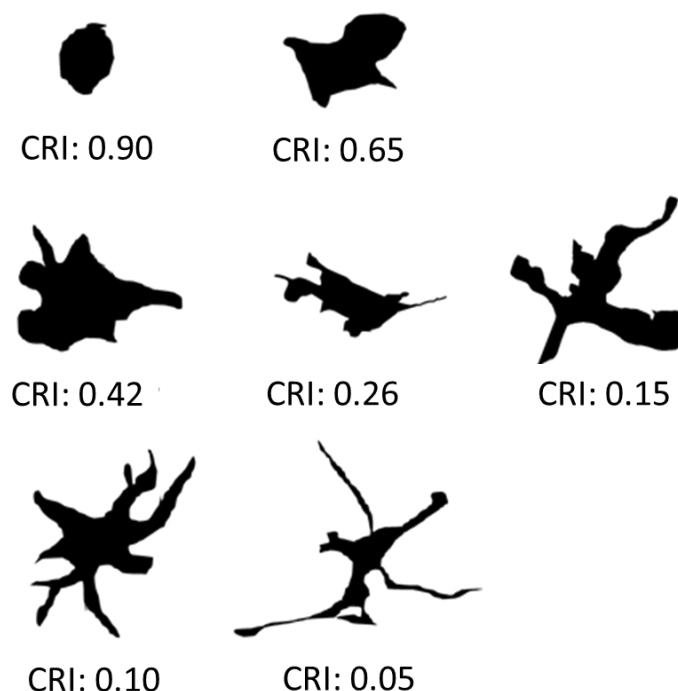
Figure 2.8. Representation of the microglia shapes translating to a cell roundedness index.

2.3.9 Statistical analysis

In all cases the number of experiments, n, refers to experiments obtained from separate mice litters however there were multiple repeats within each n number. Spinal cord and brain experiments were quantified to an n of 4. GraphPad Prism v5.0 software was used for all statistical analysis performed. All values were expressed as the mean ± the standard error of the mean (SEM). In the case of the GFAP analysis, where optical density was measured at increasing distances from the lesion edge, both injury-only and injury + DuraGen™ were statistically evaluated via a two-way ANOVA statistical test. This was the defined relationship between GFAP intensity and the distance from the astrocytic edge or GFAP intensity with/without DuraGen™. Both microglial cell infiltration, morphology and neurite extension into the lesion were analysed via a t-test, a statical test which assesses the difference of two groups means. Tests for normality were carried out per analysis: the F test for variance comparison showed the results from the Iba-1 data set had significantly different standard deviations, meaning a Welch's T-

test (an equal variance t-test) had to be carried out, which assumed the standard deviations from each population were not equal. However, there was no significant difference in the standard deviations of the GFAP data set or TUJ-1 data set.

2.4 Generation of a two-dimensional (2D) cortical neuronal neuroglia injury model and three-dimensional (3D) biomimetic cortical neuronal neuroglial injury model.

Initially two dissociation methods were trialled, and the cellular characteristics of the generated cultures were assessed in 2D. The mechanical and enzymatic methods for tissue dissociation were adapted from mixed-glial protocols within our laboratory.

Following this initial assessment, the enzymatically dissociated cultures were taken forward to generate the 2D and 3D neural injury model.

2.4.1 Generation of 2D cortical neuron-glia cell culture via mechanical dissociation

The care and procedures involving the mice were in accordance with the Animals Act of 1986 (Scientific procedures UK) and with the local ethics committee approval. Pups aged postnatal day 0-1 (P0-P1) were administered with Pentobarbital, then decapitated once unresponsive to a hindfoot pinch. Mice of this age yielded the best culture results for both dissociation methods (mechanical and enzymatic). Dissociates from post-natal ages above P1, showed reduced attachment to the coverslips and remained balled up. This result was observed when using the complete neurobasal medium ((0.5% GlutaMAX-I (200mM), 0.5% pen/strep, 1% B27 in Neurobasal A). When using the previously established D10 medium (1mM sodium pyruvate, 2mM glutaMAX, 10% fetal bovine serum (FBS), 0.5% pen/strep in Dulbecco's modified Eagle's medium) for mixed-glial cultures absent of neurons, dissociates from mice up P4 can be used.

Brains were dissected as described in 2.2.1. The brain tissue was placed immediately in ice-cold dissection medium (2.5% HEPES in EBSS). The brains were then transferred to sterile blue towel and rolled to remove the meninges and blood vessels. The olfactory bulbs and the hind brain were removed using a scalpel. The subcortical tissue was then pinched off using curved forceps, leaving only the cerebral cortex. Once the cerebral cortex was isolated this was placed in fresh petri dish with fresh dissection medium. All dissected cerebral cortices were then transferred to a fresh dish and minced into small pieces via a sterile scalpel blade. Complete Neurobasal medium (0.5% GlutaMAX-I (200mM), 0.5% pen/strep, 1% B27 in Neurobasal A) was added to the minced cerebral cortices to aid transfer to a universal tube. Using a plastic Pasteur pipette the cortices and medium was carefully triturated avoiding frothing of the suspension. Using a 10ml syringe with a 21g green hypodermic needle attached, the suspension was triturated a further 3 times. The needle was then switched to a 23g blue hypodermic needle, and the suspension was again triturated an additional 3 times. Once the tissue had been appropriately broken down the cell suspension was centrifuged at 1000 rpm for 4 minutes and then the supernatant removed. 1ml of complete neurobasal medium was added to the pellet for the initial resuspension of cells. Then a further 2-4ml was added depending on the number of brains used. Next, cells were put through 70 µM cell strainer, then a 40 µM cell strainer, to filter out any large cellular clumps that had not been dissociated. The cells within the cell suspension were then counted via a haemocytometer; by mixing 10 µL cells with 40 µL of 0.4% trypan blue and then adding 10 µL to the haemocytometer. The suspension was then appropriately adjusted to a seeding density of 1×10^6 cells/mL and 300 µL per well was seeded onto pre-prepared Poly-D-Lysine (PDL) and laminin coated glass coverslips (please see section 1.4.3) in a 24-well plate and incubated at 37˚C 5% CO2. 24 hours post seeding all media was removed and the wells carefully washed to remove any debris or unattached dead cells, then 500ul of complete neurobasal media added. A 50% media change was carried out every two days. This culture method generates a monolayer of neurons, astrocytes, oligodendrocytes, microglial and oligodendrocyte precursor cells. Once the 2D cultures reach 90%+ confluency (around 7 days *in vitro*) cells were fixed in 4% PFA for 20 minutes.

2.4.2 Generation of the 2D cortical neuronal neuroglia cell culture via enzymatic dissociation

The subcortical tissue was isolated from CD1 mice brains P0-P1 (see section 2.4.1) and kept in ice cold dissection medium (2.5% HEPES in EBSS). Following the isolation of the tissue, the dissection medium was removed leaving the only the cortical tissue. Using a scalpel, the tissue was minced into small pieces, then transferred into a fresh universal tube. Next, 1ml of Trypsin-EDTA and 500ul of DNase were added to the minced cortices to submerge the tissue (8-10 brains). This was then shaken at 150rpm at 37°C for 20-30 mins (checking the condition of the tissue regularly). After 20-30 mins the tissue became soft and gel-like and was then very gently triturated 5-10 times with a P1000 pipette to completely dissociate the cells (it is vital this is carried out slowly and gently). Once dissociated, 2ml of FBS was added to stop the reaction, along with 2ml of complete Neurobasal medium to wash the cells and then centrifuged for 5 mins at 1200rpm. Following this, the supernatant was discarded very cautiously as the pellet can be loose, then the pellet was resuspended in 1ml of complete Neurobasal medium. Then a further 2-4ml was added dependant on the number of brains used. Next, cells were put through 70 µM cell strainer, then a 40 µM cell strainer, to filter out any large cellular clumps. Cells were counted, seeded and maintained as in section 2.4.1. This tissue dissociation method produces a robust multicellular model with a high-density neuronal network and the five major cell types of the brain illustrated in **figure 2.9**.
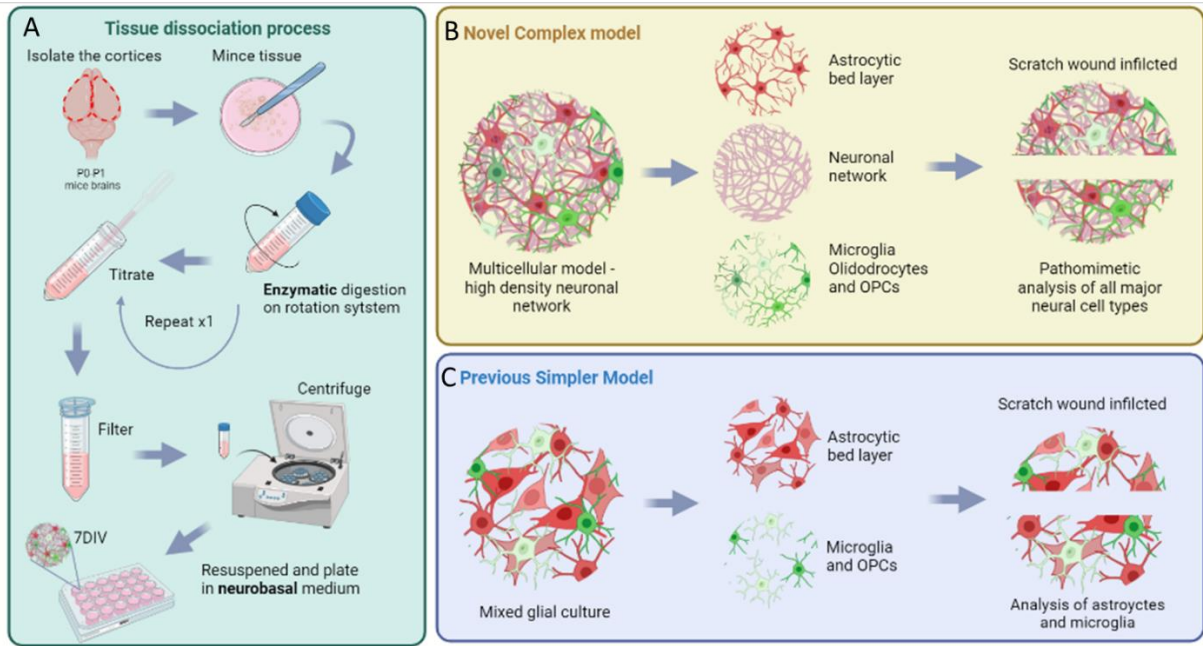
Figure 2.9: Schematic of the tissue dissociation method and the novel multicellular complex model generated versus the previous model. A established tissue dissociation procedure from cortices isolation to enzymatic digestion and then plating. **B** schematic of the novel complex model comprising of the five major cell types; a bed layer of astrocytes, neuronal network throughout and microglia, oligodendrocytes and OPCs residing at the top. Analysis of the pathomimetic responses of all neural cell types to a scratch wound injury. **C** schematic of the previously established mixed glial culture injury model; with only astrocytic and microglia analysis.

2.4.3 Coating coverslips

Coverslips placed into wells of a 24-well plate were coated with PDL and laminin. Glass coverslips were first sterilised in 70% EtOH for 5 minutes and washed with sterile deionised (ds) H_2O. Sterile PDL solution was added for 1 hour, then washed with sdH2O for 5 minutes. Following the sdH$_2$0 wash sterile laminin solution (20µg/mL in sdH$_2$0) was added for 1 hour at 37˚C. After 1hr wells were washed 3 times with sdH$_2$0 and left in the last wash until further use. Plates were coated on the same day as dissection and seeding.

2.4.4 Introducing an 'injury site' via a scratch method

Once cultures had reached 90%+ confluency (around 7 days *in vitro*), a scratch was introduced down the centre of the well (**figure 2.10**). Using a sterile P200 pipette tip at a 90˚ angel to the well bottom, the tip was moved smoothly from the top of the well to the bottom in one continuous movement, keeping an even pressure throughout. The tip removed all cells in its path creating a lesion area the width of the tip (1000µm). The cultures were left for 24 hours, or 3 days post lesioning then fixed with PFA for 20 minutes.
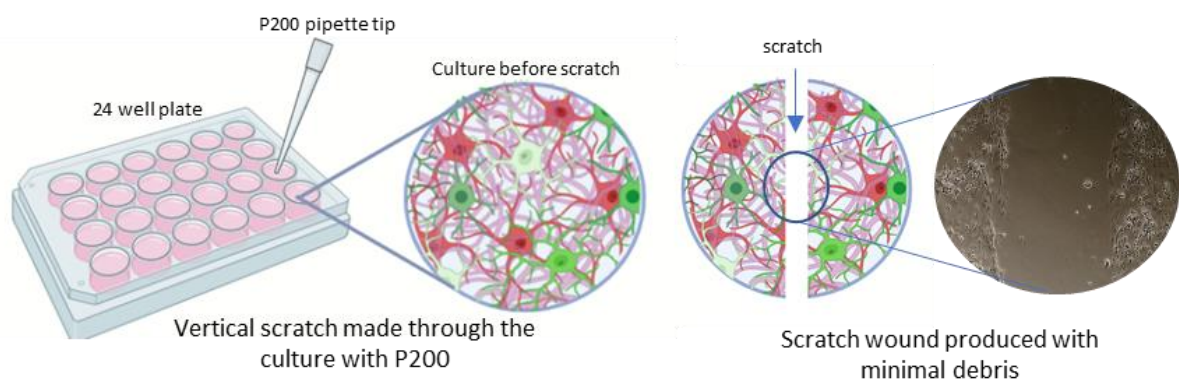
Figure 2.10. Schematic of 2D injury.

2.4.5 Immunocytochemistry for 2D cultures

At desired timepoints, the cultures were fixed in 4% paraformaldehyde (in PBS) for 20 minutes at room temperature. Post fixation the PFA was removed, and cells were washed 3 times with PBS. Following this, samples were incubated with the appropriate primary antibodies in the blocking buffer: TUJ-1 (1:500), GFAP (1:500), Iba1 (1:200), NG2 (1:200) or MBP (1:200) overnight at 4˚C (**Table 2.2**). Coverslips were washed 3 times with PBS, 5 minutes per wash, then incubated with the appropriate secondary antibodies in blocking buffer (1:200) (**Table 2.2**) for 2 hours at RT (or overnight at 4˚C) in dark conditions. Subsequently, secondary antibody solution was removed, and coverslips were washed 3 times with PBS (5min/wash) and mounted on glass slides with Vectashield mounting medium (containing DAPI). Mounted coverslips were sealed with nail varnish.

Table 2.2 Antibodies and dilution factor used to identify neural cell types

Cell type immunolabelled	Primary antibody	Secondary antibody
Astrocytes	1:500 Rabbit anti-GFAP	1:200 Donkey anti-rabbit
Neurons	1:500 Mouse anti-Tuj1	1:200 Donkey anti-mouse
Microglia	1:200 Goat anti-Iba1	1:200 Donkey anti-goat
OPCs	1:200 Rabbit anti-Ng2	1:200 Donkey anti-rabbit
Oligodendrocytes	1:200 Rat anti-MBP	1:200 Donkey anti-rat

2.4.6 Addition of nanoparticles to the lesion site

Detailed characterisation of the magnetic nanoparticles (MNPs) used in this experiment was done by Jenkins, et al., 2016. Both carboxymethyl dextran-coated magnetic nanoparticles (nano-screen MAG-CMX) and polyethylene glycol-coated magnetic nanoparticles (nano-screen MAG-PEG/P) were supplied by Chemicell as an aqueous suspension. They contain magnetite cores with a lipophilic dye (BODIPY) layer, overcoated with either carboxymethyl dextran (CMX-MNP) or 2 kDa diphosphate PEG (PEG-MNP). At 4 hours post-lesion (7 DIV) MNPs (CMX and PEG) were added (2 µg mL-1), to the media. Following this, the 24-well plate was placed onto a magnetic plate (magnefect-nano, nanoTherics Ltd., Stoke-on-Trent, UK) within the incubator. This encourages the MNPs sediment over the cells at the well bottom rather than staying suspended in medium. MNP administered plates were analysed after 24hr and 3 days post administration.

2.4.7 Imaging and cellular analysis

2.4.7.1 Fluorescence imaging

Fluorescence imaging of 2D and 3D cultures and z-stack imaging of 3D cultures was carried out on the Zeiss, Axioscope A1 microscope with an AxioCam ICc1 digital camera processed with Axiovision software (Carl Zeiss Microimaging GmbH, Goettingen, Germany). Quantitative imaging of 2D and 3D cultures was performed using an Axio Observer.Z1 equipped with an AxioCam MRm powered by Zen 2 (blue edition) software (Carl Zeiss MicroImaging GmbH, Goettingen, Germany).

2.4.7.2 Cell population assessment

Cells immuno-positive for Tuj-1, GFAP, Iba1, NG2 and MBP were quantified from respective fluorescent micrographs. Here, 5 regions per culture were selected using the DAPI-only channel on the fluorescent microscope; minimum 100 nuclei assessed per condition. Percentages of each type was calculated via counting the proportion of cell marker positive cells compared with total nuclei within the field.

2.4.7.3 Neuronal outgrowth quantification

Lesion sites were immunostained for TUJ-1 to identify neurite extension into the lesion gap and co stained with DAPI to assist with identification of the lesion edge. Micrographs were opened in ImageJ and the global scale was set; a grid was overlayed with intervals of 100µm. Fibre sprouting at the lesion edge was measured by the freehand line drawing tool. At every 100µm interval an axon length from the lesion edge to its distal end point was traced and length measured. Note neurite extension was not in a uniform direction so this measurement was not distance into the lesion. Averages were calculated per coverslip then per experiment.

2.4.7.4 Microglia infiltration and morphological quantification

Microglial infiltration was evaluated via counting the number of Iba1+ cells within the lesion site. Five lesional areas were analysed per repeat and averages were calculated and used for statistical comparison within GraphPad.

Microglial morphology was characterised via assessment of cell roundness, to determine the reactive state. Iba1 fluorescent high magnification micrographs were analysed in ImageJ with a global scale set. Here, the freehand drawing tool was used to draw around Iba1+ cells peri-lesional and distal to the lesion producing measurements such as cell perimeter, area and Ferets diameter which were subsequently entered into the cell roundness formulae (4*3.142*area)/perimeter^2). A value of 1 denotes a complete circle, anything less is progressively less rounded. Averages were plotted for statistical analysis.

2.4.7.5   Astrocyte morphological and astrogliosis analysis

Reactive astrogliosis was calculated similarly to section 1.3.5 via measuring optical density of GFAP+ astrocytes. OD of equidistant parallel lines (from an overlayed grid) were measured from the astrocytic edge and into the culture at 1DPL and 3DPL. Average values at 100μm intervals were plotted per experimental repeat.

In addition, semi-quantitative analysis was used to assess astrocytic morphology in peri-lesional astrocytes (within 100μm of the lesion edge) and distal astrocytes (astrocytes over 400μm from the lesion edge). Here, GFAP+ cells were marked type 1 flat unprocessed astrocytes, type 1 fibrous astrocytes (multiple processes), or reactive astrocytes (lamellipodia reaching over the injury margin). It should be noted that type 2 astrocytes were not present in the 2D cultures (which have a central soma and fine long processes).

2.4.7.6   OPC infiltration

OPC infiltration was evaluated via counting the number of NG2+ cells within the lesion site from low magnification micrographs at 1/3DPL, and 5 lesional areas were analysed per repeat. Averages were plotted for statistical comparison.

2.4.7.7   Quantification of nanoparticle uptake

Here, a semi-quantitative analysis was utilised; microglia were allocated a morphological category: ramified (microglia with two or more long spindle like processes) or amoeboid (including large bushy microglia and small rounded microglial) and defined as lesional (with lesion or at lesion boundary) or distal (400μm+ from lesion) microglia. Categorised microglia were then assigned a class of MNP uptake either no uptake, low-level: <10 MNPs, mid-level: 10+ MNPs or high-level: 50+ MNPs. An average percentage was then calculated to allow the overall relationship between cellular morphology, location and MNP uptake to be assessed.

An overall cellular MNP uptake per cell type was analysed. A percentage of cells with MNP-labelling colocalised with the cell marker was calculated. It was not conclusive whether some particles were

membrane associated or adhered to the culture itself therefore these were not classed as cellular uptake. Nanoparticle uptake was determined by MNPs that were associated near or around the nucleus i.e perinuclear trafficking.

2.4.7.8   Statistical analysis

Data are expressed as mean ± SEM. Data sets were analysed using Prism software (v5.0, GraphPad, USA). N = number of cultures from separate mice litters. A combination of unpaired two-tailed t-tests, two-way ANOVA and one-way ANOVA statistical tests were employed and stated within the results.

2.4.8   Production of a 3-dimensional (3D) injury model – a mixed cortical neuronal neuroglial culture encapsulated within a neuro-mimetic substrate.

A self-polymerising collagen gel was chosen for the 3D encapsulation of the mixed cortical neuronal model. Collagen was used as the encapsulation substrate as the production of collagen gels had been previously set up within our laboratory. Gel formulation was adapted from Adams, 2015 for the encapsulation of cells. The stiffness values of these gels were not determined and this was not feasible due to time constraints and the COVID-19 restrictions in place throughout a large part of this work. However, stiffness of collagen gels at a particular concentration found within the literature is discussed on page 172.

2.4.8.1   Construction of the 3D cellular hydrogels

Preliminary experiments were performed to establish the appropriate collagen concentration and cell density that gave the best outcome in terms of cell response and cell morphology within the system (see results section 5.3).

Collagen is stored as a monomer at 4°C diluted in acetic acid. To form a gel, this solution must be neutralised, upon which the collagen polymerises and then sets at room temperature. For the cellular 3D gels, enzymatically dissociated cortical neuronal and neuroglial cells were incorporated into the

collagen solution prior to setting. This allows the cortical cells to be encapsulated within the collagen fibres as part of a 3D network. Gels were set in 24 well plates on top of glass coverslips as this was found to facilitate the removal of gels from the wells. Stock seeding densities were trialled at **5×10^6** cell/mL, **10×10^6** cells/mL and **2.5×10^7** cells/mL with collagen concentrations of 1mg/mL and 1.5mg/mL.

For gel formation several components were combined in a particular order. To generate certain collagen concentrations within the gel a set of formulae were used to calculate volumes of each reagent (**Table 2.3**) (this table was taken from Adams et al., 2015). All reagents were kept on ice during the preparation. Firstly, the collagen was dissolved in acetic acid to the required concentration, then 10X MEMα solution was added. Subsequently, the appropriate volume of cells was added which needs to be immediately titrated throughout the solution or it can cause aggregations. Lastly the solution was neutralised with NaOH, and this was added drop wise whilst at the same time swirling the mixture until the pH indicator (within the MEMα) turns from yellow to pink. All components were kept on ice at all times to ensure the gel did not start to set before it was seeded into the wells. 200µl of the gel solution was added to sterile glass coverslips, which forms a button shape. Prior to this, coverslips were added to a 24-well plate, treated with EtOH (5 min), washed with sdH2O and left to air dry. Once seeded plates were transferred carefully to the incubator for 30-60 minutes. Following gelation, 500ul of complete neurobasal media was added to each well. The gel media was topped up to 1ml after 2 days and had a 50% media change every 3-4 days.

Reagent	Formulae to calculate required volume for the gel
10x MEMα	$V_M = V_F \times 0.01$
Collagen	$V_C = (C_R \times V_F) / C_S$
Cells	$V_N = V_F \times 0.1$
Acetic acid (0.02M)	$V_A = V_F - V_C - V_M - V_N$
NaOH (1M)	$V_S = (V_A + V_C) \times 0.023$

Table 2.3. Formulae for deriving volumes of reagents to generate 3-D collagen gels. V_F – final volume; V_M -volume of 10x MEMα; V_C – volume of collagen; V_N - volume of cell suspension; V_A – volume of

acetic acid; VS – volume of NaOH; CR – requires concentration of collagen; CS – collagen stock concentration.

2.4.8.2   Introducing an injury into the 3D cellular gels

Once the gels had been in culture for around 7 days multiple cell types could be visualised under microscopy (**figure 2.11 A**). The injury was made when gels appeared relatively confluent with cellular processes extending in most fields of focus. Using a P1000 pipette tip, the tip end was punctured through the gel then twisted clockwise and anticlockwise several times until the gel was completely cut (**figure 2.11 B**). The waste gel was held inside the pipette tip end and removed, similar to the action of an apple corer. This action was carried out 3 times to create 3 separate lesions within the same 3D cellular gel culture (**figure 2.11 C**).
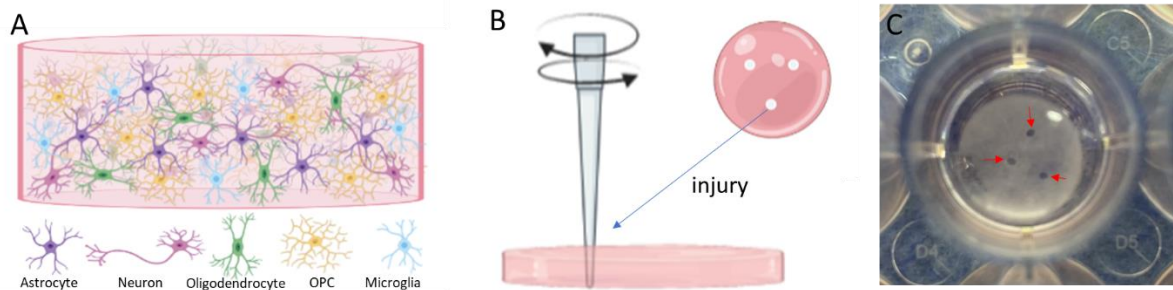
Figure 2.11. Illustration of the cellular composition within the 3D cortical neuron-glia culture and the introduction of a focal injury. A depicts the multiple cell types present within the gel. **B** shows a schematic representation of focal injury method. **C** photograph of the injured gel in culture media (red arrows indicate injury sites).

2.4.8.3   Implantation of a biomaterial with the injury site of the gels

DuraGen^{TM} was cut to 900µm wide strips by the tissue chopper. Then each strip was cut down to size with a scalpel to fit the injury within the gel. The media was removed and the material was implanted

into the injury area using forceps, the wells were then refilled with 2mL of media (the material expands to fill the injury once media added).

2.4.8.4 Fixing and staining the gels

At appropriate timepoints gels were fixed with 4% PFA for 30 minutes. Post-fixation the PFA was removed, and the gels were washed 3 times (10 minutes per wash). Gels were stained with the same 5 antibodies as previously mentioned (**table 2.2**) to identify the five major neural cell types. Gels were incubated with primary antibodies diluted with blocking solution (see section 1.4.5) for 2 days at 4°C. The gels then underwent 3x 1 hr washing steps in PBS. Following this, gels were incubated with secondary antibodies (see section 1.4.5) + 2ul/mL of DAPI for 6 hours at RT and then washed 3 times 1hr per wash with PBS. Subsequently, gels were mounted on glass slides with mounting medium (no DAPI).

2.4.8.5 Imaging the gels

Quantitative imaging of 3D collagen cellular constructs was performed using an Axio Observer.Z1 by Zen 2 (blue edition) software. For each construct, five fields were chosen for imaging (200X magnification) and a stack of images were taken for each field, with parameters set as the first fibre seen at the bottom of the gel, and the last fibre at the top to produce a Z stack of set intervals (20μm). These Z stacks could then be processed as single images or used as videos to show the distribution of cells throughout the construct. The compressed single images often come out distorted so a deconvolution function (though the zen blue software) was applied to each image for increased clarity.

2.4.9 3D culture analyses

Cellular imaging, cell population distribution, microglial morphology, and microglial infiltration were analysed as described in section 2.4.7, but astrocyte morphology and astrogliosis analysis was modified as described below. Pathologies were assessed at 3 DPL.

2.4.9.1   Astrocyte morphology and astrogliosis analysis

Astrocyte morphology was separated into 3 categories: finely-processed astrocytes with small central soma (type 2 astrocyte), short-processed astrocyte with restricted processes and unprocessed-astrocytes presenting as a spherical cell. The percent of each astrocyte morphology category was calculated for each condition.

For astrogliosis at the lesion site of the gels, optical density of the GFAP expression was evaluated. Firstly, fluorescent images were converted to 8-bit and inverted on image J and the programme was calibrated for optical density. Next, using the freehand drawing tool, astrocytes at the lesion margins were traced and the overall optical density within the trace was calculated. A background optical density was also taken from an astrocyte free area. The background OD was then subtracted from the OD each astrocyte for that image. This was repeated for distal astrocytes 400µm+ from the lesion edge. The same exposure was used for imaging both lesional and distal areas of the gels. An average from each biological repeat was plotted for statistical analysis.

2.4.9.2   Microglial morphology analysis

Microglia morphology within the 3D injury modelling system were analysed through determining the CRI as described in section 2.3.8. It is also important to note that since microglia were often distributed in patches throughout the gels, injuries did not always fall near or within a microglial patch. Though this rarely occurred, injuries without microglia nearby were not including within the quantification.

2.5 Seeding, maintenance and recording of neuron-glial cultures on glass multi-electrode arrays (MEAs).

Bespoke MEA probes were built and fabricated at the University of Cambridge and delivered to Keele University. MED64 probes were commercially bought from MED64. The probes and specifications are illustrated in **table 2.4.**

2.5.1 Cambridge MEA fabrication process

Glass substrates were cleaned in soap solution followed by a dH_2O, acetone and isopropyl alcohol rinse. Following dehydration baking, the glass substrates were spin coated with negative life-off photoresist AZnLOF 2035 (Microchemicals GmbH, Germany) and exposed to UV. Au contacts were established by electron beam evaporation of Ti (5nm) and Au (100nm) and subsequent lift off. The PEDOT:PSS formulation was spin coated and the film was baked for 1h at 110°C and soaked overnight in dH_2O removing excess PSS. A photoresist etch mask was lithographically defined with the photoresist AZ 5214E (Microchemicals GmbH, Germany). PEDOT:PSS layer was subsequently etched by reactive ion etching using CF_4 and O_2. The remaining photoresist was washed with acetone, then a SAM of the adhesion promoter (methacryloxypropyl trimethoxysilane) (A 174 Silane, Sigma-Aldrich, UK) was added to enhance the subsequent adhesion of the PaC insulation layer to the glass substrate. The silinization was done by dipping the plasma activated (60 s, 25 W, 0.8 mbar) substrate in 3% (v/v) A 174 solution prepared in 96% ethanol (containing 1% acetic acid) for 30 s, rinsing off with ethanol, and baking at 70 °C for 1 h. Next a PaC layer around 500nm thick was deposited by chemical vapor deposition. To define the openings of electrodes and the Au contact pads at the periphery of the glass, an etch mask of AZnLOF 2035 was patterned through the PaC layer. The etch rate of PaC was determined in previous experiments and was used to control its etching to avoid oxidation and damage to the underlying PEDOT:PSS layer. The substrates were washed with acetone, followed by isopropyl alcohol and dH_2O to remove any residual substrate. There were two separate MEAs made here, transparent and non-transparent electrodes. The difference between the transparent and non- transparent electrodes was the ratio of Au to PEDOT:PSS (**figure 2.12),** otherwise these MEAs had the same spec. Au is non-transparent whereas PEDOT:PSS is, the Au within the transparent electrodes here is not essential but is useful in lowering the resistance and therefore an improved electrode circuit is established.
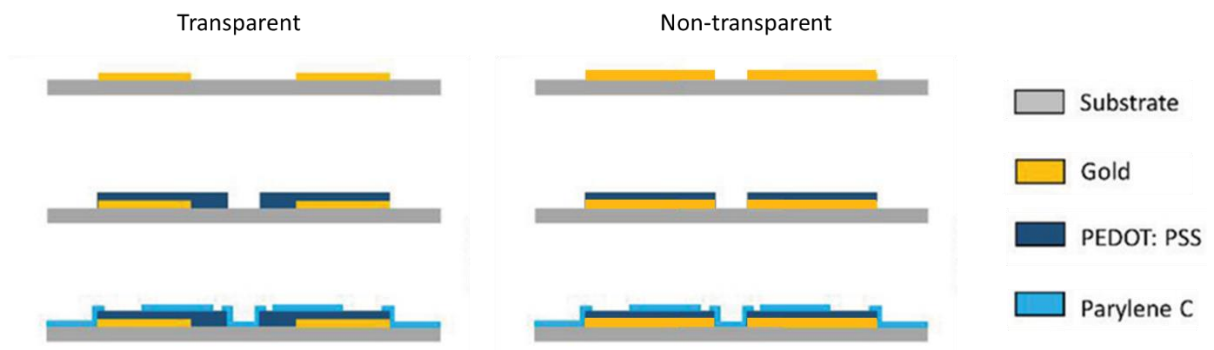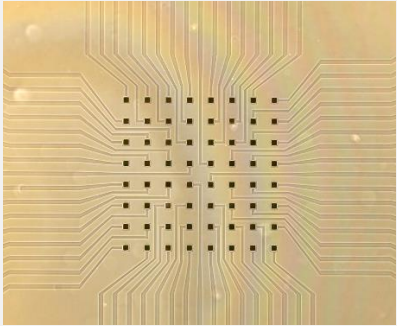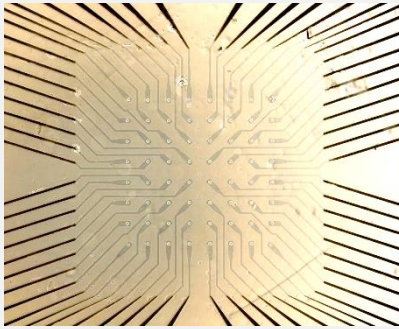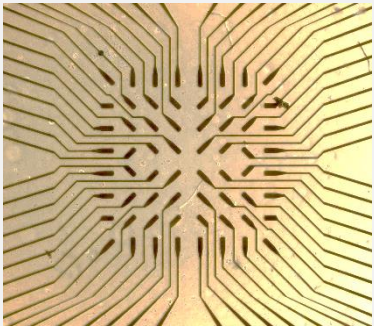
Figure 2.12. Schematic illustrating the fabrication process of the transparent and non-transparent electrodes.

	Med64 MEA probes	Bespoke Cambridge MEA probes	
		Transparent	Non-transparent
Micrograph of electrode area			
Recording electrode diameter	50µm	30µm	30µm
No. electrodes	64	64	64
Intra-electrode distance	150µm	150µm	150µm
Electrode material	Glass (substrate), Indium tin oxide (conducting layer), Platinum black (electrodes), Acrylic resin (insulating layer)	Glass (substrate), Gold PEDOT:PSS (electrodes/conducting layer), Parylene C (insulating layer)	Glass (substrate), Gold PEDOT:PSS (electrodes/conducting layer), Parylene C (insulating layer)
Software for recording/stimulating	Med64/Mobius – clear diverse reader interface	Intan/RHX – basic reader interface	Intan/RHX
Analytic software	Mobius offline toolkit – readout friendly platform	Matlab – complex platform requires specific expertise	Matlab

Advantages	-Can be reused multiple times	-Cells can be visualised through the electrodes	-Fabricated in house: i.e. possible adjustments can be made
	-Supports a comprehensive system for analysis	-PEDOT:PSS has significantly lower impedance than platinum	-PEDOT:PSS has significantly lower impedance than platinum
	-Simple mechanism for stimulation	-Fabricated In house: i.e. possible adjustments can be made	
	-Reliable		
	-Electrode wires within the glass so cannot scratch upon injury		
	-Record infinite times from one culture and can reuse the probes		
Disadvantages	-Expensive commercial system	Technically difficult to set up	Technically difficult to set up
	-Adjustments cannot be made to electrode orientation	-Electrodes and wires etched on top of glass so susceptible to damage	-Electrodes and wires etched on top of glass so susceptible to damage
		-Can only record a few times from one MEA as electrode pads deteriorate through set up (scratched)	-Can only record a few times from one MEA as electrode pads deteriorate through set up (scratched)
		-Arduous system for stimulation purposes (manual application)	-Arduous system for stimulation purposes (manual application)
		-Unreliable	-Unreliable

Table 2.4: Comparative table of MEA specifications and associated software.

2.5.2 Coating and seeding the Cambridge glass MEAs

The neuron enriched 2D neuron-glial culture model described previously (see section 1.4.2) was cultured on the MEA for recording of neuronal activity and eventual electrical stimulation of the cells within the electrode area.

The standard coating of glass coverslips for the neuron-glia culture as previously mentioned was PDL and Laminin (shown in figure **2.13 C**). However, 3 days after seeding the cells onto the PDL and laminin coated MEA the cells remained balled up and did not attach well to the MEA surface, this result was observed repeatedly (figure **2.13 A**). To resolve this problem another cell culture coating was attempted; poly-ornithine and laminin. The poly-ornithine and laminin coating on the MEA showed significant improvement of initial cell attachment and extension of cellular processes (**figure 2.13 B**).
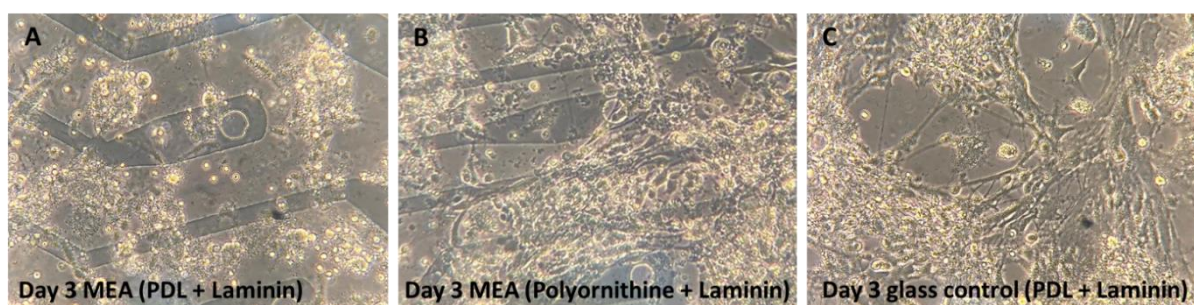
Figure 2.13. Comparison of cell attachment using two separate coating protocols for the MEA surface. **A** shows poor cell attachment on the PDL and laminin coating. **B** displays improved cell attachment on the polyornithine and laminin coating. **C** represents the standard protocol of PDL and laminin coating on glass coverslips. All images for were taken after 3 days in culture.

MEAs were placed in a sterile petri dish, then 70% ethanol (EtOH) was added to the wells and the EtOH was then washed off with sterile distilled water, then left under UV light for 15 minutes to ensure the MEA sterility. 500µL of poly-ornithine at a 1:4 dilution with sdH$_2$0 was added to the well and incubated for 1 hour at 37°C. The poly-ornithine was discarded, washed once with sdH$_2$0 and a laminin solution was added (20µg/mL sdH$_2$O) for 1 hour at 37°C. The laminin was then discarded and washed with and left in dsH$_2$O until ready to seed. The cortical cells were isolated as previously described in section 1.4.2 and 300µL per of cells were seeded per MEA well at a density of 1 x 10^6 cells/mL. After 24 hours the

MEA is topped up 500µL of complete Neurobasal medium. If there were many dead cells or debris 1-2 days post seeding the wells were washed gently and media replaced.

2.5.3 Setting up the MEA and Intan device for recording and stimulation

The glass MEA probe comprises of a central area of 64 electrodes encircled by a cell culturing well, this holds the cells and the feeding media (**figure 2.14 B:3**). When recording, parafilm was placed over the well to keep the culture sterile. The central electrodes extend via microwires out to 32 electrode pads (**figure 2.14 B:2**). 32 electrode pins were lined up with the corresponding electrode pads and secured in place at either side of the probe (**figure 2.14 A**). Misalignment of the electrode pins and pads causes breaks within the system and the impedance level would be too high to conduct a recording. Once aligned by eye, a head-stage was connected to the electrode pin blocks at either side and then the red wires were connected (**figure 2.14 D:5-6**). Next, the MEA holder was placed into an insulating Faraday box and the wires were fed through the box lid and into the Intan board to port A and port B. The grounding electrodes from both the pin blocks were sterilised with ethanol, dipped into the media within the well and secured throughout recording (**figure 2.14 C:4**). Grounding electrodes stabilise the influence of external noise on the recording system. Another grounding electrode was plugged into the power socket (**figure 2.14 E: 9**) and hooked up to the Faraday box.
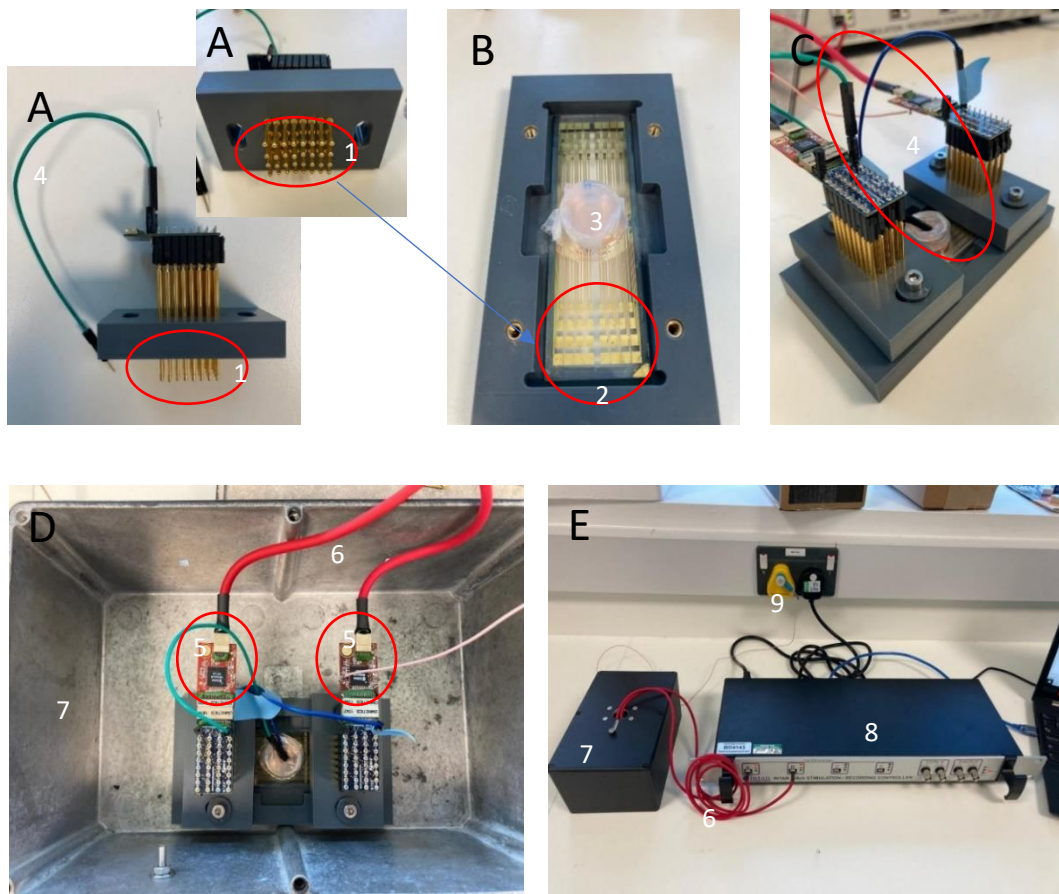
Figure 2.14. Assembly of the MEA holder and connection to the INTAN board. (1) 32 pins that line up with the electrode pads and secured with screws. (2) 32 electrode pads corresponding with the 32 electrodes (3) the cell culture area over the electrodes (covered with parafilm to keep sterile) (4) both grounding electrodes secured dipped into the media (5) 2x 32 electrode head stages connected to the pin blocks and the red wires. (6) wires connect the head-stages to the Intan board in ports A and B. (7) faraday box. (8) Intan board. (9) ground electrode attached to faraday box.

2.5.4 Running the RHX software for recording electrical signals

RHX data acquisition software was downloaded from Intan Technologies (https://intantech.com/RHX_software.html). Once the MEA was connected to the Intan board and connected to the laptop, the RHX software was opened and the panel below was shown (**figure 2.15**). To start with, a 30 kHz sample rate and 127.5 µA range was selected to open the programme (**figure 2.15 A**). The programme then displayed all the electrode channels within the MEA system, shown in

figure 2.15 B. An impedance test was initially run to determine the impedance value of each electrode circuit within the system (figure 2.15 B). This helped to determine which electrodes were damaged or whether the MEA was correctly set up. The drop-down menu at the bottom changed the values and data from port A to port B (figure 2.15 B). The impedance values for each electrode were shown on the left-hand side of the graphs (figure 2.15 B); impedance values between $10 - 100$ kΩ were ideal however some electrodes with values up to 300 kΩ were accepted when reading neuronal spikes. Figure 2.15 shows two electrodes (17 and 19) that were in the mΩ range. This generally indicated the electrodes were damaged, which often results in electrical noise evident on channel 17 and 19. After running the impedance check, the recording parameters were chosen. On the band width (BW) tab amplifier bandwidth was set to 1.17 Hz – 7.60 kHz, notch filter was set to 50Hz, the low and high pass filters were set to Bessel, Order 2 and cutoff 250 Hz (figure 2.15 C). The filter display was set to high and the bar on high gauge was moved to the highest position. The play button was used to display the live channel signals and the system was manipulated in attempt to reduce any noise displayed on the channels. To magnify the electrical readings from the electrodes, the 'zoom into the scale' button was used (figure 2.15 B). Once noise was minimised and parameters inputted, the recording could start. First the recording must be saved then the recording could commence using the record button. Recordings were taken for 5 minutes, and the stop button ended and saved the recording. Neuronal spike signals detected by some electrodes were evident in figure 2.15 C: channels 14, 15 and 31 show neuronal spike readings. By hovering the cursor over the channel lines this displayed the visual scale hence an estimated spike size could be determined i.e. the cursor scale in figure 2.15 was 100mV. Spikes above 20mV were considered to be neuronal spikes.
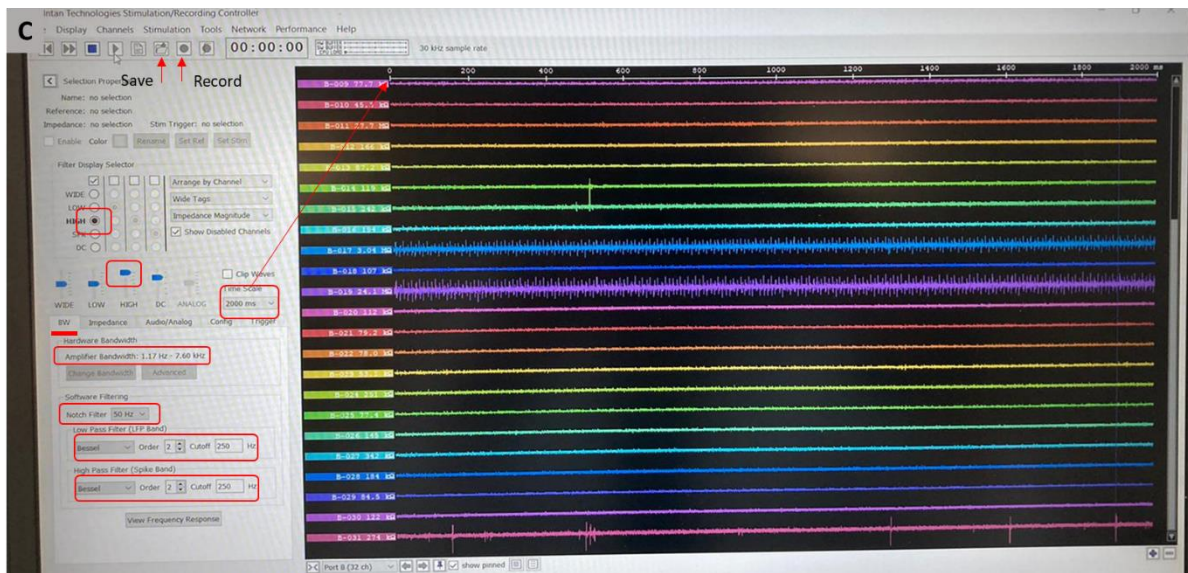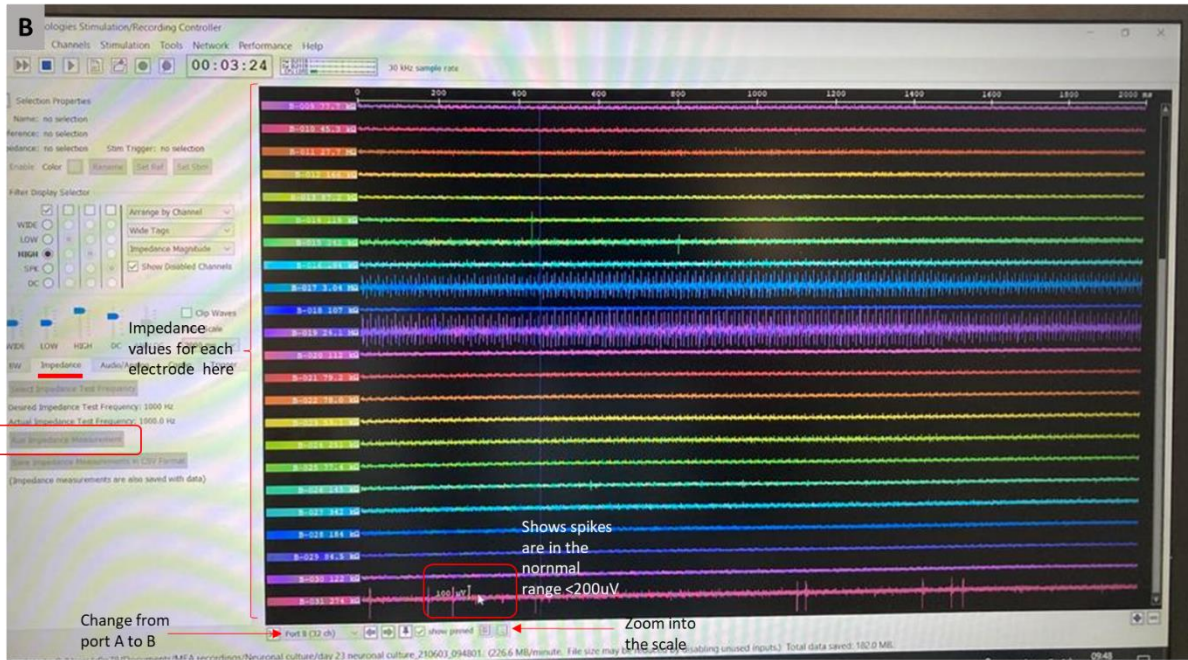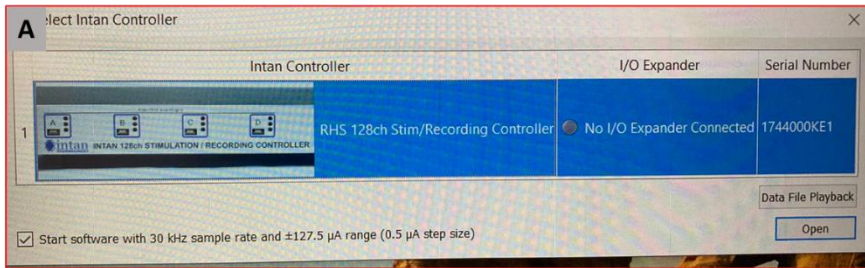
Figure 2.15. Annotated screenshots of how to use the RHX recording software and the parameters chosen for these experiments. A B and C show consecutive screens and the actions/parameters chosen.

2.5.5 Setting up mixed cortical cultures on the MED64 MEA system: coating, seeding and recording

Commercially produced MED64 probes were used as a comparative approach to the in-house fabricated Cambridge MEA probes. Following over ten experiments with the Cambridge probes, electrophysiological data was generated from one culture only, despite the high-density neuronal network observed within the cultures. Additionally, due to the assembly method of the probe holder, the electrode receiver pads at the periphery of the glass slide (**figure 2.14 B2**) would become scratched and lose their conductivity over time and multiple use. This meant recording multiple times over a long period caused deterioration of the probe, hence an alternative well established commercial MEA probe was chosen.

MED64 probes were sterilised and coated as the Cambridge MEA system (see section 1.5.1). The enzymatic cortical dissociate (see section 2.4.2) was also seeded onto the sterile MEA. Once the laminin had been washed off, the MEAs were left to dry for a few minutes and then a 100µL drop of 2 x 10^6 cells/mL was seeded directly over the electrode area. There are 4 sets of grounding electrodes at a distance surrounding the central grid of electrodes; at least one of the 4 must be free from cells, hence the 100ul drop is added initially. The cells were allowed to attach overnight, then 1ml of complete neurobasal medium was added gently. Medium was changed once/twice a week (50% media change). Media was not changed within 24 hours of a recording. Recordings were generally taken at 2, 7, 14, 21,28, 35 days *in vitro*.

The MED64 recording system was located in a separate building (15 minutes by car). Before travelling, the petri dishes were sealed with parafilm (in attempt to retain the incubator conditions for as long as possible). Petri dishes were taped down inside a box with a seal. Immediately after this the MEAs were transported by car to the relevant laboratory and placed in the incubator as soon as possible. The MED64 MEA holding plate was set up inside the incubator and heated up to 37°C, then the MEA probe

is transferred and secured in place (**figure 2.16 B**). The recording/stimulating amplifier and the heating system box was connected up outside the incubator (**figure 2.16 C**) and the incubator door closed.
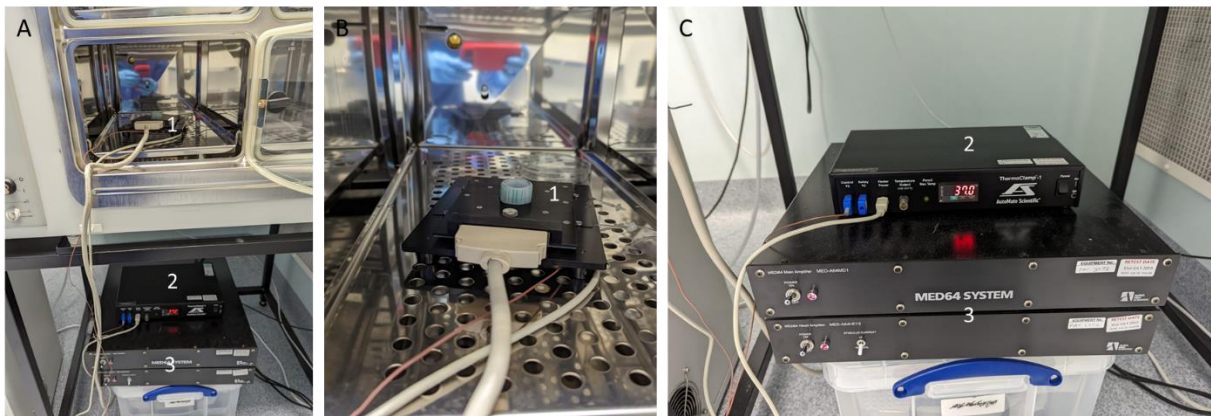
Figure 2.16: MED64 MEA system set up. A set up of both the MEA holder (1) and the recording/stimulating system (2/3). **B** MEA holder plus MEA (1) set up inside the incubator. **C** shows the system which heats up the holder to 37°C (2), and recording/stimulating amplifier underneath (3). Both remain outside of the incubator.

2.5.6 Introducing a focal injury over the electrode area

The central area between the electrodes has a gap distance of 100µm. The aim was to make an injury down the centre, through the tissue, avoiding the electrodes. As the gap was only microns in width sacrificing some electrodes was expected, however there was considerable effort to keep damage to a minimum. Using a constructed cellotape knife attached to a long tool (**figure 2.17**) the injury was carried out under a microscope. The cellotape knife was soft and used to ensure the MEA probe was not damaged/scratched and the width small enough to fit within the 100µm gap. The injury was made through the centre of the whole culture not just the electrode area, to mimic a complete transecting injury.
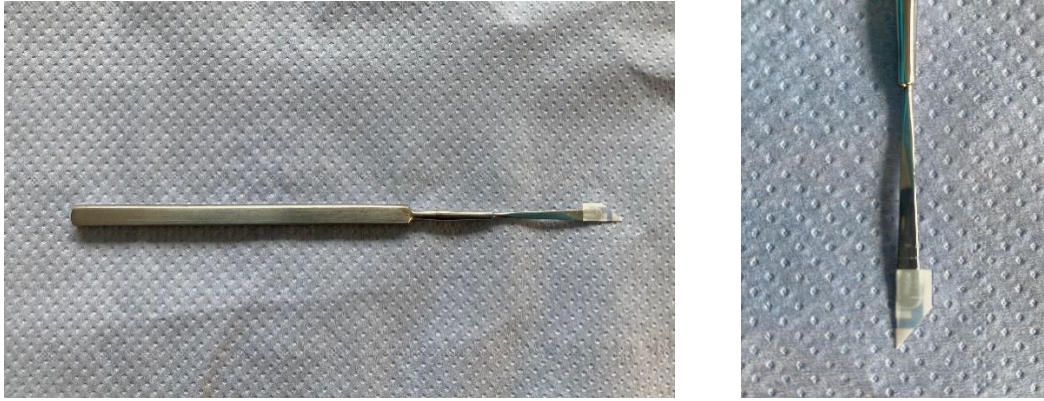
Figure 2.17: Tool used to introduce an injury to MEA seeded cells. Cellotape knife.

2.5.7 Running the Mobius software for neuronal spike recordings

The MED64 interface system for recording and data extraction is named Mobius and this had been previously installed onto the laboratory computer. Once the MEA probe is in place, Mobius was launched as a new 'spike recording' template workflow. For recording certain parameters were set on the 'Main' tab; timing trace number: 1, trace duration: 5 minutes, input range: 2.9 mV, low cut frequency: 100 Hz, high cut frequency: 1000 Hz. Through the working directory tab the file was named, and the storage folder selected. Following this, the play and record button was selected to initiate the 5-minute recording.

A new 'spike_frequency_analysis' template was opened through Mobius (**figure 2.18**) to extract the data within desired thresholds. The raw data was played and within the 'extraction' tab and a threshold value of ±0.018mV was set for spike detection (**figure 2.18 A**). This means that every neuronal spike ±18μV and over would be registered as a spike and extracted from the raw recording (i.e. signals over 18μV were considered a neuronal spike). This value was deduced via MED64 advice, additionally standard neuronal spiking values tend to range from 20μV- 200μV (Tortora and Grabowski, 1993). Channel noise can be larger than ±0.018mV, thus every channel was manually inspected and if the noise was larger than the threshold, the range was moved beyond the noise. A degree of external and internal noise is inevitable within these systems. Additionally, a threshold value of 0.050mV was used for some data extraction, this was to filter out the common smaller signals and analyse the frequency of larger signals.

Once the threshold parameters were set appropriately, on the 'spike' tab there are 3 options for data extraction; 1. time stamps only 2. time stamps and spikes. 3. spike frequencies (**figure 2.18 B**). All data extractions were selected, named appropriately and the working directory chosen, then the play and record button was selected to run through the extraction. The data extraction files are saved as .csv which can be opened in excel.

In addition to the 'spike_frequency_analysis' template the 'spike_sorting' template was used for the grouping of spike waveforms detected by each channel. A colour was assigned to each waveform which can have varying voltage values yet are grouped together by waveform similarities (**figure 2.18 C**). Each electrode channel may detect multiple waveform groups. The waveform groups generally resemble separate neurons firing over that one electrode. These files were saved in the centroid filename name section under 'spike waveforms'.

2.5.8 Spike Frequency analysis

The spike frequency csv file was opened in excel for the 6 timepoints for each MEA culture. The file gives the average spike frequency (Hz) for each of the 64 channels. To calculate the average spike frequency non firing channels were removed from the dataset, leaving only spike frequency of firing channels. These averages were plotted for each biological repeat.

2.5.9 Generating typical waveform graphs from the spike sorting centroid values

Spike waveform csv file was opened in excel. Here centroids represent the average waveform for one grouping of neuronal spikes over 3.5ms. These values were extracted and voltage was plotted against time (ms) in excel to give the typical waveforms observed at each timepoint.

2.5.10 Running Mobius offline toolkit for data analysis

Mobius offline toolkit (MbT) is a software to aid the analysis of the electrophysiological data extracted from the MED64 system.

Using the 'burst detector' platform analysis of single- or multi-channel spiking and bursting was performed. Firstly, the appropriate file was opened i.e. the csv file named 'time stamps only'. Parameters for detectable bursting were then chosen as; bin size: 20ms, smoothing: 10bin, burst detector: normal, Upper threshold: 100 spikes/s. After clicking execute, a raster plot can then be produced by plotting each spike as a mark against time over 1 minute. Average values could also be extracted: these included the ASDR, synchronised burst rate, number of spikes with a burst and overall number of spikes. Averages across each biological repat was analysed via GraphPad. Additionally, the "voltage chart" application was used to plot the 10 second traces of spike voltage.
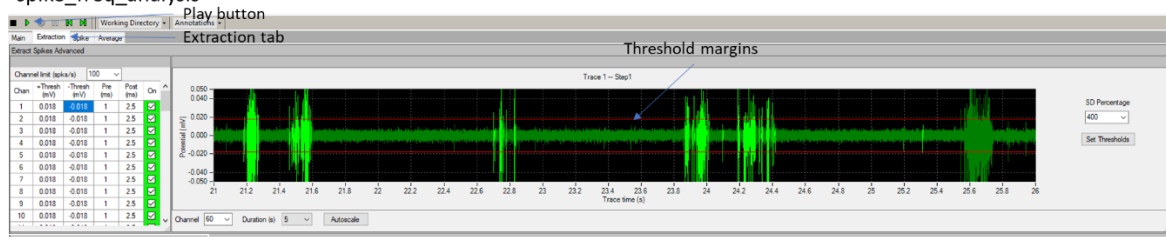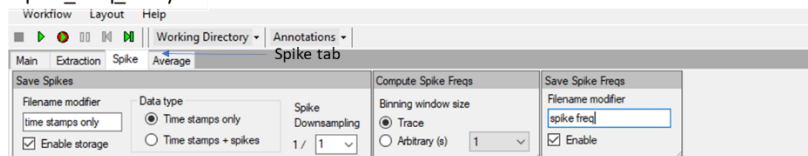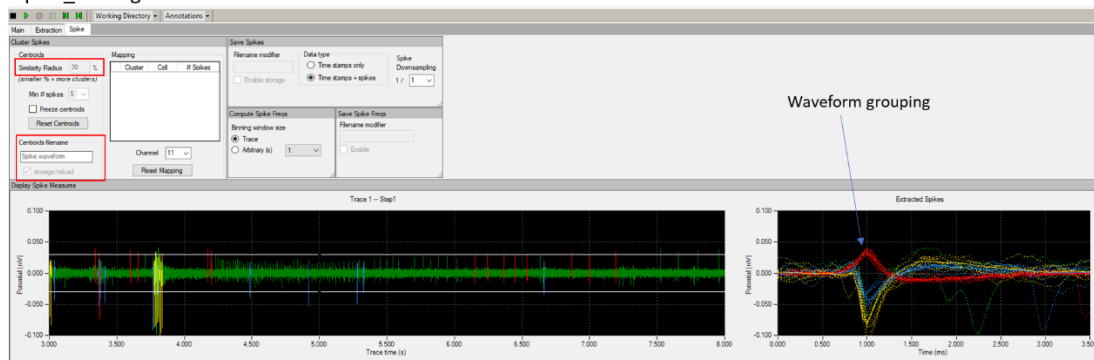
Figure 2.18: Annotated screenshots of Mobius software. **A** "extraction" tab on spike_freq_analysis is used to manage threshold margins of spikes. **B** the "spike" tab on spike_freq_analysis is used to enable data extraction of " time stamps only" or "time stamps and spikes" and "spike freq" extraction. **C** the spike_sorting_platform was utilised for extracting spike waveforms that were grouped though similarity.

3 Chapter 3: Implantation of a neurosurgical grade scaffold into organotypic models of traumatic CNS injury.

3.1 Introduction

3.1.1 Rodent brain and spinal cord organotypic tissue and injury models

To understand the complex nature and mechanism of tissue damage to the spinal cord and brain, a complex tissue model is required that is highly representative of the three-dimensional (3D) tissue organisation. Organotypic slice cultures (OSCs) of the brain or spinal cord provide a complex cellular environment with both neurons and glial cells existing in a 3D extracellular environment. In comparison to animal models, organotypic slices are reductionist yet recapitulate some of the complex cytoarchitecture of the native neural milieu and pathological cellular dynamic. Additionally, organotypic systems have the added benefit of *in vitro* culture systems including the ease of manipulation and evaluation (highlighted in section 1.3.3.1). Simpler reductionist models (i.e 2D cell cultures) although straightforward to maintain and high throughput, lack the cytoarchitecture of native tissues and do not replicate such molecular and functional ability.

Various methods to mimic mechanical TBI in organotypic slices have been documented. Most commonly reported is a tissue stretch/strain mechanism for OSCs. Here brain slices are often cultured on silicone membranes and then subject to a rapid deformation system which in turn induces a mechanical stretch to the tissue, where cell death is positively correlated with strain deformation and cellular degeneration replicates *in vivo*-like conditions (Morrison et al., 2000; Morrison et al., 2006; Pietro et al., 2013). In another model, a compression device is used to recreate a compression injury on rat neocortex brain slice cultures; in this study analysis of cell viability, axonal morphology and protein expression was shown to display results similar to compressive blunt head trauma (Bar-Kochba et al., 2016). Another paper has described a model of primary blast TBI. A compressed-air driven shock tube was used to expose mouse hippocampal slice cultures to a single shock wave. A cell damage marker revealed a damage-dependant cell death with increasing "blast strength" (Campos-Rires et al., 2018). Others describe stainless steel cylinders rolled over the OSC or dropping a weight (0.137g) on a

localised area of the OSC from a 2mm height; local ischemia, cell death and neurodegeneration was detected (Adamchik et al., 2000). Though these models can replicate various modalities of injury, in general they do not provide a robust analysis of the major injury mechanisms including: astrogliosis, microgliosis, axonal degeneration/regeneration and oligodendrogenesis.

As with the brain organotypic injury models, there are traumatic injury mechanisms reported for spinal cord OSCs. The most popular traumatic injury mechanism reported for spinal cord organotypic slices is the weight drop model which generates a contusion-like injury (Krassioukov et al., 2002; Pandamooz et al., 2019). Pandamooz et al. have also demonstrated this type of injury model could be achieved with adult rat spinal cord slices, where cellular death, motor neuron survival and inflammation hallmarks through cytokine mRNA analysis were assessed. Another model used a modified forceps mechanism producing a compression injury by constant mechanical force for 15 seconds (Chen et al., 2012). Furthermore, Weightman et al., in 2014 described a complete transection penetrating injury model which replicated the major pathological cellular responses to neurological transecting injury observed *in vitro*; including astroglial scarring, microglial infiltration and varying degrees of neurite outgrowth (Weightman et al., 2014).

Here, for both spinal cord and brain organotypic slice models a complete transection injury was chosen. Complete transection over other injury mechanisms including partial transection is regarded more favourable in terms of the ability to analyse post-injury responses due to the ease of identifying the injury location. For example, axonal regeneration is easier to anatomically verify in focal injuries compared with non-penetrating, contusion force or stretch models because of the incomplete nature of these injuries. In addition to this a complete penetrating injury leaves a clear identifiable injury cavity, and the cavity is ideal for implantation of a biomaterial for developmental testing. The clear cavity also allows for straightforward analysis of cellular infiltration and behaviours within or at the periphery of the lesion. Complete transecting injuries are not the most common primary mechanisms for either SCO or TBI. Spinal cord compression (contusions injuries) are the most frequent mechanism of SCI, with

lacerations (incomplete/complete transection) following and these usually cause the most significant symptoms, particularly cervical complete transection injuries (Zhang *et al.*, 2021). Similarly, the most common mechanism upon which TBI occurs is classified as "blunt traumas" (i.e. contusion injuries), however penetrating (laceration injuries) are the most fatal.

3.1.2 Interfacing biomaterials with organotypic CNS tissue models

Many studies have been conducted on the therapeutic efficacy of biomaterials alone and in combination with other therapies for SCI/TBI, and undoubtably these have been effectively interfaced with the spinal cord and brain tissue of various animal injury models and in clinical trials (Jeong, et al., 2021). Initially biomaterial structure (i.e. appropriate biomimicry of neural tissue softness) and safety (i.e. does not exacerbate glial scarring or provoke immune response) must be optimised (Talac et al., 2004). Secondly the biomaterial is assessed for its trophic ability and whether it can promote neural cell survival and growth, it is important here that neurons will extend their axons using the biomaterial for topographical cues (Enoke et al., 2020).

Biomaterials interfaced with organotypic models of the spinal cord have been used to show the outgrowth of motor neurons from transverse slices as a platform for biomaterial screening (Gerardo-Nava et al., 2014; Allodi & Esther, 2011). Both these approaches do not incorporate a "traumatic injury" in the organotypic spinal cord within their model to assess the functionality of the biomaterial. Consequently, this type of model does not recapitulate the pathology of an injury environment and in turn this may alter the response to a biomaterial. Yet interfacing materials with an ex vivo model of spinal cord can provide an important assessment of individual cell-material interaction at various timepoints (Gerardo-Nava et al., 2014). This type of analysis is considerably more difficult within *in vivo* models as many animals are required for multiple timepoints and analysis parameters. A study by Weightman et al., is amongst the first to apply a biomaterial evaluation to an organotypic model of spinal cord injury. Aligned nanofibre frames were incorporated over longitudinal injured slices

(Weightman et al., 2014). This application allowed a cellular comparison of the response to injury alone and injury with an overlaying aligned scaffold; here neuronal axons extending from the lesion site were observed to align with the nanofibers.

There are a very limited number of reports in which biomaterials are studied in organotypic brain or spinal cord tissue models (Gerardo-Nava et al., 2014; Biancotti et al., 2020; Prang et al., 2006; Weightman et al., 2014; Ucar et al., 2021; Ucar and Humpel 2019; Guijarro-Belmar et al., 2019), **two of which are traumatic injury models**, others include tissue models for motor neuron outgrowth, disease models (Parkinson's), and co-culture slice models interfaced with biomaterials. The current study reports the first time a biomaterial has been successfully implanted directly into the transecting lesion area of brain and spinal cord organotypic slice models for a comparative study.

3.1.3 FDA-approved surgical grade biomaterials as an avenue for implantation therapy

Clinical biomaterials undergo extensive safety assessment prior to approval for human use, and through clinical safety governing authorities such as the Food and Drug Administration (FDA), this process can take up to seven years. Research of biomaterial therapies predominantly uses laboratory grade materials unsuitable for human use. Despite the clinical relevance and efficacy these biomaterials proved through animal testing, there is no guarantee that such biomaterials will be suitable for clinical translation and are often refused (Norman et al., 2016). A solution for this would be to use neurosurgical grade materials.

Neurosurgical biomaterials offer a unique advantage of being FDA-approved for human transplantation with the nervous system. Thus, research employing clinical-grade biomaterials with a new regenerative purpose, is one strategy to avoid the arduous clinical safety testing and the lack of success in reaching clinical trials. Currently, collagen biomaterials are broadly used in FDA-approved nerve conduits for peripheral nerve guidance i.e. NeuroFlex[TM], NeuroMend[TM] and NeuroMatrix[TM] which are all

semipermeable structures that permit nutrient diffusion while they wrap around and provide an encasement for peripheral nerve injuries (Chrzaszcz et al., 2018). These have been shown to support nerve guidance in the PNS for gaps up to 2-3cm. In addition, there are various dural grafts material FDA-approved for neurosurgery i.e. DuraGen™ (Jain et al. 2006).

3.1.3.1 DuraGen™ as a regenerative matrix

DuraGen™ is an FDA-approved clinical grade biomaterial widely used in neurosurgery as a dural substitute once the dura becomes compromised during neurosurgery. Its matrix is composed of semi-synthetic, 95% ultra-pure type 1 collagen and is derived from bovine deep flexor tendons. DuraGen™ is described as "minimally immunogenic" due to the purification process (Integra, 2018). Its collagen matrix provides a framework that induces initial fibroblast ingrowth from the intact dura and this enhances closure of the dural layer to prevent cerebrospinal fluid seepage (Narotam et al. 1993; Narotam et al. 1995). It is a biodegradable substrate that naturally degrades in 3 months and allows the repair of the dura without the formation of scar tissue or encapsulation (Integra LifeSciences, 2019).

Previous research has demonstrated that DuraGen™ is non-toxic and promotes the survival of cortical neurons. Here, glutamate-induced toxicity of the cultured neurons on the DuraGen™ showed no adverse effects in comparison with a glass substrate (Rabinowitz et al 2005). Interestingly, Finch et al. demonstrated that DuraGen™ can act as an effective protective matrix for the encapsulation of neural cell types, where NSCs seeded within the biomaterial matrix had above ca 94% cell viability and maintained appropriate cellular phenotypes. A single report within the literature demonstrates the pro-regenerative potential of DuraGen™ for CNS repair. Rats subject to cortical impact brain injury received implantation of the ECM graft DuraGen™ over the injury. The rats with DuraGen™ graft (18 days post implantation) showed a significant enhancement of spatial memory gain, yet motor function was not affected. After tissue analysis, the collagen matrix was shown to reduce the contusion lesion area and improve neuronal survival, suggesting that DuraGen™ has a neuroprotective mechanism and possibly a pro-regenerative influence on neurorepair (Shin et al. 2015). These results reinforce and support the idea for this scaffold to be used within a 3D neural tissue engineering implantation therapy.

In summary, the collagen hydrogel material DuraGen™ shows promise in facilitating tissue repair and potential functional recovery. Currently there are no studies which investigate the use the DuraGen™ as an implantation therapy for penetrating TBI or transecting SCI. To facilitate this, appropriate *in vitro* models of CNS injury, that also allow biomaterial implantation and assessment of multiple neural cell responses and regenerative parameters is essential.

3.1.4   Objectives

The aims of this chapter are:-

    i)   To efficiently reproduce and modify a previously described organotypic spinal cord injury (SCI) model (Weightman et al., 2014); and adapt this organotypic SCI model to an organotypic TBI model. Assessment and comparison of the TBI and SCI models will be through tissue characterisation and quantification of the major neuro-pathological events such as reactive gliosis, immune cell infiltration and neuronal outgrowth/degeneration following lesion induction.

    ii)   To assess the biomaterial DuraGen™ as a regenerative matrix using the developed organotypic slice spinal cord and brain transecting injury models. Protocols were developed to analyse the feasibility of material implantation within the lesion gap and to visualise the tissue responses to the material implantation.

3.2 Results

3.2.1 Cell viability assays show viable scOSC and bOSCs up to 18 DIV

To assess whether the organotypic SCI and TBI models reproduced in this study displayed viable slice cultures, (similar to the previously established organotypic SCI model) slice viability assays were carried out. Live and dead cells stained with calcein and ethidium homodimer-1 (EthD-1) respectively were assessed at 5 days *in vitro* (DIV), 11 DIV, 18 DIV, 7 days post lesioning (DPL) and 14 DPL (slices were lesioned at 4 DIV).   Initially, post-slice sectioning cell death (red) accumulated mainly at the slice periphery while the main body of the slice showed high viability (green) **(figure 3.1 scOSC A-B; bOSC F-**

G). Similarly, initial cell death post-lesioning was localised to the lesion boundary (**figure 2.1 scOSC C; bOSC H**). By 18 DIV or 14 DPL, cell death localised at the slice periphery/lesion margin appeared to diminish, and dead cells are predominantly seen within the body of the slice (**figure 3.1 scOSC D-E; bOSC I-J**). These slices still demonstrate clear high viability within the slice body. This suggests that over time, the initial wave of cell death induced by slicing or lesioning is diminished. This evidence provides a good indication of slice viability pre- and post-lesioning for both cultures at up to 18 DIV. These micrographs also highlight a complete transecting injury can be reproducibly generated within the spinal cord and brain slices. This slice viability response is consistent with previous evaluation on scOSCs carried out by Weightman et al., 2014.

3.2.2 Cellular characteristics of intact slices

It is important that the cell types expressed within the scOSCs and bOSCs show normal and healthy phenotypes up to the latest timepoint when evaluating pathological mechanisms to injury and biomaterial implantation. Figure 3.2 displays the cell types assessed within this study at 18 DIV: astrocytes (GFAP+), neurons (TUJ-1+) and microglia (Iba1). Microglia were distributed throughout both tissue cultures and exhibited distinct ramified 'resting' morphologies (**figure 3.2 scOSC A; bOSC B**). Within the main body of scOSCs and bOSCs, healthy type 2 fibrous astrocyte morphologies are seen up to 18 DIV, which form an astrocytic network of processes (**figure 3.2 scOSC C; bOSC F**). However, at the slice periphery, astrocytes express two patterns of responses to the initial sectioning of the tissue; presenting either palisading astrocytes (yellow arrows) or astrocytes appear to undergo gliosis and knit together producing a scar like edge (blue arrows) (**figure 3.2 scOSC D-E; bOSC G-H**). Both these astrocytic behaviours are typical of reactive astrocytes. Furthermore, neuronal networks are retained within the scOSCs (**figure 3.2 I-J**), retaining visible spinal cord neuronal tracts (**figure 3.2 J**) (up to 18 DIV). Neuronal networks within the bOSC were also retained **figure 3.2 K**).
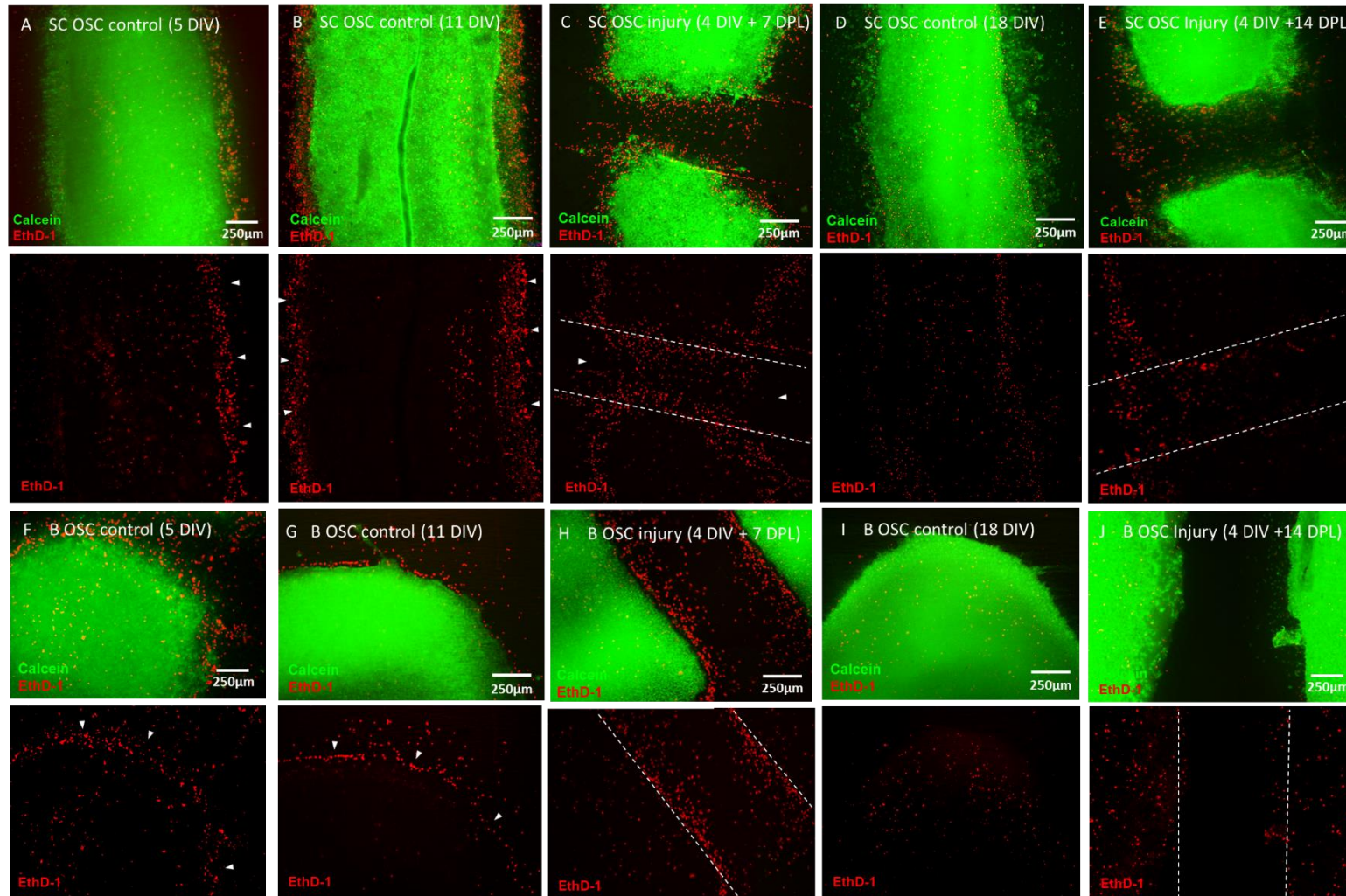
Figure 3.1. Viability of intact and injured scOSCs and bOSCs. Representative micrographs of scOSCs (**A-E**) and bOSCs (**F-J**), top panel merge Calcein (live) and EthD-1 (dead), lower panel dead cell only (arrows highlight dead cell localisation, dotted lines signify injury margins). **scOSC** - F control slice at 5 DIV, **G** control slices at 11 DIV, **C** injured slice 4 DIV + 7DPL, **D** control slice at 18 DIV, **E** injured slices at 4DIV + 14 DPL. **bOSC - F** control slice at 5 DIV, **G** control slices at 11 DIV, **H** injured slice 4 DIV + 7DPL, **I** control slice at 18 DIV, **J** injured slices at 4DIV + 14 DPL.
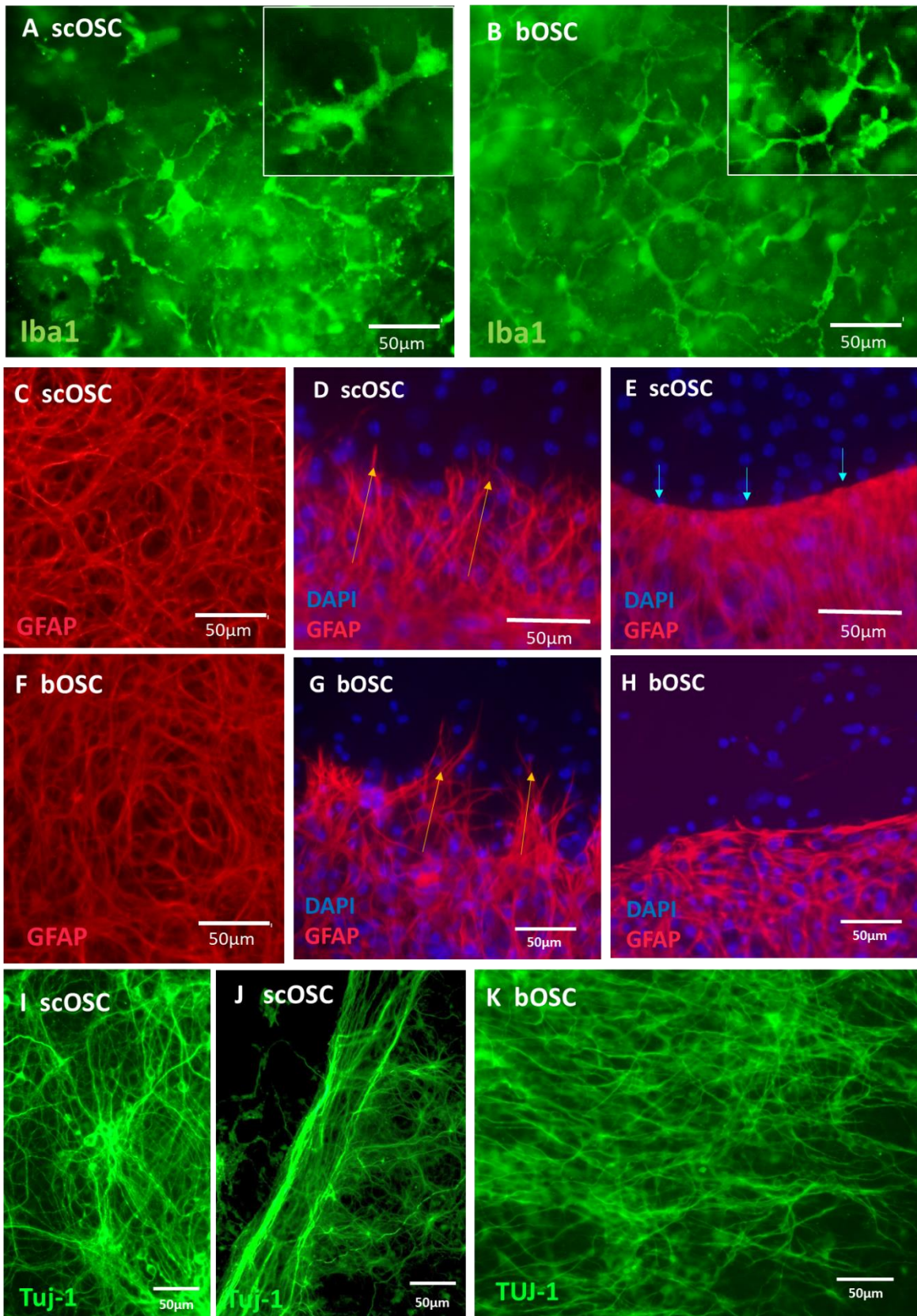
Figure 3.2. Cellular characteristics of the intact slices at 18 DIV. Representative fluorescence micrographs of Iba1+ microglia, GFAP+ astrocytes and TUJ-1+ neurons. Microglia express ramified morphologies throughout both **A** scOSCs and **B** bOSCs. Astrocytes in the main body of the slice express

typical type 2 morphologies forming an astrocytic network in both scOSCs **C** and bOSCs **F**. At the slice periphery of both scOSC and bOSC palisading astrocytes are observed **D** and **G** respectively. Astrocytes also present a glial scar-like meshwork of astrocytes at the scOSC (**E**) and the bOSC (**H**) slice periphery. **I** shows that neuronal networks are retained within the scOSCs, **J** including visible neuronal tracts in **M** shows neuronal network retained within the bOSC.

3.2.3 Efficient DuraGen™ implantation within the transecting injury - generating the material-slice interface and evidence for tissue infiltration

The efficient implantation of DuraGen™ into the lesion site where the material interact with both lesion boundaries is a technically challenging procedure. Light microscopy of the spinal cord slice lesion area at 0hr (immediately post implantation) demonstrates the lesion area implanted with the biomaterial (**figure 3.3 bOSC A-B; scOSC C-D**). The biomaterial interacts with the lesion boundary, generating a material-slice interface which was further investigated. Through light microscopy of a 1-micron thick cross-section of a TEM prepared sample, the material-slice interface was visualised in more detail (**figure 3.3 E-F**). The cross-section view at 14 DPL illustrates that the biomaterial was implanted efficiently within the lesion margins and does not overlap the spinal cord tissue at the lesion boundary (**figure 3.3 E**). Further magnification of this material-slice interface (**figure 3.3 D**) revealed that tissue ingrowth appears at the bottom, middle and upper level of the DG. This confirmed the tissue ingrowth was through the materials matrix rather than only growing over or under the material. DuraGen™ has a non-uniform porous nature, and there may be evidence in figure 3.3 E that the biomaterial topography could be blocking further extension of the infiltrating tissue across the lesion, i.e. the pore pocket may cause the tissue to change direction rather than growing directly across the lesion.

Transmission electron microscopy (TEM) imaging generates an ultra-magnified cross section view of the area of interest, instead of the top-down system typical microscopy imaging offers. TEM was applied in this case to provide information on whether the tissue was using the intra-material fibres to grow through. The TEM prepared sample was placed onto a copper grid which supports the ultra-thin sample

section, the copper grid was then placed into the transmission electron microscope. At low magnifications, the grid lines of the copper grid were visible when imaging the entire area of interest, evident in **figure 3.4 A**. In order to visualise the full material-slice interface and tissue ingrowth a low magnification image was required where grid lines were also visible (**figure 3.4 A**). These images demonstrated that the spinal cord tissue extending from the lesion edge was growing through the material using the matrix topography as guidance. The dotted line signifies the material boundary, the red dotted point at which the material interacts with the body of the spinal cord tissue and arrows indicate the direction of tissue ingrowth (**figure 3.4 A, E, F**). Material-slice interface 1 (**figure 3.4 B**) shows clear tissue ingrowth and was examined further (**figure 3.4 C**). Through ultra-magnification of figure 3.4 D and E, neural cell types could be distinguished interacting with the material. **Figure 3.4 D** shows a microglial cell migrating through the pores of the matrix. This nucleus structure is typical of a microglial cell (MG) with the cytoplasm containing what appears to be inclusion bodies. Additionally, a typical structure of an axon growth cone (AGC) could be identified, the AGC appears to also show the formation of a tight junction with a neighbouring cell. This may suggest synaptic connections forming within the material. Material-slice interface 2 (**figure 3.4 F**), also clearly demonstrates tissue ingrowth through the matrix of the material. Two areas were magnified further where tissue structures could be observed (**figure 3.4 G, I**), both these micrographs indicate astrocytic-like cells following the material fibres. At higher magnification these were confirmed as astrocytic fibres (AF), signified by their heavily fibrous intracellular composition (**figures 3.4 H, J**). The astrocytic processes (AF) were in direct contact with the material (M) and followed the materials topography (blue arrows in **figures 3.4 H, J**).
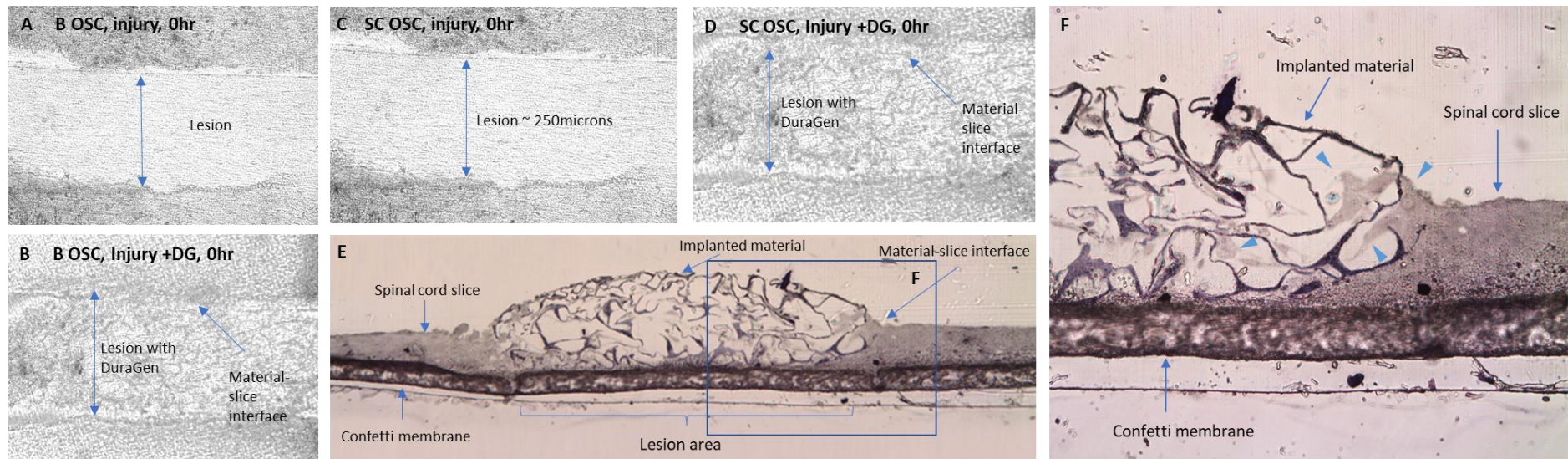
Figure 3.3. Evidence for the implantation of the biomaterial and producing a material slice interface. A-B. representative micrographs of injured bOSCs without and with biomaterial implantation respectively at 0hr. **C-D**. representative micrographs of injured scOSCs without and with biomaterial implantation respectively at 0hr. **E** representative cross section view reveals efficient biomaterial implantation at 14 DPL and evidence of the material slice interface. **F** magnification of the material slice interface reveals tissues ingrowth into the material (blue arrows).
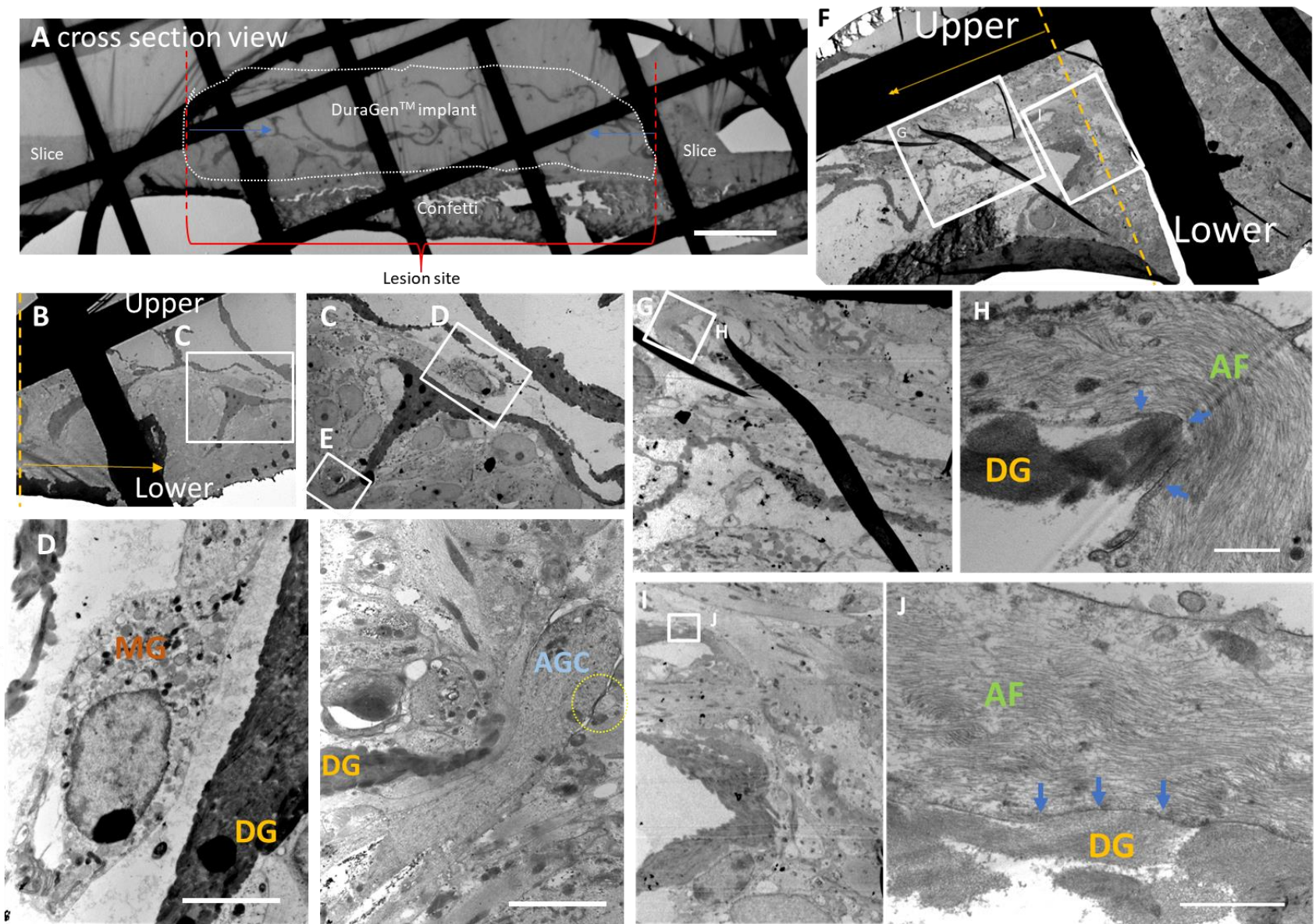
Figure 3.4. Transmission electron microscopy reveals various cell types within the DuraGen™. A annotated low magnification image showing the cross section of lesion area with implanted material. **B** shows one area of tissue ingrowth into the material (material-slice interface 1). **C** further magnification of B. **D** high magnification image of infiltrating microglia (MG). **E** high magnification image of what appears to be an axon grow cone (AGC) proximal to DG matrix fibre. Dotted circle signifies a possible tight junction. **F** second area of tissue ingrowth (material-slice interface 2), white boxes signify 2 areas of further magnification **G** and **I**. G and I are further magnified to **H** and **J** respectively where astrocytic fibres (AF) are shown to make tight connections with the material fibres. DG = material, MG = microglia, AGC = axon growth cone, AF = astrocytic fibres. Scale bar = 5 µm.

3.2.4 Apparent morphological disruption of the glial scar in both scSOCc and bOSCs following biomaterial implantation

Glial scar formation in response to injury and therapeutic biomaterial implantation is often assessed to establish any pro-regenerative or pro-scarring potential of the transplanted material. Control scOSCs at 14 DPL (18 DIV) demonstrated astrogliosis along the periphery of the slice, this is defined by enhanced expression of GFAP (**figure 3.5 A**). Reactive astrocytes that upregulate GFAP and form an interconnected network of astrocytic processes can be visualised as a red band of increased GFAP expression. Injured slices (at 14 DPL) display astrogliosis/glial scar at the lesion margins, and at the periphery of the slice (**figure 3.5 B**). In contrast, DuraGen™ implantation into the scOSC injury site appears to disrupt the typical formation of the glial scar, and results in an apparent morphological disruption at the lesion edge (**figure 3.5 C**). Higher magnification of the glial scar at the injury site without material implantation displays the dense interconnected network of reactive astrocytes with enhanced GFAP expression (**figure 3.5 D** arrows). Also demonstrated here is the band-like appearance of enhanced GFAP expression usually around 50µm thick (**figure 3.5 D** brackets). High magnification of astrocytes at the material-slice interface reveals astrocytes aligning perpendicular to the injury and infiltrating the biomaterial (**figure 3.5 E** yellow arrows). Some astrocytes at the material-slice interface also exhibit increased GFAP expression (**figure 3.5 E** blue arrows). **Figure 3.5 F** shows extensive infiltration of

astrocytic fibres within the biomaterial with associated nuclei; which is characteristic of astrocytes migrating or proliferating into the biomaterial.

At 14 DPL measurements of astrogliosis were taken as defined in section 2.3.4. Astrocytic optical density at the lesion edge (0-100µm) of injured slices displayed over a 2-fold increase (2.09 ± 0.31 OD) (Two-way ANOVA with Dunnett's multiple comparisons, $p<0.05$, n=4), compared to baseline expression of astrocytes **(figure 3.5 G)**. Similarly, biomaterial implantation displayed a 2-fold increase in GFAP expression at the lesion margins (1.9 ± 0.32 OD) (Two-way ANOVA with Dunnett's multiple comparisons, $p<0.05$, n=4). Furthermore, there is no significant difference in GFAP reactivity between injured slices and injury + biomaterial implantation, meaning the biomaterial neither attenuates nor exacerbates this pathological response.

The overall pattern of response of astrocytes within the bOSC model is highly similar to responses seen within the spinal cord OSC model. Comparable to the scOSCs, the bOSCs show astrogliosis at the slice periphery and the lesion margins (**figure 3.6 A**). Again, upon implantation of DuraGen™ the normal glial scar like formation was disrupted and astrocytes appear to grow into the material (**figure 3.6 B**). Higher magnification of the lesion edge of injured brain slices and the material-slice interface of implanted brain slices (**figure 3.6 C and D** respectively), once again show a comparable response to the scOSCs to injury and implantation. Additionally, there is evidence in **figure 3.6 E** for astrocytic nuclei within the material, from either migrating or proliferating astrocytes. Finally, astrocyte reactivity was measured by optical density calculations of the GFAP expression. Brain OSCs display significantly enhanced GFAP expression levels towards the lesion margins (0-100µm), 2-fold increase (2.06 ± 0.5 OD) compared to the corresponding baseline astrocyte GFAP expression. Biomaterial implantation into the injury site of brain OSCs induced a similar 2-fold increase (1.97 ± 0.12 OD) from the baseline level [two-way ANOVA, Tukey's multiple comparisons, $p<0.01$**, n=4, **figure 3.6 F**). No difference was observed between the astrocytic reactivity at the injury only lesion edge and the material slice interface.
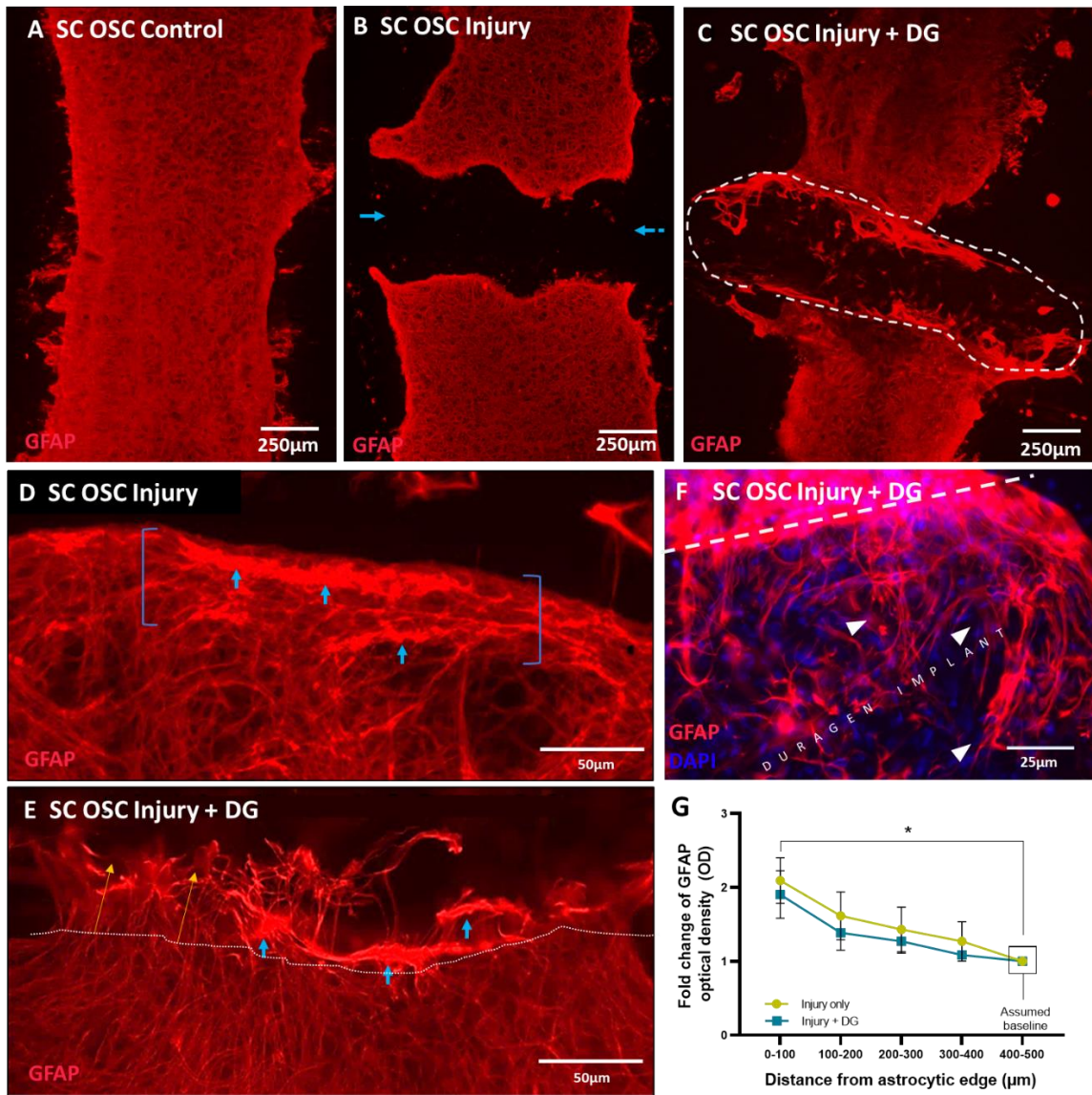
Figure 3.5. GFAP stained micrographs of spinal cord OSCs revealing morphological change of the glial scar (astrogliosis) with DuraGen™ implantation, along with astrocytic in growth (14 DPL). A representative of GFAP+ astrocytes within intact slice (no injury) (astrogliosis observed at the periphery of the slice i.e. enhanced GFAP expression). **B** representative micrograph of GFAP+ astrocytes with injured slices (gliosis can be observed at the periphery of the slice and at the lesion margins). Blue arrows indicate the injury cavity devoid of astrocytic debris. **C** representative micrograph of GFAP+ astrocytes of injury + biomaterial implantation. Dotted line outlines the perimeter of the biomaterial. The typical glial scar structure is disrupted, where astrocytic processes infiltrate the material and in some areas increased GFAP expression is displayed. **D** representative micrograph of the typical scar formation at the lesion edge. Arrows signify over expression of GFAP and brackets signify the band-like appearance of the scar. **E** representative micrograph of astrocytes at the injury + DG interface, disruption of typical glial: scar formation and an ingrowth of astrocytes into the material (yellow arrows)

114

is observed. Overexpression of GFAP is still observed in some astrocytes (blue arrows). Dotted line signifies original lesion edge. **F** shows the clear ingrowth of astrocytic fibres into the material, and what appears to be evidence of migration into the material (white arrows). **G** graph demonstrating the fold change of GFAP optical density (OD) from the lesion edge into the slice. OD at the lesion edge (0-100µm) was significantly higher than the OD of baseline astrocytes (400-500µm) for both injury and injury + DG scOSCs. DG implantation showed no obvious enhancement or reduction in GFAP reactivity. (two-way ANOVA with Tukey's multiple comparisons, *$p < 0.05$, n=4).
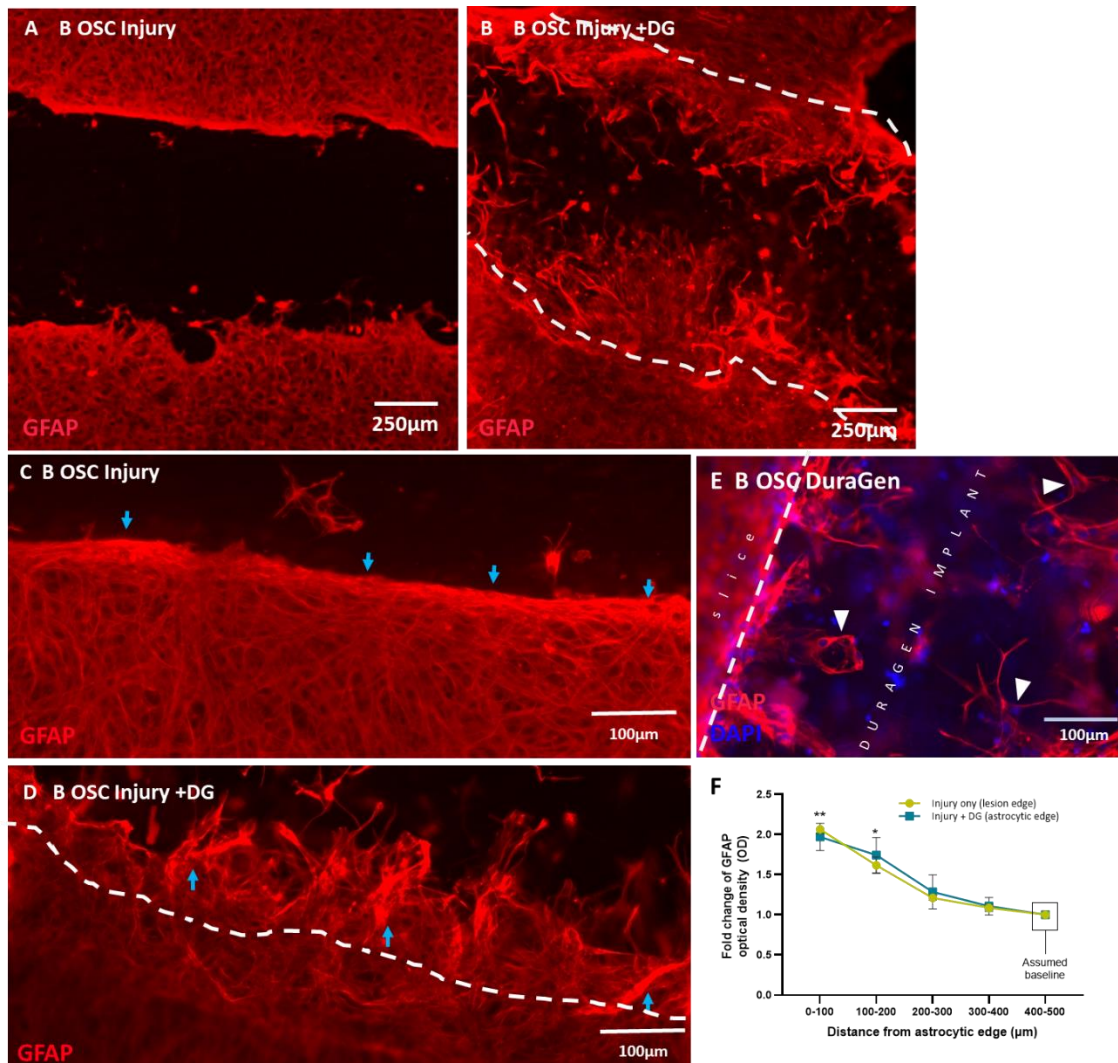
Figure 3.6. GFAP stained micrographs of brain OSCs revealing morphological change of the glial scar (astrogliosis) with DuraGen^TM implantation, along with astrocytic ingrowth (14 DPL). **A** representative micrograph of GFAP+ astrocytes with injured brain slices, astrogliosis observed at the lesion margins, (i.e. enhanced expression of GFAP). Lesion area clear of astrocytic debris was consistent. **B** representative micrograph of GFAP+ astrocytes of injury + biomaterial implantation. Dotted line outlines the perimeter of the biomaterial. The typical glial scar structure is disrupted, astrocytes infiltrate the material and enhanced GFAP expression is displayed in some areas. **C** representative

micrograph of the typical scar formation at the lesion edge. Arrows signify over expression of GFAP. **D** representative micrograph of astrocytes at the injury + DG interface, disruption of typical glial scar formation is observed with the ingrowth of astrocytes. Dotted line signifies material boundary. Overexpression of GFAP is still observed in some astrocytes (arrows). **E** shows ingrowth of astrocytic fibres into the material with lower GFAP expression. There is evidence here that astrocytes may be proliferating/migrating into the material as there are clear groups of astrocytic nuclei within the material (white arrows). **F** graph demonstrating the fold change of GFAP optical density (OD) from the lesion edge into the slice. OD at the lesion edge (0-100µm) was significantly higher than the OD of baseline astrocytes (400-500µm) for both injury and injury + DG scOSCs. DG implantation showed no obvious enhancement or reduction in GFAP reactivity. (two-way ANOVA with Tukey's multiple comparisons, *$p < 0.05$, n=4).

3.2.5 Microglia extensively infiltrate the implanted biomaterial, with evidence of a resting-like morphology

3.2.5.1 Robust colonisation with evidence of DuraGen™-residing microglia resuming a more quiescent-like state

Assessment of immune cell response to implanted materials is an important step to establishing a material's immunogenic capacity. Iba1+ (a microglial cytoskeleton marker) revealed the immune cells (microglia) within the OSC CNS injury models. At 14 DPL, DuraGen™ was robustly colonised by Iba1+ microglia in both scOSC and bOSCs (**figure 3.7 B and D** respectively), but the injury only lesion area presented considerably fewer microglial numbers (**figure 3.7 A and B** respectively). These were represented as low magnification images to show the whole DuraGen™ implant, with higher magnification micrographs are shown in figure 3.8. Microglial morphology and the rate of infiltration was assessed at separate time points 4-, 7- and 14-days post lesioning (scOSC: **figure 3.8**, bOSC: **figure 3.9**). The injury only area presented mostly bushy and rounded microglial morphologies at 4 DPL and 7 DPL, typical of activated microglia (scOSC: **figure 3.8 A,C**; bOSC: **figure 3.9 A, C**). In comparison, within the material at 4 DPL and 7 DPL microglia present more processed morphologies (scOSC: **figure 3.8 B, D**; bOSC: **figure 3.9 B, D**). Yet at this timepoint both injury slices and implantation treated slices

displayed similar infiltration numbers. At 14 DPL, typically fewer Iba1+ cells occupied the lesion site, and these exhibited small-rounded morphology (scOSC: **figure 3.8 E**; bOSC: **figure 3.9 E)**. However, the material was highly populated with microglia which again were more processed in morphology (scOSC: **figure 3.8 E**; bOSC: **figure 3.9 E)**. To quantify the apparent morphological shift of microglia within the lesion site or the material, the CRI was calculated (see methods section 2.3.8). This method proved that microglia cells were significantly more ramified within the DuraGen™ biomaterial at the injury site at all 3 timepoints (scOSC: **figure 3.8 G**; bOSC: **figure 3.9 G)** . Additionally, the microglial infiltration rate into the implant showed a gradual increase from day 4 to day 14 PL. Microglial influx in injury only slices peaked at 7 DPL and a large reduction was seen at 14 DPL (scOSC: **figure 3.8 H**; bOSC: **figure 3.9 H)**.
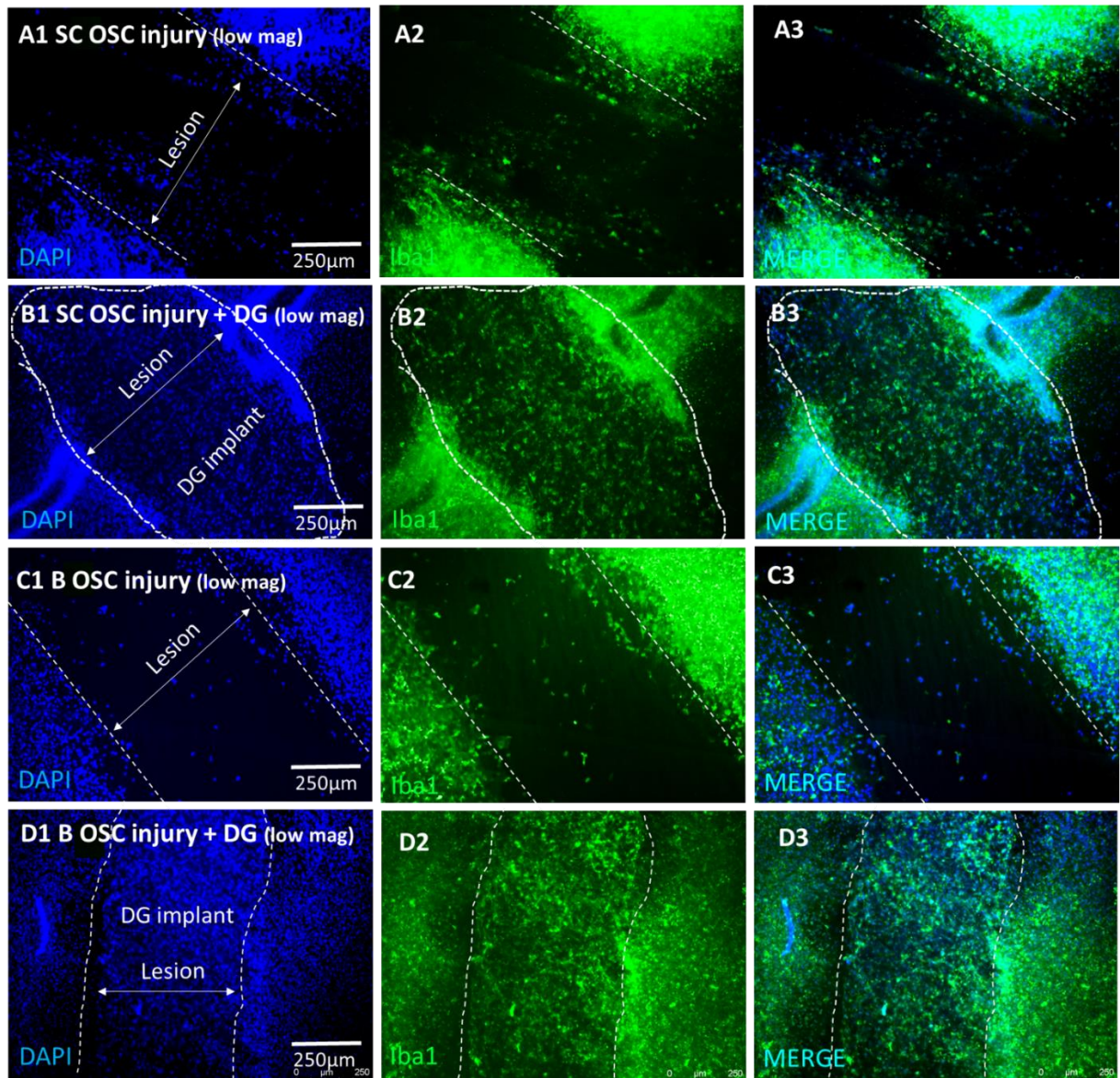
Figure 3.7. Microglia are observed to robustly colonise the material in both scOSCs and bOSCs, and not injury site alone. At low magnification. **A** representative micrograph of the scOSC injury site only, shows a relatively low microglia infiltration, DAPI (A1), Iba-1 (A2) and MERGE (A3). (Dotted lines signify injury margins) **B** representative micrograph of the scOSC injury site + DG, shows distinctively higher microglial infiltration, DAPI (A1), Iba-1 (A2) and MERGE (A3). (Dotted line signifies material boundary). **C** representative micrograph of the bOSC injury site only, showing a low microglia infiltration, DAPI (A1), Iba-1 (A2) and MERGE (A3). (Dotted lines signify injury margins). **D** representative micrograph of the bOSC injury site + DG, showing distinctively higher levels of microglia infiltration, DAPI (A1), Iba-1 (A2) and MERGE (A3). (Dotted line signifies material boundary). (14 DPL)
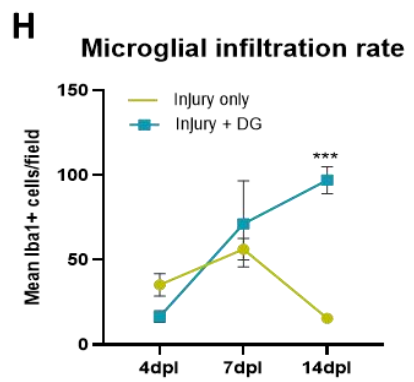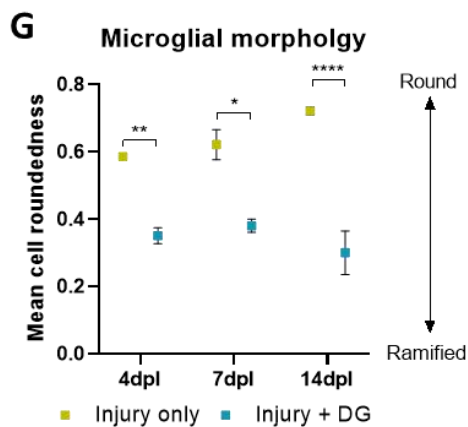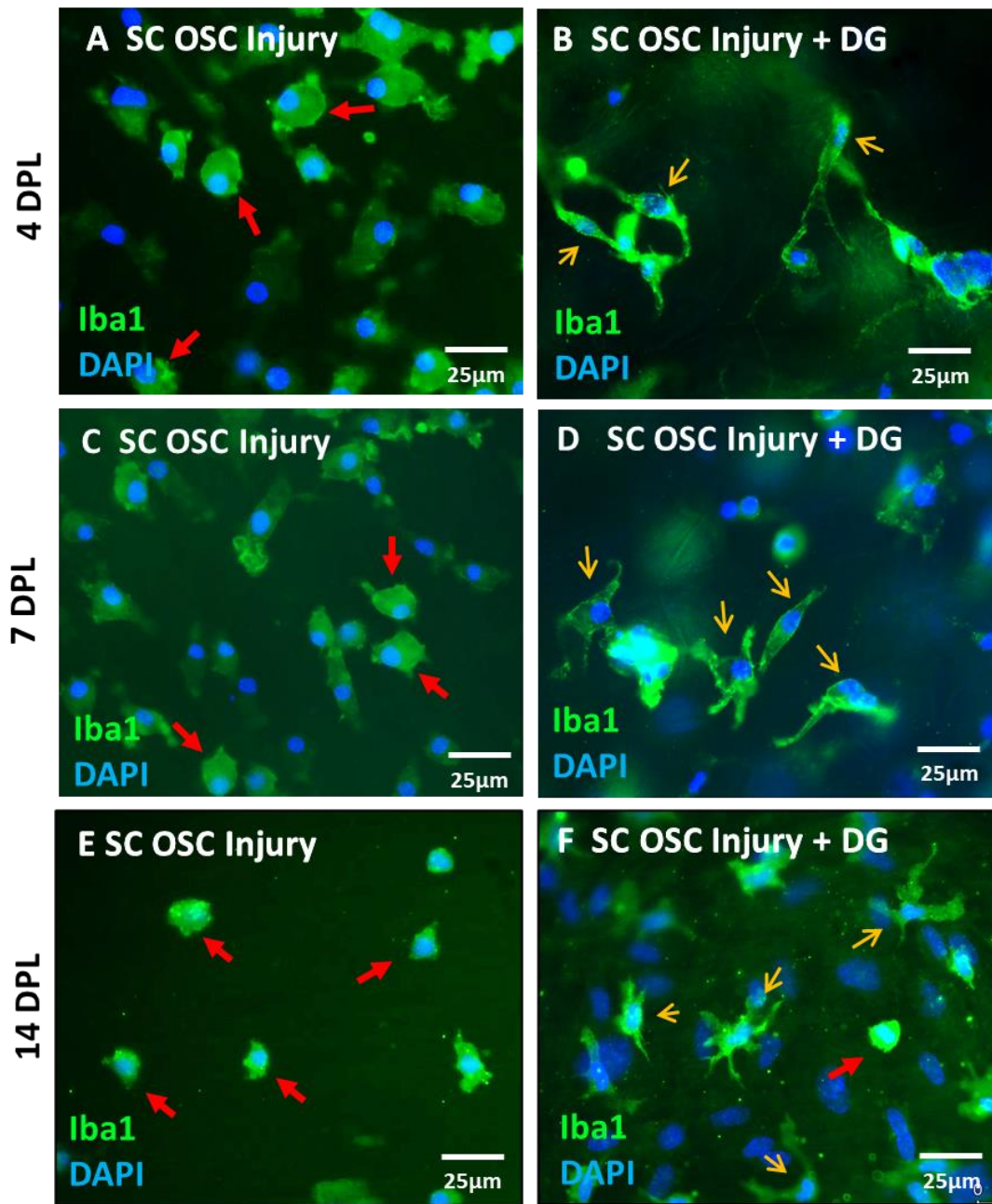
Figure 3.8. Material residing microglia appear to resume a resting-like morphology within the material (spinal cord tissue). A, C and E representative micrographs of the amoeboid/bushy activated

morphologies observed with the lesion site at 4, 7 and 14 DPL respectively. Microglia infiltration at 4 and 7 DPL is higher compared with 14 DPL. **B, D and F** representative micrographs of the more processed ramified morphologies exhibited by material-residing microglia at 4, 7 and 14 DPL respectively. **G** graph indicating mean microglial cell roundedness as various 4, 7 and 14 DPL. Microglial cells within the DuraGen™ are significantly more ramified than cells within the lesion alone (all timepoints). **H** graphs reveals an exponential increase in microglial numbers within the material over 14 days, yet within the lesion only there is an initial increases which reduces after 7 days. [two-way ANOVA with Tukey's multiple comparisons, *p<0.5, **p<0.01, ***p<0.001, ****p<0.0001, n=4].
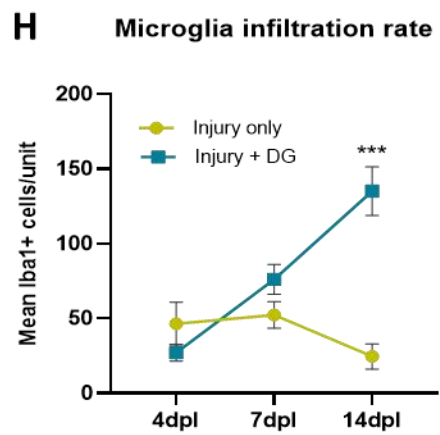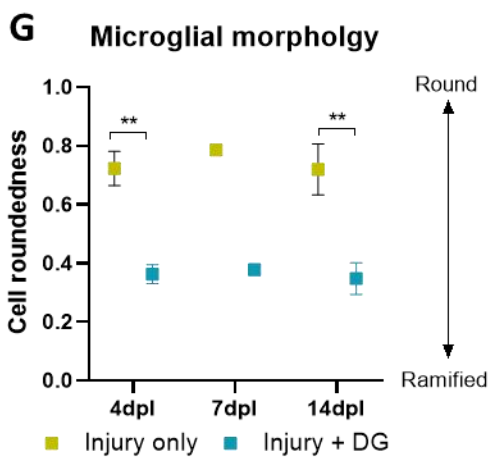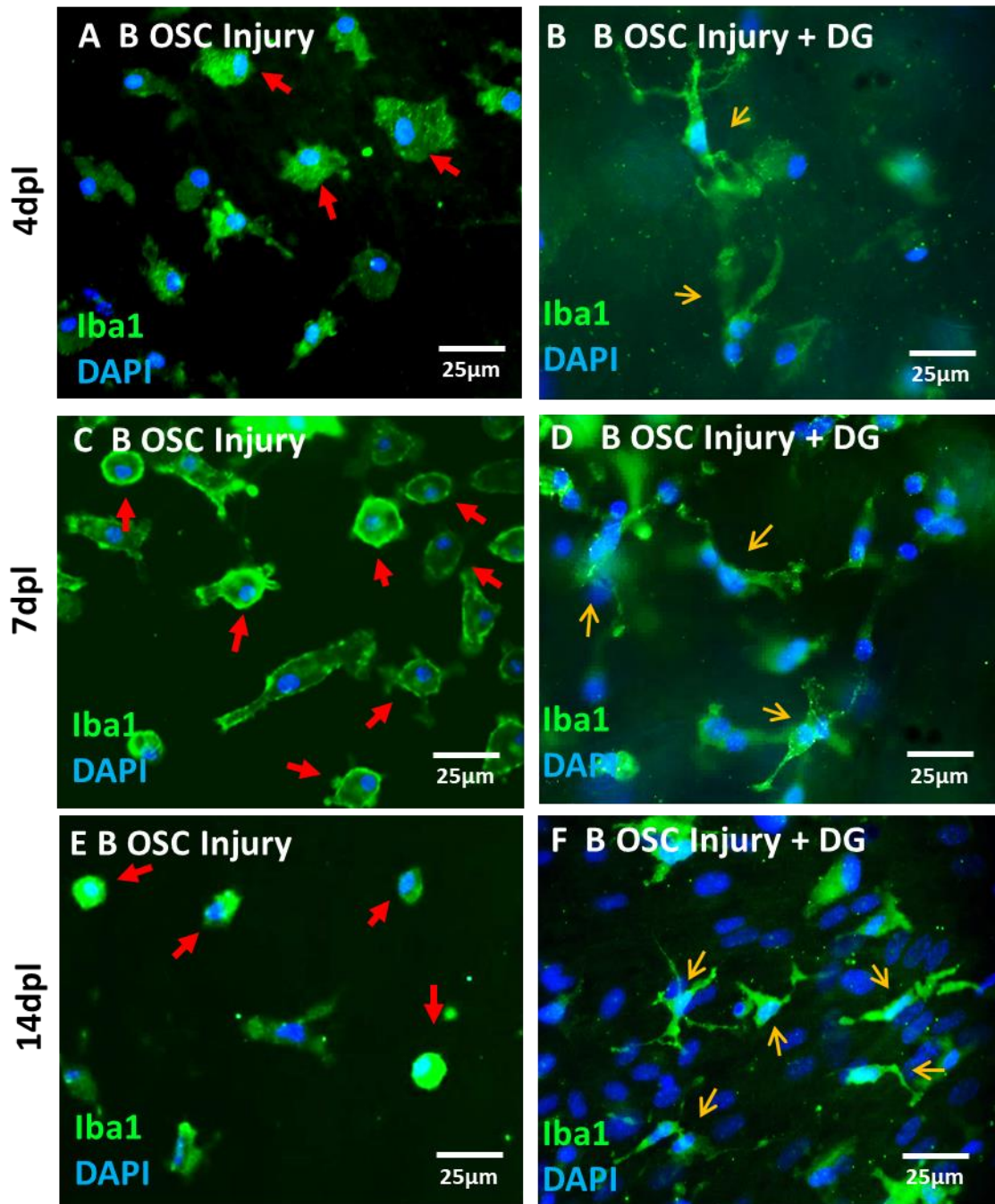
Figure 3.9. Material residing microglia appear to resume a resting-like morphology within the material (brain tissue). **A, C and E** represent the amoeboid/activated morphologies observed with the lesion site at 4, 7 and 14 DPL respectively. Infiltration drops dramatically by 14 DPL. **B, D and F** display the more processed ramified morphologies of material-residing microglia at 4, 7 and 14 DPL respectively. **G** shows that microglial cells within the DuraGen™ are significantly more ramified than cells within the lesion alone. **H** graph reveals microglia infiltration drops dramatically without the material after 7DPL with an exponential increase within the material. [two-way ANOVA with Tukey's multiple comparisons, *p<0.5, **p<0.01, ***p<0.001, ****p<0.0001, n=4].

3.2.6 Evidence of neuronal outgrowth into the DuraGen™ from scOSCs only

Lastly, the potential for neurons to extend processes into the implanted material was investigated within the study. Using a common cytoskeleton marker (TUJ-1), neurons could be visualised via immunofluorescent staining of the tissue slices. At 14 DPL there are few neuronal processes that extend past the lesion margins and into the lesion area **(figure 3.10 A)**. In contrast, with DuraGen™ implantation neurites were observed to extend from the lesion boundary and throughout the matrix of the material **(figure 3.10 B).** This result however is slice dependent. Due to inherent slicing variability of the spinal cord, certain slices present clear neuronal tracts or the central canal, whereas others can consist of mainly interconnecting neurons. The slices with observable neuronal tracts (as shown in **figure 3.2 L**) tend to show more outgrowth from the lesion edge and into DuraGen™. Therefore, only slices which demonstrated robust neuronal tracts in the slice body were chosen for neurite growth analysis. Using a line crossing analysis method outlined in section 2.3.6, neurite outgrowth within the lesion area could be quantified. This confirmed that injury plus DuraGen™ implantation significantly enhanced the outgrowth of neurites (67 ± 3.6 TNC) from the lesion edge and throughout the DuraGen™ matrix **(figure 3.10 C),** compared with lesion only (10.67 ± 2.3) [Unpaired non-parametric t-test, p>0.001, n=4].

Brain slices with normal neuronal distribution displayed little if any neuronal outgrowth from the lesion

edge. Similarly, injured bOSCs with biomaterial implantation showed no observable neuronal response

to the material.
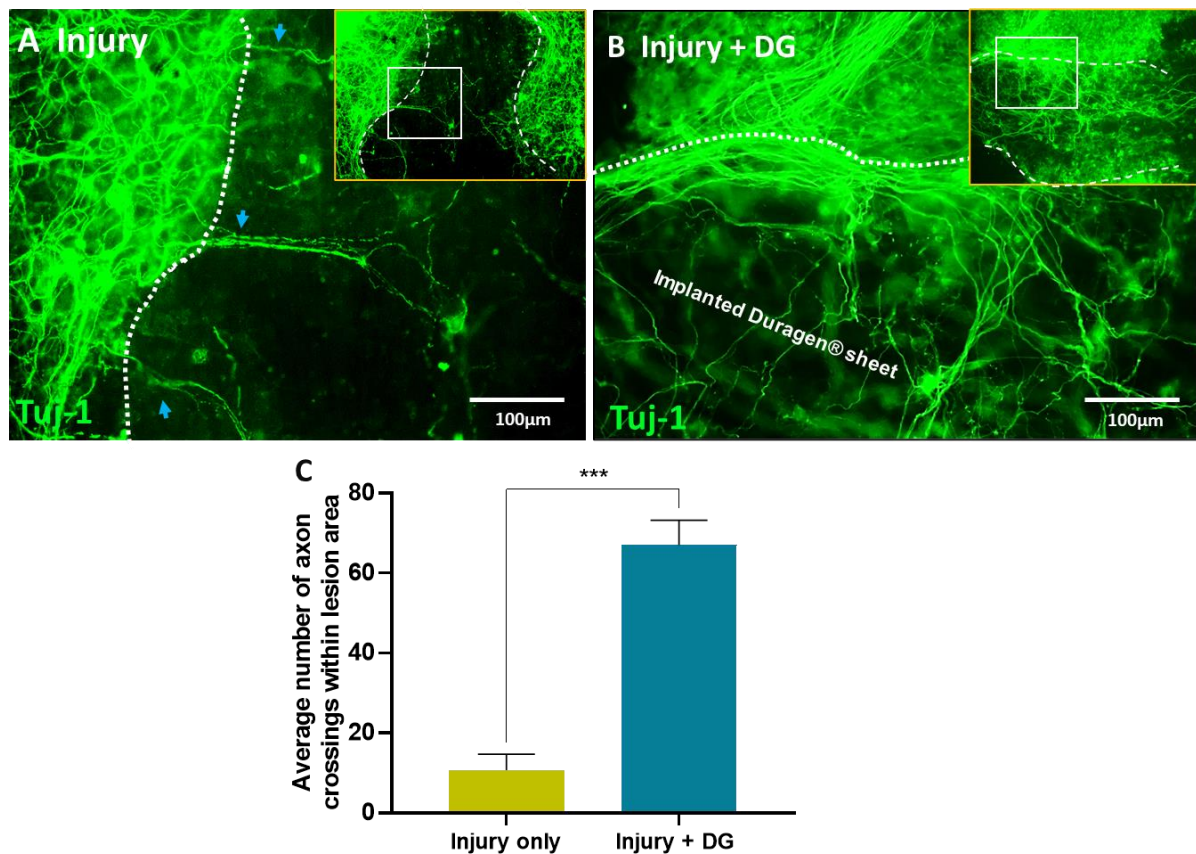
Figure 3.10. Evidence of enhanced neuronal outgrowth from scOSCs into the DuraGen™. A representative micrograph of injury only scOSCs which present some neuronal outgrowth from the lesion edge (blue arrows). **B** representative micrograph on the injury site with DuraGen™ implantation showing neurite extension throughout the material. **C** graph showing the significant enhancement of neurites within the lesion site. [one-way ANOVA, ***$p<0.001$, n=4)

3.2.6.1 Potential interaction of astrocytes and neurites within the material matrix

There is some evidence that neuronal outgrowth from injured spinal cord slices may be initially guided

by astrocyte ingrowth. Although direct co-localisation showing a spatial relation could not be

determined from these images, both astrocytes and neurons appear to initially follow a similar path surrounding the material then growing into the matrix. While astrocytes do not infiltrate very deep into the material neurites continue to extend throughout the matrix (**figure 3.11**). Additionally, the extension of neurites (and astrocytes) do not appear extend processes outside the biomaterial (outlined by the dotted lines in **figure 3.11**).
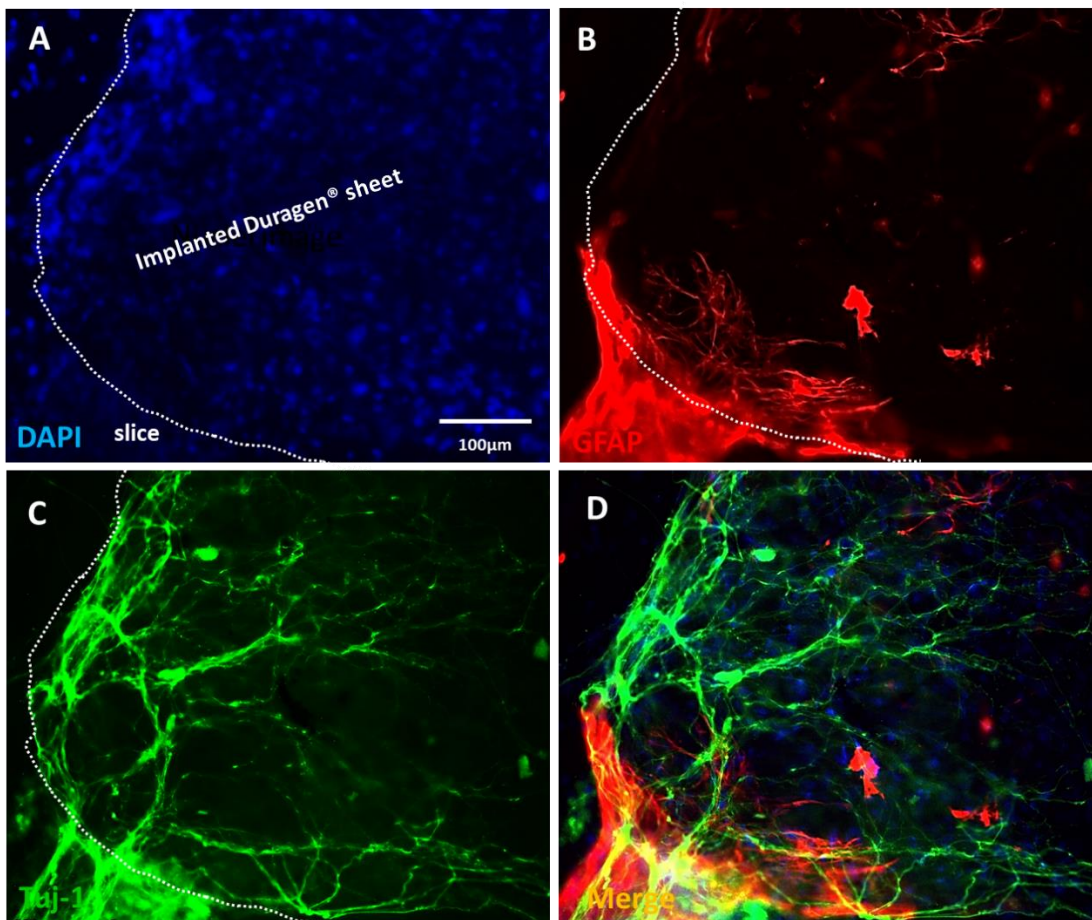
Figure 3.11. Potential interaction of astrocytes and neurites within the material matrix. 2 channel micrograph of a spinal cord slice (TUJ-1+ neurons and GFAP+ astrocytes) shows a potential interaction with astrocytes, extending neurites and the DuraGen™ matrix. Astrocytes and neurons both appear to encounter the DuraGen™ with a similar initial pattern then neuronal processes extending further throughout the matrix. Additionally, extending processes do not exceed the boundaries of DuraGen™ matrix (dotted line).

3.3 Discussion

This thesis is the first comparative study of pTBI and SCI in brain and spinal cord organotypic slice cultures. Both models act as complex *in vitro* injury systems that recapitulate some of the cardinal features of *in vivo* injury. In addition, pathological mechanisms following biomaterial implantation can be efficiently assessed for SCI and TBI within these models. Approximately 4-6 spinal cord slices and 10-15 intact brain slices can be routinely obtained from a P2-P4 mouse (on average 8-12 mice per litter). This permits the simultaneous assessment of several treatment conditions, and various tissue/cellular assessments along with two tissue types from a single litter of pups. As a result, this mitigates some experimental variability and reduces the number of animals required for therapeutic assessment, thereby successfully addressing the 3R's principle of animal usage reduction. Both injury models showed high viability and desired cellular phenotypes up to 18 days *in vitro* and displayed hallmark injury responses such as: infiltration of activated microglial to the injury cavity, astrogliosis at the injury margins and largely the inability of neuronal regrowth post injury. Additionally, precise implantation of a biomaterial within the transecting cavity for regenerative assessment was achieved. Investigating the implantation therapy through the scOSCs and bOSCs injury models indicated that DuraGen™ has the potential to provide a pro-regenerative or regenerative permissive matrix for neurological injury.

3.3.1 Successful replication and adaptation of the scOSC and bOSC injury models

Cell viability assays of the scOSCs and bOSCs reveals comparable results to that of Weightman et al., 2014, which showed viability of spinal cord slices with transecting injury up to 6 DIV. Here we show a longer period characterisation of slice viability up to 18 DIV. At this point we saw some deterioration of the slice yet the majority of the slice showed high viability. Other slice brain models have been successfully cultured for longer periods i.e. 60 days (Ostergaard et al., 1990), 32 weeks (Marksteiner and Humpel, 2008), and neonatal spinal cord slices have also been maintained for 4-5 weeks (Sypecka et al., 2015) thus long-term studies are possible. However, for the purpose of this investigation, to

reproduce complex testing systems for neuro-regenerative therapy screening in combination with addressing the 3Rs principles, long culturing periods are not necessarily beneficial. Concurrently, this assay reveals that clear efficient transecting injuries could be routinely reproduced in both bOSCs and scOSCs at 4 DIV. Both these CNS models displayed healthy cellular phenotypes within the non-injured tissue, including cytoarchitecture and long fibre trajectory within the spinal cord slices. Similarly, Bonnici et al. found longitudinal parasagittal spinal cord cultures maintained ventro-dorsal patterning and contained motor neuron bundles (Bonnici et al., 2008). Additionally, the maintenance of long fiber neuronal trajectory was also shown in longitudinal adult rodent slices, however only surviving for 7 DIV (Sypecka et al., 2015).

3.3.2 Hallmark responses to injury and biomaterial implantation comparison of scOSCs and bOSCs

This study demonstrates that both tissue models can mimic three cardinal pathological features of *in vivo* SCI or TBI. Spinal cord and brain organotypic slices displayed comparable responses to a focal penetrating injury. To my knowledge this is the first report of bOSCs subject to a penetrating injury mechanism, (as opposed to other previously stated mechanisms i.e. weight drop, stretch and cylinder roller). The response of the organotypic brain showed patho-mechanism corresponding to rodent models of *in vivo* penetrating brain injury; including astrogliosis and microgliosis (Cernak et al., 2014, Williams et al., 2005; Elias & Spector, 2012). Penetrating injuries within scOSC have similarly reported glial scarring and microgliosis at the injury site (Weightman et al., 2014, Guijarro-Belmar et al., 2019).

Here, two ex vivo modelling systems for SCI and TBI evaluate the responses to transecting injury and biomaterial implantation. These platforms have allowed us to follow the pathophysiological mechanisms of injury and to assess a potential therapy for both tissues simultaneously *in vitro*. DuraGen^{TM} was implanted acellular and without any modifications, to study its regenerative permissiveness as a biomaterial alone. The cellular ingrowth was observed growing through DuraGen^{TM}

rather than only under or over the material, which confirmed the use of the material as a scaffold rather than a bridge. This is ideal, as repair of damaged tissues would require a comprehensive tissue growth throughout the biomaterial to regenerate the pre-existing cavity.

Unfortunately, due to time constraints and COVID19 restrictions the materials stiffness could not be evaluated as we do not have the equipment on site for these experiments. Material stiffness as mentioned previously is incredibly important for the growth and support of certain cell types. However we do show a robust analysis of the cellular infiltration that occurs when DuraGenTM is implanted into the lesion site of the OSCs.

We report a modification of the glial scar morphology with material implantation, where astrocytes elongate into the biomaterial. Astrogliosis evaluation in both the scOSC and the bOSCs suggests the material neither enhanced or reduced astrogliosis within the injury environment and the material showed support of astrocytic growth across the lesion to bridge the transecting cavity. These results are in line with some *in vivo* studies, which reported no exacerbation or reduction of the glial scar after biomaterial implantation (Dominguez-Bajo et al., 2020; Galli et al., 2018), and another *in vivo* study which reports a disruption of the glial scar through an architectural change (Hurtado et al., 2011). Some studies with using functionalised scaffold treatment have reported a reduced presentation of the glial scar (Yin et al., 2018, Guijarro-Belmar et al., 2019, Giannetti et al., 2001). The use of a collagen impregnated acrylic hydrogel made of 2-hydroxyethyl methacrylate implanted into adult rat SCI showed minimal astrocytic reactivity at the material-tissue interface, no cystic cavitation and axonal penetration along the full length of the hydrogel (Giannetti et al., 2001). An implantable hydrogel functionalised with Epac2 agonist S-220 significantly mediated the lesion environment within an ex vivo model of SCI by reducing both microglia and astrocyte activation (Guijarro-Belmar et al., 2019). On the contrary, a collagen scaffold functionalised with hippocampal progenitor cells implanted into a rat model of penetrating brain injury failed to observe any modifications to the injury-induced glial scarring (Elias & Spector, 2012). The discrepancy between these studies is the length of time post-injury before

treatment, the latter study applies the implantation at 7 days post initial injury however the others are more or less immediately. Implantation timepoint may be a pivotal factor on the effect of the treatment. Additionally, it would appear that collagen scaffolds themselves do not attenuate astrocyte reactivity however to have the ability to effectively reduce glial scarring a functional molecule or cellular component may be necessary. The unpredictable nature of *in vivo* tissue and the potential responses to biomaterial implantation highlights the importance of biomaterial screening through *in vitro* models before testing in complex *in vivo* models. In this case, the data suggests that DuraGen™ implantation does not result in astrocyte reactivity, emphasising its capacity as a biomaterial-based therapy for SCI and TBI.

The data in this chapter indicated that microglial infiltration into the lesion area is particularly enhanced with biomaterial implantation up to 14 DPL. Without implantation this peaked at 7 DPL then began to reduce. Weightman et al., 2014 reported that microglia infiltration into the lesion site peaked at 5 DPL and had reduced significantly by 12 DPL. The large increase in biomaterial-mediated microglial infiltration observed in our study, in principle, would lead to the conclusion the biomaterial may be immunogenic. Integra life sciences report this material to be minimally immunogenic. On morphological investigation it was indicated that the material-residing microglia appear to resume morphologies more typical of "resting" state microglia. Similarly, hydrogel treatment of organotypic SCI model observed a reduction in microglial activation. This was determined through a reduced microglial perimeter within the injury, and treatment with a functionalised hydrogel further reduced microglial perimeter (Guijarro-Belmar et al., 2019). Additionally, implantation of a gelatin hydrogel into the injury site of a transecting SCI mouse model, reported an increase microglia expressing a ramified phenotype compared to the control (injury only). This ramified phenotype was further increased in the lesion site with a microglial depletion and repopulation treatment prior to implantation (Dezun et al., 2020). In these cases it would appear that these soft biomaterials can reduce immune responses to a certain degree and when assessing soft versus stiff biomaterial implantation within the brain it is clear to see that the stiffer materials initiate a significant "foreign body" reaction (Maclean et al., 2018). It is possible that within

an injury environment, the soft 3D nature of the implant that mimics healthy endogenous environment of uninjured neural tissue could be encouraging microglia away from their reactive injury-induced state. Although we have not shown evidence that the infiltrated microglia are not doing harm to neurites or the material itself, we can assume from the evidence that the microglia are moving away from their initial-injury activated state once residing in the materials matrix. Therefore this reduces the chance of the impact activated microglia can have on the injury environment.

Lastly, this study reports significant axonal outgrowth into the injury site with biomaterial treated spinal cord slices. This finding of neuronal outgrowth into implanted biomaterials has also been reported for *in vivo* studies (Wu et al., 2018; Galli et al., 2018; Yang et al., 2015; Yeh et al., 2020) and *in vitro* (Weightman et al., 2014; Guijarro-Belmar et al., 2019). In fact, Bonnici and Kapfhammer (2008) demonstrated that with a very small injury site into spinal cord slice model, axons can regenerate and cross the lesion site with no treatment in an age dependant manners. In our study it was not clear if the axonal outgrowth extended into the other side of the spinal cord or whether the neurite extension remained within the materials matrix. As the neurite extension followed the fibres of the 3D material in a random fashion it was difficult to distinguish any possible physical reconnection to establish this an electrophysiological analysis could be performed. Nevertheless, the high density of neurites within the material would suggest a possibility of synaptic connections. Alternatively, a biomaterial with an aligned fibrous matrix would be beneficial for directed growth across the lesion site and enhancement of neuronal reconnection. Nguyen et al., (2018) reported the implantation of a functionalised three-dimensional aligned nanofiber-hydrogel scaffold into a rat SCI transecting model. Here, they showed aligned neurofilaments throughout the injury site at just 1 week post injury. Additionally, they reported alignment of oligodendrocytes within the material, and no adverse effect on the microglia and astrocytes of the spinal cord. Furthermore, the enhanced neuronal outgrowth observed with DuraGen™ is indicative of the regeneration permissive role of this material. Integra Life Sciences, has now release NeuraGen™ an aligned matrix adapted from DuraGen™. This aligned 3D architecture would ensure appropriate directionality of neurite extension across the lesion and would be an

important development in the testing of the material and the spinal cord injury model. Neurite extension into the biomaterial is shown in close approximation with infiltrating astrocytes. Although no definitive co-relationship was determined it is possible that initial astrocytic ingrowth could help in facilitating initial neurite extension from the lesion edge which then go on to extend throughout the matrix. Within the literature there is evidence that elongated astrocytes (like those seen infiltrating the biomaterial) show similarity with the guidance-providing radial glial progenitors for neuron growth in CNS development (Garcia et al., 2004), suggesting a co-relationship that leads to ingrowth into the material. Guijarro-Belmar et al, 2019 have also shown elongated astrocytes processes to be associated with extending neurites in the lesion area of treated scOSCs. Additionally extending neurites and astrocytes demonstrate a preferential affinity to the implant over the confetti membrane, it is likely they are using the fibres of the DG as topographical cues for directed outgrowth (this agrees with TEM data).

Contrary to this, though astrocytes are observed to extended into the material, we do not see this neuronal outgrowth response in the injured brain tissue. Anatomical regions of the CNS differ significantly in their mechanical stiffness, this includes differences between the regions of the brain and the spinal cord (Bartlett et al., 2020). In light of this information, it is unlikely that the stiffness of an implantable material suited for the spinal cord is going to match the stiffness required for the brain. It may be that DuraGen^{TM} as an implantable biomaterial (although mechanical stiffness could not be measured), exceeds the stiffness required for brain implantation, hence contributing to the explanation of why neurons did not extend their processes post injury with brain tissue slices. Neurons prefer the softer substrates (<1 kPa) and it may be that brain neurons require a softer substrate for regeneration compared to spinal cord neuronal regeneration.

In conclusion, the scOSC and bOSC injury models were successful in testing the biomaterial therapy. In future it may be necessary to test material implantation at a later timepoint after initial injury and observe the influence this has on the pro-regenerative effects. The use of organotypic models like this

close the gap between simple cellular *in vitro* testing and complex *in vivo* testing and have the potential to be the standard practice in place prior to therapeutic testing on live animal models. In theory, detecting failure in organotypic models, for therapeutics such as biomaterials, could limit therapeutic failure within live animals.

4 Chapter 4a: Developing an *in vitro* 2D cortical multicellular injury model.

Chapter 4b: Developing a 3D neuro-mimetic cortical construct with induction of traumatic injury.

4.1 Introduction

While organotypic slice cultures are complex models, they are moderate throughput and technically challenging and pure neural cell cultures or co-cultures are often overly simplistic. Hence there is an unmet requirement for a high-throughput system with the advantages of *in vitro* culture that comprise of all five major neural cell types of the brain (neurons, astrocytes, microglia, oligodendrocytes and oligodendrocyte precursor cells (OPCs). The cellular model also needs to support an injury mechanism, recapitulate pathomechanism and have the capacity to evaluate regenerative therapies.

4.1.1 Primary cultures from rodent postnatal brain tissue for modelling injury

Majority of primary mixed cellular brain cultures report mixed-glial models, lacking neuronal content (see section 1.3.3.3). Before the development of mixed glial culture, primary neuronal cultures were established but have been somewhat challenging in comparison, particularly in harvesting the tissue (Banker and Cowan, 1997), this in turn has made it more difficult for the production of neuronal-glial models from post-natal tissues. Since the original developments for neuronal cultures, *in vitro* neuronal models have made radical advancements regarding neuronal cell survival and enhanced neurite extension, including methods for dissociation, culture conditions and media supplements such as basic fibroblast growth factor (bFGF) and B27 (Ray et al., 1993; Sünwoldt et al., 2017). Neural dissociation can be conducted via mechanical dissociation (through chopping techniques, pipette or needle tritutration and filters), enzymatic digestion or a combination of both. Enzymes such as papain, dispase, collagenase, hyaluronidase, DNase and trypsin are commonly used for dissociation. Enzymes dissociate the cell-cell connections and breakdown the ECM that encapsulates the cells, as opposed to physical breakdown through mechanical disruption. **These dissociation methods can differ largely in their yield of cells and the percent on viable cells produced i.e. the least harsh dissociation processes will yield higher neuronal content**. The produced cell suspensions may vary in their quality i.e. the extent of subcellular debris, undissociated cell clumps and the proportions cell populations. While mechanical

dissociation methods are still routinely used, many believe enzymatic dissociation provides a more effective method for isolating neural cells (Volovitz et al., 2016; Trujillo et al., 2021). Another significant development from by Brewer et al. (1993), was the systematic optimisation of a novel serum-free medium combination: Neurobasal™ supplemented with B27. This medium supported optimal survival and growth of papain digested primary hippocampal neurons *in vitro*. Soon after (1995), Brewer went on to prove the efficiency of Serum-free B27/Neurobasal medium in supporting growth of neurons isolated from six other brain regions, with cortical neurons showing the same high survival rate (ca 70%) and distinctive morphologies observed with the hippocampal neurons. Neurobasal™ is now used in multiple cultures to support optimal survival of neurons including primary mixed neuron-glial cultures (Goshi et al., 2020) and mixed cell cultures from neural stem cells (Barbora et al., 2020). Developments like these have also allowed post-natal neuronal cultures (that originally did not yield robust cultures) to be achieved for use in neuro-regenerative research i.e. to study Parkinson's disease, genetic engineering, electrophysiological studies and biomaterial encapsulation (Weihe et al., 2006; Beaudoin et al., 2012; Lautenschlager et al., 2018; Moutin et al., 2020).

Neuronal cell cultures first became established as assays to study *in vitro* processes, followed shortly after by the equivalent studies of purified glial populations. At this time, it was revealed that glial cells produce many of the growth factors, neuropeptides and neurotransmitters that are similarly generated by neurons (McMillian et al., 1994). This meant scope for investigations that used mixed populations of glial and neuronal cells to begin to dissect the interaction between the two. It is these types of cultures that lend themselves as *in vitro* platforms as more complete cellular models for therapeutic testing. While purified neuronal and glial cultures are useful for determining cellular responses and pathways, they lack the interactions between all these cell types of the brain, which is critical when studying responses to brain injury and therapeutics strategies. Though not as well recognised as the mixed glial model, neuron-glial methods have been reported within the literature, and for the most part consist of a viable population of immune cells and neuronal networks (Goshi et al 2020; O'Meara et al., 2016).

However, these are predominantly embryonic cultures that typically produce 40% neurons, 50% astrocytes, and 10% microglia (Yang et al., 2008; Demestre et al., 2008; Pedachenko et al., 2020).

Like pure neuronal cultures, these use of embryonic tissue, is driven by the expectation that older mice do not yield good quality cultures. However, with a chemical substitute, i.e. employing enzymatic dissociation in place of the harsh action of mechanical dissociation can conserve the tissue at an older age. Few post-natal dissociations for mixed neuron-glial models have been established, and often do not offer a characterisation of cellular profile (Kaiser et al, 2013), however one study of rat P0 tissue reports 80% neuronal cells, 15% astrocytes and 5% microglia (Goshi et al., 2020). Though this study reports high neuronal content, the glial cells populations again are not representative of the brain. **More importantly there as of yet there are no primary neuron-glia models which report assessment of the five major neural cell types.**

Alternatively, a "pure" primary neuronal culture can be seeded on top of a two-week cultured confluent layer of glial cells to achieve the multicellular culture (Ioannou et al., 2019; Deshpande and DeLorenzo, 2020). Others have achieved co-culture of primary glial cells and NSCs with an insert for the separation of cellular layers (Wen et al., 2021). Yet these techniques over complicate the establishment of the culture and need longer experimental periods.

There are particular advantages to an *in vitro* 2D model of brain represented in **figure 4.0.** Firstly, a complete cellular model encompassing all major neural cell types of the brain, to achieve a neuronal network (to replicate the dense network throughout the brain) and a representative microglia population for immune modulation would be beneficial. A post-natal culture with a high cellular yield i.e. enzymatic over mechanical, would reduce the number of mouse pups required. In terms of the technical procedure and reproducibility, primary cell 2D cultures are generally reproducible, high-throughput systems with a simple and low-cost maintenance. Furthermore, in the study of traumatic injuries this brain tissue model must allow induction of various injury mechanisms which can effectively

mimic relevant pathologies, specifically glial scarring, immune activation, and neuronal outgrowth. Added benefits would be a platform adaptable to human tissue.
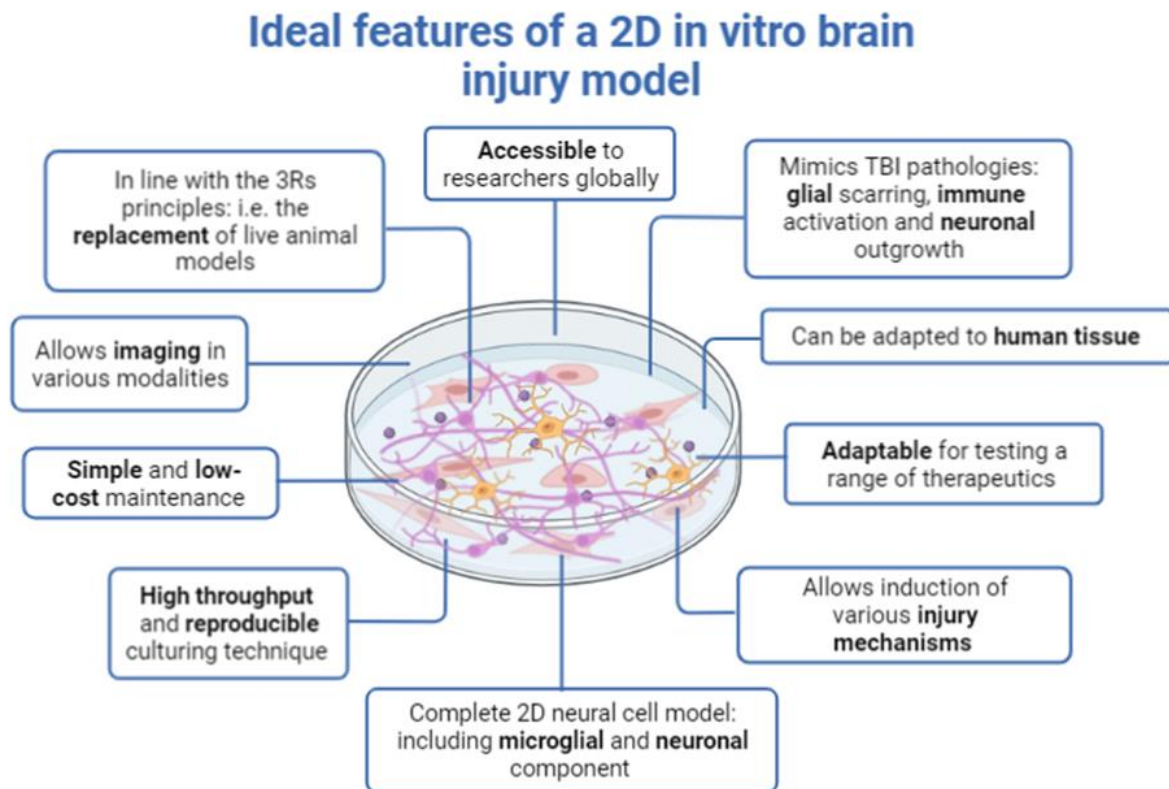
Figure 4.0. Schematic representation depicting the ideal features of a more complex 2D *in vitro* neural injury modelling system.

4.1.2 Application of magnetic nanoparticles to assess the multicellular responses within the injury environment.

Magnetic nanoparticles (MNPs) are nanomaterials that can interact with a magnetic field and be functionalised to perform separate tasks. In general, they possess a magnetic core (most commonly iron oxide) coated with a biocompatible layer and further functionalised with small targeting molecules, fluorophores or delivery molecules. The key attribute for biomedical application is the superparamagnetism displayed by these particles (of a core size <30nm) whereby particles show high sensitivity to an exposed magnet field but do not retain magnetism after the magnetic field has been

removed. This is particularly beneficial for *in vivo* safety as aggregation of the particles within the host is avoided once the field is removed (Laurent et al., 2008; Yui et al., 2011; Hofmann and Montet, 2010; Fang et al., 2009).

In recent decades, MNPs have been employed in promising therapeutic strategies for regenerative neurology. This includes a safe method of targeting magnetically labelled cells to the CNS (Connel et al., 2015), a non-invasive tool to track transplanted cells prelabelled with MNPs (Edmundson et al., 2013), gene transfer (magnetofection) of transplant or endogenous cells to enhance neurotrophic protein expression, delivery of neurotherapeutic molecules to neural trauma sites (Thomsem and Moos, 2015), and magnetic actuation of target cells to manipulate cellular processes (Modo et al., 2002). Previously, delivery of functionalised MNPs have had successful results *in vivo* models TBI and SCI, including: reduced astrogliosis, promoted functional recovery and reduced immune cell activation (Liu et al., 2016; Sharma et al., 2020).

It is important to note that there are limitations with current methods of evaluating nanoparticle therapies *in vitro* and models commonly are mostly isolated pure cell cultures. Nanomaterials are generally endocytosed by the cells that are exposed to them, however differing rates of uptake is observed for separate cell types. Additionally, in a dynamic cellular environment, individual cell types show competitive uptake of NPs, with microglia dominating uptake. For example, a pure astrocyte culture may display significant NP uptake yet within a microglia co-culture astrocytes do not show as much uptake (Jenkins et al., 2016). Consequently, nanoparticle application to a comprehensive multicellular system where many cell types are interacting simultaneously is likely to cause distinct nanomaterial uptake behaviours compared to cells in monoculture. Furthermore, when these cells are within an injury environment this could further alter their uptake profile. There are few *in vitro* CNS injury models that have been used for nanoparticle testing within the literature, therefore pathomimetic *in vitro* high-throughput models are in demand.

4.1.3 Importance of neuro-mimetic three-dimensional (3D) culture constructs

Three-dimensional (3D) cellular constructs have been rapidly emerging as a means to study pathological mechanisms and therapeutic strategies for neural disease and injuries. While more technically challenging due to complex fabrication processes (compared with 2D), they retain simple maintenance needs and cellular analysis can remain high throughput. A 3D architecture provides a more tissue-like environment where cell-cell and cell-matrix interactions allowing a more biologically relevant response (Haycock, 2010). 2D cultures are inadequate representations of the 3D microenvironment within living tissues, making them unreliable predictors of *in vivo* mechanisms. Cells undergo artificial responses in order to adapt to the flat, stiff surface of 2D monolayer and only become partly polarised; this intrinsic asymmetry of cells is important for their function (Schneider et al., 2020). Cells grown in 3D have been confirmed to be more physiologically relevant recapitulating several biological mechanisms, such as: cell viability, morphology, proliferation, differentiation, migration, response to stimuli, gene expression, general cell function, and drug metabolism (Antoni et al., 2015). Furthermore, 3D cellular cultures within soft substrates provide more accurate representation of cell polarisation and display more mature electrophysiological properties compared to their 2D counterparts cultured on glass (Evans et al., 2019). Additionally, open porous scaffolds in which cells are seeded into are said to be pseudo 3D environments and to achieve a true 3D model, neural cells must be encapsulated within hydrogels (Aregueta-Robles et al., 2014). Generally, 3D cultures can be maintained in culture for much larger periods of time than in 2D. In order to maintain cells in 2D culture for longer periods cells must undergo regular trypsinisation in order to provide enough space and nutrients for normal cell growth (Raimondi et al., 2020).

The majority of these 3D neural models rely on the clonal cell/stem cell lines (Wang et al., 2018; Lowry Curley and Moore, 2017; Mahoney and Anseth, 2006) or pure neuronal culture (Tang-Schomer et al., 2014). **Despite the reports of primary mixed glial or neuron-glial cultures in 2D conditions, there are limited reports of translation to 3D systems** (Koss et al., 2017). A significant hurdle to the development

of primary 3D neural tissue constructs is the need to support multiple cell types within the same environment (Valleho-Giraldo et al., 2020).

4.1.4 Objectives

In light of the information given, an ideal *in vitro* model must: i) retain all neural cell types, ii) allow high throughput experimentation iii) display neuropathomimetic mechanisms iv) be capable of supporting biomaterial implantation/nanoparticle uptake/electrical stimulation, and v) have a facile methodology. An additional beneficial feature would be to incorporate a biomimetic 3D nature.

Accordingly, the chapter objectives were:

(i)   To generate a complex 2D injury model with the capacity to incorporate and evaluate the behaviours of the five major cell types of the brain (neurons, astrocytes, microglia, oligodendrocytes and OPCs). In particular, the aim was to incorporate a high-density neuronal network which has not previously been achieved with this primary culture procedure. This involved developing an advanced version of a mixed glial injury model (reported by our laboratory, Basit, et al. 2021), evaluating astrocytic and microglial responses to injury.

(ii)   To expand the 2D injury model to a 3-dimensional injury model, where the cortical cells were suspended and encapsulated within a neuro-mimetic hydrogel. Following this, generate a reproducible penetrating injury mechanism that allows assessment the injury responses and the implantation of a biomaterial.

4.2 Results (4a)

4.2.1 Characterisation and comparison of cultures established from the mechanical versus enzymatic dissociation method.

To determine the dissociation method that generates the highest cell viability, comparisons of trypan blue staining of cortical dissociates obtained using mechanical versus enzymatic methods was conducted. The mechanical dissociation process produced a higher observed cell death (yellow arrows) and more cellular debris (red arrows) compared to dissociation with enzymes (**figure 4.1 A, B**). Enzymatic cell viability through trypan blue exclusion was significantly higher (94.8 ± 1.3%) than the mechanical method (54.8 ± 6.1%) [independent t-test, $p<0.01$, n=5, figure 4.1 C].

Post seeding, the cell cultures were tracked via light/phase microscopy over 7 days. Mechanically dissociated cortical cell cultures displayed slower initial attachment speeds and different cellular characteristics to cells from the enzymatic method. At 0-2 DIV, mechanical cell dissociates showed numerous rounded cells and cellular debris with no distinct cellular morphologies (**figure 4.2 A**). Within 4 DIV, debris and rounded cells were still present, but distinct cellular morphologies had emerged; clear OPCs, neuronal and astrocytic morphologies could be observed (**figure 4.2 B**). By 7 DIV, cultures had formed a confluent stratified layer; most cell types were distinguishable, and a reduction of cellular debris was observed. Here, astrocytes formed a bed layer with distinct polygonal and fusiform morphologies. Some neuronal projections were present, and microglia and OPCs appeared to reside at the surface (**figure 4.2 C**). Oligodendrocytes were hard to distinguish under brightfield conditions.

Enzymatic cell dissociates appeared to recover from the dissociation process earlier, with identifiable cellular profiles by 2 DIV; this includes less cellular debris and fewer rounded/unattached cells. (**figure 4.2 D**). By day 4, a neuronal network was visible with other distinct identifiable cell types (**figure 4.2 E**). At day 7, a confluent stratified culture was observed, including an identifiable dense neuronal network of intersecting neurites (**figure 4.2 F**). Note this neuronal network could not be seen in the mechanical cultures.
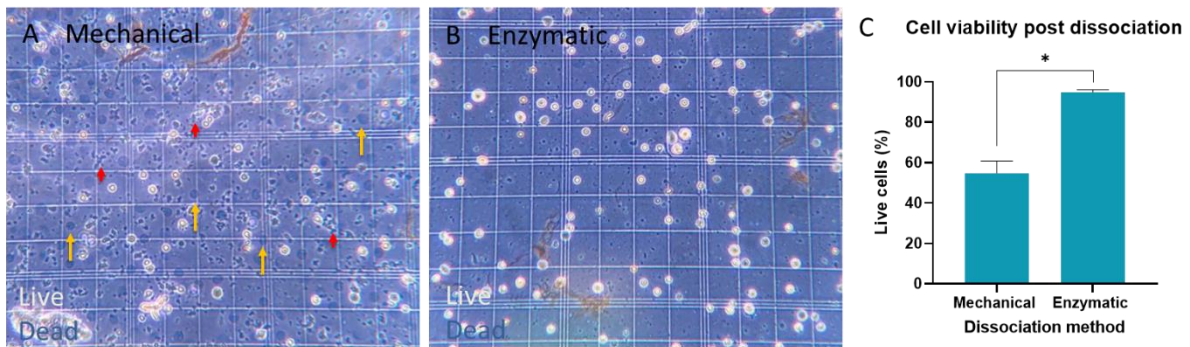
Figure 4.1. Mechanical and enzymatic tissue dissociation cell viability comparison through trypan blue exclusion. **A** Brightfield image of mechanical cell dissociate. **B** enzymatic cell dissociate. Trypan blue staining. Dead cells: yellow arrows, debris: red arrows. **C**, cell viability graph (independent t-test, n=5, *<0.01).
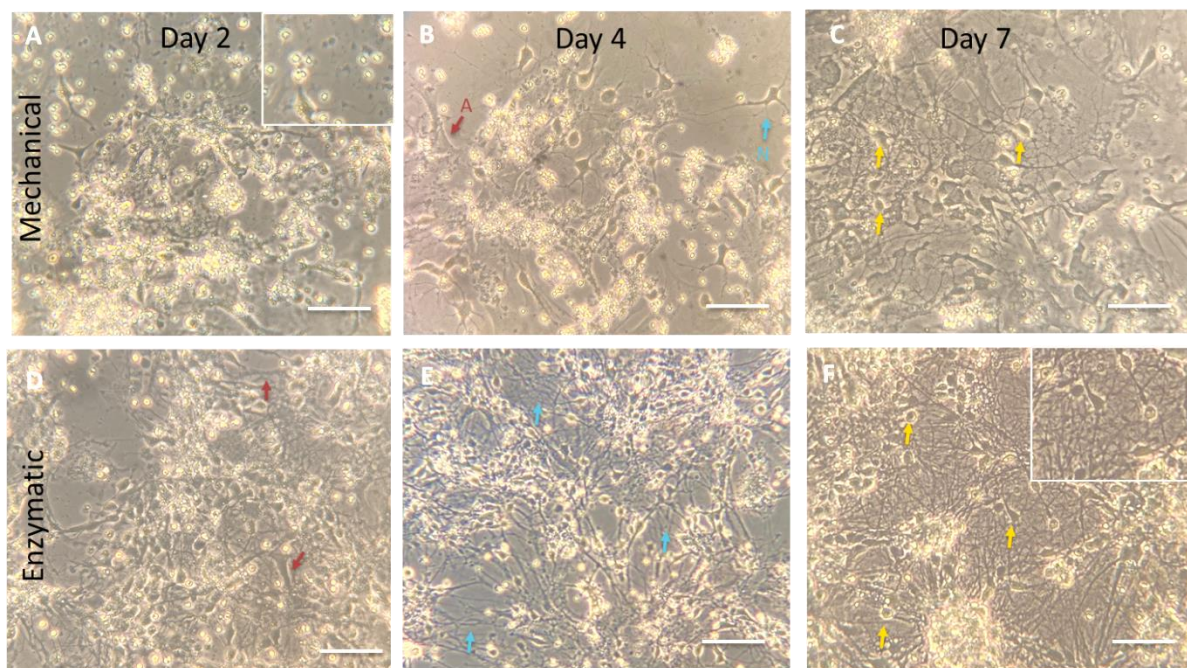
Figure 4.2. Culture recovery and development over time: mechanical (M) versus enzymatic (E) cell dissociates, shown via bright field images. **A** representative bright field micrograph M 2 DIV. Inset shows rounded dead/unattached cells and cellular debris. **B** representative micrograph of M 4 DIV. Arrows show some distinct morphologies emerging (N=neuron, A=astrocyte). **C** representative micrograph of M 7 DIV. Confluent stratified layer of cells formed. Arrows show OPC/microglial morphologies residing at the top. **D** representative micrograph of E 2 DIV. Cellular morphologies detectable (arrows signify astrocytes) with some cellular debris and rounded cells. **E** representative micrograph of E 4 DIV. Neuronal network emerging and rounded cells still present. **F** representative micrograph of E 7 DIV. Dense neuronal network identifiable (inset), with OPCs and microglia visible at the top (arrows). Scale bar: 250 microns. a dense neuronal network (**F**). M GFAP+ astrocytes

For cellular characterisation, cells were fluorescently immunostained with their corresponding biomarker (see section 2.1). Both cultures presented the five major cell types of the brain (**figure 4.3**). Enzymatic cultures displayed a dramatic increase in TUJ-1$^+$ axonal densities (**figure 4.3 F**), while TUJ-1$^+$ neurons within mechanical cultures were less dense and appeared to elaborate shorter axons (**figure 4.3 A**). GFAP+ astrocytes within the enzymatic cultures exhibit a more fibrous processed phenotypes (**figure 4.3 G**), compared to the flatter polygonal morphologies observed in the mechanical cultures (**figure 4.3 B**). We believe both these phenotypes fall under the type 1 (T1) category of astrocyte morphology. For the purpose of this analysis, they have been categorised as T1 flat and T1 processed. Proportionately enzymatic astrocytes displayed significantly more T1 processed morphologies [(mechanical: T1 flat – 71.4 ± 3.9%, T1 processed – 28.2 ± 3.9%) (enzymatic: T1 flat – 23.0 ± 4.5%, T1 processed – 76.9 ± 4.5%) (two way ANOVA with Tukey's, post-hoc analysis, p<0.001 n=5, figure 4.3 L)]. In both cultures, Iba1+ microglia displayed largely ramified with some amoeboid morphologies (**figure 4.3 C,H**), and oligodendrocytes presented both immature and mature morphological states (**figure 4.3 D,I**). NG2+ OPCs expressed processed multipolar morphologies in both models (**figure 4.3 E,J**).

Individual neural cell types were quantified to determine the cellular population distribution between either culturing process. The enzymatic cultures produced a significant increase in the number of neurons (enzymatic: 45.8 ± 2.1% vs mechanical: 21.9 ± 1.8%), with a substantial reduction in astrocytic numbers (enzymatic: 35.3 ± 0.2% vs mechanical: 62.7 ± 2.6%) [two-way ANOVA with Tukey's, post-hox analysis, p<0.001 n=5, figure 4.3 K]. Population distribution of microglia (enzymatic: 10.4 ± 3.9% mechanical: 11.3 ± 0.5%), OPCs (enzymatic: 11.2 ± 0.3% mechanical: 13.0 ± 1.8%) and oligodendrocytes (enzymatic: 2.7 ± 0.2% mechanical: 4.0 ± 0.3%) do not significantly differ (**figure 4.3 K**).

Immunolabelling for two separate cellular markers simultaneously revealed the relationship with certain cell types within the cultures. Co-staining for neurons (TUJ-1+) and oligodendrocytes (MBP+) has the potential to determine myelination within a culture. **Figure 4.4 A, B** shows oligodendrocytes were proximate to neurons however no definitive myelination could be concluded in either culture.

142

Micrographs in **figure 4.4 A2, B2** also further indicate the difference in neuronal network density from mechanical to enzymatic. Co-immunolabelling of MBP and NG2 reveals distinct populations of oligodendrocytes and OPCs respectively (**figure 4.4 C3, D3**). Immature and mature oligodendrocytes are observed throughout both cultures (**figure 4.4 A1, B1, C1, D1**), (**figure 4.4 A3, B3**).

Lastly, simultaneous triple immunolabelling revealed the spatial relationship between astrocytes, neurons and microglia. As the field of focus is altered, it is apparent there is a bed layer of astrocytes (**figure 4.5 B + E**), a dense neuronal network interweaving through the astrocytic layer (**figure 4.5 C + E**), and 'resting' ramified microglia residing at the top of the culture (**figure 4.5 D + E**).

Both dissociation methods generate robust cultures with all the major cell types of the brain. However due to the higher viability (i.e. higher cell yield from the same amount of brain tissue), the presence of fibrous astrocytes (as opposed to polygonal astrocytes) and a higher density neuronal network; only the enzymatic dissociation method was taken forward.
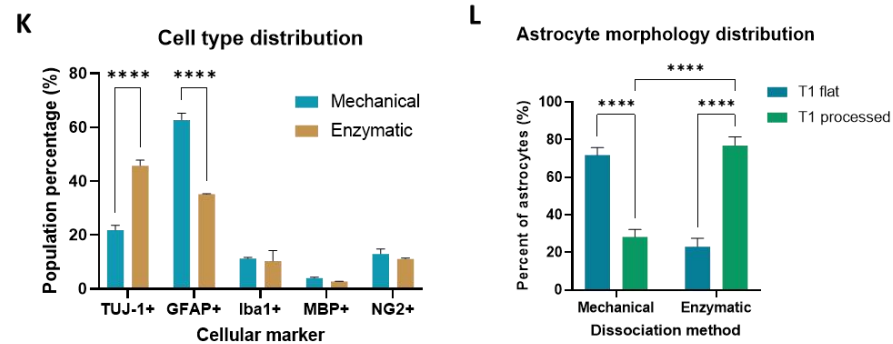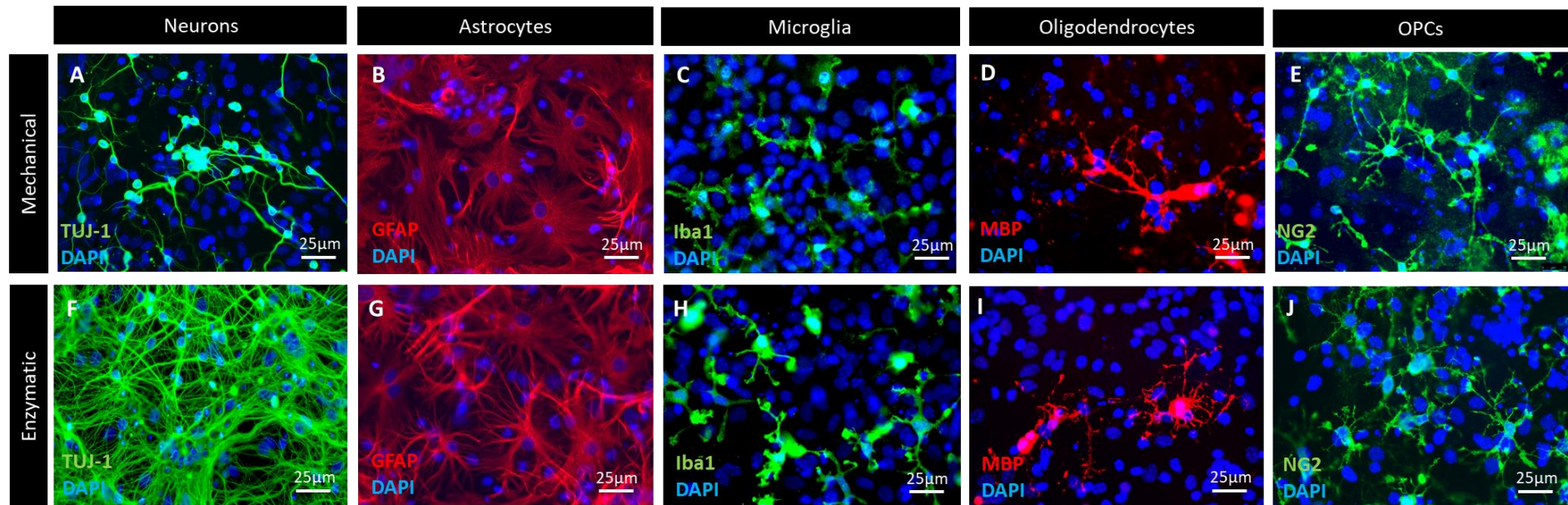
Figure 4.3. Characterisation of neural cell morphologies and population distribution (mechanical versus enzymatic). Representative fluorescence micrographs of TUJ-1^{+} neurons, GFAP[+] astrocytes, Iba1^{+} microglia, MBP[+] oligodendrocytes and NG2^{+} oligodendrocyte precursor cells; **A-E** mechanical (M) and **F-J** enzymatic (E) at 7 DIV. **A** M TUJ-1+ neurons were low density with short axonal processes, while E TUJ-1+ neurons displayed presented mostly flat polygonal morphologies

Figure 4.3 continued... (**B**), E GFAP+ astrocytes exhibited more fibrous processed phenotypes (**G**). Iba1+ microglia displayed mostly ramified with some amoeboid morphologies in both cultures (**C,H**). Immature and mature oligodendrocytes morphologies were observed throughout both cultures (**D,I**). OPCs expressed multipolar morphologies in both models. Bar graph in **K** demonstrates a comparison the population distribution between cultures, enzymatic dissociation significantly increases neuronal and reduces astrocytic numbers. Bar graph **L** demonstrates the shift in astrocyte morphology from T1 flat to T1 processed. (two-way ANOVA with Tukey's, post-hox analysis, p<0.001, n=5).
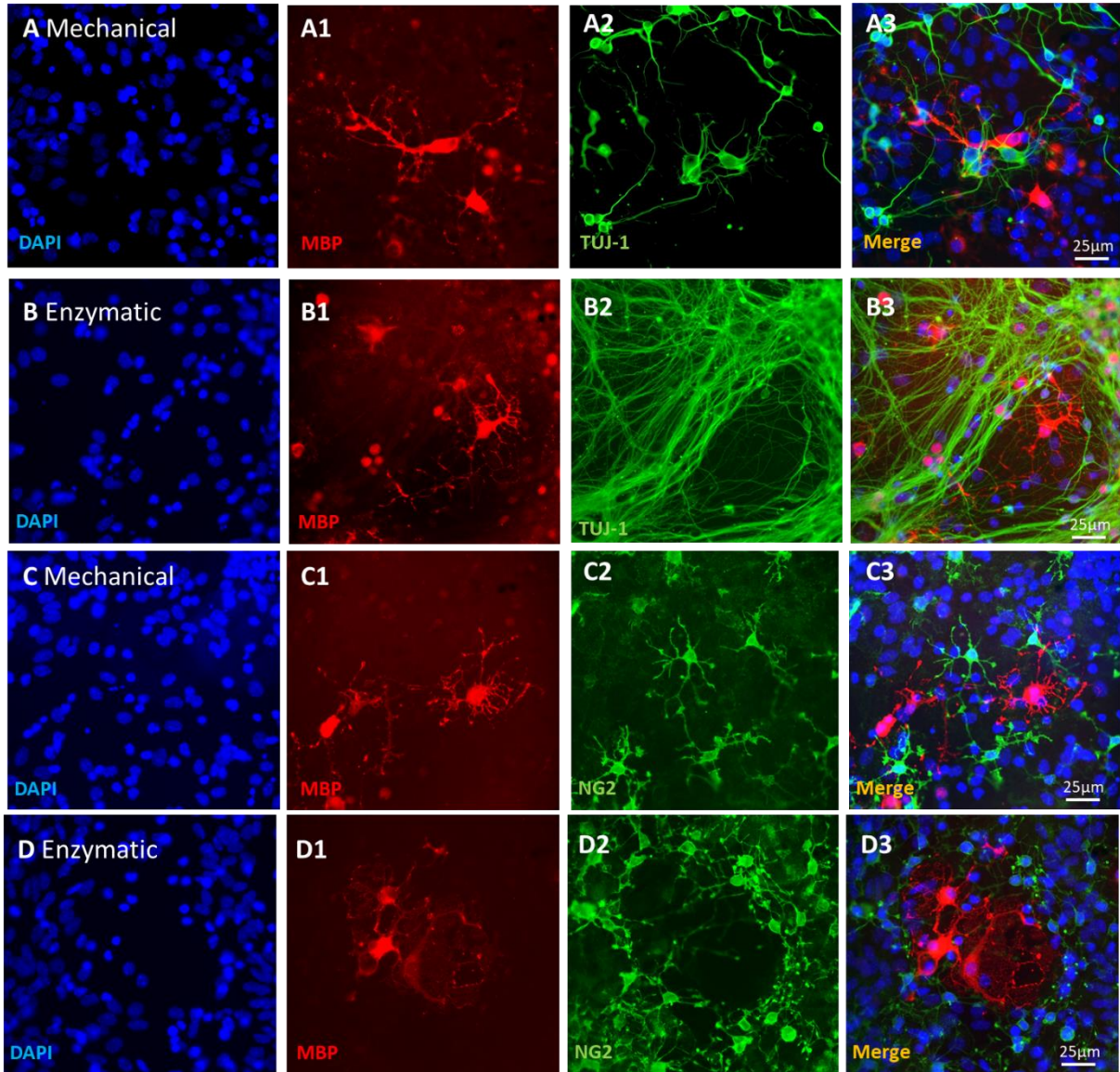
Figure 4.4. Co-immunolabelling to determine cellular relationships. A-B. representative fluorescence micrographs showing no definitive myelination (MBP+) of axons (TUJ-1+) within either culture. Higher density neuronal network evident within enzymatic cultures. **C-D** representative fluorescence micrographs demonstrating distinct oligodendrocyte (MBP+) and OPC (NG2+) populations.
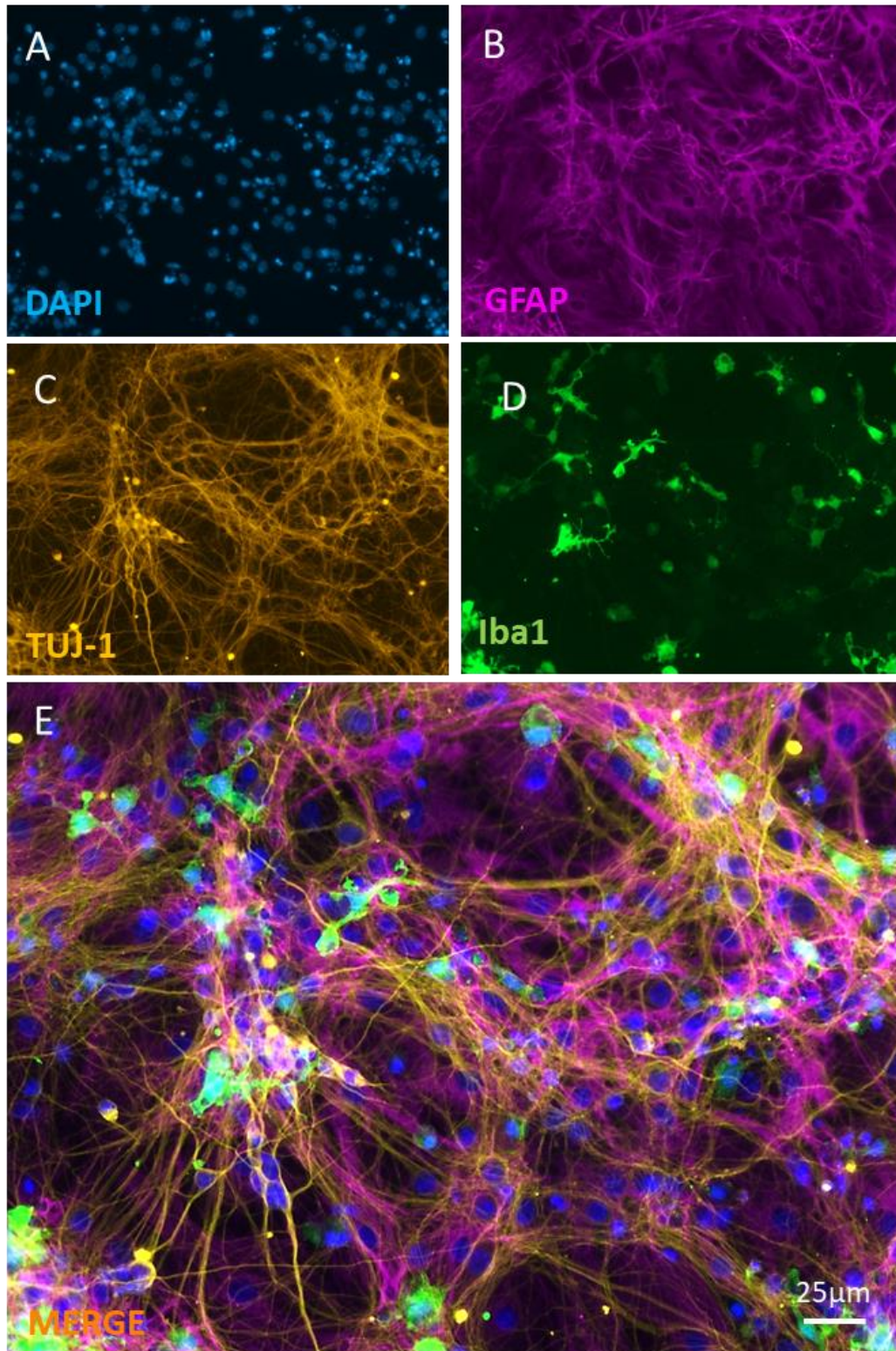
Figure 4.5. Triple immunolabelling for GFAP, TUJ-1 and Iba1 demonstrate stratified relationships. **A** DAPI reveals nuclei. **B** Bed layer of astrocytes (GFAP+). **C** Neuronal network (TUJ-1+) at the second field of focus. **D** Iba1+ microglia resting at the top of the culture. **E** Merge. Scaler bar 25 μm.

4.2.2 Generation and characterisation of a focal traumatic injury

4.2.2.1 Reliable introduction of penetrating lesion

Penetrating focal injury lesions were introduced into the cultures at 7 DIV; these produced distinct injury margins with minimal intralesional debris immediately post injury (**figure 4.6 A**). The DAPI nuclear stain revealed defined injury margins at 1 day post lesioning (DPL) with some cellular migration into the lesion area (**figure 4.6 B**). The lesions produced were consistent and reproducible over all cultures (**figure 4.6 C**).

4.2.2.2 Analysis of neuronal response to injury

Following penetrating injury, axons were severed at the injury margins. Substantial axonal outgrowth was observed from the lesion edge by 1 DPL (**figure 4.7 A**) (211.86 ± 23.37 μm), and by 3 DPL neurite outgrowth had increased by almost 2-fold (**figure 4.7 B**) (394.40 ± 29.34 μm) [independent t-test, $p < 0.01$, n=5, **figure 4.7 C**]. The distribution of neuronal outgrowth was uneven and small patches along the lesion edge showed no outgrowth. These areas were avoided in axonal measurements due to this being able to skew the neurite growth analysis.
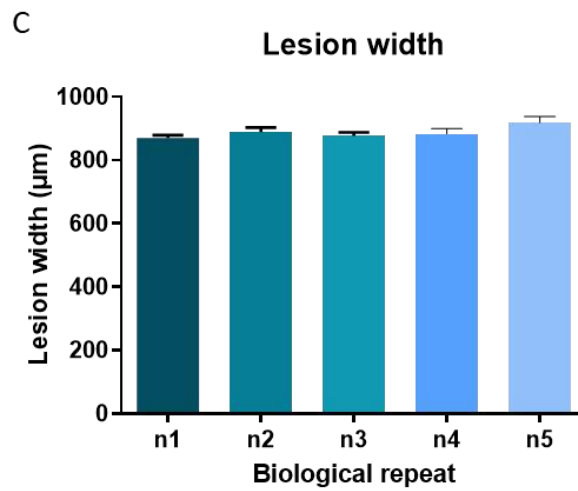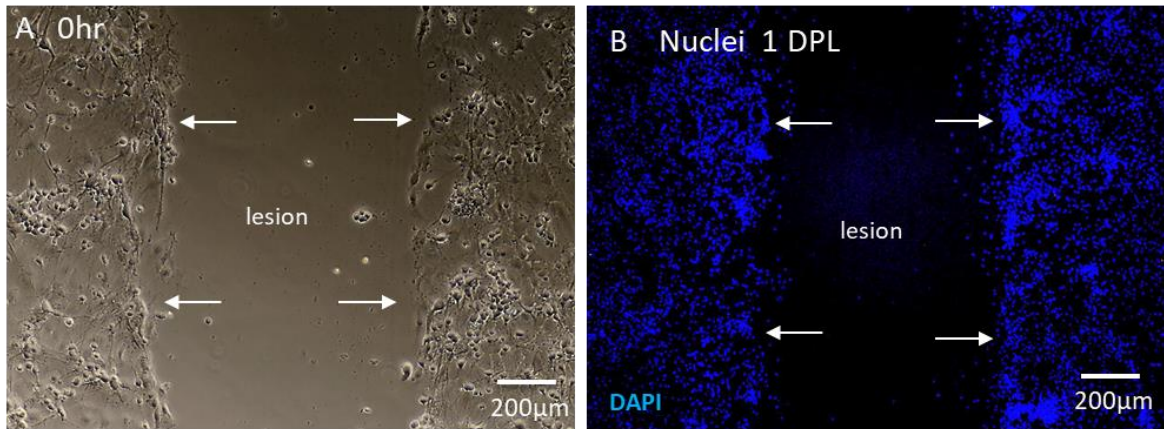
Figure 4.6. Lesion width reproducibility. A Representative brightfield micrograph demonstrating the defined injury margins with minimal intralesional debris immediately post injury. **B** Representative fluorescent micrograph demonstrating a defined lesion margin can be distinguished under the nuclear immunolabel DAPI. **C** Shows consistent reproducible lesion widths were generated.
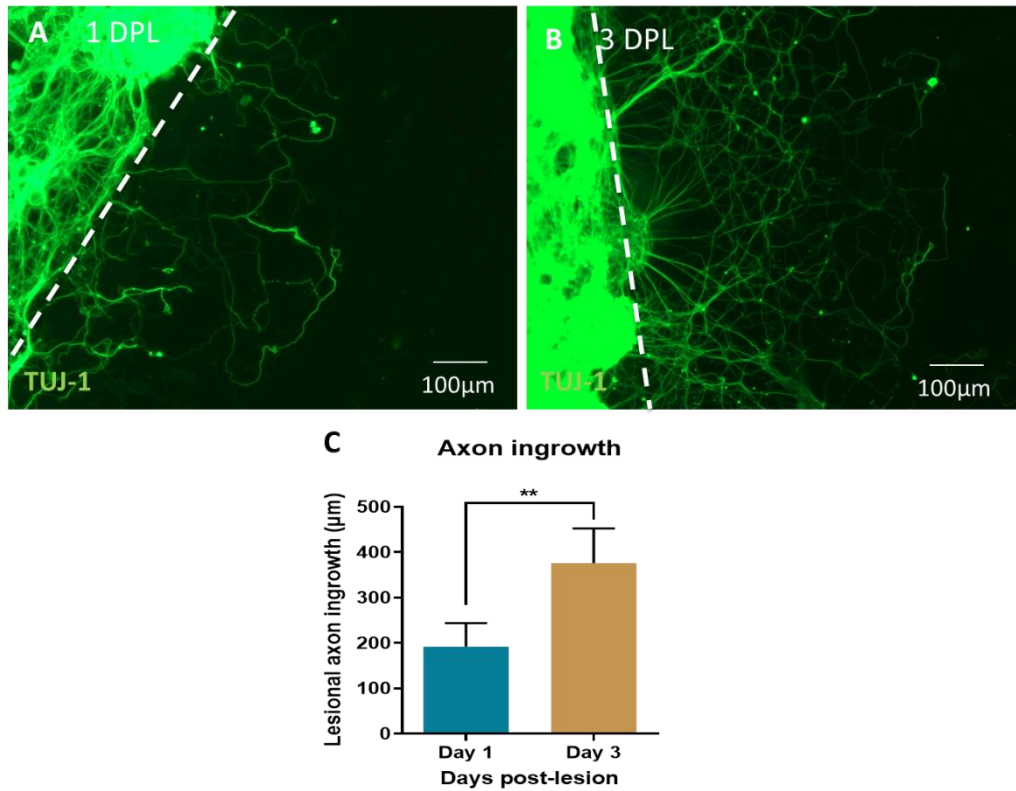
Figure 4.7. Axonal outgrowth from the lesion boundary. A Representative micrograph of the substantial TUJ-1+ axonal outgrowth from the lesion edge observed at 1 DPL. **B** Representative micrograph of the more extensive TUJ-1+ outgrowth observed at 3 DPL. **C** bar graph demonstrating a near 2-fold increase of axonal outgrowth from day 1 to day 3 (independent t-test,**p < 0.01, n=5).

4.2.2.3 Hallmark reactive astrogliosis in response to penetrating lesions

To establish if this model demonstrated injury-induced astrogliosis, astrocyte morphology and GFAP expression were evaluated at the injury site. Peri-lesional astrocytes (astrocytes proximal to the scratch wound) predominantly exhibit profiles of hypertrophic/reactive astrocytes. Here astrocytic ruffles of injury-activated astrocytes project out from the injury border (**figure 4.8 C, D**) or a glial scar type web of fibrous astrocytes with enhanced GFAP expression is observed (**figure 4.8 D inset, E, F**). Perilesional astrocytes presented mostly reactive morphologies (hypertrophic and/or extending ruffles) ((day 1: 84.3 ± 6.7%) / (day 3: 76.3 ± 3.8%) compared with resting astrocytes (fibrous/processed/fusiform) ((day 1: 15.7% ± 6.8) / (day 3: 23.7% ± 3.8)) [independent t-test, ***p<0.001, **figure 4.8 G**]. Astrocytes away from the lesion edge or distal astrocytes present mostly processed fibrous phenotypes ((1 DPL: 72.3% ± 7.6) / (3 DPL: 81.7% ± 6.1)), with some flat polygonal morphologies (1 DPL: 27.7% ± 7.6)/ (3 DPL:18.3% ± 6.1) (**figure 4.8 A, B**), comparable to the control distribution (**figure 4.3 L**). This suggests injury does not induce an astrocytic morphological response over 400 microns in distance from the lesion.

In addition, overall GFAP immunoreactivity was increased in perilesional astrocytes (astrocytes 0-100 microns from the lesion edge, day 1/3 (**figure 4.8 E, F**): (71.1 OD ± 1.9)/ (83 OD ± 2.1)) versus distal astrocytes (astrocytes 301-400 microns from the lesion edge) day 1/3 (34.2 OD ± 0.4)/ (55.5 OD ± 1) [two-way ANOVA with Dunnett's post-hoc analysis, *p<0.1, n=5, **figure 4.8 I, J**]. There was no apparent difference between injury GFAP expression at 1 DPL and 3 DPL. Although overall significance was observed it was noted that both the degree and extent of GFAP immunoreactivity was not uniform in the lesion as is seen in the representative fluorescent micrographs (**figure 4.8 E, F**).
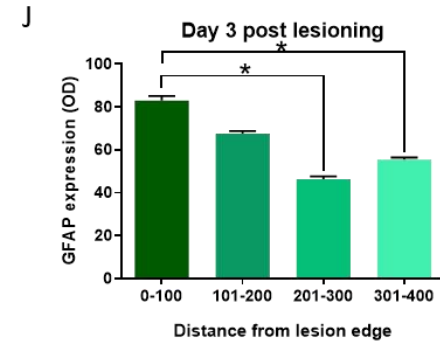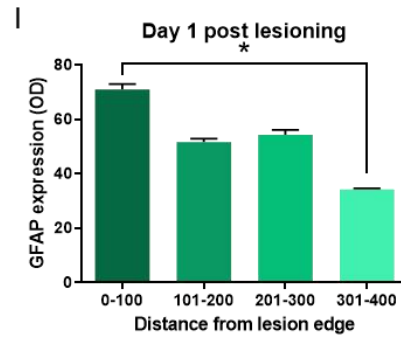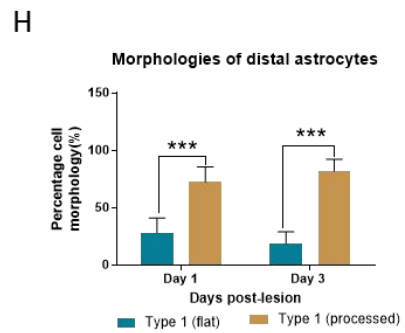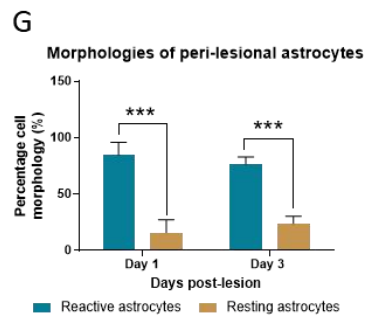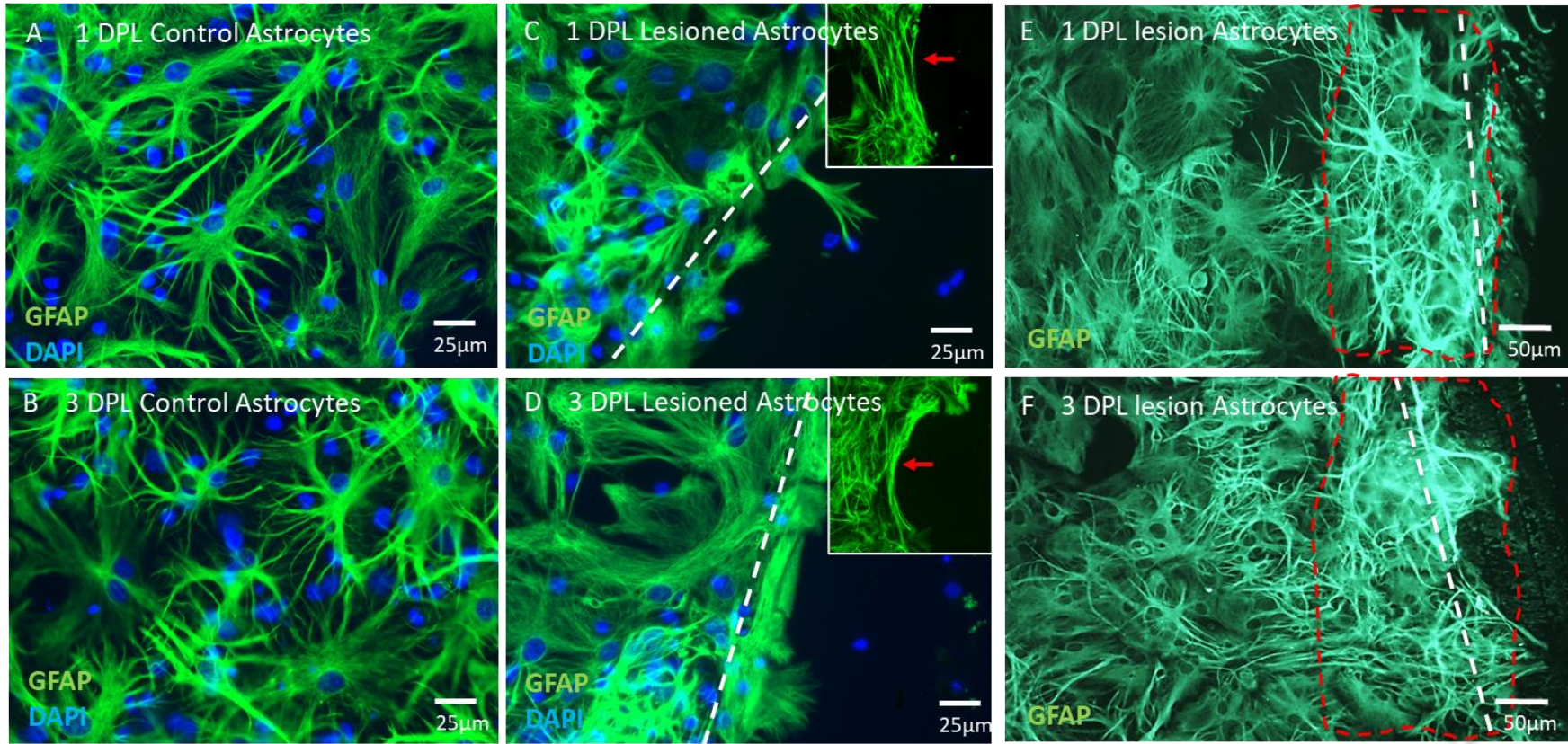
Figure 4.8. Morphology and reactivity of perilesional/distal astrocytes at day 1 and day 3 post lesioning. **A-B** Distal astrocytic morphologies at day 1/3 show predominantly processed fibrous profiles. **C-D** Perilesional astrocytic morphologies at day 1/3 exhibit reactive profiles with ruffles extending out from the injury border. Inset in D shows a glial scar like structure also generated at the lesion edge (red arrows). **E-F** Micrographs display an increase in GFAP expression at the lesion margins at day 1/3, indicated by the red dotted line. **G-H** Graphs demonstrate the morphology distribution of distal astrocytes (**G**) and perilesional astrocytes (**H**) and the GFAP reactivity at day 1 (**I**) and day 3 (**J**). (G,H; two-way ANOVA, I,J; one-way ANOVA, n=5, * < 0.05, **p < 0.01, ***p < 0.001)

4.2.2.4 Hallmark reactive microgliosis and OPC infiltration observed within the injury site

It was apparent that the penetrating injury also consistently induced Iba1+ microglial and NG2+ OPC responses. Iba1+ microglia infiltrated the lesion, increasing from (**figure 4.9 A**) 18.3 ± 3.8 cells/field at 1 DPL to 33.3 ± 6.9 cells/field at 3 DPL (**figure 4.9 B**) [independent t-test, p<0.05, n=5, **figure 4.9 G**]. Lesional microglia exhibited distinct activated hypertrophic profiles (**figure 4.9 C,D**) compared with ramified resting microglia morphologies (**figure 4.9 E,F**) distal to the injury site (>100μm distance). The lesional microglia exhibited significantly larger surface areas (i.e. hypertrophic) at 1 DPL (2671.1μm^2 ± 315.4) and 3 DPL (3114.4 μm^2 ± 445), versus their distal counterparts 1 DPL (412.2 μm^2 ± 23) and 3 DPL (512.9 μm^2 ± 36.9) [two-way ANOVA with Tukey's, post-hoc analysis, p<0.001, n=5, **figure 4.9 H**]. Furthermore, microglial morphology was characterised via a cell roundedness index (CRI). Microglia within the lesion area exhibit mostly amoeboid hypertrophied morphologies (1 DPL: (0.645 ± 0.023 CRI) (3 DPL: 0.396 ± 0.022 CRI) compared with distal microglia (1 DPL: 0.080 ± 0.013 CRI) (3 DPL: 0.112 ± 0.010 CRI) [two-way ANOVA with Tukey's, post-hoc analysis, p<0.001, n=5, **figure 4.9 I**].
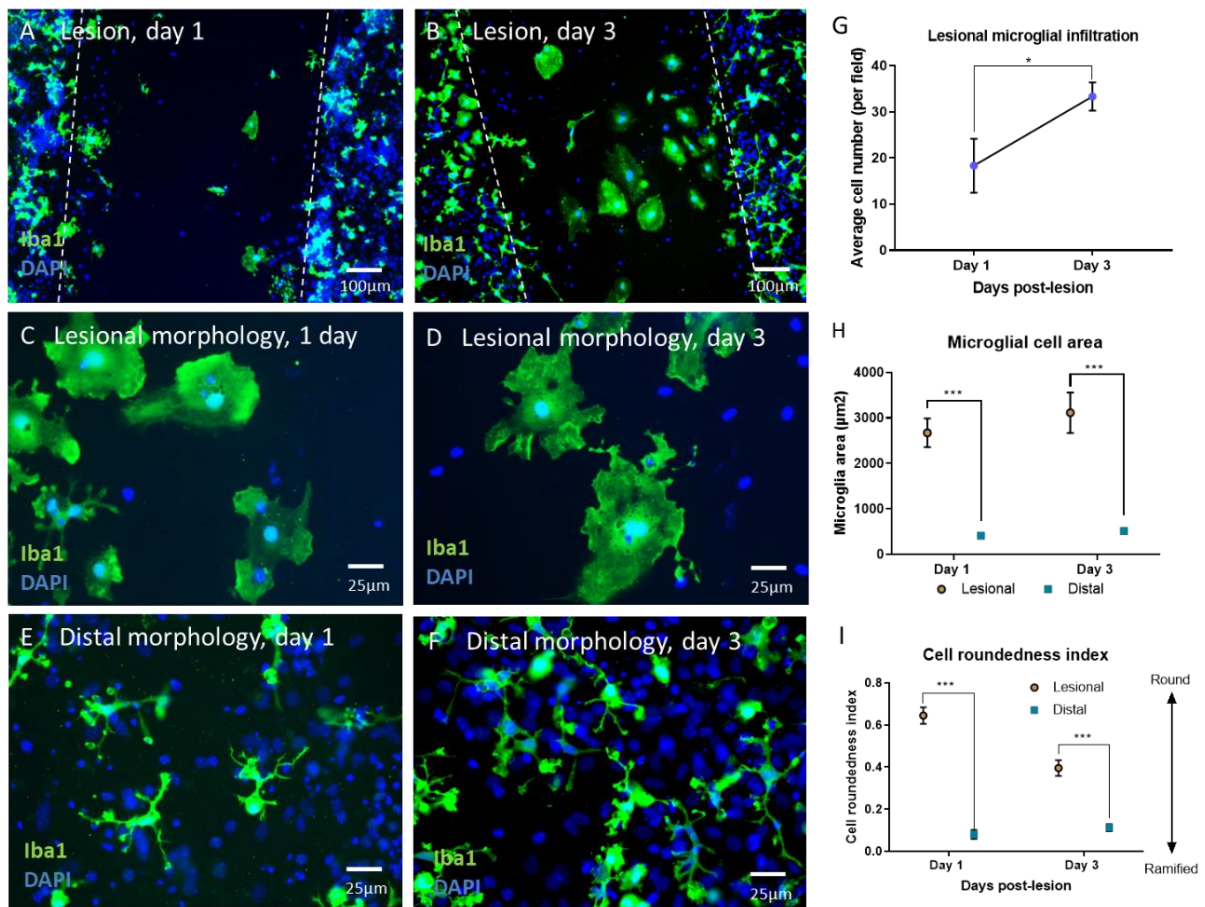
Figure 4.9. Injury-induced microglial lesion infiltration and morphological change at days 1 and 3 post lesion. Fluorescent micrographs (**A-B**) depict the lesional infiltration of microglia at day 1 and 3 respectively. (**C-D**) Lesional microglia present large hypertrophic morphologies at day 1 and 3. (**E-F**) Distal microglia exhibit distinctively more ramified and processed morphologies at day 1 and 3.(**G**) Bar graph showing a significant increase of microglia infiltration at day 3. (**H**) Lesional microglial areas are significantly larger than the cell areas of distal microglia. (**I**) Cell roundedness analysis reveals distal microglia are significantly more ramified than lesional microglia. ((G) independent t-test, (H,I) two-way ANOVA, n=4, * < 0.1, **$p < 0.01$, ***$p < 0.001$).

Concomitantly, NG2+ OPCs also infiltrate the lesion site post injury. This significantly increased by over 2-fold from 1 DPL (**figure 4.10 A**) (21.8 ± 1.7 cells/field) to 3 DPL (**figure 4.10 B**) (45.3 ± 3.5 cells/field) [independent t-test, p<0.001, n=5, **figure 4.10 G**]. Migratory bipolar profiles of the OPCs were observed within the lesion area at day 1 and day 3 (white arrows **figure 4.10 C + D**), along with multipolar non-migratory profiles (yellow arrows **figure 4.10 C + D**). This suggests the OPCs may initially migrate from the lesion margins into the lesion site and subsequently resume a multipolar non-migratory phenotype.

153

There was no evidence of OPC nuclear doublets within the lesion which would indicate proliferation into the lesion site.

Note oligodendrocytes displayed no obvious morphological response to injury within this model therefore no analysis was carried out.

Lastly, we reveal through quadruple staining that the pathomechanisms previously described can be detected simultaneously (**figure 4.11 D**). Micrographs from the same field in figure 5.11 simultaneously show: random neuronal outgrowth from the lesion (white arrows) (**figure 4.11 A**), large, hypertrophied injury-activated microglia that have migrated into the lesion area (**figure 4.11 B**) and injury-activated perilesional astrocytes extending lamellipodia into the lesion (**figure 4.11 C**).
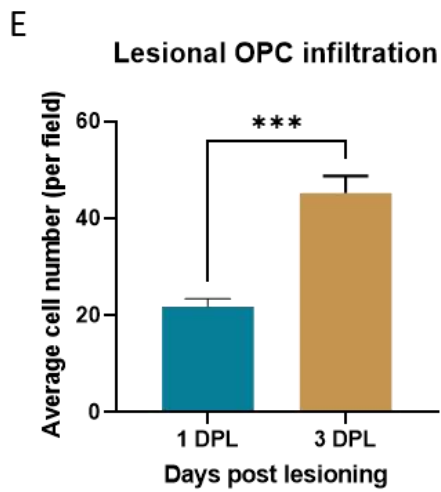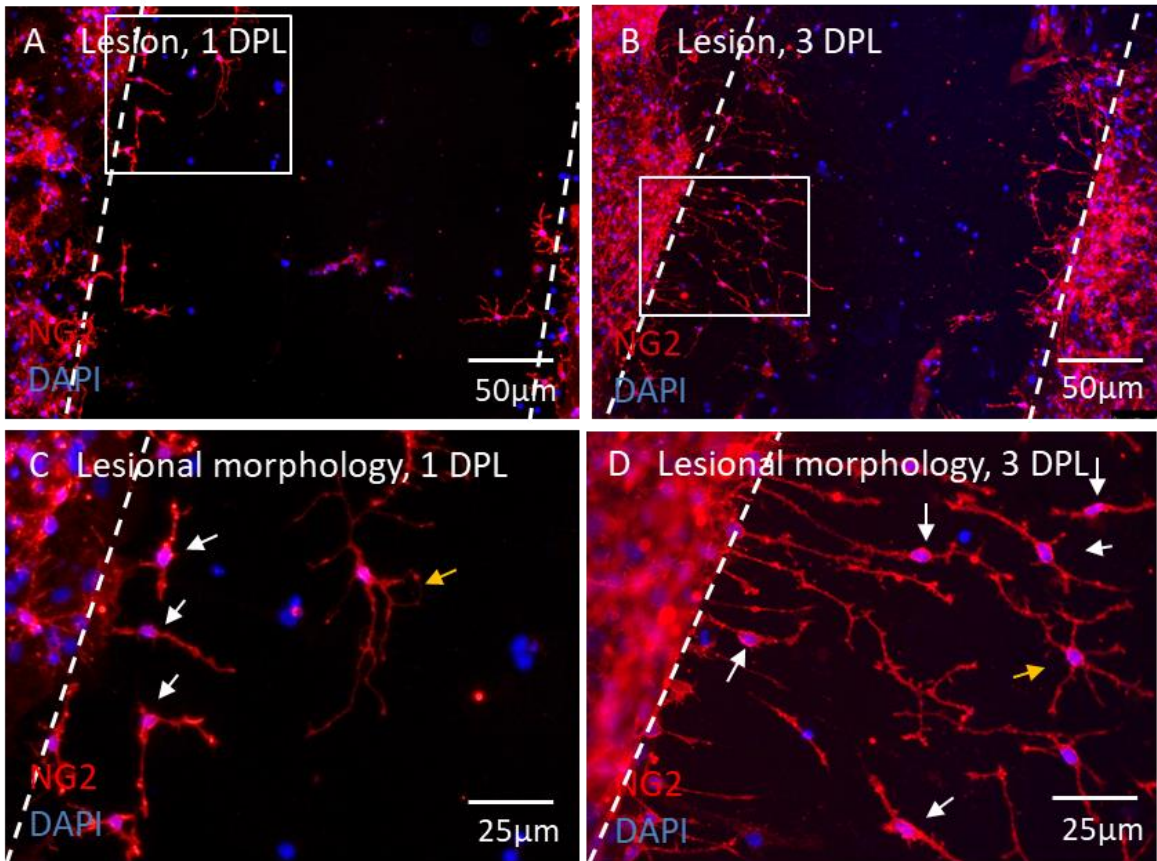
Figure 4.10: OPC infiltration and morphology in response to injury. A-B Representative micrographs demonstrating OPCs infiltration into the lesion area at day 1 vs day 2 post lesion. **C-D** higher magnification images corresponding to A and B. OPCs present bipolar migratory morphologies (white arrows) and multibranched morphologies (orange arrows) at day 1 and 3 post lesion. (**E**) Bar graph showing significant increase in OPC infiltration at day 3 post lesion (unpaired t-test, n=5 ***p<0.001).
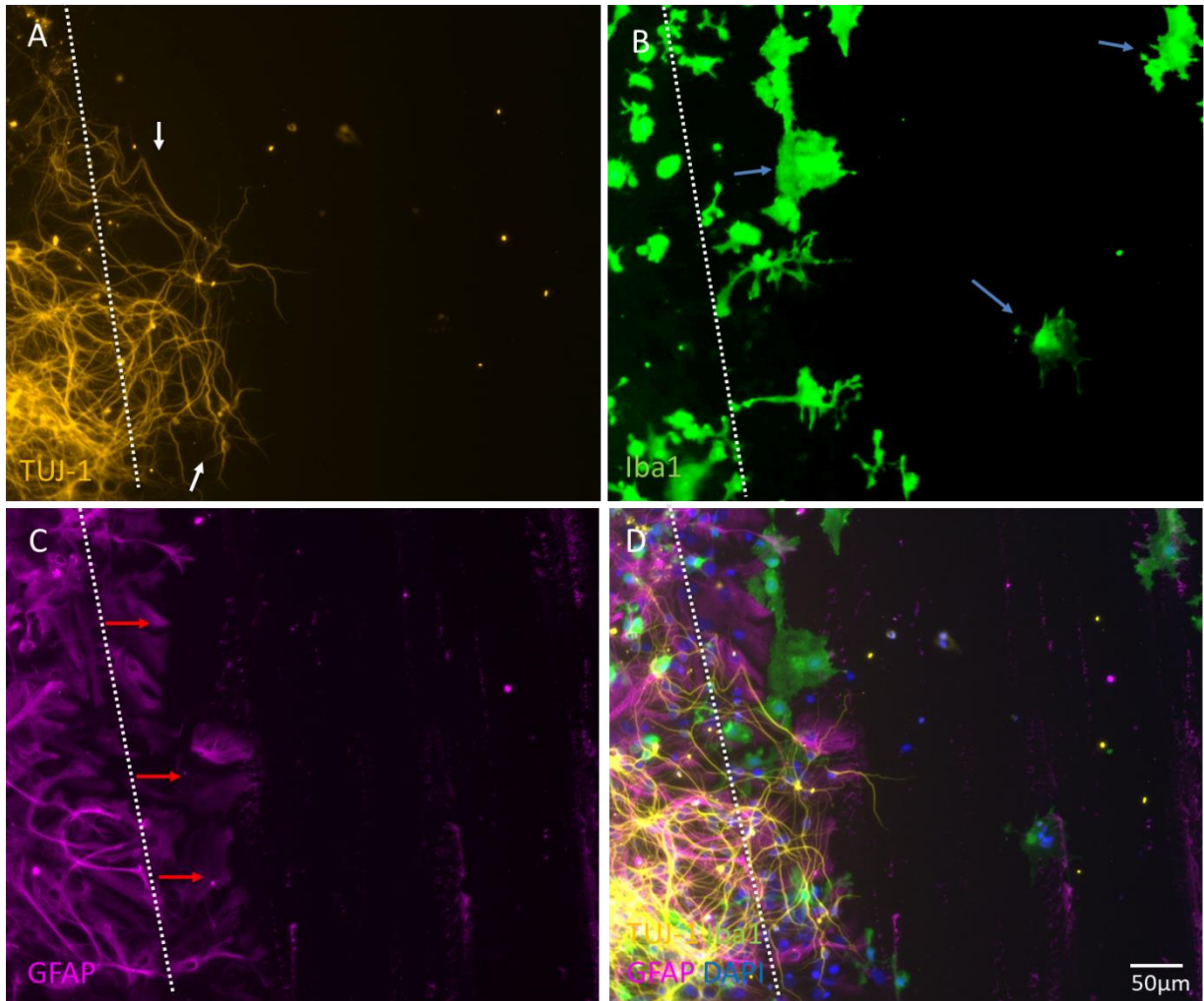
Figure 4.11: Quadruple stain revealing the simultaneous pathomechanisms of *in vitro* injury. White arrows in **A** show random neuronal outgrowth from lesion edge, blue arrows in **B** reveal large, hypertrophied microglia infiltrating the lesion site, red arrows in **C** show injury-activated astrocytes extending into the lesion site and **D** shows a quadruple merge of these responses.

4.2.3 Application of nano-materials to test the cortical injury model

4.2.3.1 Nanoparticles are predominantly taken up by microglia

Nanoparticles (NPs) were administered to the 2D cortical injury model, and assessed at day 1 and 3 post injury + administration. In control unlesioned cultures, neurons and OPCs displayed no detectable NP uptake (**figure 4.12 A-D**). Astrocytes showed some perinuclear uptake (**figure 4.12 E,F**) (CMX/PEG: (13.7 ± 1.1%)/ (15.7 ± 6.5%) (% of astrocytes)), however microglial cells show perinuclear trafficking of clusters of nanoparticles (**figure 5.11 G,H**) (CMX/PEG: (78.5 ± 2.5%)/ (65.6 ± 8.4%) % of microglia) (two-way ANOVA, with Tukey's analysis, p<0.001, n=3, **figure 4.12 M**). As injury induces morphological and behavioural changes in OPCs and astrocytes at the injury site, nanoparticle uptake by these 'activated' cells was also investigated, however both cell types in the injury environment displayed no further uptake of the NPs (**figure 4.12 I-L**). In contrast, the response of injury activated microglia to the NPs differed significantly and is described within the next section.

A — CMX neurons — CMX / Tuj1 / DAPI — 50μm

B — PEG neurons — PEG / Tuj1 / DAPI — 50μm

C — CMX OPCs — CMX / Ng2 / DAPI — 50μm

D — PEG OPCs — PEG / Ng2 / DAPI — 50μm

E — CMX astrocytes — CMX / GFAP / DAPI — 50μm

F — PEG astrocytes — PEG / GFAP / DAPI — 50μm

G — CMX microglia — CMX / IBA1 / DAPI — 50μm

H — PEG microglia — PEG / IBA1 / DAPI — 50μm

I — Lesional astrocytes — CMX / GFAP / DAPI — 50μm

J — Lesional astrocytes — PEG / GFAP / DAPI — 50μm

K — Lesional OPCs — CMX / Ng2 / DAPI — 50μm

L — Lesional OPCs — PEG / Ng2 / DAPI — 50μm

M — CMX vs PEG uptake

Cells with MNP labelling (%) vs Neural cell type (Microglia, Astrocytes). CMX, PEG. ***

Figure 4.12: Fluorescent micrographs illustrating the distinct cellular uptake of nanoparticles. A-D Neurons and OPCs demonstrate no CMX or PEG uptake. E-F Astrocytes show very little uptake of either nanoparticle. G-H Microglia show considerable labelling with both nanoparticles. White arrows signify uptake. I-L Activated astrocytes and OPCs at the lesion edge do not increase their uptake of CMX or PEG. M graph shows that CMX and PEG are mostly engulfed by microglia. (2-way ANOVA, ***p < 0.001, n=3) (24 hours post administration).

4.2.3.2 MNPs are exclusively engulfed injury-activated microglia within the lesion site.

It was evident that MNP uptake was localised predominantly within intralesional space at both timepoints (within white dotted lines in **figure 13 A-B**). At 3 DPL microglia demonstrated greater CMX vs PEG MNP uptake and peri-nuclear trafficking within the lesion site (**figure 13 C-E**) (49.2 ± 2.5% (CMX) vs 32.7 ± 1.4% (PEG), n=3, **figure 13 F**). In addition, it was noted that these intralesional microglia demonstrated significantly greater levels of CMX/PEG MNP uptake than peri-lesional microglia (figure C-D) (19.6 ± 0.8% (PEG), or 14.5 ± 3.2% (CMX) (two-way ANOVA with Tukey's, p<0.0001, n=3, **figure 13 F**).

.
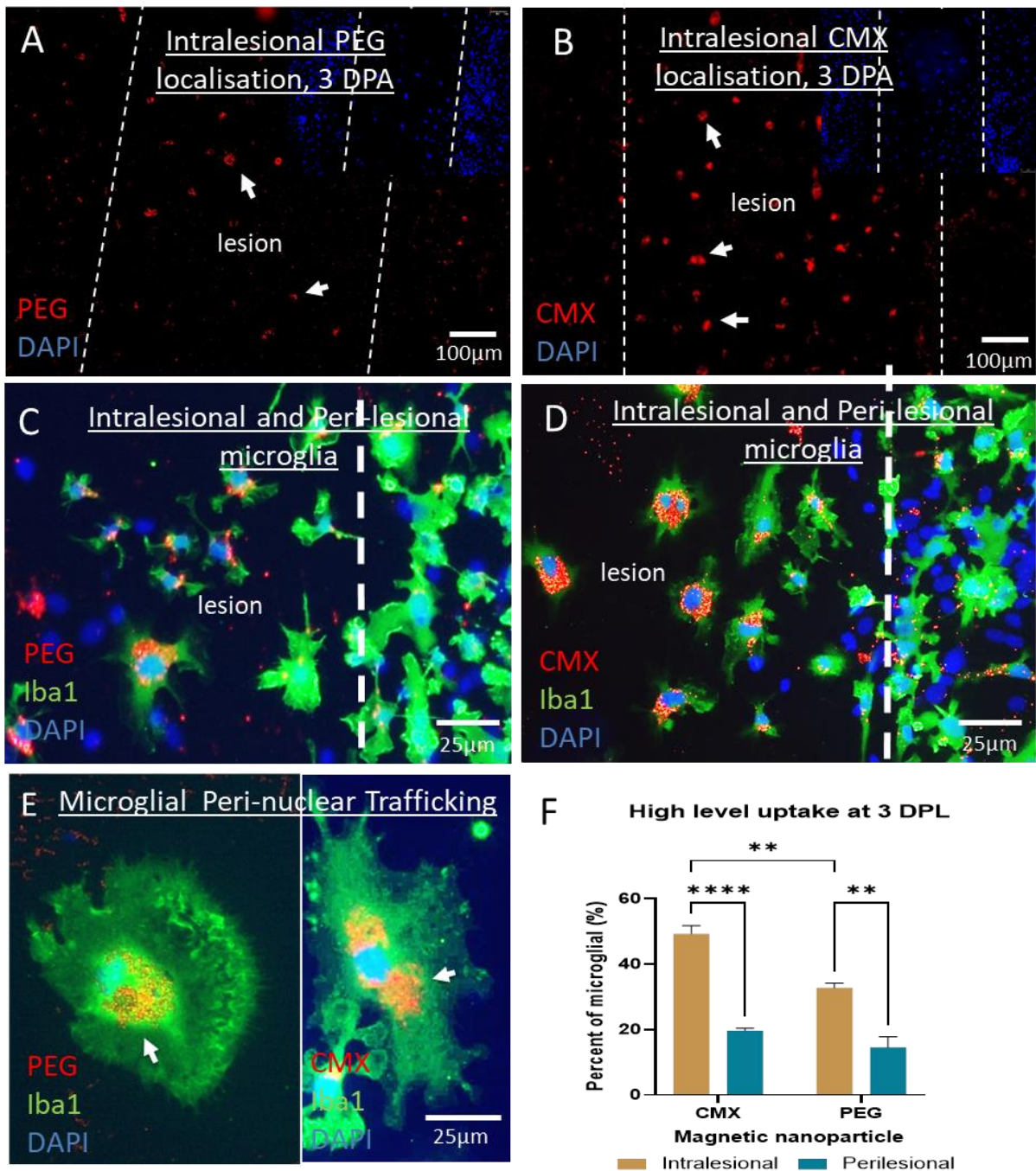
Figure 4.13: Competitive MNP uptake in injury activated microglia. **A,B** Representative micrographs of MNP aggregates localised to the lesion area (dotted lines), PEG, CMX respectively. **C,D** Representative micrographs showing perinuclear trafficking of MNPs with lesion site 'activated' microglia compared with perilesional microglia PEG and CMX respectively. **E** Perinuclear trafficking of CMX is higher than PEG trafficking. **F** Graph demonstrates a significant increase in MNP uptake by intralesional microglia

and a significant rise in CMX uptake over PEG. [two-way ANOVA, with Tukey's, *p<0.05 **P<0.01 ***p<0.0001, n=3].

4.3 Results 4b

4.3.1 Development of initial protocol and seeding densities for 3D culture

Following establishment of an effective 2D pathomimetic injury model using the cortical cells from enzymatic dissociation, the next goal was to develop this into a 3D neuro-mimetic construct where cortical cells would be encapsulated within a 3D microenvironment. Cells were encapsulated within collagen constructs as described in the section 2.4.8.1. Collagen concentrations of 1.5mg/ml and 0.6mg/ml (note 0.6mg/ml cellular gels did not form well so this concentration was then dropped) and various cell seeding densities were trialled. Initially either a stock density of 5×10^6 or 10×10^6 cells/ml was added to the gel formulation solution at the last step: producing final densities of 1.5×10^6 or 3×10^6 cells per gel.

After 7 DIV cellular growth, morphology and distribution through the gels were assessed through immunostaining for cell selective markers. Cells within these gels did not express typical morphologies of that observed *in vivo* or culture on glass. Astrocytes presented as spheroids (**figure 4.15 A,B**), while neurons were sparse with short processes (**figure 4.15 C,D**), oligodendrocytes exhibited some recognisable morphologies but were also rounded (**figure 4.15 E,F**) and were sparsely distributed through the culture. Microglia and OPCs could not be detected/visualised in these cultures. Collagen concentrations above 1.5mg/ml were not trialled, as previous studies show higher collagen concentration cause cells to remained balled up (Adams et al., 2015).
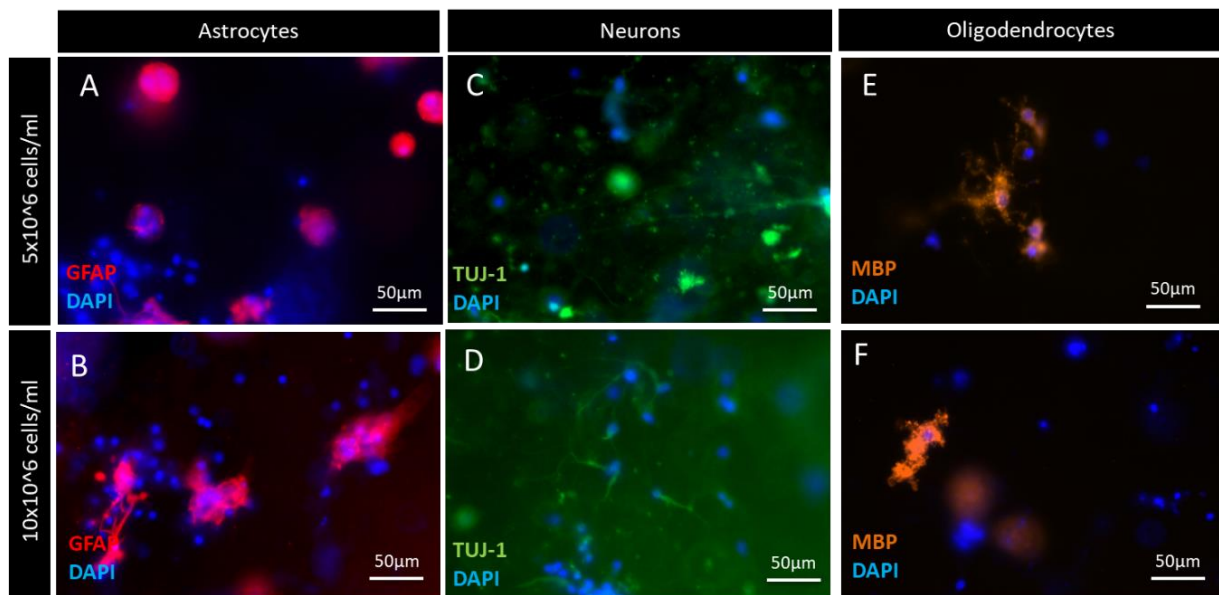
Figure 4.15: Initial cell encapsulation experiments with 1.5mg/ml collagen concentrations. Two separate cortical cell densities of the cell stock solution were used initially, 5 x 10^6cells/ml and 10 x 10^6 cells/ml. **A-B** GFAP+ astrocytes. **C-D** TUJ-1+ neuronal cells. **E-F** MBP+ oligodendrocytes. Astrocytes were predominantly spherical of minimally processed. Neurons showed no or very short processes. Oligodendrocytes had familiar morphologies but were rarely expressed. [n=4]

4.3.2 A modified protocol and cell seeding density resulted in improved morphological features within the 3D construct.

As the initial encapsulation experiments repeatedly displayed undesirable cellular architecture, a series of adjustments were made to the gel making process, in particular the seeding density was modified (2.5 times the previous density). This was performed to achieve a more compact cellular gel resembling a tissue-like density. 2.5 x10^7 cells/ml stock was added to the gel formulation solution, resulting in an overall gel density of 7.5 x 10^6 cells per gel. The cellular construct at this density presented visible improvements using light microscopy (compared with the initial experiments). Microscopy was used to track the gel progression in the live cultures. Cells remained balled up at first (**figure 4.16 A**), but by 3 DIV some cellular processes could be identified projecting from cellular bodies (**figure 4.16 B**). Some

cellular morphologies could be identified here through the fields of focus. By 7 DIV multiple cellular morphologies could be identified across the gels (**figure 4.16 C**) (also seen in supplementary video 1).

Following this, high magnification immuno-stained images were taken to confirm the neural cell types and evaluate the effect of the 3D environment on cellular morphology. GFAP+ astrocytes displayed many fine long processes from a central body (**figure 4.17 A**) (supplementary video 2). These are likely type 2 (T2) astrocytes (differing from 2D model cortical T1 astrocytes). Though harder to visualise than the other cell types, a TUJ-1 + neuronal network was detected; processes were ultrafine and faint in contrast to the large amount of debris/background fluorescence observed with TUJ-1 staining (**figure 4.17 B**). MBP+ oligodendrocytes presented usual multiple-processed morphologies (**figure 4.17 C**). Iba1+ microglia presented ramified morphologies, with some amoeboid (**figure 4.17 D**) (supplementary video 3. NG2+ OPCs exhibited processed morphologies with a large surface area (**figure 4.17 E**), distinct to the OPCs in the 2D model. Furthermore, a triple stain was also achieved depicting the relationship between multiple cell types (**figure 4.17 F**).

Cellular proportions established within the 3D cellular collagen constructs were astrocytes: 25.97 ± 3.1%, neurons: *45% estimate*, oligodendrocytes: 10.7 ± 0.85%, microglia: 4.77 ± 0.69% and OPCs: 12.5 ± 1.48%) (**figure 4.17 G**) and these differed from the 2D model (astrocytes: 35.3 ± 0.2%, neurons: 45.8 ± 2.1%, oligodendrocytes: 2.73 ± 0.17%, microglia: 10.35 ± 3.89%, OPCs: 11.15 ± 0.32%).

Neuronal distribution was estimated within the 3D model via a subtraction process, the ~45% of nuclei that were unaccounted for were presumed to be neurons. The 3D model here presents over 3-fold increase in oligodendrocytes survival and growth (3D: 10.7± 0.85%; 2D: 2.73 ± 0.17%). Microglia were also in lower numbers in the 3D model (3D: 4.77 ± 0.69%; 2D: 10.35 ± 3.89%). This suggests that microglia may be in a less proliferative state within the 3D model versus 2D model.
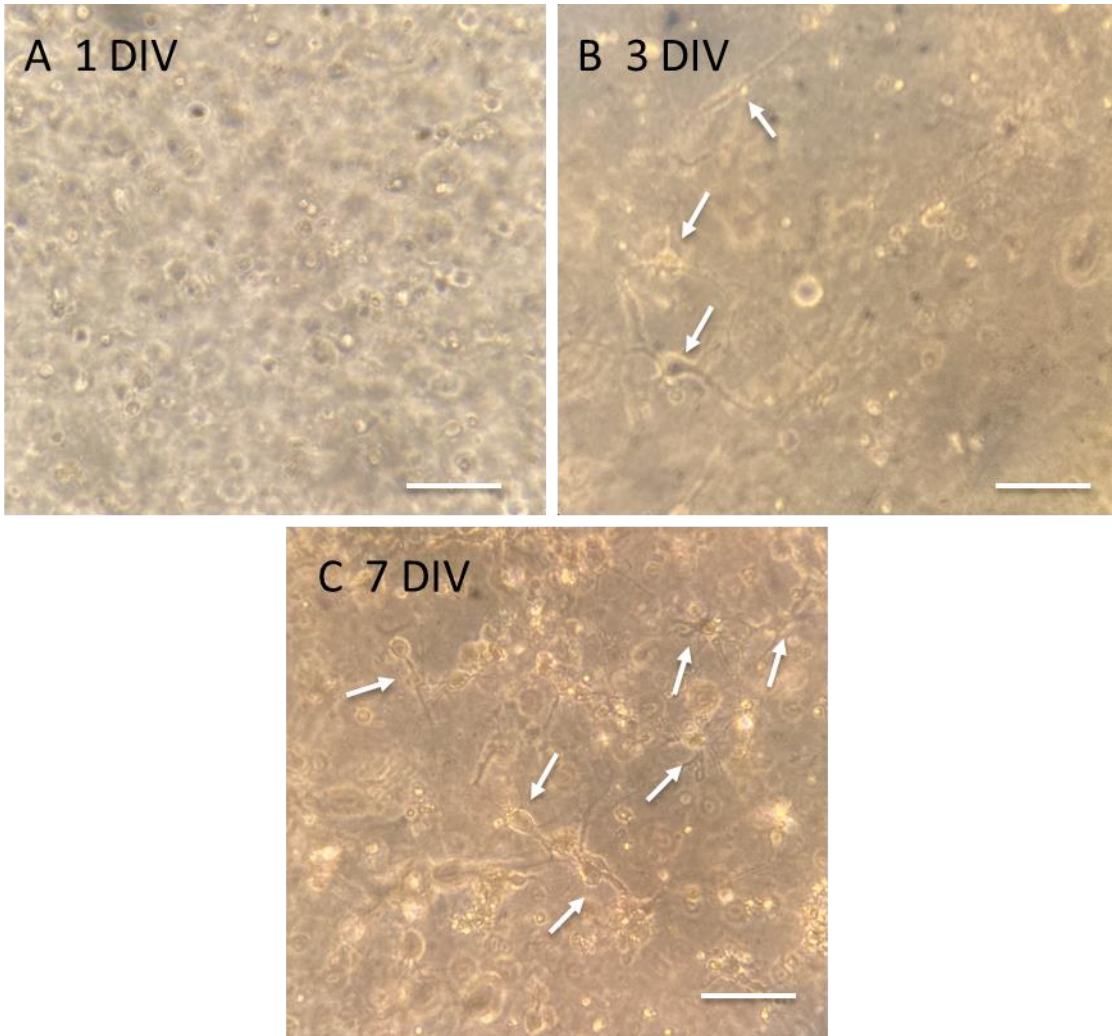
Figure 4.16: Brightfield images of the cellular progression over 7 days in culture. A Representative micrograph of 1 DIV. Cells remained balled up. **B** Representative micrograph of 3 DIV. Cellular processes begin to emerge. **C** Representative micrograph at 7 DIV. Distinct cellular morphologies can be seen throughout. Scale bar: 100 microns.
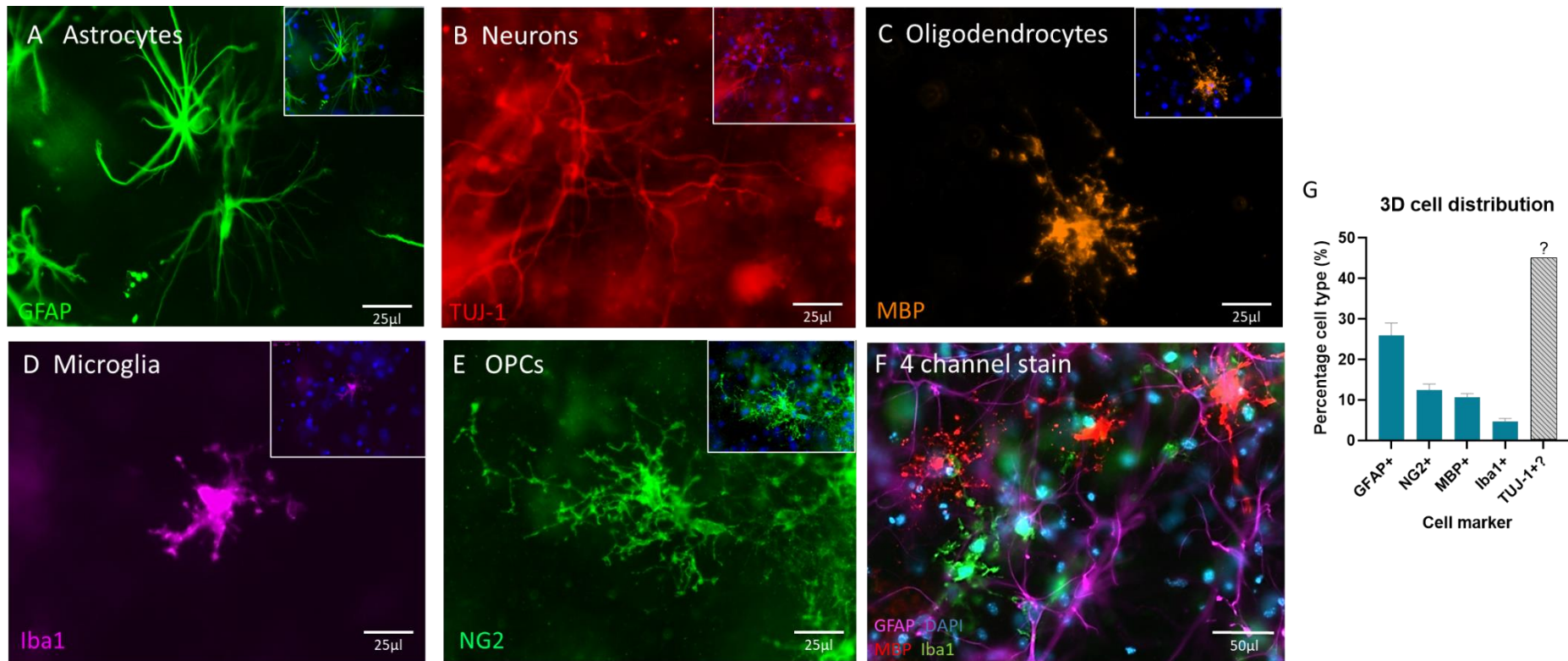
Figure 4.17: Cellular morphology of the 5 major neural cell types encapsulated within the 3D hydrogel construct. Representative fluorescent micrographs demonstrate, **A** fibrous (GFAP+) astrocyte morphology, **B** TUJ-1+ neuronal network forming, (**C**) mature MBP+ oligodendrocyte morphology, **D** ramified 'resting' Iba1+ microglia, **E** highly processed NG2+ OPCs. (**F**) Reveals a quadruple stained micrograph revealing the relationship of astrocytes, oligodendrocytes and microglia. Bar graph in (**G**) demonstrates the cellular distribution throughout the construct, neuronal population were not quantifiable therefore predicted in the graph. Note TUJ-1+ cell numbers are estimated. [n=4]
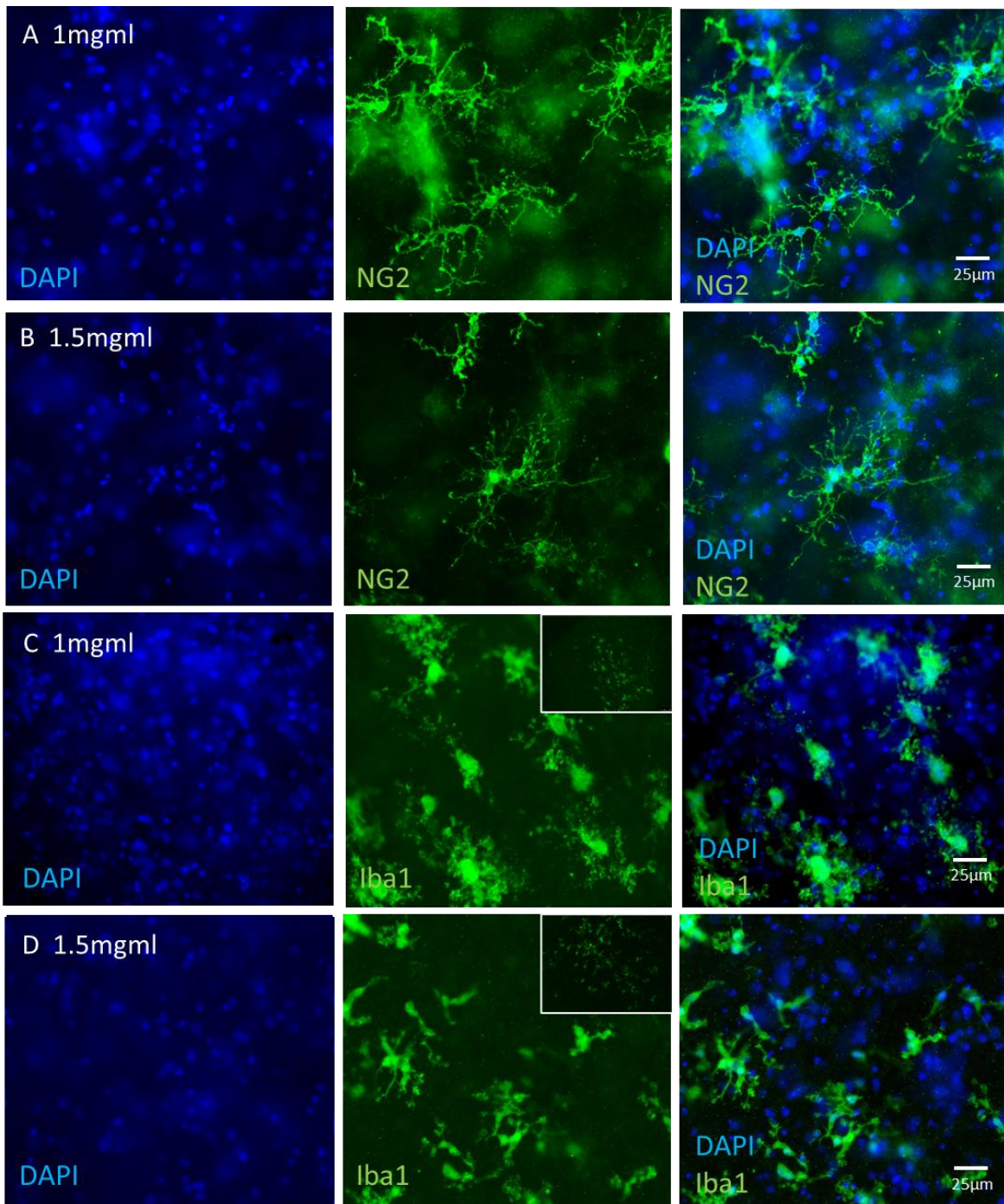
Figure 4.18: Cellular morphology and distribution of OPCs and microglia within 1mg/ml or 1.5mgml collagen constructs. **A,B** representative micrographs of NG2+ OPC morphology and distribution throughout the collagen gels 1mg/ml and 1.5mg/ml respectively. Multi-processed and evenly distributed throughout. **C,D** representative micrographs of Iba1+ microglia morphology and distribution throughout the collagen gels 1mg/ml and 1.5mg/ml respectively. Microglia were ramified and distributed in patches as shown in the insets. [n=4]

4.3.3 Cell morphology and distribution patterns within two collagen gel concentrations

Cell morphology and distribution was assessed within 1.5mg/ml and a lower concentration of 1mg/ml with the higher seeding density at 7 DIV. NG2+ OPCs maintained their multi-processed morphologies as described previously and they were distributed evenly throughout both 1mg/ml and 1.5mg/ml gel constructs (**figure 4.18 A,B**). Ramified Iba1+ microglia were expressed in distinct patches (insets **figure 4.18 C,D)** throughout both gels, but there appeared to be in fewer numbers compared to the 2D model (section 1.2.1).

The 3D constructs showed three distinct astrocytic morphologies; the most abundant were long fine processes emerging from a central cell body (**figure 4.19 A**), less frequently observed were astrocytes with very short, restricted processes (**figure 4.19 B**) or unprocessed spherical astrocytes (**figure 4.20 C**). The latter two astrocytic morphologies were the predominant forms expressed within the lower cell seeding densities cells (section 1.3.1). Finely processed type 2 astrocytes were evenly distributed throughout both gels (**figure 4.19 D,E**). At lower magnification, it appeared that the higher collagen concentration gel consisted of a larger number of unprocessed astrocytes. 84.8 ± 2.4% of astrocytes within the 1mg/ml gel were the long finely processed astrocytes compared to 71.4 ± 6.5% within the 1.5mg/ml gels. Additionally, 9.5 ± 2.7% of astrocytes were short processed and 5.5 ± 0.3% were unprocessed within the 1mg/ml gels, this was almost double in the 1.5mg/ml gels (16.9 ± 3.3% and 11.6 ± 4.3%) (**figure 4.19 F**). These astrocytic differences did not reach statistical significance.

Furthermore, a distinct neuronal network was present within both gel concentrations. TUJ-1 staining presented a large amount of unspecific staining, however, fine neuronal processes could be identified at a high magnification in both collagen concentrations (**figure 4.20 A,B**). Finally, MBP+ oligodendrocytes were seen regularly throughout the gels (**figure 4.20 C,D**).
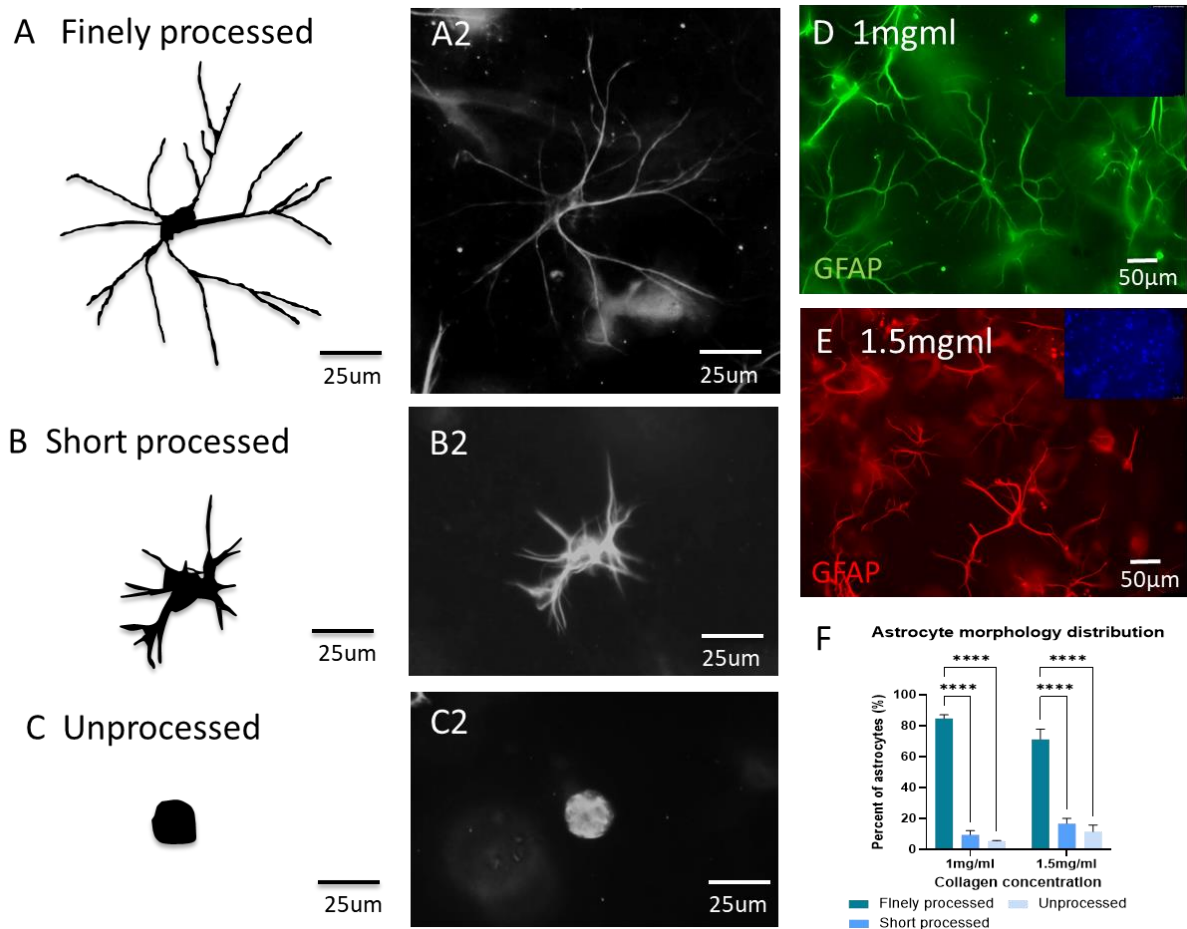
Figure 4.19: Astrocyte morphology analysis in 3D culture. Three distinct astrocytic morphologies identified: (**A**) finely processed, (**B**) short processed and (**C**) unprocessed. Representative diagrams are individual traces from micrographs in **A2, B2, C2**. Representative fluorescent micrographs of GFAP+ astrocytes throughout the gel 1mg/ml (**D**) and 1.5mg/ml collagen (**E**). Bar graph **F** displays the distribution of the astrocytic morphologies. [two-way ANOVA, with Tukey's, ****$p < 0.0001$, n=4]
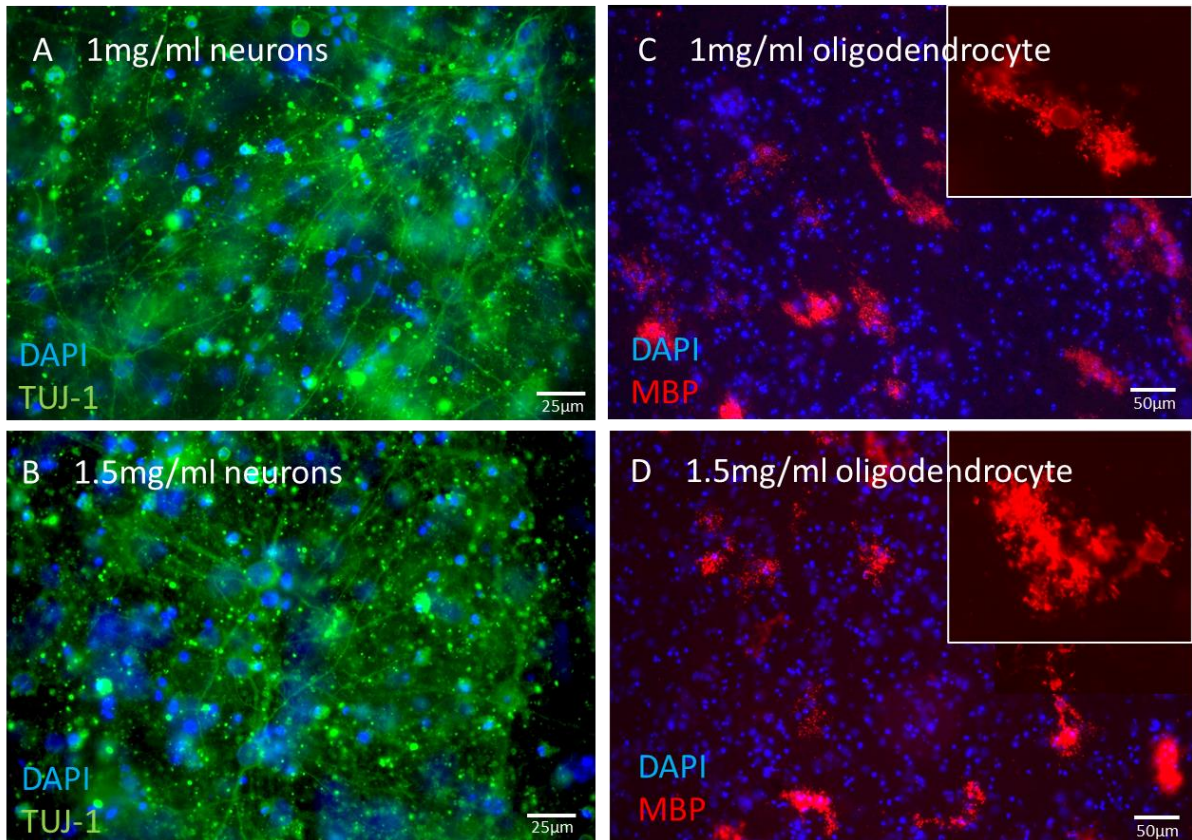
Figure 4.20: Fluorescent micrographs demonstrating neuronal and oligodendrocytes distribution. A-B shows fine neuronal processes in 1mg/ml and 1.5mg/ml gels. **C-D** oligodendrocytes were widely distributed throughout both gels with usual morphologies. [n=4]

4.3.4 Generation of focal injury within the 3D cellular construct induced injury specific responses.

Focal injuries in the 3D cellular culture (section 2.4.8.2), produced consistent, clear and measurable lesion sites (**figure 4.21 A**). The inner part of the injured gel was removed to allow for a distinct injury cavity that was: easily detectable, supported the analysis of injury responses and permitted the implantation of a biomaterial for testing. At 1 DPL, average injury diameters per gel were 860.12 ± 41.01µm (1mg/ml) and 724.81 ± 23.6µm (1.5mg/ml).
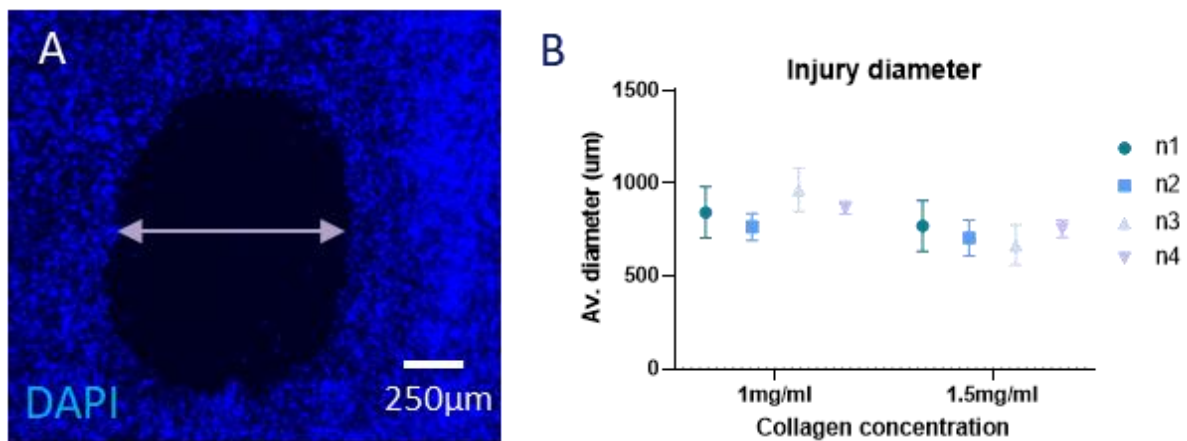
Figure 4.21: Introduction of focal injury with reproducible injury diameters. **A** representative fluorescent micrograph of the DAPI nuclear stain at the injury site highlighting injury area. **B** graph showing reproducible injury diameter per biological repeat. [n=4]

GFAP+ astrocytes displayed injury-induced astrogliosis at the lesion margins, evidenced by visual significant increase in GFAP expression (**figure 4.22 A,C**), while distal astrocytes remained at a 'baseline' expression level (**figure 4.22 B,D**), similar to observations in injured cell monolayers. Optical density of perilesional astrocytes and non-injured distal astrocytes was assessed to determine the degree of injury-induced astrogliosis (Section 2.4.9.1). The upregulation of GFAP at the injury margins showed a significant increase (around 3-fold) (1mg/ml: 0.41 ± 0.045 OD) (1.5mg/ml 0.4 ± 0.043 OD) compared to the baseline level GFAP expression of distal astrocytes (1mg/ml: 0.127 ± 0.011 OD) (1.5mg/ml: 0.152 ± 0.022 OD) (**figure 4.22 E**, two-way ANOVA with Sidaks analysis, $p < 0.001$, n=4).

An injury-activated microglial response was also observed. Microglia proximal to the injury site displayed rounded (amoeboid) and bipolar morphologies post injury (yellow arrows **figure 4.23 A,B**). The bipolar morphologies observed towards the lesion are indicative of migratory profiles. Microglia cannot migrate into the lesion itself, since the injury is a 3D cavity with no substrate for migration. Corresponding distal microglial patches away from the lesion exhibit multipolar morphologies, indicating a resting profile(**figure 4.23 C,D**). The microglia cell roundedness index (CRI) revealed that

perilesional microglia (0.266 ± 0.064 CRI) were significantly more rounded than their distal counterparts (0.564 ± 0.091 CRI) at 3 DPL (**figure 4.23 E**).
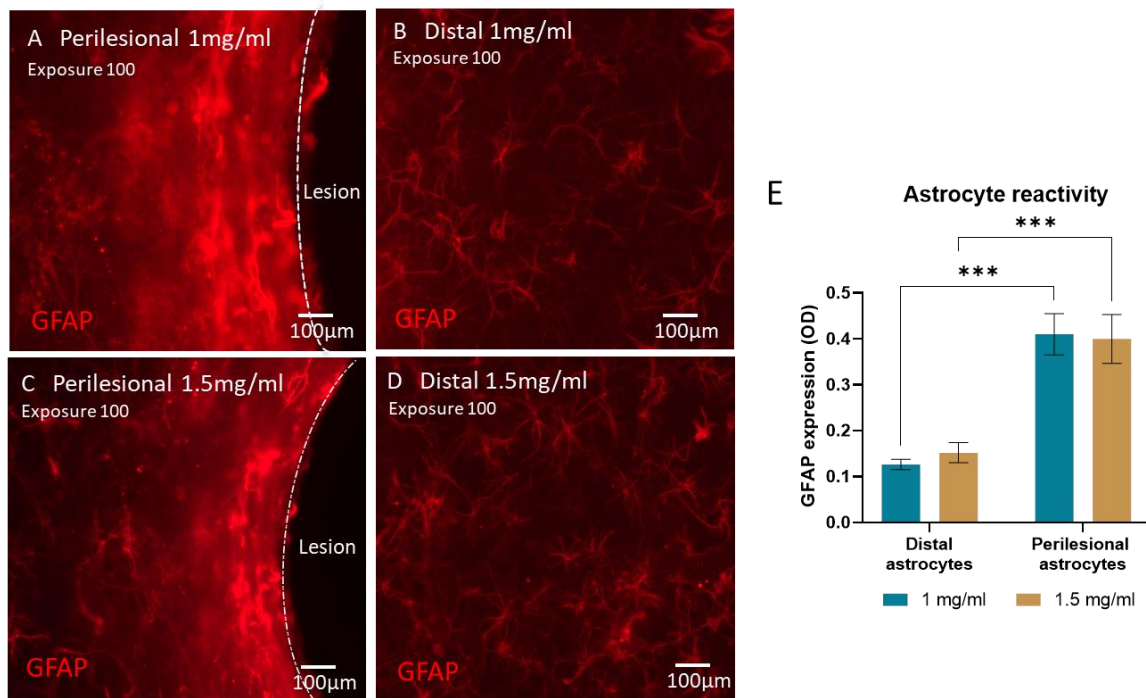
Figure 4.22: Injury-induced astrogliosis proximal to the lesion cavity. A + C fluorescent micrographs representing GFAP+ astrocytes at the lesion margins upregulating GFAP expression **B + D** fluorescent micrographs of GFAP+ astrocytes away from the lesion area representing normal GFAP expression. **E** bar graph reveals a significant increase in GFAP expression of perilesional astrocytes. (two-way ANOVA with Tukey's, **p<0.001, n=4). (3DPL)

Additionally, injury to the 3D cellular system induced an OPC response. NG2+ OPCs proximal to the lesion displayed bipolar migratory morphologies (**figure 4.24 A,B**) distinct from the phenotypes observed in the non-injured model. NG2+ OPC away from the lesion site retained the multi-processed phenotypes detected initially (**figure 4.24 C,D**).
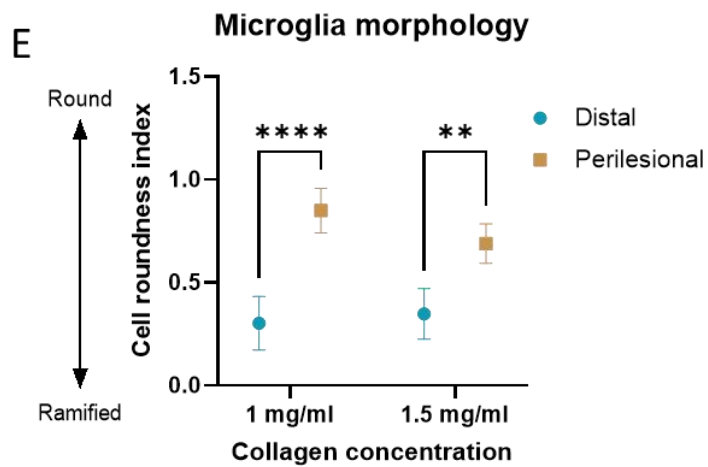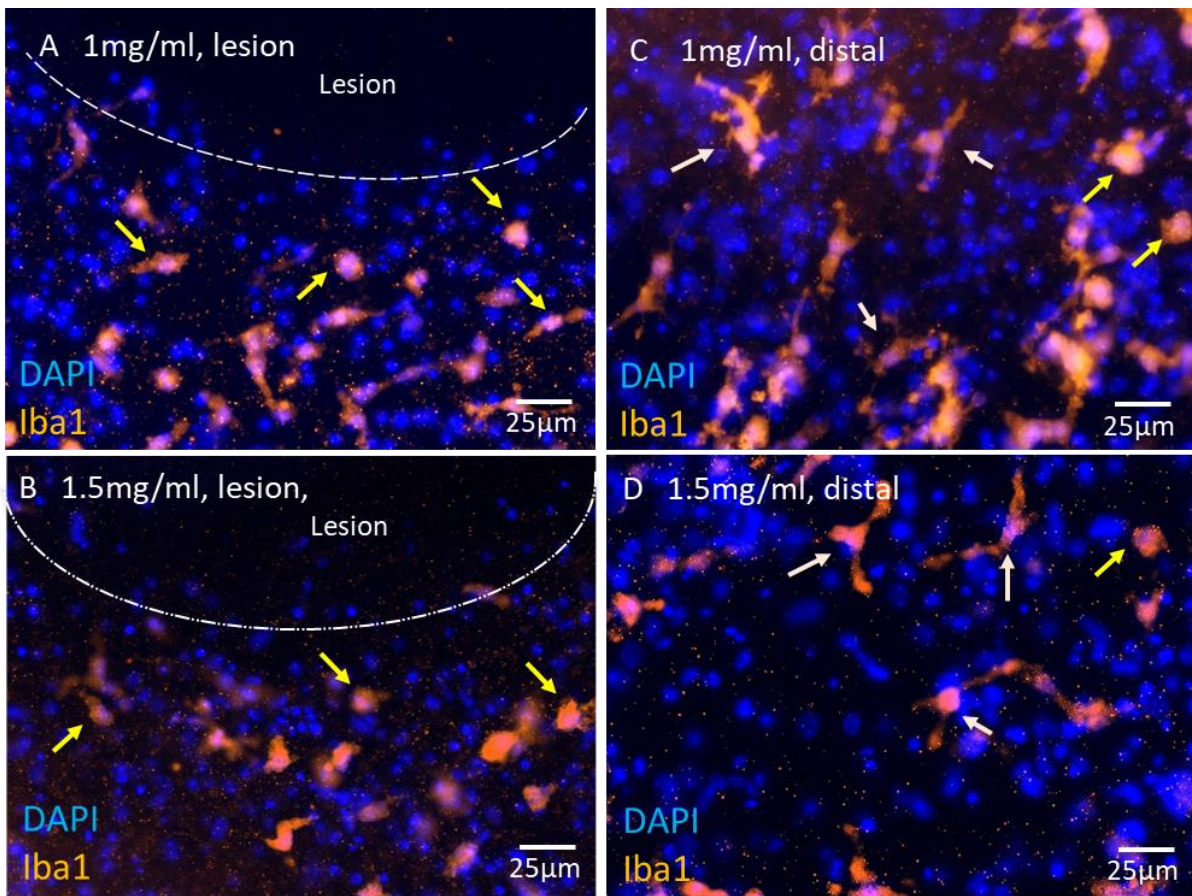
Figure 4.23: Injury-induced microglial reactivity observed close to the lesion cavity within gels. A-B mostly amoeboid/bipolar morphologies observed near the injury cavity (yellow arrows). C-D more multipolar morphologies of distal microglia of the same gel (white arrows)). [Unpaired t-test, n=3, *p<0.05]. (3DPL)
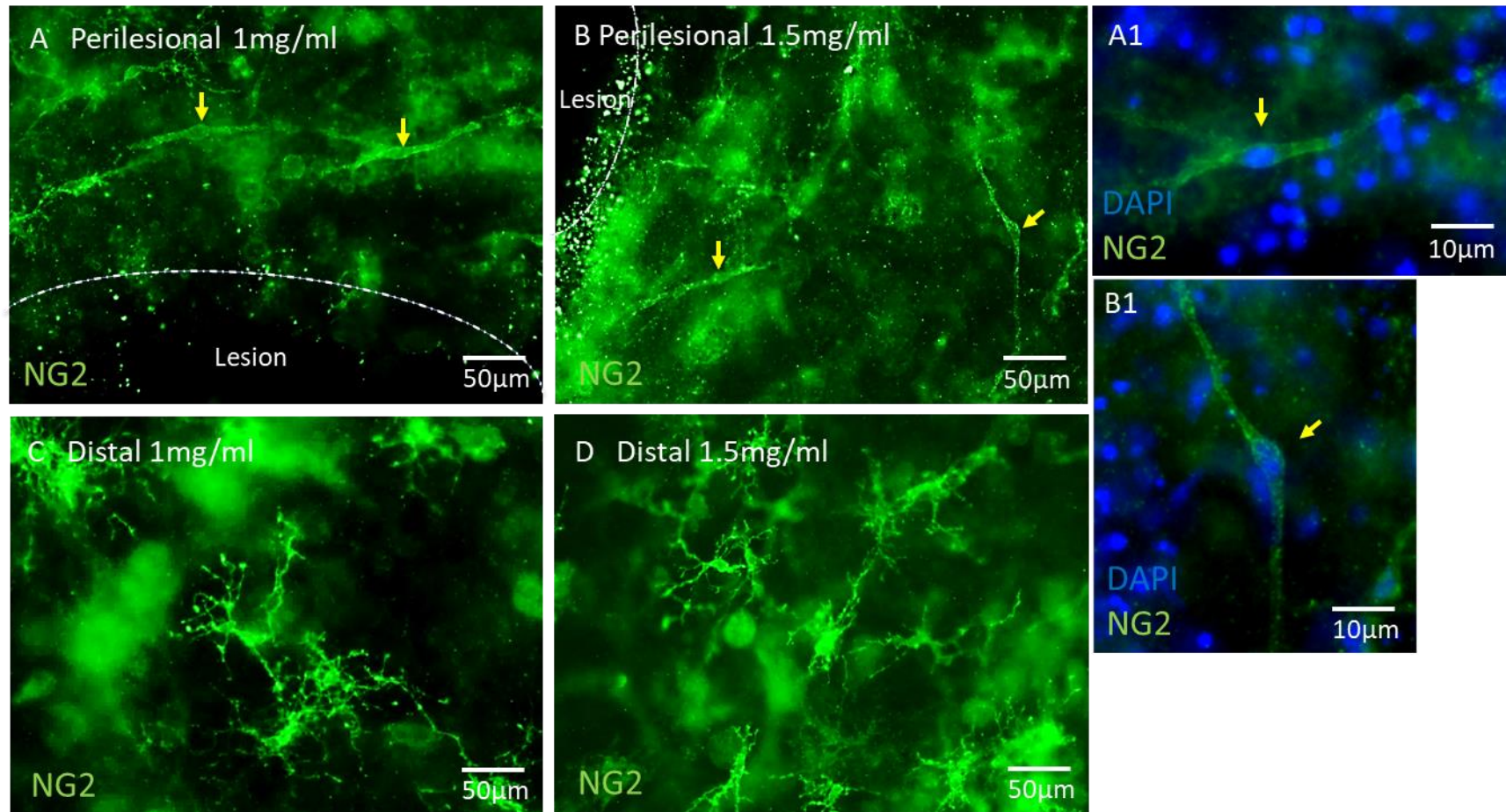
Figure 4.24. NG2+ OPCs show migratory morphologies near the lesion site. A-B representative micrographs of OPC morphology proximal to the lesion. Distinct bipolar migratory morphologies shown (arrows). **A1-B1** shows migratory morphologies respectively from A and B, associated with nuclei (yellow arrows). **C-D** representative micrographs of distal OPC. OPCs express usual multi-processed morphologies.

4.3.5 Implantation of the DuraGen™ into the injury cavity induced OPC and microglial cell responses.

The ability of the 3D multicellular injury model to support the implantation of a biomaterial was assessed as a proof-of-concept and the cellular responses to the implantation investigated. The injury cavity produced left a clear gap in which to implant a biomaterial, carried out immediately after injury. Day 3 post injury, nuclei were detected within the DuraGen™ (inset of **figure 4.25 A**), associated with activated microglia migrating in response to injury and biomaterial implantation. These microglia exhibited rounded and bipolar morphologies (**figure 4.25 A**), indicative of activated migratory microglia. Over three biological repeats, the number of Iba1+ microglia within the DuraGen™ was calculated. On average 106.5 + 7.75 microglia cells were migrating into the DuraGen™ per injury site (**figure 4.25 B**). NG2+ OPCs were observed to exhibit clearly distinctive bipolar migratory morphologies with an orientation towards DuraGen™ implant (**figure 4.25 C**). This may indicate migration towards the biomaterial. Furthermore, bipolar OPCs were observed directly at the gel-biomaterial interface in and around the DuraGen™ (**figure 4.25 C1,C2**), indicating an implantation-induced response. The material appeared to induced no ingrowth of injury-activated astrocytes.
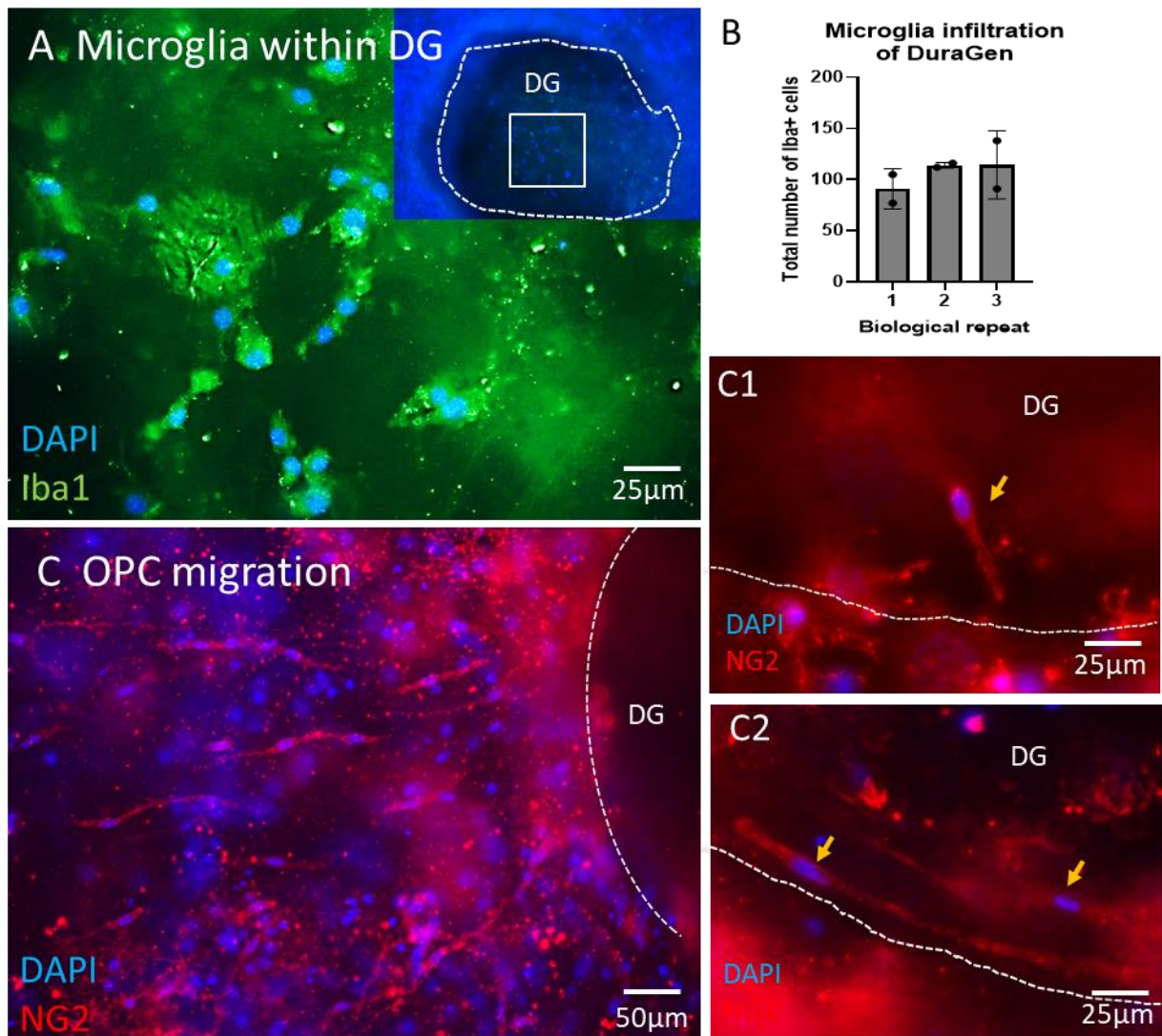
Figure 4.25: DuraGen™ biomaterial implantation induces a microglial and OPC response. A reveals Iba1+ microglia cells migrated to within the DuraGen™ implant. These presented rounded and bipolar morphologies. Inset in A, shows nuclei (DAPI) within the DG (white dotted lines) implanted into the injury cavity. **B** graph showing total Iba1+ cell infiltration per injury implanted with DuraGen™. **C** demonstrates clear bipolar NG2+ OPC morphologies indicating migration to the lesion site with implanted DuraGen™. **C1 C2** bipolar morphologies at the gel-biomaterial interface and possibly extending into the DuraGen™. (3DPL)

4.4 Discussion

As far as I am aware, this is the first time primary postnatal cortical tissue dissociates have been cultured in 2D, whilst supporting a clear transecting focal injury, to achieve assessment of all five major neural cell types. This allows the simultaneous evaluation of the multi-modal cellular response to mechanical disruption and therapeutic agents. Employing this injury model to test nanoparticles, as achieved in this chapter, could provide a new strategy for initial therapeutic testing of nano/biomaterials. Compared with other simplistic or over complicated cellular models, this model has the potential to be a preliminary high-throughput screening platform for other injury modulation or regenerative therapeutic approaches. Furthermore, encapsulating cells within neuro-mimetic substrates has been considered desirable in recent years due to the *in vivo* like microenvironment that is generated by the 3D topography. To my knowledge, this is also the first-time a primary cortical multi-culture has been successfully encapsulated within the 3D collagen matrix with effective demonstration of physiological-like cellular profiles of the five neural cell types. Moreover, the 3D model developed here offers the capacity to support a transecting injury method and mimic pathological mechanisms, with subsequent assessment of biomaterial implantation. Alternatively, given this model encompasses desirable morphologies of the five major neural cell types within a neuro-mimetic substrate, it offers as a versatile adaptable platform for other injury mechanisms, therapeutics and drug testing within the neuro-regenerative field.

4.4.1 Establishing a complete facile multicellular *in vitro* injury model with patho-mimetic injury mechanisms to evaluate therapeutics.

Previously, a pTBI model for high throughput and facile screening of biomaterials was developed within our laboratory. Although the model enables analysis of the key neuroinflammatory responses; the lack of a neuronal component means neuronal responses to therapeutics and regeneration cannot be assessed. Additionally, OPC responses to the focal injury were not documented in this study. As such this neuronal model has been developed by a modification of the tissue dissociation process and a

chemical switch of the growth medium, enabling the multi-culture of all the major neural cell types. Neurons were the most abundant cell type followed by astrocytes and microglia. This protocol shift improved survival and culture of OPCs and oligodendrocytes, and induced growth of a large neuronal network in comparison to our simpler model (Basit et al, 2021). The cell types visualised within this high-density model without injury display morphologies and behaviours comparable to that of the *in vivo* profiles. Additionally, all cell types were consistently widespread throughout the cultures allowing sufficient evaluation of the multiple cell responses.

This multi-culture injury model is particularly useful in modelling post-injury neuronal outgrowth. Axon growth into the lesion area reached an average of 210μm within 24 hours and this almost doubled by 72 hours to around 394μm. This outgrowth was irregular and extended in a random fashion, hence outgrowth from either lesion edge did not converge within the lesion centre. Other models have also observed this relatively extensive neuronal outgrowth, neurons of primary rodent hippocampal cultures were found to reach over 90μm in length within 13 hours (Wissner-Gross et al., 2011), and within a scratch assay of primary neuronal pure culture reach an average of 60μm in just 4hrs (Chuckowree et al., 2003) Although the outgrowth observed in this model does not mimic the pathological features of damage to adult brain tissue, substantial measurable neurite growth from the lesion is ideal for testing the following; i) neuronal efficacy for biomaterial ingrowth, ii) nanomaterial uptake, iii) the direct or indirect effects of therapeutic drugs on neurite growth, or iv) the responses to the many other therapeutic approaches.

The hallmark glial responses observed in this model are consistent with previous studies of pure astrocytes or mixed glial scratch models, organotypic TBI/SCI models, and the findings within chapter 3 of this thesis. (Cernak et al., 2014, Ray et al., 2012, Weightman et al., 2014, Basit et al., 2021).

In addition, OPCs were found to populate the lesion. *In vivo*, OPCs enter the lesion site via proliferation and migration and are known to play a role in neuroinflammation and neuroregeneration (Goshi et al., 2020). Within this study it could not be determined if OPCs were proliferating or migrating into the

lesion site post injury induction. Nevertheless, some lesional OPCs express bipolar migratory profiles at both timepoints, in addition to multibranched non-migratory phenotypes. It is possible that OPCs were proliferating in the main body of the culture proximal to the injury, subsequently migrating into the injury site then become stationary and multibranched. An *in vitro* migration assay of murine OPCs demonstrated radial OPC migration from aggregates on only laminin coated coverslips, reached 400μm distance from the core within 10 hours (O'Meara et al., 2016), therefore migration is likely within our injury model. Local OPC proliferation followed by migration into the lesion is important for subsequent differentiation and myelination of neurons after injury, studying approaches to improve this mechanism is a significant area of research focus (McKnee and Daneshvar, 2015). Here, in conjunction with neuronal outgrowth and the hallmark glial injury responses, our model represents a platform to evaluate OPC responses to injury and therapeutic treatment. Lastly this model comprises around 3% oligodendrocytes, but this cell type showed no obvious response to injury.

Goshi et al., (2020) produced a triculture through mechanical dissociation of day 0 rat cortices. Their tri-culture media was supplemented with additional factors of IL-34, TGF-β, and cholesterol. Although, IL-34 is a supplement applied to enhance microglial viability, their microglial expressed amoeboid morphologies in contrast to our model (Elmore et al., 2014; Obst et al., 2020). It may be possible that in addition to an enzymatic dissociation process, the interaction of all five cell types at high density may be conducive to improved culture condition, the maintenance of ramified microglial. To appropriately understand this, a determined protein and gene profile would be required to confirm the phenotypic status of the microglia within our study. Additionally, the study by Goshi et al. 2020 did not include assessment of oligodendrocytes and OPCs with the multi-culture, despite their significance in neural pathology and regeneration cellular dynamics. Importantly they did reveal that astrocytes and neurons were found to respond differently to neuroinflammatory stimulators and neuro trauma when microglia were present. This reinforces the importance of microglia in the functioning of these mixed neural cultures, and in turn the significance of the micro-dynamics between all neural cell types (Goshi et al., 2020).

In addition, preferential NP uptake by intralesional amoeboid microglial cells is demonstrated, and this was elevated compared to non-activated microglia, showing the importance of assessing nanoparticles on *in vitro* injury models rather than pure cell cultures. Microglial sequestration of NPs *in vivo* is a major barrier to NP based neurotherapeutics, failing to reach their target cell. Here we tested a "stealth" PEG-MNP, which can evade immune uptake (Pinkernelle et al., 2012; Zhang et al., 2012). Our group previously showed decreased microglial uptake of PEG-MNP vs control CMX-MNP (Jenkins et al., 2016) with a significant difference in PEG-MNP particle uptake versus CMX-MNP observed. This study used high purity isolated neural cell populations, and MNPs administration to uninjured cells and thus lacked immunoactivation. In the current model, we simulate acute inflammatory responses comparable to *in vivo* mechanisms, thus observing increased microglial-PEG-MNP activity. As such, these findings should not be considered conflicting.

In summary, a robust, facile, high throughput neuropathomimetic model capable of bioscreening nanoparticles and most likely other therapeutic approaches, has been developed. This model can provide the research field with an ethical alternative platform for preliminary testing prior to animal experimentation. This will help to identify key modulatory or regenerative strategies for brain or spinal cord injury whilst reducing the amount of failed experimentation of strategies in animal models.

4.4.2 Development of a neuromimetic 3D cortical cell construct for injury modelling and therapeutic evaluation.

Modelling neural damage in 3D systems is crucial to closer mimic *in vivo*-specific responses and to identify the disparity between 3D and 2D models leading to development of more effective neurotherapeutic agents. Importantly, this study reveals a significant difference in the cellular morphologies and distribution of some cell types compared to the 2D model, and accordingly highlight the impact of 3-dimensional soft culture substrates on cytoarchitecture and phenotypic expression of primary cortical cells. To further confirm these "healthy" cellular phenotypes supported in this 3D system a gene/protein expression study would have to be carried out

for a full phenotypic assessment. This can also be compared with to the 2D model. In regards to microglial proportions, I propose that the encapsulated microglia are in a reduced proliferative state due to the topographical cues of the 3D environment, therefore resulting in a smaller expansion from the original microglial population.

As previously mentioned, though difficult to visualise through the background/debris staining an extensive neuronal network could be distinguished. However, the 3D neuronal network did appear less dense than the network observed within 2D culture. Initially there were concerns that a primary culture encapsulated within a 3D gel construct would have excessive debris and dead cells that result from the dissociation process. This debris in 2D cultures is cleared over time in culture, however in 3D fibrous materials debris can be lodged within the micro-fibrous nature of the hydrogels. Enzymatic dissociation was proven to reduce initial debris therefore in principle less debris should become entrapped within the gel structure. However, I do believe that neuronal debris from the initial dissociation process could be the cause of the large amount of unspecific staining for TUJ-1. Long neuronal processes are broken down within the dissociation processes while other cell types retract their process and ball up. It is possible that the neuronal staining protocol requires optimisation including attempting different antibodies (i.e. MAP2, NeuN, Tau, Neurofilament) and modifying staining and washing steps. Here we also predicted that all the nuclei unaccounted for (45%) were assumed to be neurons. This assumption may have its limitations as it is possible that the cultures are contaminated with other cell types (i.e. fibroblasts or red blood cells) as a results of the tissue isolation and dissociation process. Nevertheless, the 2D cellular distribution count suggested there aren't any nuclei that are unaccounted for, therefor if these cells were present, it is possible they would be so at such a low percentage it was undetectable. This may be translatable to the 3D model as the same cell dissociation process was used for both studies. To rule out this discrepancy we would need to perform immunocytochemistry for fibroblasts and other potential contaminating cell types.

Mimicking brain physiology through construction of 3D cellular hydrogels is a popular field. Raimondi et al., (2020) conducted a study using primary cortical neuronal cultures entrapped in collagen combined with ECM-proteins. While effective for studying neurons, this "pure" cell element does not offer a complete brain tissue model. In 2020 Raimondi et al. reported a 3D brain-like tissue model from primary cortical cells. In contrast to our model to achieve the multicell culture described, a co-culture of independently isolated glial cells and neuronal cells was carried out. Though this may achieve a 3D multi-cellular environment it is a time-consuming process to prepare

each cell type individually (waiting 20 days to harvest astrocytes from a confluent flask), hence is not a high throughput technique. Giraldo et al., (2020) similarly achieved 3D culture of primary ventral mesencephalic mixed neural cells encapsulated within a biosynthetic hydrogel. Both studies carried out by Raimondi et al. and Giraldo et al. only characterise neurons and astrocytes within their 3D mixed cell models and neither show particularly promising cytoarchitecture of a neural network. An important factor consider for the survival and desired phenotype expression of particular neural cell types in 3D culture is their response to substrates of varying stiffness. Unfortunately, the lack of immediate facilitates within our University for testing the stiffness of materials and COVID19 restrictions in place at the time this did not allow us to measure the stiffness of the constructs we developed. With reference to the literature for an appropriate an answer a pure acellular collagen gel of 2 mg/mL has been determined a modulus of 6 kPa (Dewitt et al., 2009), meaning our construct may be <6 kPa without cells however with the seeding of cells this would probably increase the modulus back to ~ 6 kPa at 7 DIV. This may be the rationale as to why these constructs displayed favourable OPC and astrocyte morphological expression, as these cell types favour a modulus of ~6 pKA (Lourenco et al., 2016).

While there are several injury mechanisms investigated within 3D constructs, a 3D neural brain-like tissue model that studies penetrating injury and biomaterial implantation has not yet been reported. Liaudanskaya et al (2020), reported a controlled impact study on a brain-like tissue model of a 3D cortical neuronal culture, this was through an established impact device. Others involve calcium dependant injury and oxygen/glucose deprivation injury on 3D constructs of primary human NSCs (Vagaska et al., 2020) or the use of a compression device on cortical neuronal 3D hydrogels (Kochba et al., 2016). The results from this chapter, demonstrated a functioning 3D injury model that recapitulated some injury mechanisms previously reported in *in vivo* and *in vitro* organotypic injury models. To my knowledge this is the first time these cellular responses have been reported within a 3D construct model. These key observations were; enhanced GFAP expression, rounded microglial morphology and OPC migratory profiles at the lesion margins. It was also possible to implant the biomaterial into a 3D injury "cavity", here we saw an influx of microglia and OPC migrations towards the biomaterial implant, both these responses could indicate an immunogenic response to the injury. Additionally, we did not observe any infiltration of astrocytes into the implanted material. This was not expected and does not agree with the previous organotypic studies with implantation of the same material. Astrocytes at the injury site require direct close contact of the material to infiltrate their processes otherwise they will produce a glial scar like web of hypertrophic processes

(as observed in the organotypic cultures). The limitation in this study is that the material implanted is not a perfect fit for the 3D injury space meaning a large percentage of the injury may not have the construct-material interface required for activated-astrocytic infiltration. On the contrary there was some microglial and OPC infiltration however it may be possible that these cells can migrate to an area of construct-material and infiltrate the material this way, it is unlikely for astrocytes to behave in this manner. This study may need to be optimised in which cylindrical pieces of DuraGen™ would be cut prior and then implanted into the injury site to ensure a closer match to the injury cavity.

4.4.3 Conclusions

The data presented in this chapter shows it was possible to produce a dense neuronal network along with other major neural cell types within a 2D environment. This culture system was efficiently adapted to a 3D environment which displayed physiological cell morphologies. Following induction of an injury, both the 2D and 3D injury model successfully recapitulated major pathological responses to CNS injury. Both models showed capacity to study delivery of therapeutic agents. Overall, these can offer high throughput testing models for experimental neurology research and can reduce live animal experimentation.

5 Chapter 5: Interfacing injury models with bioelectronic (multielectrode array) systems

5.1 Introduction

5.1.1 The need for *in vitro* electrical interfacing systems

Currently there are major limitations with evaluation of electrical stimulation (ES) for regenerative studies. Firstly, development of ES parameters and understanding the direct mechanism on the CNS parenchyma is difficult to achieve *in vivo*. Since *in vivo* modelling systems are highly complex and observing the effects of ES is not straightforward, the development of ES would require many parameters, timepoints and techniques to achieve suitable assessment. This means many animals would be required for this kind of development study *in vivo*. Sacrificing this many animals for a multitude of parameters it not considered ethical and hence an alternative method is essential. Additionally, the **electrophysiological characteristics of injury environments of are not yet widely understood** hence these require a diverse investigation to facilitate development of a robust ES therapy. Secondly**, most *in vitro* studies of electrical stimulation of neural cells are employed to a non-injury environment, therefore not appropriately modelling the response of injury-activate cells to the stimulus.** Unfortunately, interfacing electrical recording/stimulation systems with *in vitro* traumatic injury modelling systems for the CNS has rarely been reported. An ideal scenario for a robust development would be to incorporate an understanding of the underlying electrophysiological signature of the injury environment in combination with a subsequent investigation into the influence of an electrical stimulus.

When recapitulating brain physiology and the mechanisms of injury within *in vitro* models, it is critical to understand the maturation of neuronal networks and the developmental changes in electrophysiological (EP) activity. For electrically active neuronal cells in 2D environments, recording of electrophysiological data is relatively well established for "pure" neuronal cell cultures (Eytan and Marom, 2006; Spira and Hai, 2013; Obien at al., 2015, Negri et al., 2020). However, an ES assay platform for the study of multicellular CNS models and associated pathologies must fulfil certain criteria namely, to capture network wide neuronal activity within dense mixed cultures of neurons and glia in 2D or 3D

circumstances, to support the assessment of an injury mechanism and post injury-recovery and allow the developmental assessment of ES therapy.

Traditional techniques for EP analysis of neurons in culture include whole-cell patch-clamp recording methods and calcium imaging (Negri et al., 2020). Patch-clamping is achieved through passing a micro-pipette through a cell's membrane without rupturing it. The pipette is sealed to the cell membrane and records signals passing through ion channels within that area (Segev et al., 2016). This technique is time consuming, requires significant skill, and the practice is almost exclusively performed by expert electrophysiologists (Ross, J., 2021). Regardless of the expertise, patch-clamp recordings are still limited. Although patch clamping does enable the measurements of intracellular action potentials (which can be more informative than extracellular recordings) (Kodandaramaiah et al., 2012), only one cell can be recorded at a time and only a handful of measurements can be made within one day. Consequently, this recording approach cannot capture the dynamic synchronous network activity of *in vitro* multicellular neurological models (Ross J., 2021). On the other hand, calcium imaging is an optical technique which measures the levels of Ca^{2+} released by cells. Calcium indicators are applied to cultures (for example, GFP-linked calmodulin molecules) which upon binding to Ca^{2+} ions respond by emitting fluorescence (Negri et al., 2019). This platform provides an indirect indicator of neural activity by measuring changes in intracellular calcium concentrations. However, fluctuations in calcium levels are much slower than individual spiking events and reflect a summation of signals rather than neuronal spike measurements (Wei et al., 2019).

Multi-electrode array (MEA) systems have the potential to record culture-wide activity dynamics through recording changes in extracellular ionic concentrations generated by endogenous action potentials (Aqrawe et al., 2017; Slavik et al., 2019). In addition to recording data, these electrodes have the capacity to electrically stimulate cells in close proximity (Wageneer et al., 2005). MEAs consist of multiple (potentially hundreds) of planar microelectrodes embedded into the base of a tissue culture chamber, allowing for the parallel detection of local field potentials produced by spontaneous or

evoked firing of neurons (Negri et al., 2019). MEAs employ a system which measures the signal difference between recording and reference electrodes, and spikes or action potentials are determined when values deviate from the background potential. Activity within cultures can then be quantified by assessing the frequency and amplitude of spiking events, or the occurrence of synchronised spiking events called "bursts" (Spira and Hai, 2013; Obien at al., 2015). Recordings are non-invasive to the cultures so can be repeated over many timepoints with no detriment to culture integrity. Additionally, MEAs do not rely on other microscopy instruments or fluorescent dyes/proteins that are required for techniques like calcium imaging (Negri et al, 2019). MEAs are also compatible with imaging techniques employing immunofluorescence to reveal cellular morphologies

Despite the long history and increased use of MEAs in recent years, methodologies and novel devices are still being developed. Single-well and multi-well systems that have been developed each having ~60 recording electrodes within one well. These are commercially available from various companies including Axion Biosystems, Med64, Multichannel Systems, Alpha Med Scientific, or MaxWell Biosystems. Additionally, academic research groups are developing MEA systems fabricated in-house, testing varying electrode sizes, electrode/insulator materials and electrode orientation (Xiang et al., 2007; Aqrawe et al., 2017; Pas et al., 2018; Middya et al., 2021).

MEA systems have been predominantly employed in monitoring neuronal firing activity for the *in vitro* application of many human CNS disease models, for example, Alzheimer's disease, Parkinson's disease, schizophrenia, amyotrophic lateral sclerosis (ALS) and epilepsy (Negri et al., 2019; Ross, J. 2021), neurotoxicity studies (Novellino et al., 2011) or non-penetrating injury mechanisms such as excitotoxicity (Mladinic & Nistri, 2013). A comprehensive assessment of multiple MEA systems was carried out across various laboratories (Novellino et al., 2011), this involved the study over 100 experiments before the final conclusions were drawn. The results obtained showed reproducibility of intra- and inter-laboratory experimentation with consistent results in the compounds tested. The outcome of this study highlights that MEA technology is a robust tool with the potential to be the

standard for *in vitro* neurotoxicology/neuropharmacology evaluation (Novellino et al., 2011). **A novel challenge has been to apply this technology to reveal the underlying pathological mechanisms provoked by traumatic injury to the CNS.** The application of MEAs is considered a paradigm for detailed mapping of functional damage and time-dependent evolution of injury (Krishna et al., 2020). To achieve this goal, it is necessary to identify the characteristics of neuronal networks in a model which replicates the complexity of the *in vivo* environment but remains reductionist for developmental analysis. **Currently, these systems have not been applied to an *in vitro* model of penetrating CNS injury.**

5.1.2 Neuronal culture dynamics and MEA-induced electrical stimulation

Dissociated neuronal cell cultures from both embryonic and postnatal rodents have the inherent capacity for spontaneous neuronal activity. Within these reductionist *in vitro* models, as with cortical neuronal cultures, the spontaneous activity can be characterised by a mixture of spikes and bursts, and synchronised bursts lasting from a few to hundreds of milliseconds (Marom and Shahaf, 2002). However, in contrast to an *in vivo* system, there are no afferent sensory inputs or efferent motor outputs. Yet neuronal cultures exhibit patterns of activity broadly comparable to those recorded from developing brains (Zulu et al., 2012). During the first stages of *in vitro* development, dissociated cortical/hippocampal cultures display predominantly irregular asynchronous spiking activity. This activity develops over time, and from the second week *in vitro* spikes tend to cluster into synchronised bursts. This signature feature persists over time in culture representing a mature network state (Brewer et al., 2009; Chiappaline et al., 2007; Maeda et al., 1995). Those bursts have been found to have similar activity patterns to *in vivo* systems where animals are engaged in a motor, sensory or cognitive task (Eytan and Marom, 2006). In contrast, some experts consider that when these persist over a long period of time, this is unlike *in vivo* mammalian activity, and the constant bursting may be due to a lack of input from other brain areas. Nevertheless, in earlier stages of culture there is some degree of comparable functional representation (Wagenaar et al., 2006). It has been noted that spiking and bursting activity

from culture to culture exhibits a high degree of variability, and this can make it difficult to assess these cortical-MEA devices (Zullo et al., 2012).

There have been attempts to modulate such neuronal network dynamics through electrical stimulation. Slow stimulation through individual electrodes has been shown to increase bursting, while rapid stimulation reduced bursting characteristics within cultures of cortical neurons and glial cells (Wagenaar et al., 2006). Additionally, application of electrical stimulation patterns (750 mV 250 μsec phasic pulse) tailored to endogenous readouts has been shown to efficiently stimulate modifications in the network synchronicity, particularly affecting bursting properties (Zullo et al., 2012). Furthermore, electrical stimulation of *in vitro* models have been employed to study epileptic seizures in the human cortex, as the phenomenon of excessive bursting within these cultures strikingly resembles epilepsy (Wagenaar et al., 2006). Electrical stimulation employed through MEAs has been used to elicit spiking activity and control network behaviours in various model systems; including dissociated brain cultures (Jimbo et al., 2000; Gross et al., 1993; Wagenaar et al., 2006), brain and spinal cord slices (Echevarria and Albus, 2000; Tscherter et al., 2001; Mladinic & Nistri, 2013), isolated retina (Maturna et al., 2016) and *in vitro* models of CNS disease (Xiao et al., 2019).

MEA systems employed to study network activity after *in vitro* TBI is poorly documented within the literature. Two accounts of mild TBI on organotypic hippocampal slice cultures have utilised MEA technology for electrophysiological assessment. In both cases, stretch devices are used to recapitulate a mild TBI pathology mechanism, and slices are inverted onto the MEA surface for recordings post-injury (Kang et al., 2015; Effgen and Morrison, 2017). It is unlikely that multiple recordings can be achieved in this system; eventually slices may become damaged from repeated transfer/inversion, therefore only a limited number of recordings can be achieved per slice culture in this system. Besides this, there is very little information on MEA systems employed to study the electrophysiological effect of penetrating injury of *in vitro* cultures. Additionally, the concept of utilising MEAs capacity for

electrical stimulation as a pro-regenerative approach within *in vitro* models of brain injury has received limited attention.

5.1.3   Detection of neuronal activity through MEAs

MEAs record local field potentials (LFPs) and extracellular action potentials (EAPs) simultaneously. Neuronal EAPs are usually from tens to hundreds of µV and are less than 2 milliseconds in duration. EAPs generate ionic fluctuations, and this detectable extracellular electrical field is often referred to as the local field potential (Buzsaki et al., 2012). Microelectrodes detect variances in the LFP generated by current streams of ionic activity closest to the electrode (Quiroga et al., 2013). While this is not restricted to neuronal cells, ionic fluctuations produced by astrocytes are significantly weaker and slower, generating electrical flows lasting for several seconds with amplitude of a few µV. To record these types of signals, electrodes with low intrinsic thermal noise are required (below 1 µV). Thermal noise is defined as the electrical fluctuations that arise from the random thermal motion of electrons. A larger thermal noise will essentially generate a noisy background. In comparison, the thermal noise of commercial MEA systems is typically 10 µV. Consequently, these MEAs are not suited to study the extracellular ionic activity of astrocytes (Mestre et al., 2017). Recording the ionic activity of microglial or oligodendroglia presents further significant challenges as ionic fluctuations are on an even lower scale (Quiroga et al., 2013).

When action potential LFPs are detected at the electrode exceed a determined voltage threshold, they are referred to as neuronal spiking events (**figure 5.1 A**). Several spikes occurring in quick succession with an inter-spike-interval of less than 3 ms (the period between each spike) constitutes a neuronal burst (Lewicki, 1998) (**figure 5.1 A**). Neuronal spike signals exhibit distinct features, including the waveform and amplitude **figure 5.1 B**). Action potentials are generally observed as negative spikes however recordings can also present as positive spiking, it is hypothesised that these signals are detected from electrodes distant from the neuronal cell soma. As spiking events can be negative and

positive an upper and lower threshold limit must be in place for detection. While individual neurons will have a unique waveform, the distance between the signal source and the electrode can strongly influence the amplitude of the signals recorded (Aqrawe et al., 2017). It is essential these spike features are extracted and grouped in order to analyse the communication within a neuronal network. Similar kind of spike detection analysis can be assessed in vivo with MEA wire probes. Furthermore, the threshold value for spike detection must be determined by the user. This value must consider the inherent background noise of the electrodes within the system to ensure signals detected are of action potential origin. Although the global network activity of *in vitro* cultures is spontaneous; this feature can also be evoked, accelerated or modified by particular substances or electrical stimulation (Hales et al., 2012).
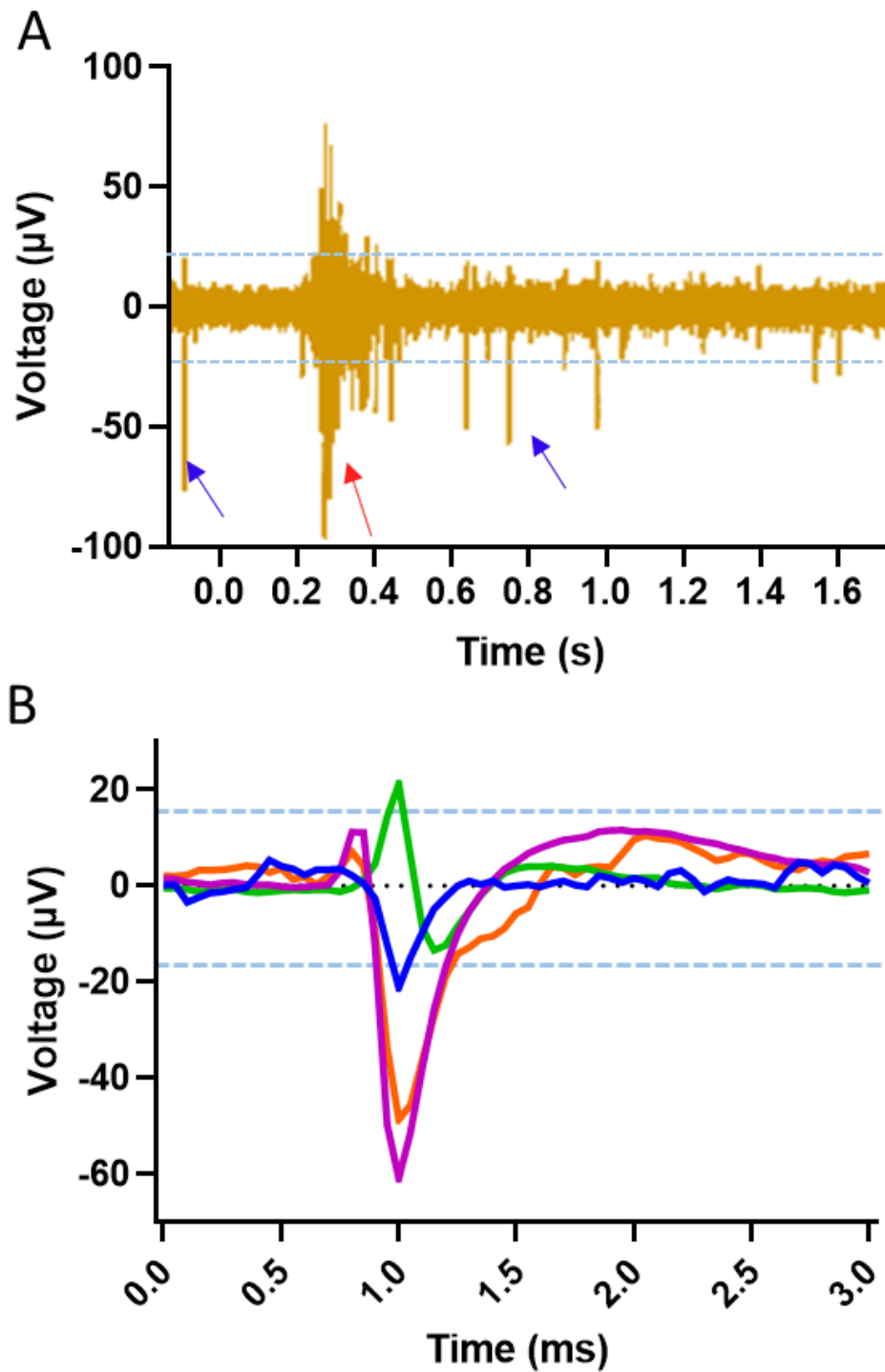
Figure 5.1. Illustration of signals recorded with multielectrode arrays. A 1.6 second recording stream from a single electrode, indicating spikes (blue arrow) and bursts (red arrow). **B** Overlay of spikes of distinct waveforms suggesting separate neurons as the source. Blue dotted lines indicate the signal threshold at which spikes are recognised for extraction.

5.1.4   Objectives

Given the lack of available detail on the global network analysis of *in vitro* CNS models, this chapter will explore the use of MEAs to characterise neuronal network development over time within a primary mixed cell culture. In conjunction with this, a penetrating focal injury will be generated with the culture-MEA system, to study the effect of a penetrating injury on network-wide activity.

For MEA-mediated assessment of *in vitro* brain injury models and possible pro-regenerative electrical stimulation therapy, we refer to this concept as a "patho-MEA".

A proof of principle for a patho-MEA will be determined, showing a penetrating injury can be efficiently generated within cell culture-MEA interface and recordings can be taken at multiple timepoints (pre- and post- injury). Lastly, a pilot study to examine electrical stimulation evoked activity in injured cells will be carried out. The specific objectives were:

(i)   To establish and characterise the electrophysiological properties of the newly developed cortical neuron-glia model over multiple timepoints in culture.

(ii)   To establish a method for the induction of penetrating injury with minimal damage to the electrodes.

(iii)   To evaluate the electrophysiological effects of penetrating injury on the network-wide spike activity, and study post-injury responses

(iv)   To conduct a pilot electrostimulation study, for the investigation of electrostimulation therapy for transecting injuries.

Initially, this was achieved through employing the 2D cortical neuron-glial model previously developed (chapter 4), with two separate MEA systems (as mentioned in section 2.2): bespoke MEA probes fabricated at the University of Cambridge and commercial probes from MED64. As detailed in methods section 2.5 the bespoke Cambridge MEA system failed to produce consistent results and was subsequently removed from the data analyses.

5.2 Results

5.2.1 Interfacing mixed cortical cultures with bespoke Cambridge MEAs

The Cambridge MEA interfaced with the 2D mixed cellular model was trialled and tested over 15 times. This system repeatedly failed to produce spiking activity read outs, even when leaving the cultures to develop over 30 days. In addition, throughout the course of culture only a few recordings could be taken due to the nature of the manual setup; over time the connecting pins began to damage the electrode pads that receive the information. With this system, we achieved only two instance of spike detection starting at DIV 21 (this timepoint was advised to prevent excessive wear of the electrode pads). On day 21, spontaneous spike detection was obtained from 10 channels. On day 23, spontaneous spike detection was obtained from 13 channels (**figure 5.2**). Compared with day 21, day 23 displayed new channels exhibiting regular spiking activity, and some channels appeared to have a complete loss of activity. This result is unlikely to be due to the network changes within the culture over this 2-day period, meaning the observations were not consistent. Combined with the high recording failure rate, this result led to the decision to drop these MEAs from further study.
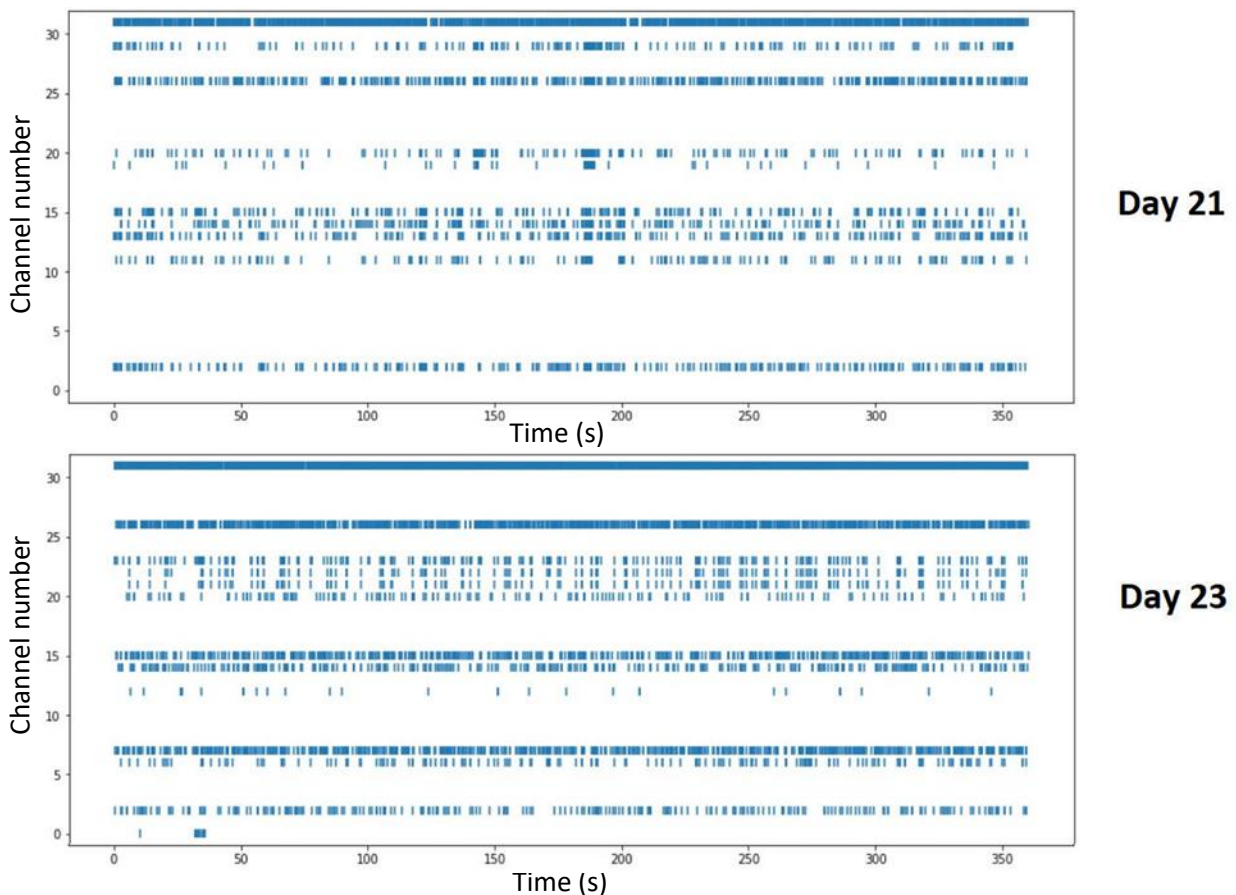
Figure 5.2 Single successful recording output through Cambridge MEA system. 350 second trace raster plot. Strikes indicate single neuronal spiking event. This plots show that at both timepoints around 50% of the channels were detecting spontaneous neuronal firing. However this couldn't not be detected before day 21 or day 23 on this occasion. Spikes could not be detected in any other culture using the Cambridge MEA system. N=1

5.2.2 Evidence of neuronal networks with microglia and astrocytes cultured on MED64 MEA probe

The established 2D cortical neuronal-glial culture system was employed for electrophysiological analysis using the MED64 MEA electrode probes. Cultures were grown for > 21 DIV and monitored using phase-contrast imaging. **Figure 5.3** demonstrates the development of the culture over three weeks *in vitro*. By day 4, dense cellular patches begin to form (outlined in red in figure 5.3). At day 7, a neuronal network is identifiable in addition to the emergence of larger neuronal tract-like structures. By day 14, these neuronal bundle structures are more defined stretching between the denser cellular patches

194

(**figure 5.3** arrows). The overall relationship of these structures can be visualised in the low magnification image at day 21.

To ensure neurons, astrocytes and microglia displayed normal phenotypes in culture at the late timepoint, a quadruple staining of these cell types was performed. The staining shown in **figure 5.4** is represented by two MEA areas; directly over electrodes (**figure 5.4 A**) and adjacent to electrodes (**figure 5.4 B**). These micrographs show evidence for the maintenance of the multicellular 2D culture. GFAP+ astrocytes display fibrous resting morphologies throughout the culture. TUJ-1+ staining shows an extensive neuronal network (many neurites pass over individual electrodes). Microglial staining (Iba1+) over the electrode area was not clear (probably as a result of the electrode substrate), however staining in the adjacent area showed clear ramified microglia. These images indicate that, although this culture was 42 DIV, desired cellular morphologies are expressed including an extensive neuronal network throughout the culture.
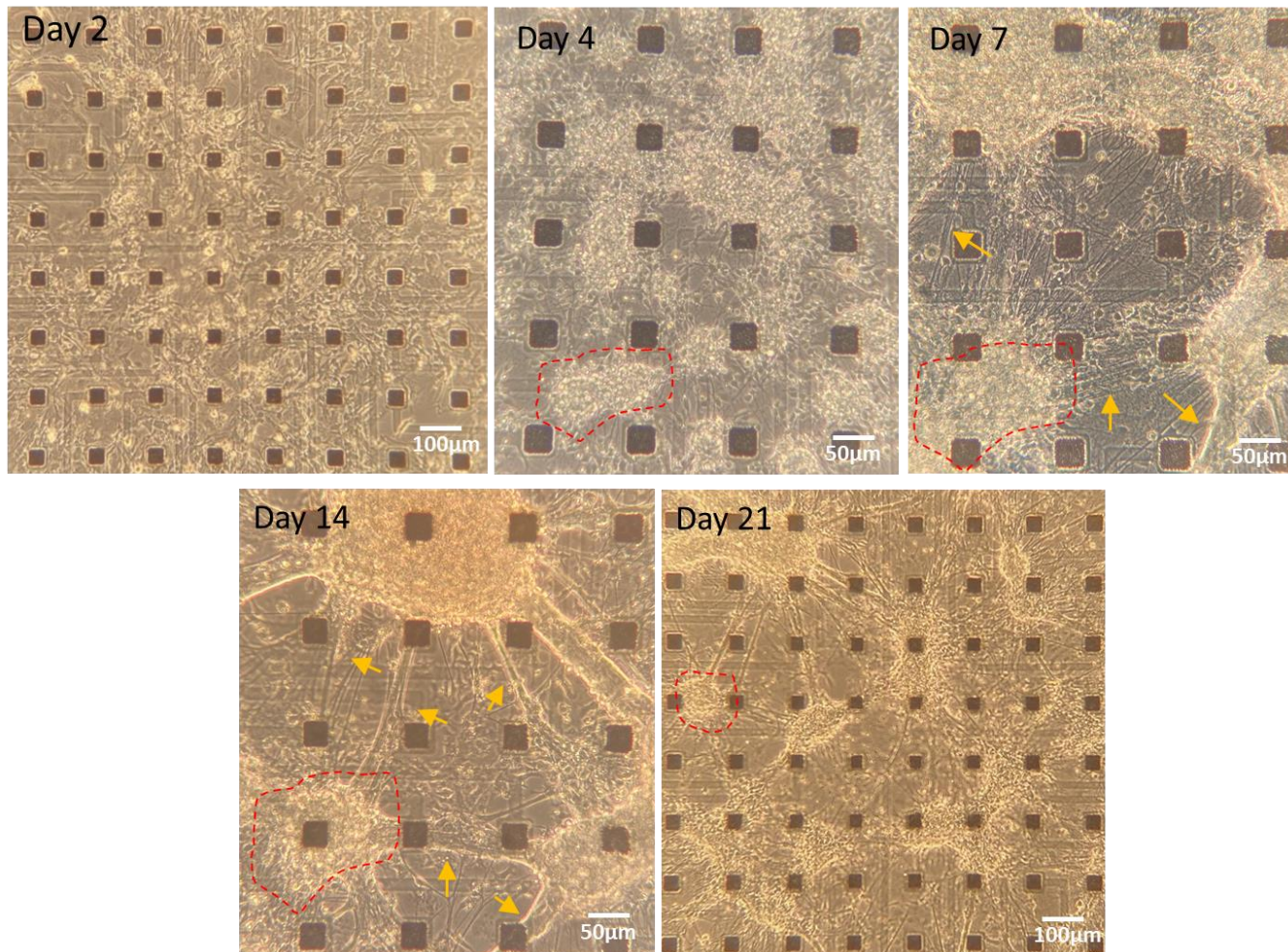
Figure 5.3. Phase contrast micrographs showing the development of the MEA culture over time. Representative micrographs from day 2 to 21, showing the development of the culture. At day 4 dense cellular patches begin to form (outlined in red). Day 7 a neuronal network can be observed with neuronal bundle-like structures forming (yellow arrows). Day 14 these neuronal bundle structures are more defined connecting the denser cellular patches (yellow arrows). Day 21 lower magnification shows the relationship across the whole electrode area.

A <u>Electrode area</u>

GFAP

TUJ1

electrode

Iba1
DAPI

DAPI GFAP
TUJ1 Iba1

50μm

B <u>Adjacent to electrode area</u>

GFAP

TUJ1

Iba1

DAPI GFAP
TUJ1 Iba1

50μm
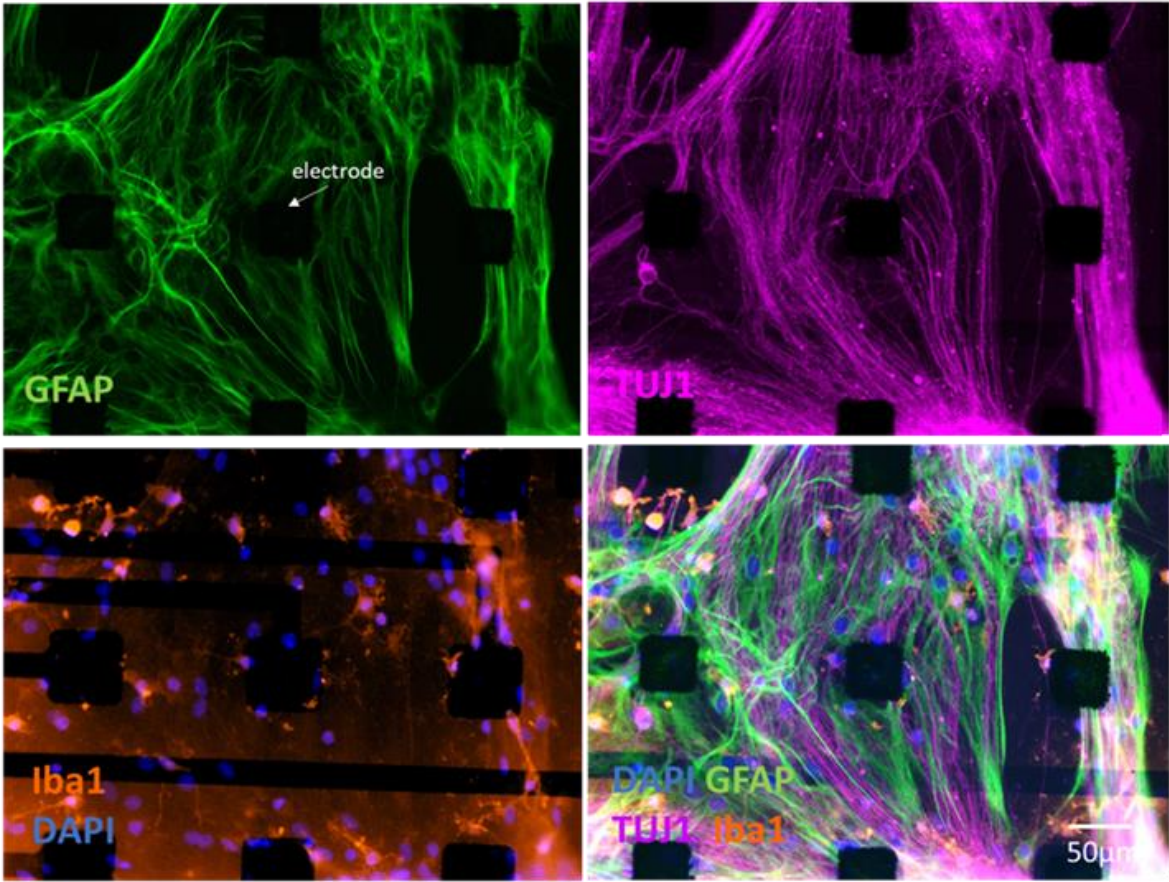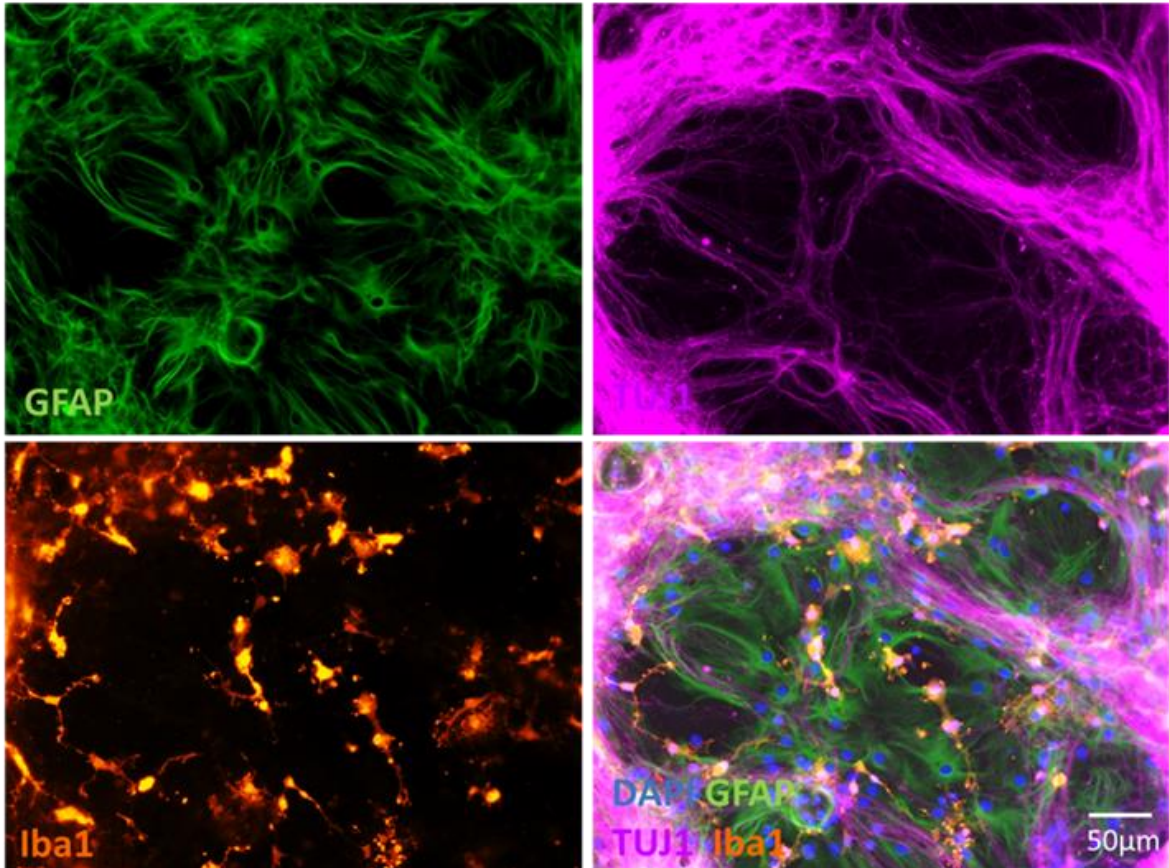
Figure 5.4. Quadruple fluorescent staining of the neuro-glia culture on the MED64 probe. Micrographs reveal GFAP+ astrocytes, TUJ-1+ neurons and Iba1+ microglial cells. **A** staining over the electrode area (dark squares are electrodes, arrow indicates one electrode). **B** reveals of cells adjacent to the electrode area. Images show a widespread neuronal and astrocytic network with processed microglia distributed throughout. Staining carried at out 42 DIV. Scale bar 50 μm.

5.2.3 Electrophysiological characterisation of the cortical multicellular culture

For the MED64 recordings a 3.5 second trace overview of the 64 channels simultaneously was produced, where array wide simultaneous spiking and bursting events can be visualised (**figure 5.5 A**). The data from a 5-minute recording can be extracted and expanded through random representative 10 second traces (**figure 5.5 B**). These traces depict the frequency and amplitude of the spontaneous spiking activity including bursting events. At 7 DIV, there are many small voltage spiking events occurring throughout 10 seconds, with maximum spike voltage reaching 35 μV, but no bursting events (in this particular trace). At 14 DIV, spiking events become more frequent, reaching an amplitude of 95 μV, yet the majority of spikes are around 20 μV, and bursting events were observed. At 21 and 28 DIV, regular bursting events were observed, along with an increased number of higher voltage spikes (maximum 120 μV and 160 μV respectively). Neuronal spiking events occur within milliseconds ranging in their waveform and voltage, and to show this, centroid values (common waveforms from one channel) were extracted and plotted over a 3.5 millisecond timeline (**figure 5.5 C**). These correspond with the typical waveforms of neuronal signals as seen in figure 5.1 and show the rise in spike amplitude over time. Additionally, an array-wide average in spike voltage was calculated for each timepoint, which demonstrated a positive correlation between voltage size and days *in vitro* from 7 DIV (24.25 ± 1.88 μV) to 28 DIV (44.75 ± 1.54 μV (**figure 5.5 D**). Lastly, in the 10 second traces it was evident there was a high frequency of low voltage spikes. To assess the development of high voltage spiking within the cultures, the detection threshold was set to 50 μV, removing the high frequency smaller voltage spikes seen in the 10 second traces. The array wide spike detection rate (ASDR) for spikes above 50 μV displayed positive correlation over time, with the largest increase from 7 DIV (4.3 spikes/sec) to 14 DIV (17.6 spikes/sec) (**figure 5.5 E**).

A
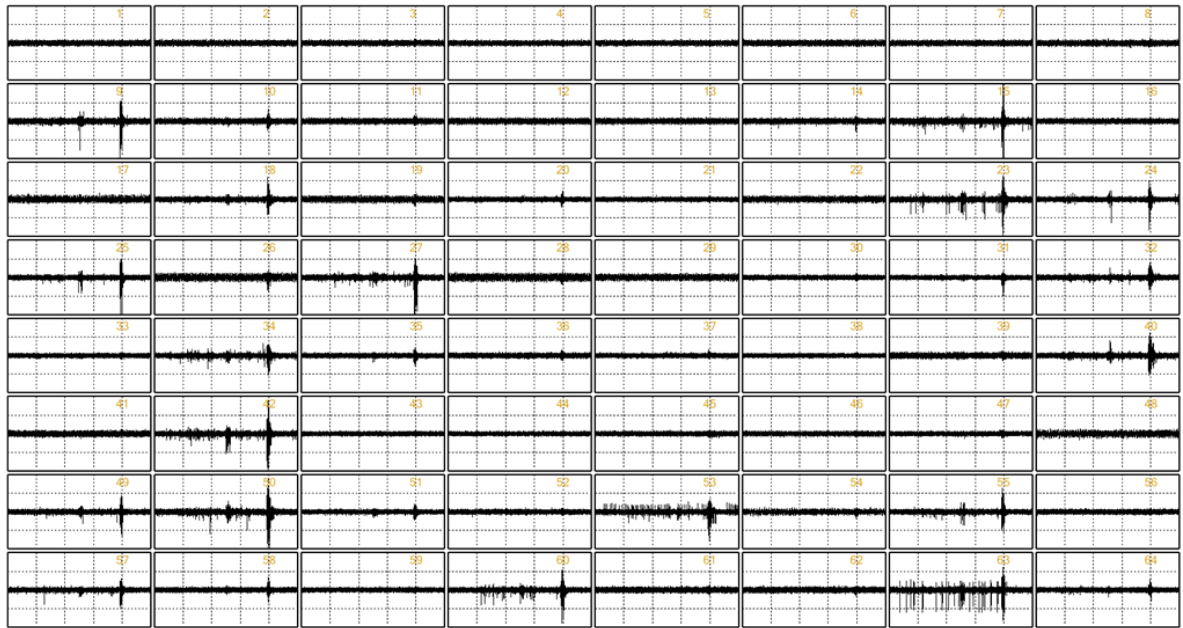
B
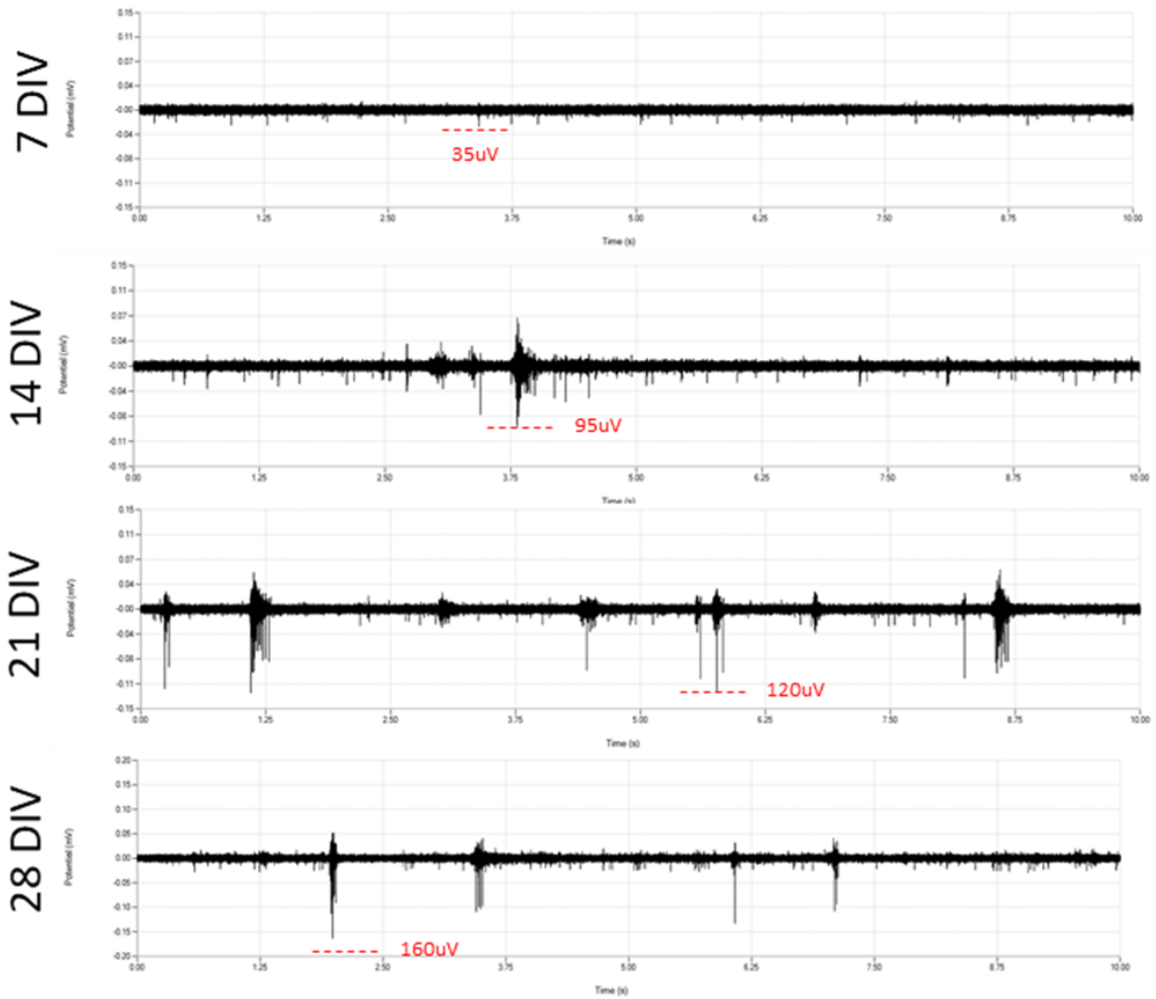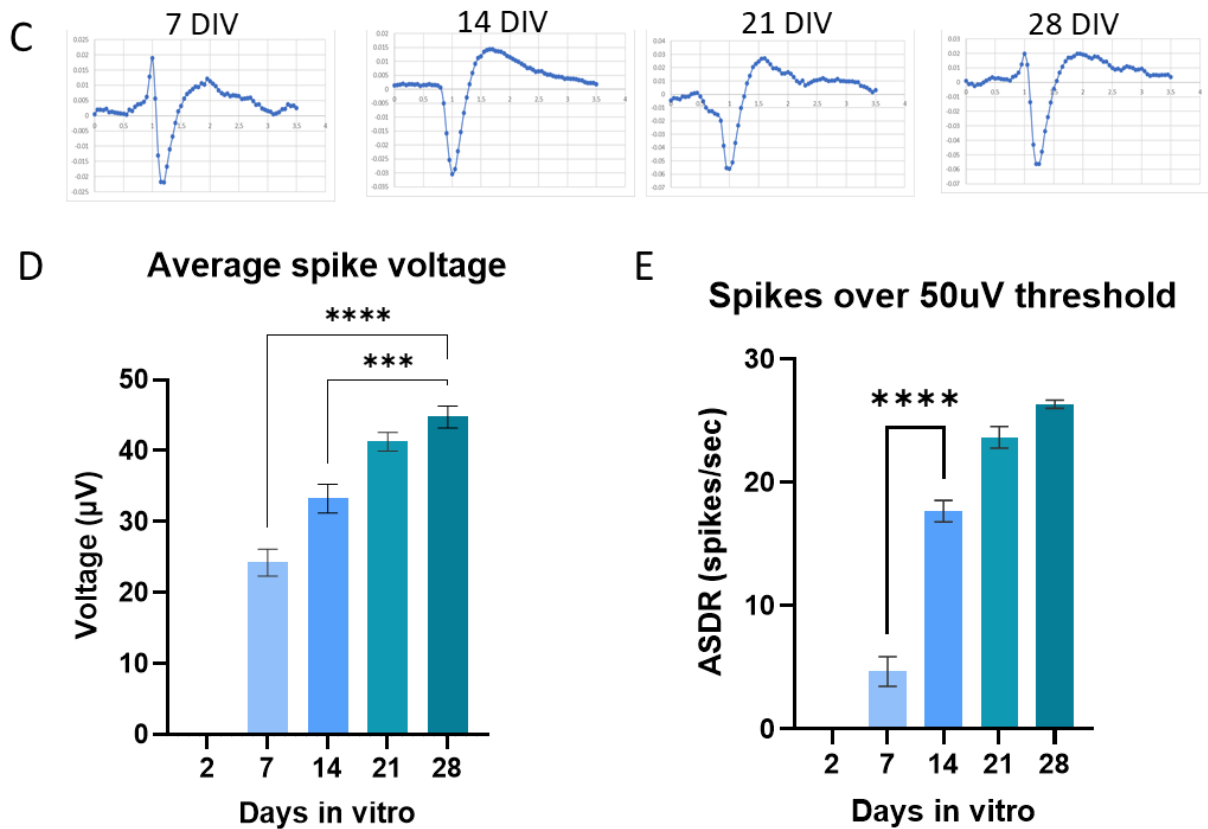
Figure 5.5. Spontaneous neuronal spiking observed over a 28 DIV. A represents an array-wide spiking view over the 64 channels (3.5 second traces), neuronal firing does not occur in all channels simultaneously. **B** shows representative 10-second traces recorded from the same electrode channel over the separate timepoints. This depicts the shift in pattern of activity over 28 DIV. **C** representative waveforms observed within this channel. 3.5 second trace. Voltage axis differ. **D** bar graph shows average spike voltage over DIV (spike threshold = 0.018 V) (n=4). **E** graph shows the array-wide spike detection rate (ASDR) of high voltage spikes (i.e. spikes over 50 μV threshold), showing the largest increase in high voltage spiking is from day 7 to day 14 *in vitro*. [one-way ANOVA with Tukey's, n=4, p<0.001**** p<0.01***]

Spontaneous neuronal spiking detected over the course of the recording can display many waveforms, amplitudes and frequencies, and these waveforms can be sorted into groups. Each electrode can detect signals from multiple neurons and each neuron will fire signals of a particular waveform, due to its signature and spatial relationship to the electrode. These similar waveforms are grouped based on their size and shape; separate waveform groups are most likely to be distinct neurons. The waveform groups shown in figure 5.6 have been given separate colours for explanatory purposes. In **figure 5.6,** there are 4 distinct neurons firing regularly over this electrode by 28 DIV. Initially at 2 DIV there are no signals

extracted from this channel, yet by 7 DIV spikes start to emerge. These extracted spikes/waveforms become more regular and uniform over time in culture, reflecting neuronal development.

Furthermore, an ASDR raster plot can also be used to depict the activity characteristics of the cultures, and these encompass all spiking events from the 64 electrodes plotted against time. Each spike/bursting event is plotted as a mark on the graph; the signals seen on these raster plots are a merge of many spikes due to the long timescale of 60 seconds. At a shorter timescale i.e. a 10 seconds, individual spiking events would be marked. The raster plots for each time point reveal the change in the array wide neuronal spike behaviours (**figure 5.7**), demonstrating the increase in spiking events and global bursting synchrony over time in culture from 2 DIV to 32 DIV. At DIV 2, there is very little activity, yet by DIV 7 there is substantial increase in neural firing observed. Raster plots at 14 DIV appear to be considerably more organised in comparison to 7 DIV plots (in terms of global synchrony). Synchrony is characterised by simultaneous bursting events occurring in multiple channels within milliseconds, as outlined via the orange box in **figure 5.7** 14 DIV. By 32 DIV, the majority of signals are a part of synchronised bursting events.

The average spike frequency and synchronised neuronal burst rates of the separate cultures was quantified and compared. The ASDR follows a general upwards trend over time in culture, reaching 222 ± 27.3 spikes/s at 28 DIV from 0.9 ± 0.6 spikes/s at 2 DIV (**figure 5.8 A**). The greatest rise in ASDR was between DIV 14 and 21. Average spike frequency demonstrates a similar pattern (with slight variances between each biological repeat) rising from 0.1 ± 0.06 Hz at 2 DIV to 5.2 ± 0.05 Hz at 28 DIV (**figure 5.8 B**). Increases in spike frequency were most significant between DIV 7 and 21. A one-way ANOVA statistical test demonstrated no significant differences between the biological repeats. Lastly, each culture appears to have a unique pattern in terms of synchronised burst rates (**figure 5.8 C**), with little uniformity observed across each biological repeat. However, there was yet a general upwards trend of increased synchronised bursting over time in culture. The most substantial developments in global synchrony events are observed between DIV 7 and 21.
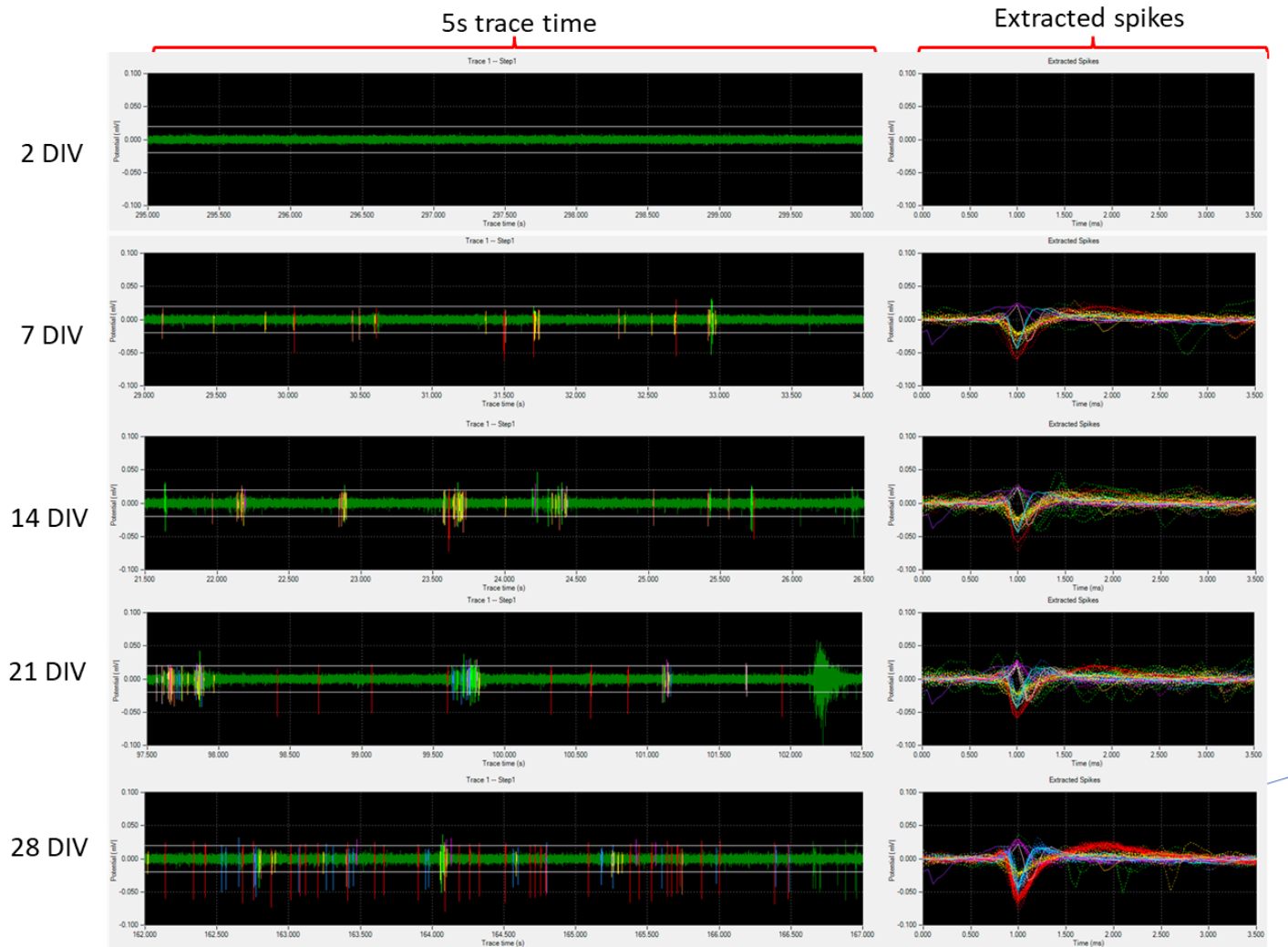
Figure 5.6. Progression of neuronal waveforms recorded at one electrode over four weeks *in vitro*. The lefthand panel '5s trace time' shows spontaneous spiking occurring over 5 seconds. Spiking appears to become more regular and larger in voltage over the 3 weeks in culture. The righthand panel showing extracted spikes reveals recorded waveforms that are grouped by similarity. Separate colours identify separate neuronal waveforms and each waveform group is likely to be a distinct neuron.

Figure 5.6 continued... By 28 DIV 4 distinct neurons are firing regularly. Dotted lines indicate the waveform detected. Solid lines indicate the centroid waveform of each neuronal group.

Figure 5.7. Array-wide 60 second raster plots from the same culture over 32 DIV. These spike detection plots show an increase in spontaneous spike frequency, bursting and synchronicity recorded from 64 electrodes. Yellow box indicates one of the many synchronised bursting events.
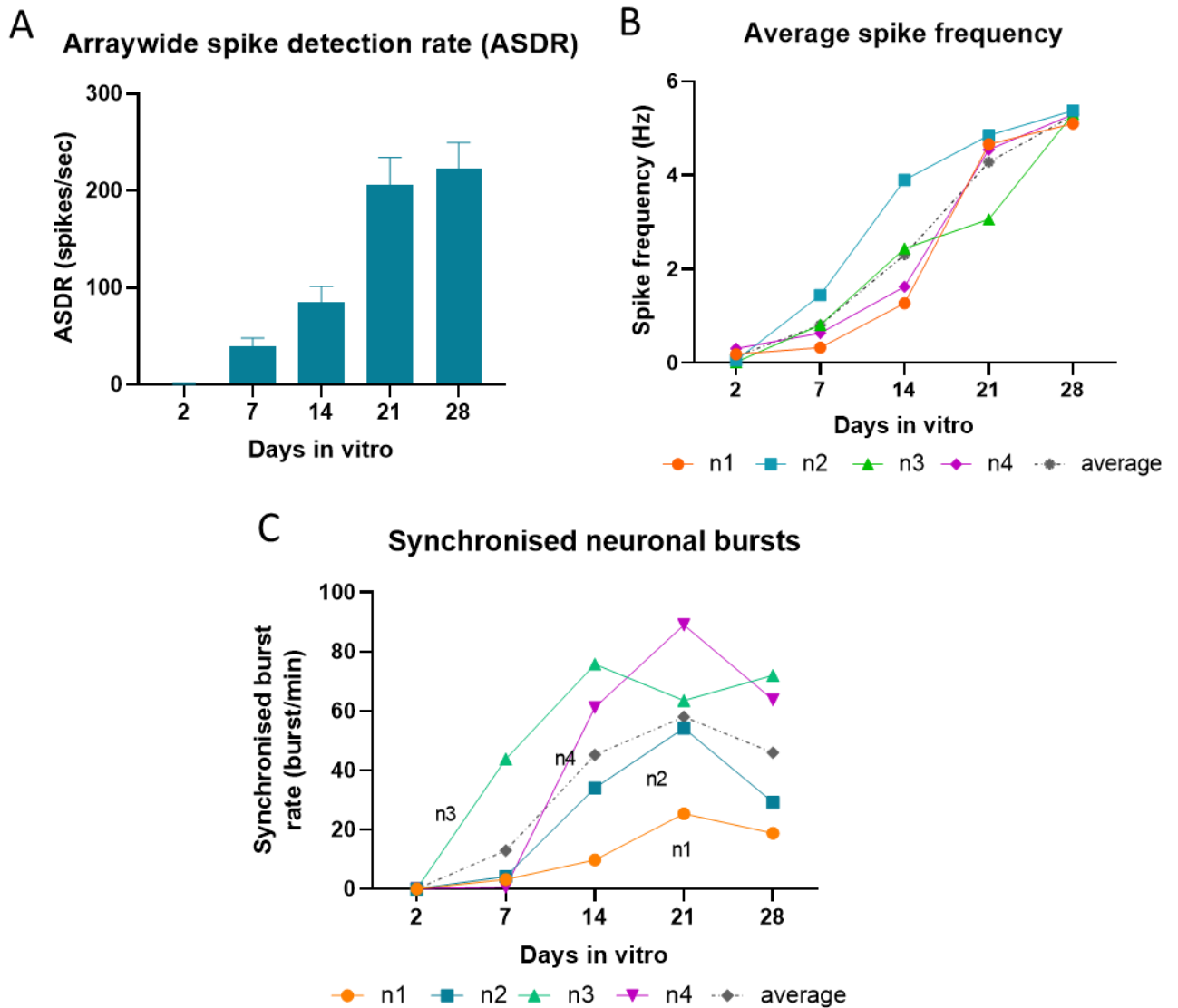
Figure 5.8. Spontaneous neuronal spiking and synchronised burst analysis over days *in vitro*. A Graph showing the array-wide detection rate (spikes/second) increasing over the 28 days *in vitro*. **B** Graph showing a positive correlation between spike frequency and days *in vitro*. **C** shows the synchronised burst rate over time (synchronised bursting events/minute). Global bursting synchrony is relatively unique per culture, however there is a general positive trend over time. N1-4 represents separate biological repeats.

5.2.4   Tetrodotoxin application blocks spiking activity

TTX application to neuronal cultures is often through a perfusion system where the TTX is progressively added over the culture to diminish neuronal activity. In our system, TTX must be added manually to the culture through a medium change. Adding TTX to the medium means an even distribution of the

chemical. However, as media changes are known to disturb the electrical activity of neurons, a sham treatment was tested in parallel (media change without TTX). Hales et al., advises not to take neuronal recordings within the first 24 hours after a media change (Hales et al., 2010). Recordings were taken pre- and post-treatment (sham: **figure 5.9A and B**; TTX: **C and D**). Raster plots show the array wide change in the level of activity. Activity (spiking and synchronised bursting events) was dramatically reduced by the sham treatment compared with the pre-treatment (**figure 5.9 A and B**). However TTX application appeared to abolish activity completely, which was maintained for at least 15 minutes (**figure 5.9 D**) (figure 5.8 D shows the last minute of a 15-minute recording). Post removal of TTX, the activity within the culture resumed to an expected level (**figure 5.9 E**). To put this data into perspective for comparison purposes, a proportional reduction in relative ASDR and synchronised bursting was assessed. The sham treatment reduced activity to 18.5% of the ASDR and 11.2% of global synchrony, while the TTX treatment blocked all spiking and bursting activity (**figure 5.9 F**). Data recorded at 4-days post TTX treatment displays a similar profile to pre-TTX signals, showing the TTX-induced reduction in activity was not due to neuronal toxicity. Both the sham and TTX treatment assessment indicate that the recorded electrical activity is of neuronal origin.

5.2.5   Patho-MEA proof of concept; establishing an injury mechanism and the electrophysiological characteristics of injury

After the characterisation of the electrophysiology of the multicellular culture over time, a focal injury was induced at 32 DIV as described in section 2.5.6. The electrode area pre- injury, 0hr post- injury and 4 days post-injury is shown in representative phase contrast images (**figure 5.10 A-C**), and electrode channel 36 is starred throughout as a reference point. Upon lesioning within this system a full transection could not be complete on both occasions, leaving a small section of connecting tissue (**figure 5.10 B**). At 4 days post injury, the lesion width doubled in size, most likely reflecting a response of the perilesional tissues retracting away from the injury site. Raster plots (**figure 5.10 D-F**) highlight

the impact of injury on spike detection levels. Prior to the injury, cultures displayed high numbers of spiking events and global synchrony throughout the majority of channels (**figure 5.10 D**). The injury was made between the central rows of electrodes, and the red dotted lines on the raster plots illustrate the positional relationship of the injury to the electrodes (**figure 5.10 E**). A complete loss of activity was observed within the electrodes between the injury margins with a large reduction in electrical activity detected in electrodes on either side of the injury. Lastly, activity appeared to be reduced in the remaining electrodes away from the injury. Electrodes adjacent to the injury (indicated by the yellow box) regained some degree of activity after 4 days post injury (**figure 5.10 F**). However, within the injury area, one channel appears to re-establish activity post injury (channel 36). Channel 36 lies under the section of un-lesioned tissue which connects the two sides of injury (refer to figure 5.10 B-C). Furthermore, to quantify the neuronal activity response to injury, an average ASDR was plotted against the synchronised bursting rate. Immediately after injury there is a large drop in global spiking rates, and after a 4-day recovery period this activity increases (**figure 5.10 G**). Interestingly, there is no major difference in the synchronised burst rate. Bursting synchrony was investigated further by looking at the number of spikes within the synchronised burst events. This was dramatically reduced immediately post injury and with only a small increase after 4 days (**figure 5.10 H**), meaning synchronised bursting events are still occurring but with a lower number of neurons firing together. Additionally, high voltage spiking rates were investigated (**figure 5.10 I**), which dropped dramatically immediately after injury, and recovered somewhat post injury, however there remained a generally lower level of high voltage spikes post injury.

The injury area of one MEA probe was quadruple stained for astrocytes, microglia and neurons at 4 days post lesion (**figure 5.11**), (channel 36 is starred for reference) to identify injury responses. Hypertrophic reactive astrocytes at lesion margins and infiltration of amoeboid reactive microglia were identified. At this timepoint, there was no visible outgrowth of neurites from the injured tissue.
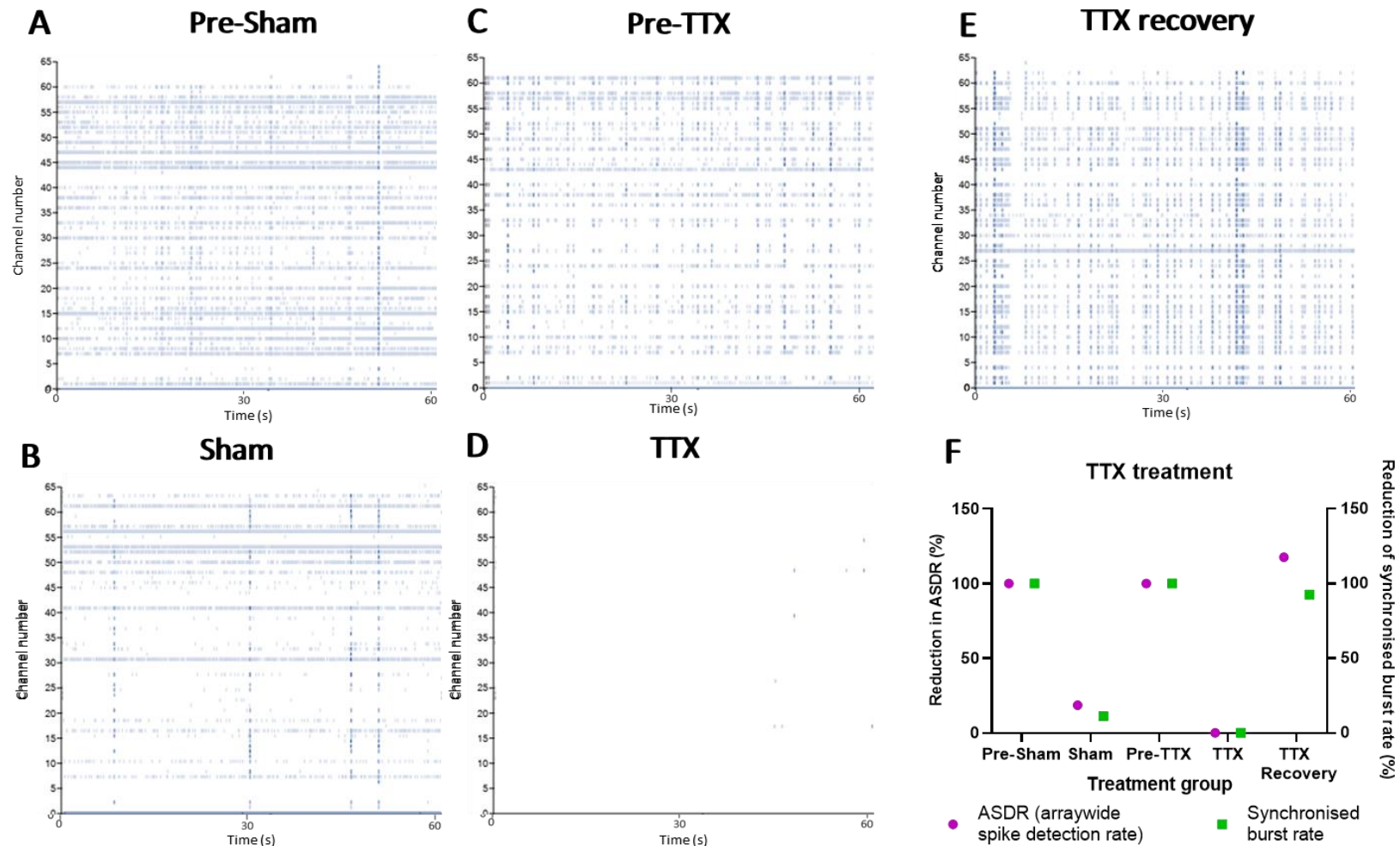
Figure 5.9. Tetrodotoxin application blocks action potentials, proving spike detection is of neuronal origin. Raster plots in **A-E** show the spike detection over 60 seconds from 64 channels. **A** spike detection prior to sham treatment. **B** spike detection 15 minutes post sham (50% media changed without TTX). **C** spike detection prior to TTX treatment. **D** spike detection 15 minutes post TTX treatment. **E** spike detection 4 days post TTX treatment showing the recovery of the culture. **F** graph showing percent reduction of the array-wide detection rate (ASDR) vs synchronised bursting rate from each recording (spikes per second). N=1
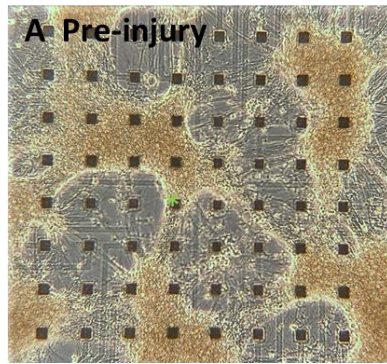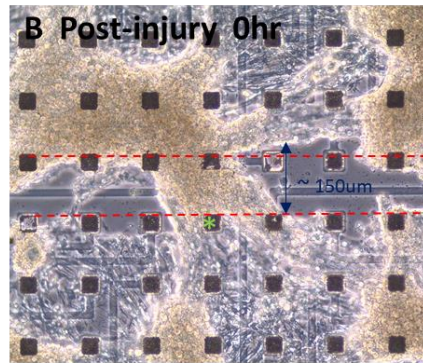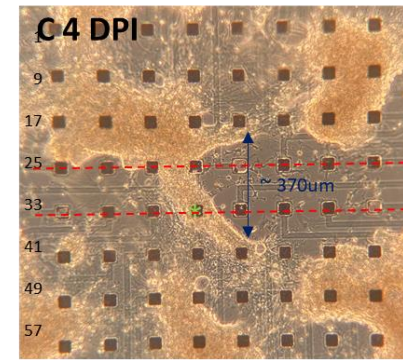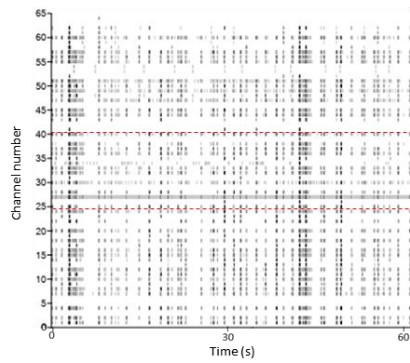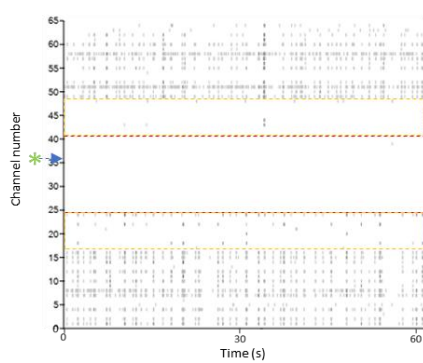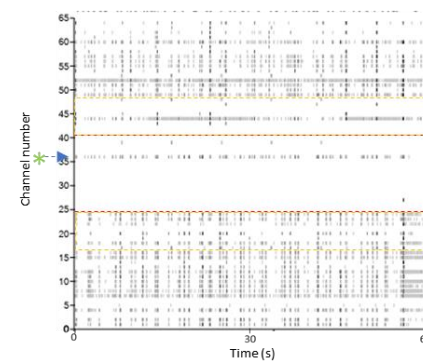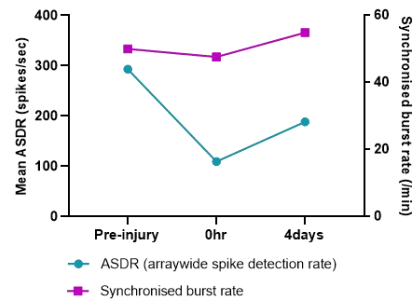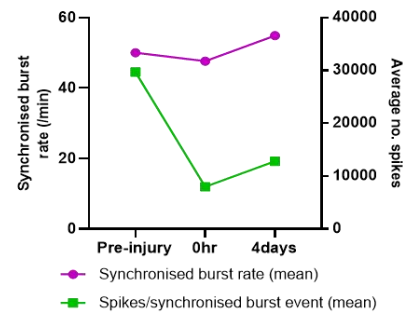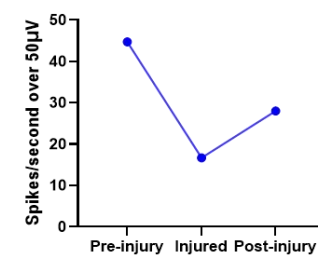
Figure 5.10. Establishing a mechanical injury mechanism and the injury-induced impact on electrophysiological properties of the culture. A-C representative phase contrast images show cellular characteristics pre-injury, 0hr post-injury and 4 days post injury (DPI) respectively. **D-F** representative raster plots showing neuronal spike detection pre-injury, 0hr post-injury and 4 days post injury respectively. Red dotted lines signify the position of injury over the electrodes. Orange dotted line indicates the electrodes adjacent to the injury site. *Channel 36 is starred for reference throughout. **G** shows the change relative array-wide spike detection rate and synchronised burst rate post-injury. **H** demonstrates the relationship between average synchronised bursting rate and the average number of spikes per burst event. **I** illustrates the change in high voltage spiking. n=2 Injuries was inflicted at 35 DIV.
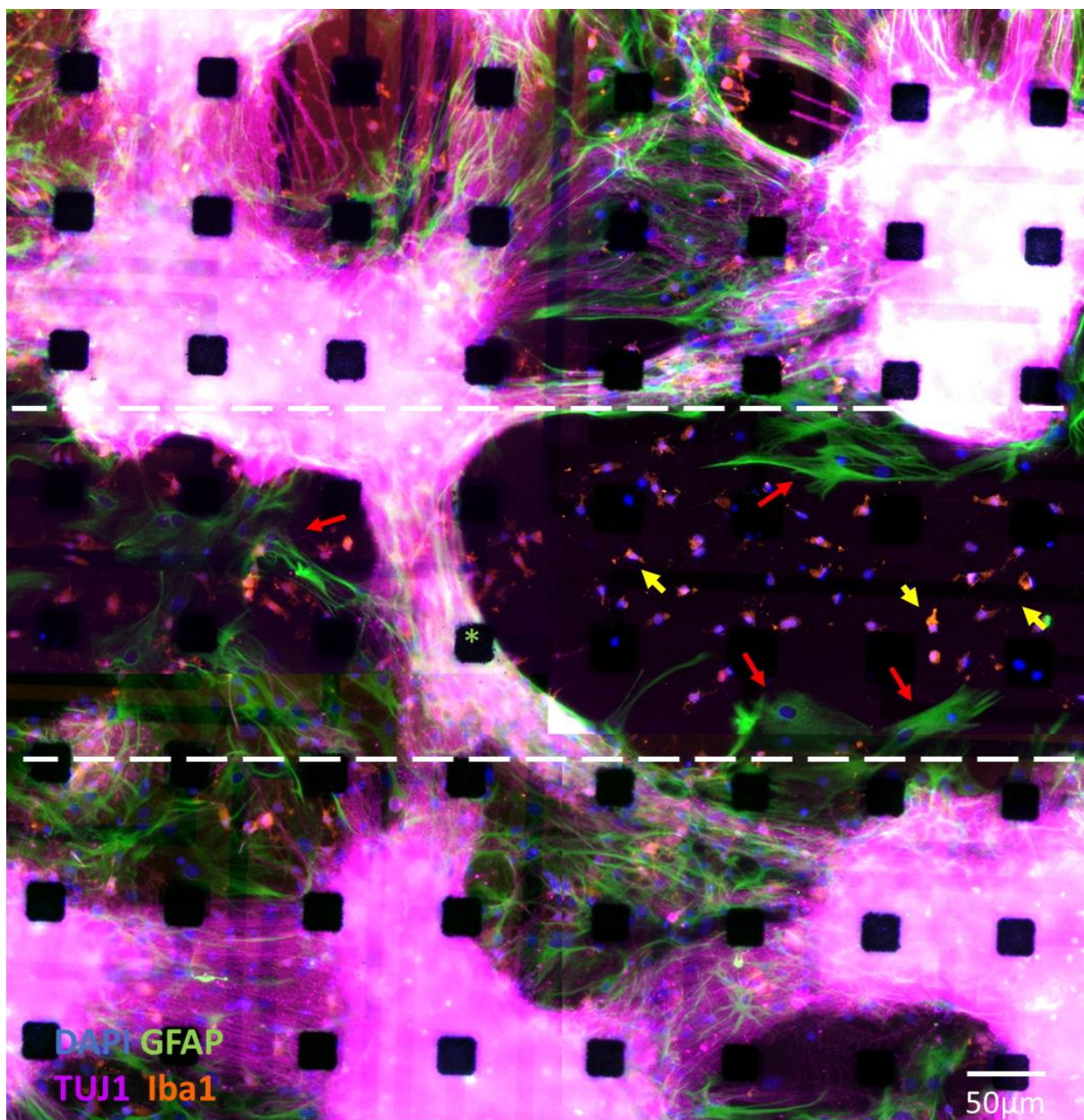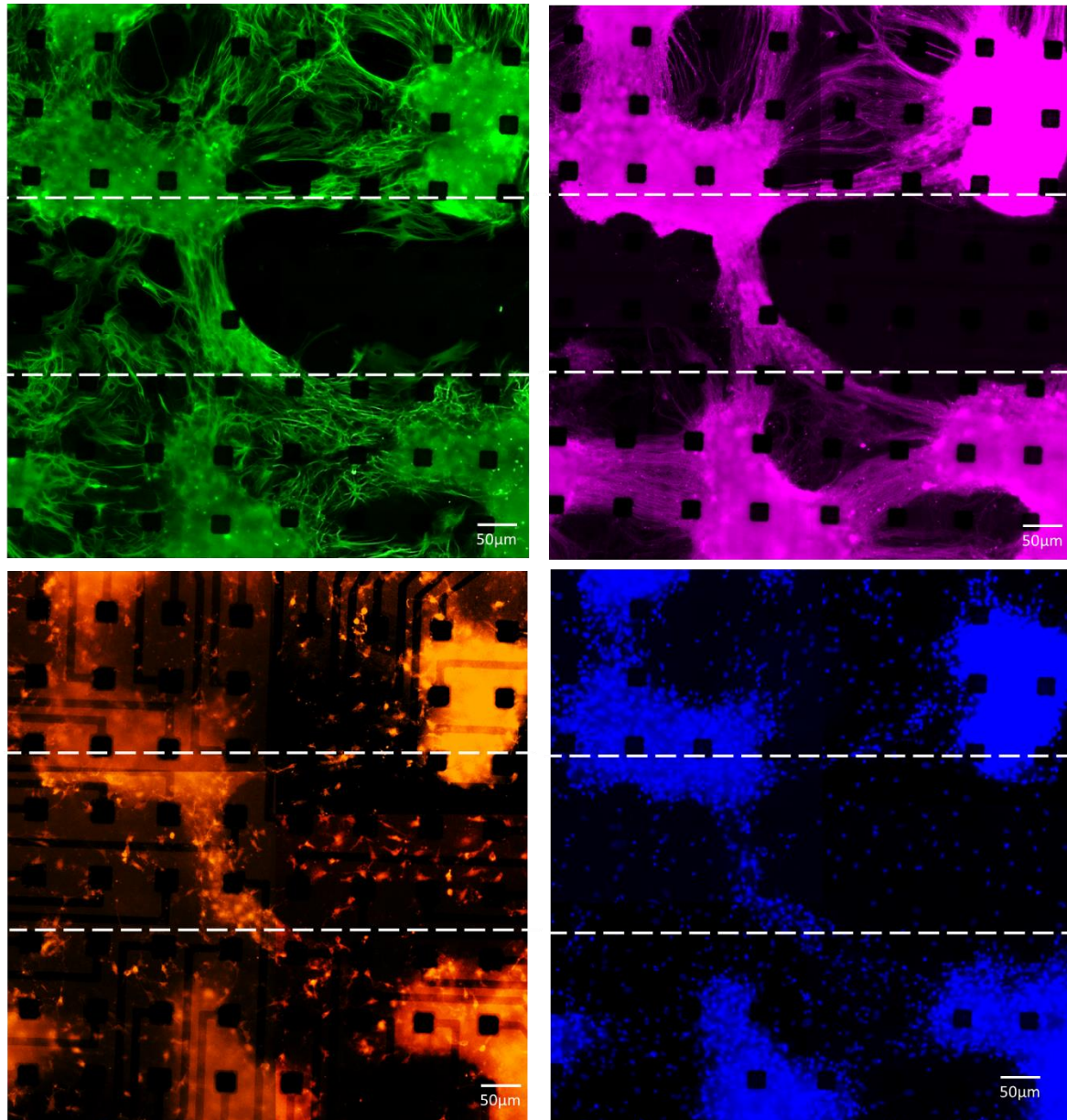
Figure 5.11. Quadruple immunofluorescent staining of electrode area 7 days post injury. First panel: Red arrows indicate typical hypertrophic reactive astrocytes within the injury site. White arrows indicate infiltration of reactive amoeboid microglial cells. No neuronal outgrowth is observed at this timepoint. Second panel of images shows individual staining. All these images are 4 separate images stitched together.

5.2.6 Electrical stimulation of the mixed cortical culture: pilot study

Lastly, a pilot study was carried out to investigate whether electrical stimulation (ES) within the system could evoke neuronal spiking events. Electrical stimulation (200µA, 1Hz for 5 minutes) was delivered through one electrode and this elicited detectable signals in all channels, shown by a large voltage spike

(blue arrows in **figure 5.12 B**). By expanding the electrical readouts from an active channel (spontaneous spiking without ES) (channel 24), a stimulation-induced spiking response could be observed. Spontaneous firing alone could also be observed in this channel (**figure 5.12 C**). Comparing this response to a channel with no spontaneous spiking data i.e., no active neurons nearby (channel 10), ES induced a small residual change in the voltage only. All active channels displayed an evoked response to ES. This stimulation evoked a small bursting event on average lasting for ~24.5 milliseconds, and the spikes in these bursts were typically all over 50 µV the maximum voltage reached was 230 µV. We do appreciate that these cultures were stimulated at 80 DIV rather than the ideal time period at 35 DIV when the injuries were induced, unfortunately due to a break down in laboratory reagents and equipment results in delays towards the end of this experimental work and due to time constraints, this could not be performed with newer cultures at the relevant timescale. This issue also applies to the explanation behind only having an n=2 for the injury over the MEA cultures. However, these were proof of concept studies and valuable information was gathered.
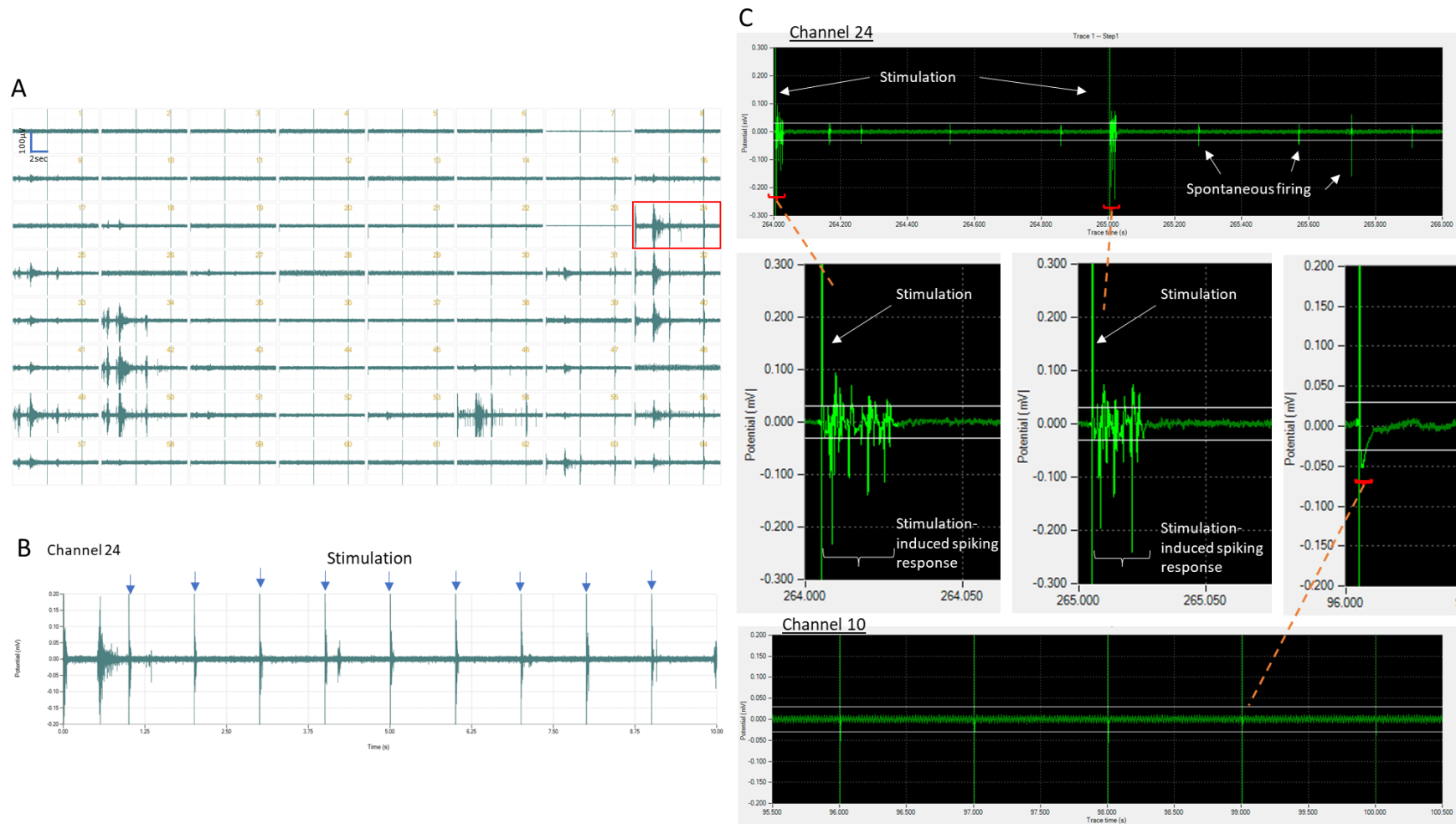
Figure 5.12. Electrical stimulation pilot study. 80 days *in vitro*. **A** 10 second traces from an array overview of 64 channels. **B** expanded view of the 10s trace of channel 24. Blue arrows indicate stimulation. **C** demonstrates stimulation-induced spiking from a channel with neuronal activity (channel 24). Expanded views of the spiking shows induced spiking for a short period of time immediately post stimulation. These spikes can be of similar amplitude to spontaneous spikes. Channel 10 had no detectable spontaneous spiking. When subject to stimulation a small residual change in voltage is observed, yet no stimulation-induced spiking. Channel 24 X axis = 2 second trace from 5-minute recording. Channel 10 X axis = 5 second trace from a 5-minute recording.

5.3 Discussion

To my knowledge, this is the first demonstration that a new, complex *in vitro* model of TBI, can be interfaced with an MEA system, to study pre and post-injury responses. Despite some inter-culture variability, electrophysiological development of the cultures followed a common trend over time. A transecting lesion was effectively induced through the central rows of electrodes (100 μm gap), with proof of principle for the analysis of the electrophysiological profiles of neuronal networks post injury. Additionally, a pilot study demonstrating evoked action potentials through electrical stimulation was shown in cultures aged 80 days *in vitro*. Employing this multicellular brain injury model in combination with an MEA system could provide a strategy for understanding the electrophysiological impact of transecting injuries at various ages of the dissociated tissue, with application to a range of traumatic neurological injuries. An added benefit of this system is the capacity for the analysis of possible pro-regenerative effects of long-term electrical stimulation studies, combined with delivery of therapeutics (such as functionalised biomaterials) to the injured system.

Prior to electrophysiological analysis of the transecting injury model, a comprehensive characterisation of the neuronal network behaviour was necessary to establish a baseline of cellular electrophysiological features between cultures, which required assessment over multiple developmental timepoints in culture. Observations were broadly uniform across cultures at 2 DIV, where cultures showed almost no spiking activity. By day 7 all cultures had begun considerable array-wide spiking activity and this continued to rise over weeks in culture. Other studies have reported neuronal activity to begin around 4 DIV from embryonic dissociated cortices and progresses over time, this trend has been observed in multiple cultures. In addition, there is a consensus in these studies that *in vitro* preparations of hippocampal or cortical neurons are said to reach a mature level at 3-4 weeks of culture (Bakkum et al., 2014; Brewer et al., 2009; Chiappaline et al., 2007; Maeda et al., 1995; Kamioka et al. 1992). The gradual increase in array-wide spike detection rate, the average spiking frequency, and the synchronised burst rates within our study all suggest an increased level of maturity towards 28/32 DIV. Spiking at early DIV

was sporadic and unorganised and became progressively more organised with time. Older cultures present very little random spiking and signals occur in large simultaneous bursting. Wagenaar et al. (2006) also reports a in cortical neuronal culture, that burstiness steadily increases over time, until bursting dominates all activity at 20-25 DIV. After this the bursting fluctuated for as long as they observed (up to 45 DIV) (Wagenaar et al., 2006). Furthermore, the average spike voltage dramatically increases over weeks in culture and large voltages are believed to indicate more maturity within the culture (Zulu et al., 2012). ASDR, spike frequency, synchronised bursting events and spike amplitude developed primarily between 7 and 21 DIV. This suggests that culture maturity predominantly develops in this period, and in terms of the timepoints for application of potential treatments this is something to consider; i.e. application may be intended for fully mature cultures or developing cultures. Another study claimed a rapid maturation between DIV 5 and DIV 12 of a primary cortical rat culture. However, these cultures were not characterised post DIV 12 and hence are probably missing valuable information regarding culture development past 12 days (Cotterill et al., 2016). Our longer-term study shows that culture dynamics are still changing up to 3 weeks in culture. This is important for injury modelling and determining ideal times for injury induction to replicate *in vivo* scenarios and pathologies.

Following this developmental characterisation of the neuronal cultures, an injury mechanism was established. The focal injury generated over the MEA system provided an understanding into the immediate impact on the neuronal network activity. It was also noted on both occasions that the lesion gap doubled in size post injury, indicating a retraction of the tissue at either side of the injury. This response could be due to the age of tissue in culture, where reduced tissue plasticity results in retraction rather infiltration into the lesion site observed with younger tissue. However, the aim of this study was to established the electrophysiological readings pre- and post- injury and to determine their characteristics through data analysis therefore tissue age was not a limiting factor in these experiments. After injury some spiking and bursting synchrony was restored in the injury and neighbouring area. While a high global bursting synchrony was still detected, these bursts contained a largely reduced number of spikes per burst. This could mean that though some network synchrony is maintained the

injury dramatically reduced the numbers of neurons firing together, indicating a large network disturbance. It is also possible the connecting neuronal tissue is the electrophysiological link between the two sides of the injury, allowing the global synchrony to continue in this case. As the LFPs of *in vitro* penetrating or transecting injuries has not yet been measured, it is currently difficult to interpret our findings within the context of wider studies. Although a proof-of-concept was proved here, it would be beneficial to further investigate the neuronal connections effected at varying injury induction timepoints, over a longer period of time post injury and with more biological repeats.

As these cultures undergo substantial development through to 28 DIV + it would be interesting to observe the potential effect of injury on neuronal network signals at different stages of development, and whether this corresponds to a degree of neurite outgrowth from the lesion site. When transecting injuries are made at DIV 7, there is significant outgrowth from the lesion edge, whereas at DIV 32 shown in this chapter there is no observable neuronal outgrowth. It is well established that younger neurons have a higher regenerative capacity (Al-Ali et al., 2018), and will show neuronal outgrowth from a transecting injury. DIV 32 neurons have most likely lost their inherent regenerative capacity due to their age in culture or "maturity", it is well documented within the literature that neurons lose their regenerative capacity with age (Belin et al., 2014). It is possible that the degree of neurite outgrowth from injury is associated with the level of bursting events and network synchrony within the culture at the given timepoint. Younger cultures may show distinct electrophysiological features to injury because of their unorganised spiking nature. It is likely that DIV 7 would show the most outgrowth in comparison with the later timepoints and there could be particular "immature" spiking patterns that facilitate this inherent capacity for regeneration. Considering this, using ES-mediated patterned control (as performed by Wagenaar et al.) it could be possible to transform the organised signals detected in older cultures back to the unorganised spiking characteristics observed at DIV 7, to enhance regeneration. Wagenaar et al., describe a method for controlling particular parameters i.e. voltage-control can evoke determined responses of dissociated neurons in culture, influencing bursting and random spiking events. Here the electrical stimulation (100-900mV with pulse widths of 400 μsec and frequency 0.5-

10 stim/sec) that was used determined that evoked spiking events occurred in the first 30 ms post-stimulation (Wagenaar et al., 2006). This is directly in line with our finding of post-stimulation responses occurred in the first 25 ms. This highlights that expected evoked action potentials can be achieved through this system and in turn the potential to control of network characteristics and influence neurite outgrowth. Alternatively, rather than neuronal patterning, the ES delivered within this system could enhance neuronal outgrowth after injury as described in section 1.5.

5.3.1   Ideal patho-MEA design

In this study, a commercial MEA was employed to study an *in vitro* model of cortical injury, however there were significant challenges. An injury was made between the central electrodes (a 100-micron gap) this was technically challenging and required a high degree of precision. In an ideal situation, the central electrodes would be separated by a larger inter-electrode space in which a more efficient reproducible injury mechanism can be generated. This would also prevent potential damage to the electrodes during the injury process. The large inter-electrode space would generate two distinct sides of injury with 32 electrodes on either side (**figure 5.13 A-B**).

As MEAs can provide a stimulation, this could be utilised to enhance neuronal outgrowth and regeneration over the injury area. Additionally, ES in this circumstance has the potential to reduce glial scarring, reduce immune response, and facilitate re-myelination of the regenerated axons within this *in vitro* system (highlighted in section 1.5). Enhancing neurite outgrowth is a particularly attractive feature of ES and development of such therapy could be achieved through this patho-MEA platform. Another design feature would be the capacity for a one-sided stimulation. For example, only one side of the injury would be stimulated, therefor a direct investigation on whether this ES would facilitate one-sided neurite outgrowth within the mixed culture could be performed (**figure 5.13 C**).

Furthermore it may be beneficial to further optimise the lesioning tool for this patho-MEA to ensure a complete transecting injury can be made if necessary for the study.

5.3.2 Interfacing 3D *in vitro* models of the CNS with MEA systems

While electrophysiological data is largely established for 2D environments (Obien at al., 2015; Segev et al., 2016; Negri et al., 2020)., the development and optimisation of recording/stimulation electrode devices for 3D cellular constructs is an emerging field of research (Frampton et al., 2011). As mentioned in chapter 4, there are fundamental benefits observed when considering cellular relationships in a 3D environment. Since the recording of cellular electrical signals or stimulation of cells relies on electrodes contacting the target cells, an intricate 3D electrode system would be necessary to achieve the positional relationship required for efficient network recording and stimulation.

Commercial electrodes penetrate 50-100µm into tissues and are often cone shaped (Raimondi et al., 2020). In respect to cellular gel constructs, this would not extend deep enough into the gel to effectively record signals. Additionally, electrode penetration could potentially damage cells in the proximal vicinity. Therefore, it would be essential for preloaded cellular hydrogels to polymerise in situ around the 3D electrode system. Soscia et al. developed and validated an integrated 3D microelectrode array of this nature. This system consisted of ten flexible polyimide probes of the length of 1100µm (Soscia et al., 2020), with 8 electrodes per flexible probe (**figure 5.14**). This results in 80 recording electrodes per array and has the potential to analyse cell loaded gels up to 1000µm in thickness. This system would be ideal to test the electrophysiological development of the 3D multicellular cortical model developed in chapter 4. Here the 3D multicellular gel construct begins as a solution and subsequently polymerises encapsulating the cells within its matrix. In order to significantly advance the utility of 3D neuronal models, novel MEA designs are necessary to capture networkwide electrophysiology of neurons in a 3D *in vitro* matrix. For example, 3D neuronal constructs in multi layers of microbeads placed over a planar MEA probe produced considerable differences to their 2D counterpart. Frega et al. 2014, showed that their simultaneous 2D and 3D cultures differed in terms of synchronised bursting. At 4 weeks, the 2D hippocampal preparation showed predominantly synchronous bursts typically of amplitude 100 µV and a duration of 300ms. In contrast, their 3D culture had developed less global synchrony yet more random

spiking and random bursting. Bursts were of similar amplitude (100 µV) but longer in duration (up to 1 second). This team concluded that the 3D environment resulted in a more complex network, contributing to the wider and longer interactions. They hypothesised that this contributes to the desynchronised and temporally differentiated network activity, hence bursting confined to sub-populations, rather than a global synchrony (Frega et al., 2014). Nevertheless, as a planar MEA was employed in this system, and this cannot depict the true signal dynamics of the 3D construct as the electrodes do not penetrate through the 3D environment. In this sense, they are taking a more two-dimensional measurement of a three-dimensional network.

5.3.3   Conclusion

In vitro cortical preparations are fundamentally different from in-vivo networks in terms of anatomy and synaptic connections; nonetheless they provide a rich environment when interfaced with MEA systems in which external manipulation, electrical stimulation, and signal recordability allow investigation of controllable and reliable aspects of the central nervous system. This chapter provides proof of principle data supporting the concept and need for development of a sophisticated patho-MEA system in which the electrophysiological features of an injury model can be investigated, to aid discovery science into efficient ES patterns and parameters for successful neurite regeneration.

.
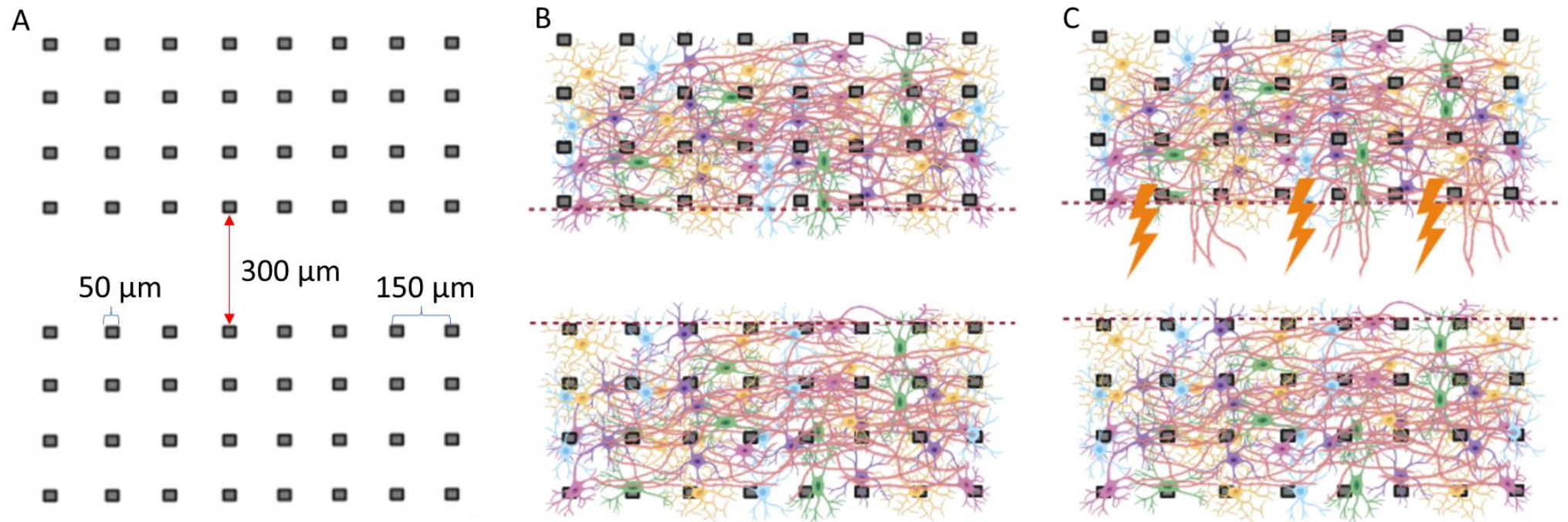
Figure 5.13. Schematic design of a patho-MEA interfaced with an *in vitro* injury model. **A** design dimensions of the 64-electrode array. **B** multicellular culture with injury over patho-MEA design. **C** potential one-sided electrical stimulation feature for regenerative assessment.
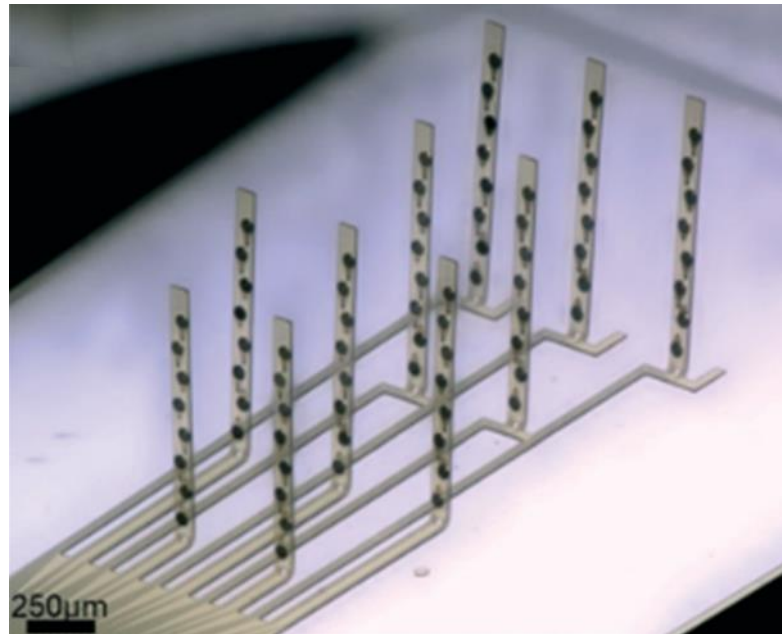
Figure 5.14. Bespoke three-dimensional MEA probe for *in vitro* **brain constructs.** Taken from Soscia et al 2016.

6 Chapter 6: Final conclusions and future directions

6.1 Summary of key thesis findings

Chapter 3: Implantation of a neurosurgical grade scaffold into organotypic models of traumatic CNS injury.

- Both scOSC and bOSCs subject to a penetrating focal injury can efficiently mimic the pathomechanisms of CNS injury and show comparable responses.

- These organotypic models represent important platforms for biomaterial testing prior to the use of animal models which when produced side by side provide an effective system towards the reduction of animal usage.

- The neurosurgical biomaterial DuraGen^{TM} promotes a pro-regenerative environment when implanted into the lesion site.

Chapter 4a: Developing an *in vitro* 2D cortical multicellular injury model.

- Enzymatic dissociation methods generate cultures with higher density neuronal networks and fibrous astrocyte morphologies.

- The cortical mixed cellular injury model can allow the simultaneous assessment of the 5 major neural cell types which show comparable pathomechansims to *in vivo* injury.

- Injury-activated microglia have elevated nanoparticle uptake.

- Nanoparticle uptake is not enhanced in other neural cells types within the injury environment.

4b: Developing a 3D neuro-mimetic cortical construct with induction of traumatic injury.

- A soft collagen hydrogel with high seeding density can successfully support a mixed cellular cortical culture with morphologies similar to *in vivo* phenotypes – generating a 3D brain tissue model.

- An efficient penetrating injury mechanism of the 3D brain construct was developed, and hallmark responses of injury were observed.

- The injury mechanism also allowed for biomaterial implantation and analysis of pathological responses.

- Electrophysiological activity of the 2D cortical multicelluar model was appropriately characterised over 3 weeks.

- An injury mechanism was achieved over the multielectrode array and electrophysiological events of injury were assessed.

- The cortical culture responded to evoked electrical stimulation (a pilot study for further ES).

6.2 Implications of findings and future research directions

This thesis has established and analysed three distinct *in vitro* techniques for modelling neurological injury for the developmental testing of therapeutic strategies. This thesis aimed to reproduce a facile, high throughput injury modelling system, which also acts in accordance to reduce the number of animals where possible. **Table 6.1** summarises the repeats generated per culture system. The 2D mixed cortical culture not only is the most facile technique but offers the highest throughput model generating around 60 repeats per average litter (8 pups). The increase in repeats increases the number of potential treatments to be screened simultaneously and increases the number of parameters that can be assessed per experiment.

The OSCs generate the lowest number of repeats per litter however, if both the brain and the spinal cord tissues are collected simultaneously this increases the utility and ethics of the model. This means responses can be compared between both tissues which is very useful for the development of interchangeable therapeutics between CNS tissues (Zhang and Gensel., 2014). However, processing both tissues simultaneously can be problematic to achieve and is relatively time consuming compared with the 2D and 3D cortical models. The data in chapter 3 shows comparable responses apart from the pathological event in which injured brain tissue (at 4 DIV) did not produce any neuronal outgrowth with or without the biomaterial implantation. This highlights the potential differences in these CNS tissues

and the necessity to analyse both independently for therapeutic strategies. Interestingly, dissociated cortical tissue from similar age postnatal mice displayed vast neuronal extension in culture thus producing a dense neuronal network (chapter 4). Additionally, after injury at 7 DIV a relatively extensive neuronal outgrowth from the lesion edge was observed. Retaining some neuronal outgrowth is desirable as a clear distinction can be determined between a positive and a negative effect on pre-existing neuronal extension. This model therefor is more favourable for the assessment of neuronal behaviour.

	Organotypic spinal cord slices	Organotypic cortical brain slices	3D hydrogels from mixed cortical cultures	2D mixed cortical cultures on glass coverslips
Seeding density	na	na	2.5×10^7	1×10^6
Slice thickness	350µm	350µm	na	na
Repeats per average litter (8 pups)	~18	~24	~30 wells	~60 wells

Table 6.1 Details of how many repeats are obtained from the three *in vitro* modelling systems.

In regards to the assessment of cell morphologies and responses to injury the 2D and 3D gel constructs were simpler to assess in comparison with OSCs due to the compact cellular composition of slices. The culturing process and the injury mechanism were found to be more straightforward within the gel constructs and 2D cultures. Although both the 3D and 2D cultures systems efficiently recapitulate some vital mechanisms of injury, the 3D environment may be more advantageous when considering the responses most comparable to native tissues and the representation of physiological cell morphologies.

Due to the higher through put nature of the 3D constructs, easier experimental procedure whilst retaining cellular complexity makes this an important development for *in vitro* therapeutic testing. As this model would be adaptable to other injury mechanisms and therapeutic strategies, it would be

interesting to assess cellular responses through different inducers of neuroinflammation or other injury mechanisms. It would also be an effective model for drug screening. One drawback within this model is the visualisation of neurons within the construct. Optimisation of this element would be a next step towards a successful complex high throughput *in vitro* model. An additional benefit to this system would be to interface this with a 3D MEA system that can appropriately measure electrophysiological characteristics of the culture and injury.

Although the original goal of this thesis was set out to develop a system for an electrical stimulation therapy, this could not be achieved in the given time frame. Nevertheless, the fundamental preliminary study characterising the injury model itself has provided the scope for a robust study on stimulation at separate points of injury and what this means for the multicellular dynamics this model encapsulates. This patho-MEA concept is completely novel and has the potential to understand the complex dynamics of electrical stimulation as a therapy for injured tissue. Whether that be a reprogramming of the cortical cells into a state of plasticity through ES pattering or a physical stimulation that initiates neurite outgrowth and attenuates other pathological processes. Furthermore adaptation to other 3D modelling systems as studied in this thesis would mean there would be potential for a combinatorial approach, where biomaterial implantation can support the neurite outgrowth initiated through the ES. An additional area of interest for the 3D models would be to analyse the electrophysiological signature of biomaterial implantation and how the culture dynamics change.

Appendix 1: Article published by Neural Regeneration Research

Raja Haseeb Basit, Jessica Wiseman, Farhana Chowdhury, Divya Maitreyi Chari

Simulating traumatic brain injury *in vitro*: developing high throughput models to test biomaterial based therapies

Review

Simulating traumatic brain injury *in vitro*: developing high throughput models to test biomaterial based therapies

Raja Haseeb Basit[1, 2], Jessica Wiseman[2, 4], Farhana Chowdhury[3, 4], Divya Maitreyi Chari[4, *]

From the Contents

Abstract

Traumatic brain injuries are serious clinical incidents associated with some of the poorest outcomes in neurological practice. Coupled with the limited regenerative capacity of the brain, this has significant implications for patients, carers, and healthcare systems, and the requirement for life-long care in some cases. Clinical treatment currently focuses on limiting the initial neural damage with long-term care/support from multidisciplinary teams. Therapies targeting neuroprotection and neural regeneration are not currently available but are the focus of intensive research. Biomaterial-based interventions are gaining popularity for a range of applications including biomolecule and drug delivery, and to function as cellular scaffolds. Experimental investigations into the development of such novel therapeutics for traumatic brain injury will be critically underpinned by the availability of appropriate high throughput, facile, ethically viable, and pathomimetic biological model systems. This represents a significant challenge for researchers given the pathological complexity of traumatic brain injury. Specifically, there is a concerted post-injury response mounted by multiple neural cell types which includes microglial activation and astroglial scarring with the expression of a range of growth inhibitory molecules and cytokines in the lesion environment. Here, we review common models used for the study of traumatic brain injury (ranging from live animal models to *in vitro* systems), focusing on penetrating traumatic brain injury models. We discuss their relative advantages and drawbacks for the developmental testing of biomaterial-based therapies.

Key Words: astroglial scar; biomaterial; cortical culture; *in vitro* model; microglial infiltration; multicellular model; penetrating injury; scaffold; traumatic brain injury

7   References

1.   Adamchik, Y., Frantseva, M. V., Weisspapir, M., Carlen, P. L., & Perez Velazquez, J. L. (2000). Methods to induce primary and secondary traumatic damage in organotypic hippocampal slice cultures. Brain research. Brain research protocols, 5(2), 153–158. DOI: 10.1016/s1385-299x(00)00007-6

2.   Ahuja, C. S., Nori, S., Tetreault, L., Wilson, J., Kwon, B., Harrop, J., Choi, D., & Fehlings, M. G. (2017). Traumatic Spinal Cord Injury-Repair and Regeneration. Neurosurgery, 80(3S), S9–S22. https://doi.org/10.1093/neuros/nyw080

3.   Akhtar, A. Z., Pippin, J. J., & Sandusky, C. B. (2009). Animal studies in spinal cord injury: a systematic review of methylprednisolone. Alternatives to laboratory animals: ATLA, 37(1), 43–62. https://doi.org/10.1177/026119290903700108

4.   Alexander, J. K., Fuss, B., & Colello, R. J. (2006). Electric field-induced astrocyte alignment directs neurite outgrowth. Neuron glia biology, 2(2), 93–103. https://doi.org/10.1017/S1740925X0600010X

5.   Al-Majed, A. A., Brushart, T. M., & Gordon, T. (2000). Electrical stimulation accelerates and increases expression of BDNF and trkB mRNA in regenerating rat femoral motoneurons. The European journal of neuroscience, 12(12), 4381–4390.

6.   Al-Majed, A. A., Neumann, C. M., Brushart, T. M., & Gordon, T. (2000). Brief electrical stimulation promotes the speed and accuracy of motor axonal regeneration. The Journal of neuroscience : the official journal of the Society for Neuroscience, 20(7), 2602–2608. https://doi.org/10.1523/JNEUROSCI.20-07-02602.2000

7.   Antoni, D., Burckel, H., Josset, E., & Noel, G. (2015). Three-dimensional cell culture: a breakthrough in vivo. International journal of molecular sciences, 16(3), 5517–5527. https://doi.org/10.3390/ijms16035517

8.   Aqrawe, Z., Montgomery, J., Travas-Sejdic, J., & Svirskis, D. (2017). Conducting Polymers as Electrode Coatings for Neuronal Multi-electrode Arrays. Trends in biotechnology, 35(2), 93–95. https://doi.org/10.1016/j.tibtech.2016.06.007

9.   Aurand, E. R., Wagner, J., Lanning, C., & Bjugstad, K. B. (2012). Building biocompatible hydrogels for tissue engineering of the brain and spinal cord. Journal of functional biomaterials, 3(4), 839–863. https://doi.org/10.3390/jfb3040839

10.   Bacova, M., Bimbova, K., Fedorova, J., Lukacova, N., & Galik, J. (2019). Epidural oscillating field stimulation as an effective therapeutic approach in combination therapy for spinal cord injury. Journal of neuroscience methods, 311, 102–110. https://doi.org/10.1016/j.jneumeth.2018.10.020

11.   Bakkum, D. J., Radivojevic, M., Frey, U., Franke, F., Hierlemann, A., & Takahashi, H. (2014). Parameters for burst detection. Frontiers in computational neuroscience, 7, 193. https://doi.org/10.3389/fncom.2013.00193

12.   Bang, S., Jeong, S., Choi, N., & Kim, H. N. (2019). Brain-on-a-chip: A history of development and future perspective. Biomicrofluidics, 13(5), 051301. DOI: 10.1063/1.5120555

13.   Banker, G. A. and Cowan, W. M. (1977) 'Rat hippocampal neurons in dispersed cell culture', Brain Research, 126(3), pp. 397–425. doi: 10.1016/0006-8993(77)90594-7

14.   Bar-Kochba, E., Scimone, M. T., Estrada, J. B., & Franck, C. (2016). Strain and rate-dependent neuronal injury in a 3D in vitro compression model of traumatic brain injury. Scientific reports, 6, 30550. DOI: 10.1038/srep30550

15. Bartlett, R. D., Eleftheriadou, D., Evans, R., Choi, D., & Phillips, J. B. (2020). Mechanical properties of the spinal cord and brain: Comparison with clinical-grade biomaterials for tissue engineering and regenerative medicine. Biomaterials, 258, 120303. https://doi.org/10.1016/j.biomaterials.2020.120303

15.   Bayraktar, O. A., Fuentealba, L. C., Alvarez-Buylla, A., & Rowitch, D. H. (2014). Astrocyte development and heterogeneity. Cold Spring Harbor perspectives in biology, 7(1), a020362. https://doi.org/10.1101/cshperspect.a020362

16.   Becerra-Calixto, A., & Cardona-Gómez, G. P. (2017). The Role of Astrocytes in Neuroprotection after Brain Stroke: Potential in Cell Therapy. Frontiers in molecular neuroscience, 10, 88. https://doi.org/10.3389/fnmol.2017.00088

17.Belin, S., Norsworthy, M., & He, Z. (2014). Independent control of aging and axon regeneration. *Cell metabolism*, *19*(3), 354–356. https://doi.org/10.1016/j.cmet.2014.02.014

17.   Benabid, A. L., Chabardes, S., Mitrofanis, J., & Pollak, P. (2009). Deep brain stimulation of the subthalamic nucleus for the treatment of Parkinson's disease. The Lancet. Neurology, 8(1), 67–81. https://doi.org/10.1016/S1474-4422(08)70291-6

18.   Biancotti, J. C., Walker, K. A., Jiang, G., Di Bernardo, J., Shea, L. D., & Kunisaki, S. M. (2020). Hydrogel and neural progenitor cell delivery supports organotypic fetal spinal cord development in an ex vivo model of prenatal spina bifida repair. Journal of tissue engineering, 11, 2041731420943833. DOI: 10.1177/2041731420943833

19.   Birey, F., Andersen, J., Makinson, C. et al. Assembly of functionally integrated human forebrain spheroids. Nature 545, 54–59 (2017) https://doi.org/10.1038/nature22330

20.   Birey, F., Andersen, J., Makinson, C. et al. Assembly of functionally integrated human forebrain spheroids. Nature 545, 54–59 (2017). https://doi.org/10.1038/nature22330

21.   Bloom BM, Newcombe V, Roberts I. What's in a number? Problems with counting traumatic brain injuries. Emergency Medicine Journal 2022;39:233-234. http://dx.doi.org/10.1136/emermed-2021-212076

22.   Borgens, R. B., Blight, A. R., Murphy, D. J., & Stewart, L. (1986). Transected dorsal column axons within the guinea pig spinal cord regenerate in the presence of an applied electric field. The Journal of comparative neurology, 250(2), 168–180. https://doi.org/10.1002/cne.902500204

23.   Borgens, R. B., Toombs, J. P., Blight, A. R., McGinnis, M. E., Bauer, M. S., Widmer, W. R., & Cook, J. R., Jr (1993). Effects of applied electric fields on clinical cases of complete paraplegia in dogs. Restorative neurology and neuroscience, 5(5), 305–322. https://doi.org/10.3233/RNN-1993-55601

24.   Borgens, R. B., Vanable, J. W., Jr, & Jaffe, L. F. (1977). Bioelectricity and regeneration: large currents leave the stumps of regenerating newt limbs. Proceedings of the National Academy of Sciences of the United States of America, 74(10), 4528–4532. https://doi.org/10.1073/pnas.74.10.4528

25.   Boyd, J. G., & Gordon, T. (2003). Neurotrophic factors and their receptors in axonal regeneration and functional recovery after peripheral nerve injury. Molecular neurobiology, 27(3), 277–324. https://doi.org/10.1385/MN:27:3:277

26.   Bradbury, E.J., Burnside, E.R. Moving beyond the glial scar for spinal cord repair. Nat Commun 10, 3879 (2019). https://doi.org/10.1038/s41467-019-11707-7

27.   Brewer, G. J., Boehler, M. D., Ide, A. N., & Wheeler, B. C. (2009). Chronic electrical stimulation of cultured hippocampal networks increases spontaneous spike rates. Journal of neuroscience methods, 184(1), 104–109. https://doi.org/10.1016/j.jneumeth.2009.07.031

28.   Brewer, G. J., Torricelli, J. R., Evege, E. K., & Price, P. J. (1993). Optimized survival of hippocampal neurons in B27-supplemented Neurobasal, a new serum-free medium combination. Journal of neuroscience research, 35(5), 567–576. https://doi.org/10.1002/jnr.490350513

29.   Buzsáki, G., Anastassiou, C. & Koch, C. The origin of extracellular fields and currents — EEG, ECoG, LFP and spikes. Nat Rev Neurosci 13, 407–420 (2012). https://doi.org/10.1038/nrn3241

30.   Campos-Pires, R., Yonis, A., Macdonald, W., Harris, K., Edge, C. J., Mahoney, P. F., & Dickinson, R. (2018). A Novel In Vitro Model of Blast Traumatic Brain Injury. Journal of visualized experiments : JoVE, (142), 10.3791/58400. DOI: 10.3791/58400

31.   Cargill, R., Kohama, S. G., Struve, J., Su, W., Banine, F., Witkowski, E., Back, S. A., & Sherman, L. S. (2012). Astrocytes in aged nonhuman primate brain gray matter synthesize excess hyaluronan. Neurobiology of aging, 33(4), 830.e13–830.e8.3E24. https://doi.org/10.1016/j.neurobiolaging.2011.07.006

32.   Carmel, J. B., & Martin, J. H. (2014). Motor cortex electrical stimulation augments sprouting of the corticospinal tract and promotes recovery of motor function. Frontiers in integrative neuroscience, 8, 51. https://doi.org/10.3389/fnint.2014.00051

33.   Carmel, J. B., & Martin, J. H. (2014). Motor cortex electrical stimulation augments sprouting of the corticospinal tract and promotes recovery of motor function. Frontiers in integrative neuroscience, 8, 51. https://doi.org/10.3389/fnint.2014.00051

34.   Carmel, J. B., Berrol, L. J., Brus-Ramer, M., & Martin, J. H. (2010). Chronic electrical stimulation of the intact corticospinal system after unilateral injury restores skilled locomotor control and promotes spinal axon outgrowth. The Journal of neuroscience : the official journal of the Society for Neuroscience, 30(32), 10918–10926. https://doi.org/10.1523/JNEUROSCI.1435-10.2010

35.   Carter, M. and Shieh, J. (2015) 'Chapter 14 - Cell Culture Techniques', in Guide to Research Techniques in Neuroscience, pp. 295–310

36.   Casha, S., Zygun, D., McGowan, M. D., Bains, I., Yong, V. W., & Hurlbert, R. J. (2012). Results of a phase II placebo-controlled randomized trial of minocycline in acute spinal cord injury. Brain : a journal of neurology, 135(Pt 4), 1224–1236. https://doi.org/10.1093/brain/aws072

37.   Cernak, I., Wing, I. D., Davidsson, J., & Plantman, S. (2014). A novel mouse model of penetrating brain injury. Frontiers in neurology, 5, 209. https://doi.org/10.3389/fneur.2014.00209

38.   Chen, B., Zuberi, M., Borgens, R. B., & Cho, Y. (2012). Affinity for, and localization of, PEG-functionalized silica nanoparticles to sites of damage in an ex vivo spinal cord injury model. Journal of biological engineering, 6(1), 18. DOI: 10.1186/1754-1611-6-18

39.   Chen, C., Bai, X., Ding, Y., & Lee, I. S. (2019). Electrical stimulation as a novel tool for regulating cell behavior in tissue engineering. Biomaterials research, 23, 25. https://doi.org/10.1186/s40824-019-0176-8

40.   Chen, J., Hsu, W., Huang, K., & Hung, C. (2019). Neuroprotective Effects of Collagen-Glycosaminoglycan Matrix Implantation following Surgical Brain Injury. Mediators of Inflammation, 2019. DOI:10.1155/2019/6848943

41.   Chen, Y. et al. (2007) 'Isolation and culture of rat and mouse oligodendrocyte precursor cells', Nature Protocols, 2(5), pp. 1044–1051. doi: 10.1038/nprot.2007.149. DOI: https://doi.org/10.1038/nprot.2007.149

42.   Cheriyan, T., Ryan, D., Weinreb, J., Cheriyan, J., Paul, J., Lafage, V., Kirsch, T. and Errico, T., 2014. Spinal cord injury models: a review. Spinal Cord, 52(8), pp.588-595. DOI: 10.1038/sc.2014.91

43.   Chiappalone, M., Vato, A., Berdondini, L., Koudelka-Hep, M., & Martinoia, S. (2007). Network dynamics and synchronous activity in cultured cortical neurons. International journal of neural systems, 17(2), 87–103. https://doi.org/10.1142/S0129065707000968

44.   Chrząszcz, P., Derbisz, K., Suszyński, K., Miodoński, J., Trybulski, R., Lewin-Kowalik, J., & Marcol, W. (2018). Application of peripheral nerve conduits in clinical practice: A literature review. Neurologia i neurochirurgia polska, 52(4), 427–435. https://doi.org/10.1016/j.pjnns.2018.06.003

45.   Cotterill, E., Hall, D., Wallace, K., Mundy, W. R., Eglen, S. J., & Shafer, T. J. (2016). Characterization of Early Cortical Neural Network Development in Multiwell Microelectrode Array Plates. Journal of biomolecular screening, 21(5), 510–519. https://doi.org/10.1177/1087057116640520

46.   Daviaud, N., Garbayo, E., Schiller, P. C., Perez-Pinzon, M., & Montero-Menei, C. N. (2013). Organotypic cultures as tools for optimizing central nervous system cell therapies. Experimental neurology, 248, 429–440. https://doi.org/10.1016/j.expneurol.2013.07.012

47.   Demestre, M., Pullen, A., Orrell, R. W., & Orth, M. (2005). ALS-IgG-induced selective motor neurone apoptosis in rat mixed primary spinal cord cultures. Journal of neurochemistry, 94(1), 268–275. https://doi.org/10.1111/j.1471-4159.2005.03184.x

48.   Deshpande, L. S., DeLorenzo, R. J., Churn, S. B., & Parsons, J. T. (2020). Neuronal-Specific Inhibition of Endoplasmic Reticulum Mg2+/Ca2+ ATPase Ca2+ Uptake in a Mixed Primary Hippocampal Culture Model of Status Epilepticus. Brain sciences, 10(7), 438. https://doi.org/10.3390/brainsci10070438

49.   Dewitt, D. D., Kaszuba, S. N., Thompson, D. M., & Stegemann, J. P. (2009). Collagen I-matrigel scaffolds for enhanced Schwann cell survival and control of three-dimensional cell morphology. Tissue engineering. Part A, 15(10), 2785–2793. https://doi.org/10.1089/ten.TEA.2008.0406

50.   Di Pietro, V., Amin, D., Pernagallo, S., Lazzarino, G., Tavazzi, B., Vagnozzi, R., Pringle, A. and Belli, A., 2010. Transcriptomics of Traumatic Brain Injury: Gene Expression and Molecular Pathways of Different Grades of Insult in a Rat Organotypic Hippocampal Culture Model. Journal of Neurotrauma, 27(2), pp.349-359

51.   Di Pietro, V., Amorini, A., Tavazzi, B., Hovda, D., Signoretti, S., Giza, C., Lazzarino, G., Vagnozzi, R., Lazzarino, G. and Belli, A., 2012. Potentially neuroprotective gene modulation in an in vitro model of mild traumatic brain injury. Molecular and Cellular Biochemistry, 375(1-2), pp.185-198. DOI: 10.1007/s11010-012-1541-2

52.   Domínguez-Bajo, A., González-Mayorga, A., López-Dolado, E., Munuera, C., García-Hernández, M., & Serrano, M. C. (2020). Graphene Oxide Microfibers Promote Regenerative Responses after Chronic Implantation in the Cervical Injured Spinal Cord. ACS Biomaterials Science and Engineering, 6(4), 2401–2414. DOI: 10.1021/acsbiomaterials.0c00345

53.   Echevarría, D., & Albus, K. (2000). Activity-dependent development of spontaneous bioelectric activity in organotypic cultures of rat occipital cortex. Brain research. Developmental brain research, 123(2), 151–164. https://doi.org/10.1016/s0165-3806(00)00089-4

54.   Edmundson, M., Thanh, N. T., & Song, B. (2013). Nanoparticles based stem cell tracking in regenerative medicine. Theranostics, 3(8), 573–582. https://doi.org/10.7150/thno.5477

55.   Effgen, G. B., & Morrison, B., 3rd (2017). Memantine Reduced Cell Death, Astrogliosis, and Functional Deficits in an in vitro Model of Repetitive Mild Traumatic Brain Injury. Journal of neurotrauma, 34(4), 934–942. https://doi.org/10.1089/neu.2016.4528

56.   Elias, P. Z., & Spector, M. (2012). Implantation of a collagen scaffold seeded with adult rat hippocampal progenitors in a rat model of penetrating brain injury. Journal of neuroscience methods, 209(1), 199–211. DOI: 10.1016/j.jneumeth.2012.06.003

57.   Ertürk, A., Mentz, S., Stout, E. E., Hedehus, M., Dominguez, S. L., Neumaier, L., Krammer, F., Llovera, G., Srinivasan, K., Hansen, D. V., Liesz, A., Scearce-Levie, K. A., & Sheng, M. (2016). Interfering with the Chronic Immune Response Rescues Chronic Degeneration After Traumatic Brain Injury. The Journal of neuroscience : the official journal of the Society for Neuroscience, 36(38), 9962–9975. DOI: 10.1523/JNEUROSCI.1898-15.2016

58.   Eugène, E., Cluzeaud, F., Cifuentes-Diaz, C., Fricker, D., Le Duigou, C., Clemenceau, S., Baulac, M., Poncer, J. C., & Miles, R. (2014). An organotypic brain slice preparation from adult patients with temporal lobe epilepsy. Journal of neuroscience methods, 235, 234–244. https://doi.org/10.1016/j.jneumeth.2014.07.009

59.   Euskirchen, N., Nitsche, M. A., & van Thriel, C. (2021). Direct Current Stimulation in Cell Culture Systems and Brain Slices-New Approaches for Mechanistic Evaluation of Neuronal Plasticity and Neuromodulation: State of the Art. Cells, 10(12), 3583. https://doi.org/10.3390/cells10123583

60.   Eytan, D., & Marom, S. (2006). Dynamics and effective topology underlying synchronization in networks of cortical neurons. The Journal of neuroscience : the official journal of the Society for Neuroscience, 26(33), 8465–8476. https://doi.org/10.1523/JNEUROSCI.1627-06.2006

61.   Fan, V. H., Grosberg, L. E., Madugula, S. S., Hottowy, P., Dabrowski, W., Sher, A., Litke, A. M., & Chichilnisky, E. J. (2019). Epiretinal stimulation with local returns enhances selectivity at cellular resolution. Journal of neural engineering, 16(2), 025001. https://doi.org/10.1088/1741-2552/aaeef1

62.   Finch, L., Harris, S., Solomou, G., Sen, J., Tzerakis, N., Emes, R. D., Lane, C. S., Hart, S. R., Adams, C. F., & Chari, D. M. (2020). Safe nanoengineering and incorporation of transplant populations in a neurosurgical grade biomaterial, DuraGen PlusTM, for protected cell therapy applications. Journal of controlled release : official journal of the Controlled Release Society, 321, 553–563. https://doi.org/10.1016/j.jconrel.2020.02.028

63.   Finley, M., Fairman, D., Liu, D., Li, P., Wood, A., & Cho, S. (2004). Functional validation of adult hippocampal organotypic cultures as an in vitro model of brain injury. Brain research, 1001(1-2), 125–132. https://doi.org/10.1016/j.brainres.2003.12.009

64.   Frega, M., Tedesco, M., Massobrio, P. et al. Network dynamics of 3D engineered neuronal cultures: a new experimental model for in-vitro electrophysiology. Sci Rep 4, 5489 (2014). https://doi.org/10.1038/srep05489

65.   Gähwiler B. H. (1981). Organotypic monolayer cultures of nervous tissue. Journal of neuroscience methods, 4(4), 329–342. https://doi.org/10.1016/0165-0270(81)90003-0

66. Gähwiler B. H. (1988). Organotypic cultures of neural tissue. Trends in neurosciences, 11(11), 484–489. https://doi.org/10.1016/0166-2236(88)90007-0

67. Gao, K., Wang, C. R., Jiang, F., Wong, A. Y., Su, N., Jiang, J. H., Chai, R. C., Vatcher, G., Teng, J., Chen, J., Jiang, Y. W., & Yu, A. C. (2013). Traumatic scratch injury in astrocytes triggers calcium influx to activate the JNK/c-Jun/AP-1 pathway and switch on GFAP expression. Glia, 61(12), 2063–2077. https://doi.org/10.1002/glia.22577

68. Garcia, A. D., Doan, N. B., Imura, T., Bush, T. G., & Sofroniew, M. V. (2004). GFAP-expressing progenitors are the principal source of constitutive neurogenesis in adult mouse forebrain. Nature neuroscience, 7(11), 1233–1241. https://doi.org/10.1038/nn1340

69. Gerard J. Tortora and Sandra Reynolds Grabowski. Principles of Anatomy and Physiology: 7th ed. New York: HarperCollins, 1993.

70. Gerardo-Nava, J., Hodde, D., Katona, I., Bozkurt, A., Grehl, T., Steinbusch, H. W., Weis, J., & Brook, G. A. (2014). Spinal cord organotypic slice cultures for the study of regenerating motor axon interactions with 3D scaffolds. Biomaterials, 35(14), 4288–4296. DOI: 10.1016/j.biomaterials.2014.02.007

71. Giannetti, S., Lauretti, L., Fernandez, E., Salvinelli, F., Tamburrini, G., & Pallini, R. (2001). Acrylic hydrogel implants after spinal cord lesion in the adult rat. Neurological research, 23(4), 405–409. https://doi.org/10.1179/016164101101198622

72. Ginhoux, F., & Prinz, M. (2015). Origin of microglia: current concepts and past controversies. Cold Spring Harbor perspectives in biology, 7(8), a020537. https://doi.org/10.1101/cshperspect.a020537

73. Gordon, J., Amin, S. and White, M. K. (2013) 'General overview of neuronal cell culture', Neuronal Cell Culture: Methods and Protocols, 1078, pp. 35–44.

74. Goshi, N., Morgan, R.K., Lein, P.J. et al. A primary neural cell culture model to study neuron, astrocyte, and microglia interactions in neuroinflammation. J Neuroinflammation 17, 155 (2020). DOI: https://doi.org/10.1186/s12974-020-01819-z

75. Guijarro-Belmar, A., Viskontas, M., Wei, Y., Bo, X., Shewan, D., & Huang, W. (2019). Epac2 Elevation Reverses Inhibition by Chondroitin Sulfate Proteoglycans In Vitro and Transforms Postlesion Inhibitory Environment to Promote Axonal Outgrowth in an Ex Vivo Model of Spinal Cord Injury. The Journal of neuroscience : the official journal of the Society for Neuroscience, 39(42), 8330–8346. DOI: 10.1523/JNEUROSCI.0374-19.2019

76. Hales, C. M., Rolston, J. D., & Potter, S. M. (2010). How to culture, record and stimulate neuronal networks on micro-electrode arrays (MEAs). Journal of visualized experiments : JoVE, (39), 2056. https://doi.org/10.3791/2056

77. Hales, C. M., Zeller-Townson, R., Newman, J. P., Shoemaker, J. T., Killian, N. J., & Potter, S. M. (2012). Stimulus-evoked high frequency oscillations are present in neuronal networks on microelectrode arrays. Frontiers in neural circuits, 6, 29. https://doi.org/10.3389/fncir.2012.00029

78. Hampton, D. W., Rhodes, K. E., Zhao, C., Franklin, R. J., & Fawcett, J. W. (2004). The responses of oligodendrocyte precursor cells, astrocytes and microglia to a cortical stab injury, in the brain. Neuroscience, 127(4), 813–820. https://doi.org/10.1016/j.neuroscience.2004.05.028

79.   Hofmann, K., Rodriguez-Rodriguez, R., Gaebler, A. et al. Astrocytes and oligodendrocytes in grey and white matter regions of the brain metabolize fatty acids. Sci Rep 7, 10779 (2017). https://doi.org/10.1038/s41598-017-11103-5

80.   Hyder, A. A., Wunderlich, C. A., Puvanachandra, P., Gururaj, G., & Kobusingye, O. C. (2007). The impact of traumatic brain injuries: a global perspective. NeuroRehabilitation, 22(5), 341–353.

81.   Hyman S. E. (2005). Neurotransmitters. Current biology : CB, 15(5), R154–R158. https://doi.org/10.1016/j.cub.2005.02.037

82.   Ioannou, M. S., Liu, Z., & Lippincott-Schwartz, J. (2019). A Neuron-Glia Co-culture System for Studying Intercellular Lipid Transport. Current protocols in cell biology, 84(1), e95. https://doi.org/10.1002/cpcb.95

83.   Jack, A. S., Hurd, C., Forero, J., Nataraj, A., Fenrich, K., Blesch, A., & Fouad, K. (2018). Cortical electrical stimulation in female rats with a cervical spinal cord injury to promote axonal outgrowth. Journal of neuroscience research, 96(5), 852–862. https://doi.org/10.1002/jnr.24209

84.   Jenkins SI, Weinberg D, Al-Shakli AF, Fernandes AR, Yiu HHP, Telling ND, Roach P, Chari DM. 2016. 'Stealth' nanoparticles evade neural immune cells but also evade major brain cell populations: Implications for PEG-based neurotherapeutics. J Control Release, 136-145, vol. 224. link> doi> full text>

85.   Jeong, D. K., Taghavi, C. E., Song, K. J., Lee, K. B., & Kang, H. W. (2011). Organotypic human spinal cord slice culture as an alternative to direct transplantation of human bone marrow precursor cells for treating spinal cord injury. World neurosurgery, 75(3-4), 533–539. https://doi.org/10.1016/j.wneu.2010.10.042

86.   Jgamadze, D., Johnson, V., Wolf, J., Kacy Cullen, D., Song, H., Ming, G., Smith, D. and Isaac Chen, H., 2020. Modeling traumatic brain injury with human brain organoids. Current Opinion in Biomedical Engineering, 14, pp.52-58. https://doi.org/10.1016/j.cobme.2020.05.004

87.   Jimbo, Y., Kawana, A., Parodi, P. et al. The dynamics of a neuronal culture of dissociated cortical neurons of neonatal rats. Biol Cybern 83, 1–20 (2000). https://doi.org/10.1007/PL00007970

88.   Jugé, L., Pong, A. C., Bongers, A., Sinkus, R., Bilston, L. E., & Cheng, S. (2016). Changes in Rat Brain Tissue Microstructure and Stiffness during the Development of Experimental Obstructive Hydrocephalus. PloS one, 11(2), e0148652. https://doi.org/10.1371/journal.pone.0148652

89.   Kaiser, O., Aliuos, P., Wissel, K., Lenarz, T., Werner, D., Reuter, G., Kral, A., & Warnecke, A. (2013). Dissociated neurons and glial cells derived from rat inferior colliculi after digestion with papain. PloS one, 8(12), e80490. https://doi.org/10.1371/journal.pone.0080490

90.   Kamioka H, Maeda E, Torimitsu K, Kawana A (1993) Developmental changes in activity of cultured cortical neural networks. Neurosci Res Suppl 18:S112. (book)

91.   Kandel, E. R., Schwartz, J. H., Jessell, T. M., Siegelbaum, S., Hudspeth, A. J., & Mack, S. (Eds.). (2000). Principles of neural science (Vol. 4, pp. 1227-1246). New York: McGraw-hill.

92.   Kang, W. H., Cao, W., Graudejus, O., Patel, T. P., Wagner, S., Meaney, D. F., & Morrison, B., 3rd (2015). Alterations in Hippocampal Network Activity after In Vitro Traumatic Brain Injury. Journal of neurotrauma, 32(13), 1011–1019. https://doi.org/10.1089/neu.2014.3667

93.   Karve, I. P., Taylor, J. M., & Crack, P. J. (2016). The contribution of astrocytes and microglia to traumatic brain injury. British journal of pharmacology, 173(4), 692–702. https://doi.org/10.1111/bph.13125

94.   Kawabori, M., & Yenari, M. A. (2015). The role of the microglia in acute CNS injury. Metabolic brain disease, 30(2), 381–392. DOI: 10.1007/s11011-014-9531-6

95.   Keough, M., Rogers, J., Zhang, P. et al. An inhibitor of chondroitin sulfate proteoglycan synthesis promotes central nervous system remyelination. Nat Commun 7, 11312 (2016). https://doi.org/10.1038/ncomms11312

96.   Khaing, Zin & Thomas, Richelle & Geissler, Sydney & Schmidt, Christine. (2014). Advanced biomaterials for repairing the nervous system: What can hydrogels do for the brain?. Materials Today. 17. 10.1016/j.mattod.2014.05.011. DOI:10.1016/j.mattod.2014.05.011

97.   Kim, K. D., Lee, K. S., Coric, D., Chang, J. J., Harrop, J. S., Theodore, N., & Toselli, R. M. (2021). A study of probable benefit of a bioresorbable polymer scaffold for safety and neurological recovery in patients with complete thoracic spinal cord injury: 6-month results from the INSPIRE study, Journal of Neurosurgery: Spine, 34(5), 808-817. Retrieved May 16, 2022, doi: https://thejns.org/spine/view/journals/j-neurosurg-spine/34/5/article-p808.xml

98.   Kodandaramaiah, S., Franzesi, G., Chow, B. et al. Automated whole-cell patch-clamp electrophysiology of neurons in vivo. Nat Methods 9, 585–587 (2012). https://doi.org/10.1038/nmeth.1993

99.   Koppes, A. N., Zaccor, N. W., Rivet, C. J., Williams, L. A., Piselli, J. M., Gilbert, R. J., & Thompson, D. M. (2014). Neurite outgrowth on electrospun PLLA fibers is enhanced by exogenous electrical stimulation. Journal of neural engineering, 11(4), 046002. https://doi.org/10.1088/1741-2560/11/4/046002

100.   Kornev, V. A., Grebenik, E. A., Solovieva, A. B., Dmitriev, R. I., & Timashev, P. S. (2018). Hydrogel-assisted neuroregeneration approaches towards brain injury therapy: A state-of-the-art review. Computational and structural biotechnology journal, 16, 488–502. https://doi.org/10.1016/j.csbj.2018.10.011

101.   Koss, K. M. et al. (2017) 'Improved 3D hydrogel cultures of primary glial cells for in vitro modelling of neuroinflammation', Journal of Visualized Experiments, 2017(130), pp. 1–11. doi: 10.3791/56615.

102.   Kotliarova, A., & Sidorova, Y. A. (2021). Glial Cell Line-Derived Neurotrophic Factor Family Ligands, Players at the Interface of Neuroinflammation and Neuroprotection: Focus Onto the Glia. Frontiers in cellular neuroscience, 15, 679034. https://doi.org/10.3389/fncel.2021.679034

103.   Krishna, G., Beitchman, J. A., Bromberg, C. E., & Currier Thomas, T. (2020). Approaches to Monitor Circuit Disruption after Traumatic Brain Injury: Frontiers in Preclinical Research. International journal of molecular sciences, 21(2), 588. https://doi.org/10.3390/ijms21020588

104.   Kuhlenbeck, H. (1975). The Central Nervous System of Vertebrates: Spinal Cord and Deuterencephalon (Vol. 4). Karger Medical and Scientific Publishers.

105.   Lam, D., Lively, S., & Schlichter, L. C. (2017). Responses of rat and mouse primary microglia to pro- and anti-inflammatory stimuli: molecular profiles, K+ channels and migration. Journal of neuroinflammation, 14(1), 166. https://doi.org/10.1186/s12974-017-0941-3

106.   Lancaster, M. A., Renner, M., Martin, C. A., Wenzel, D., Bicknell, L. S., Hurles, M. E., Homfray, T., Penninger, J. M., Jackson, A. P., & Knoblich, J. A. (2013). Cerebral organoids model human brain development and microcephaly. Nature, 501(7467), 373–379. https://doi.org/10.1038/nature12517

107.   Lawrence, T., Helmy, A., Bouamra, O., Woodford, M., Lecky, F., & Hutchinson, P. J. (2016). Traumatic brain injury in England and Wales: prospective audit of epidemiology, complications and standardised mortality. BMJ open, 6(11), e012197. https://doi.org/10.1136/bmjopen-2016-012197

108.   Lewicki M. S. (1998). A review of methods for spike sorting: the detection and classification of neural action potentials. Network (Bristol, England), 9(4), R53–R78. https://doi.org/10.1088/0954-898X_9_4_001.

109.   Li, J. Weak direct current (DC) electric fields as a therapy for spinal cord injuries: review and advancement of the oscillating field stimulator (OFS). Neurosurg Rev 42, 825–834 (2019). https://doi.org/10.1007/s10143-018-01068-y

110.   Li, N., & Leung, G. K. (2015). Oligodendrocyte Precursor Cells in Spinal Cord Injury: A Review and Update. BioMed research international, 2015, 235195. https://doi.org/10.1155/2015/235195

111.   Li, X., Tan, J., Xiao, Z., Zhao, Y., Han, S., Liu, D., Yin, W., Li, J., Li, J., Wanggou, S., Chen, B., Ren, C., Jiang, X., & Dai, J. (2017). Transplantation of hUC-MSCs seeded collagen scaffolds reduces scar formation and promotes functional recovery in canines with chronic spinal cord injury. Scientific reports, 7, 43559. https://doi.org/10.1038/srep43559

112.   Liaudanskaya, V., Chung, J. Y., Mizzoni, C., Rouleau, N., Berk, A. N., Wu, L., Turner, J. A., Georgakoudi, I., Whalen, M. J., Nieland, T., & Kaplan, D. L. (2020). Modeling Controlled Cortical Impact Injury in 3D Brain-Like Tissue Cultures. Advanced healthcare materials, 9(12), e2000122. https://doi.org/10.1002/adhm.202000122

113.   Lilley, E., Andrews, M. R., Bradbury, E. J., Elliott, H., Hawkins, P., Ichiyama, R. M., Keeley, J., Michael-Titus, A. T., Moon, L., Pluchino, S., Riddell, J., Ryder, K., & Yip, P. K. (2020). Refining rodent models of spinal cord injury. Experimental neurology, 328, 113273. https://doi.org/10.1016/j.expneurol.2020.113273

114.   Liu, Y., Ban, D. X., Ma, C., Zhang, Z. G., Zhang, J. Y., Gao, S. J., & Feng, S. Q. (2016). Photodynamic Therapy Mediated by Upconversion Nanoparticles to Reduce Glial Scar Formation and Promote Hindlimb Functional Recovery After Spinal Cord Injury in Rats. Journal of biomedical nanotechnology, 12(11), 2063–2075. https://doi.org/10.1166/jbn.2016.2300

115.   Macaya, D., & Spector, M. (2012). Injectable hydrogel materials for spinal cord regeneration: a review. Biomedical materials (Bristol, England), 7(1), 012001. https://doi.org/10.1088/1748-6041/7/1/012001

116.   Maclean, F. L., Horne, M. K., Williams, R. J., & Nisbet, D. R. (2018). Review: Biomaterial systems to resolve brain inflammation after traumatic injury. APL bioengineering, 2(2), 021502. https://doi.org/10.1063/1.5023709

117.   Maeda, E., Robinson, H. P., & Kawana, A. (1995). The mechanisms of generation and propagation of synchronized bursting in developing networks of cortical neurons. The Journal of neuroscience : the official journal of the Society for Neuroscience, 15(10), 6834–6845. https://doi.org/10.1523/JNEUROSCI.15-10-06834.1995

118.   Mahar, M., Cavalli, V. Intrinsic mechanisms of neuronal axon regeneration. Nat Rev Neurosci 19, 323–337 (2018). https://doi.org/10.1038/s41583-018-0001-8

119.   Malon, J. T., & Cao, L. (2016). Preparation of Primary Mixed Glial Cultures from Adult Mouse Spinal Cord Tissue. Journal of visualized experiments : JoVE, (117), 54801. https://doi.org/10.3791/54801

120.   Marklund, N., 2016. Rodent Models of Traumatic Brain Injury: Methods and Challenges. Methods in Molecular Biology, pp.29-46. DOI: 10.1007/978-1-4939-3816-2_3

121.   Marom, S., & Shahaf, G. (2002). Development, learning and memory in large random networks of cortical neurons: lessons beyond anatomy. Quarterly reviews of biophysics, 35(1), 63–87. https://doi.org/10.1017/s0033583501003742

122.   McTigue, D. M., & Tripathi, R. B. (2008). The life, death, and replacement of oligodendrocytes in the adult CNS. Journal of neurochemistry, 107(1), 1–19. https://doi.org/10.1111/j.1471-4159.2008.05570.x

123.   Mestre, A., Inácio, P., Elamine, Y., Asgarifar, S., Lourenço, A. S., Cristiano, M., Aguiar, P., Medeiros, M., Araújo, I. M., Ventura, J., & Gomes, H. L. (2017). Extracellular Electrophysiological Measurements of Cooperative Signals in Astrocytes Populations. Frontiers in neural circuits, 11, 80. https://doi.org/10.3389/fncir.2017.00080

124.   Mladinic, M., & Nistri, A. (2013). Microelectrode arrays in combination with in vitro models of spinal cord injury as tools to investigate pathological changes in network activity: facts and promises. Frontiers in neuroengineering, 6, 2. https://doi.org/10.3389/fneng.2013.00002

125.   Mobini, S., Leppik, L., & Barker, J. H. (2018). Direct current electrical stimulation chamber for treating cells in vitro. BioTechniques, 60(2), 95–98. https://doi.org/10.2144/000114382

126.   Modo, M., Cash, D., Mellodew, K., Williams, S. C., Fraser, S. E., Meade, T. J., Price, J., & Hodges, H. (2002). Tracking transplanted stem cell migration using bifunctional, contrast agent-enhanced, magnetic resonance imaging. NeuroImage, 17(2), 803–811.

127.   Moeendarbary, E., Weber, I. P., Sheridan, G. K., Koser, D. E., Soleman, S., Haenzi, B., Bradbury, E. J., Fawcett, J., & Franze, K. (2017). The soft mechanical signature of glial scars in the central nervous system. Nature communications, 8, 14787. https://doi.org/10.1038/ncomms14787

128.   Mogas-Barcons, A., Chari, D. M., & Adams, C. F. (2021). Enhancing the regenerative potential of stem cell-laden, clinical-grade implants through laminin engineering. Materials science & engineering. C, Materials for biological applications, 123, 111931. DOI: 10.1016/j.msec.2021.111931

129.   Mohn, T. C., & Koob, A. O. (2015). Adult Astrogenesis and the Etiology of Cortical Neurodegeneration. Journal of experimental neuroscience, 9(Suppl 2), 25–34. https://doi.org/10.4137/JEN.S25520

130.   Morrison, B., Cater, H., Benham, C. and Sundstrom, L., 2006. An in vitro model of traumatic brain injury utilising two-dimensional stretch of organotypic hippocampal slice cultures. Journal of Neuroscience Methods, 150(2), pp.192-201. DOI: 10.1016/j.jneumeth.2005.06.014

131.   Morrison, B., Eberwine, J., Meaney, D. and McIntosh, T., 2000. Traumatic injury induces differential expression of cell death genes in organotypic brain slice cultures determined by complementary DNA array hybridization. Neuroscience, 96(1), pp.131-139. DOI: 10.1016/s0306-4522(99)00537-0

132.   Morrison, B., Elkin, B., Dollé, J. and Yarmush, M., 2011. In Vitro Models of Traumatic Brain Injury. Annual Review of Biomedical Engineering, 13(1), pp.91-126. DOI: 10.1146/annurev-bioeng-071910-124706

133.   Negri, J., Menon, V., & Young-Pearse, T. L. (2020). Assessment of Spontaneous Neuronal Activity In Vitro Using Multi-Well Multi-Electrode Arrays: Implications for Assay Development. eNeuro, 7(1), ENEURO.0080-19.2019. https://doi.org/10.1523/ENEURO.0080-19.2019

134. Nguyen, L. H., Gao, M., Lin, J., Wu, W., Wang, J., & Chew, S. Y. (2018). Author Correction: Three-dimensional aligned nanofibers-hydrogel scaffold for controlled non-viral drug/gene delivery to direct axon regeneration in spinal cord injury treatment. Scientific reports, 8(1), 13057. DOI: 10.1038/s41598-018-31314-8

135. Norman, G.A. Van Drugs, devices, and the FDA: part 1: an overview of approval processes for drugs JACC Basic to Transl. Sci., 1 (2016), pp. 170-179

136. Novellino, A., Scelfo, B., Palosaari, T., Price, A., Sobanski, T., Shafer, T. J., Johnstone, A. F., Gross, G. W., Gramowski, A., Schroeder, O., Jügelt, K., Chiappalone, M., Benfenati, F., Martinoia, S., Tedesco, M. T., Defranchi, E., D'Angelo, P., & Whelan, M. (2011). Development of micro-electrode array based tests for neurotoxicity: assessment of interlaboratory reproducibility with neuroactive chemicals. Frontiers in neuroengineering, 4, 4. https://doi.org/10.3389/fneng.2011.00004

137. Obien, M. E., Deligkaris, K., Bullmann, T., Bakkum, D. J., & Frey, U. (2015). Revealing neuronal function through microelectrode array recordings. Frontiers in neuroscience, 8, 423. https://doi.org/10.3389/fnins.2014.00423

138. Ogura, T., Sakaguchi, H., Miyamoto, S., & Takahashi, J. (2018). Three-dimensional induction of dorsal, intermediate and ventral spinal cord tissues from human pluripotent stem cells. Development (Cambridge, England), 145(16), dev162214. DOI: 10.1242/dev.162214

139. Oliveira, J. M., Carvalho, L., Silva-Correia, J., Vieira, S., Majchrzak, M., Lukomska, B., Stanaszek, L., Strymecka, P., Malysz-Cymborska, I., Golubczyk, D., Kalkowski, L., Reis, R. L., Janowski, M., & Walczak, P. (2018). Hydrogel-based scaffolds to support intrathecal stem cell transplantation as a gateway to the spinal cord: clinical needs, biomaterials, and imaging technologies. NPJ Regenerative medicine, 3, 8. https://doi.org/10.1038/s41536-018-0046-3

140. Pandamooz, S., Salehi, M. S., Zibaii, M. I., Safari, A., Nabiuni, M., Ahmadiani, A., & Dargahi, L. (2019). Modeling traumatic injury in organotypic spinal cord slice culture obtained from adult rat. Tissue & cell, 56, 90–97. DOI: 10.1016/j.tice.2019.01.002

141. Papa, S., Mauri, E. and Rossi, F. (2020) Chapter 1 - Introduction to spinal cord injury as clinical pathology, Spinal Cord Injury (SCI) Repair Strategies. Elsevier Ltd. Doi: https://re.public.polimi.it/retrieve/handle/11311/1173375/622113/chapter1.pdf

142. Pas, J., Pitsalidis, C., Koutsouras, D. A., Quilichini, P. P., Santoro, F., Cui, B., ... & Owens, R. M. (2018). Neurospheres on patterned PEDOT: PSS microelectrode arrays enhance electrophysiology recordings. Advanced Biosystems, 2(1), 1700164. https://doi.org/10.1002/adbi.201700164

143. Patek, M., & Stewart, L (2017) Spinal cord injury, Anaesthesia & Intensive Care Medicine, Volume 21, Issue 8, 2020, Pages 411-416,ISSN 1472-0299, https://doi.org/10.1016/j.mpaic.2020.05.006.

144. Patel, N., & Poo, M. M. (1982). Orientation of neurite growth by extracellular electric fields. The Journal of neuroscience : the official journal of the Society for Neuroscience, 2(4), 483–496. https://doi.org/10.1523/JNEUROSCI.02-04-00483.1982

145. Pedachenko, Eugene & Liubich, Larysa & Staino, L. & Egorova, D.. (2020). Dynamics of morphological changes in neural cell culture with a model of neurotrauma in vitro under the influence of conditioned media of the rat fetal brain neurogenic cells. Cell and Organ Transplantology. 8. 177-186. 10.22494/cot.v8i2.114.

146. Pickard, M. R. and Chari, D. M. (2010) 'Robust uptake of magnetic nanoparticles (MNPs) by central nervous system (CNS) microglia: Implications for particle uptake in mixed neural cell populations', International Journal of Molecular Sciences, 11(3), pp. 967–981. doi: 10.3390/ijms11030967.

147. Prager, J., Adams, C. F., Delaney, A. M., Chanoit, G., Tarlton, J. F., Wong, L. F., Chari, D. M., & Granger, N. (2020). Stiffness-matched biomaterial implants for cell delivery: clinical, intraoperative ultrasound elastography provides a 'target' stiffness for hydrogel synthesis in spinal cord injury. Journal of tissue engineering, 11, 2041731420934806. https://doi.org/10.1177/2041731420934806

148. Prang, P., Müller, R., Eljaouhari, A., Heckmann, K., Kunz, W., Weber, T., Faber, C., Vroemen, M., Bogdahn, U., & Weidner, N. (2006). The promotion of oriented axonal regrowth in the injured spinal cord by alginate-based anisotropic capillary hydrogels. Biomaterials, 27(19), 3560–3569. DOI: 10.1016/j.biomaterials.2006.01.053

149. Qian, X., Nguyen, H. N., Song, M. M., Hadiono, C., Ogden, S. C., Hammack, C., Yao, B., Hamersky, G. R., Jacob, F., Zhong, C., Yoon, K. J., Jeang, W., Lin, L., Li, Y., Thakor, J., Berg, D. A., Zhang, C., Kang, E., Chickering, M., Nauen, D., … Ming, G. L. (2016). Brain-Region-Specific Organoids Using Mini-bioreactors for Modeling ZIKV Exposure. Cell, 165(5), 1238–1254. https://doi.org/10.1016/j.cell.2016.04.032

150. Quiroga R, Panzeri S, Anastassiou C, et al. Biophysics of Extracellular Spikes. Princ Neural Coding. 2013;15–36. https://doi.org/10.1201/b14756-4.

151. R H Basit, S I Jenkins, D M Chari, 518 New In Vitro Model of Traumatic Brain Injury to Assess Biomaterial Based Regenerative Strategies, British Journal of Surgery, Volume 108, Issue Supplement_2, May 2021, znab135.002, https://doi.org/10.1093/bjs/znab135.002

152. Rabchevsky, A. G., Sullivan, P. G., & Scheff, S. W. (2007). Temporal-spatial dynamics in oligodendrocyte and glial progenitor cell numbers throughout ventrolateral white matter following contusion spinal cord injury. Glia, 55(8), 831–843. https://doi.org/10.1002/glia.20508

153. Ramón-Cueto, A., Cordero, M. I., Santos-Benito, F. F., & Avila, J. (2000). Functional recovery of paraplegic rats and motor axon regeneration in their spinal cords by olfactory ensheathing glia. Neuron, 25(2), 425–435. https://doi.org/10.1016/s0896-6273(00)80905-8

154. Ray, J., Peterson, D. A., Schinstine, M., & Gage, F. H. (1993). Proliferation, differentiation, and long-term culture of primary hippocampal neurons. Proceedings of the National Academy of Sciences of the United States of America, 90(8), 3602–3606. https://doi.org/10.1073/pnas.90.8.3602

155. Richardson, P. M., McGuinness, U. M., & Aguayo, A. J. (1980). Axons from CNS neurons regenerate into PNS grafts. Nature, 284(5753), 264–265. https://doi.org/10.1038/284264a0

156. Savas, A., Warnke, P. C., Ginap, T., Feuerstein, T. J., & Ostertag, C. B. (2001). The effects of continuous and single-dose radiation on choline uptake in organotypic tissue slice cultures of rabbit hippocampus. Neurological research, 23(6), 669–675. https://doi.org/10.1179/016164101101199018

157. Schneider, S., Erdemann, F., Schneider, O., Hutschalik, T., & Loskill, P. (2020). Organ-on-a-disc: A platform technology for the centrifugal generation and culture of microphysiological 3D cell constructs amenable for automation and parallelization. APL bioengineering, 4(4), 046101. DOI: 10.1063/5.0019766

158. Seabrook, T. J., Jiang, L., Maier, M., & Lemere, C. A. (2006). Minocycline affects microglia activation, Abeta deposition, and behavior in APP-tg mice. Glia, 53(7), 776–782. https://doi.org/10.1002/glia.20338

159.   Segev, A., Garcia-Oscos, F., & Kourrich, S. (2016). Whole-cell Patch-clamp Recordings in Brain Slices. Journal of visualized experiments : JoVE, (112), 54024. https://doi.org/10.3791/54024

160.   Shapiro, S., Borgens, R., Pascuzzi, R., Roos, K., Groff, M., Purvines, S., Rodgers, R. B., Hagy, S., & Nelson, P. (2005). Oscillating field stimulation for complete spinal cord injury in humans: a phase 1 trial. Journal of neurosurgery. Spine, 2(1), 3–10. https://doi.org/10.3171/spi.2005.2.1.0003

161.   Sharma, S., Ifergan, I., Kurz, J. E., Linsenmeier, R. A., Xu, D., Cooper, J. G., Miller, S. D., & Kessler, J. A. (2020). Intravenous Immunomodulatory Nanoparticle Treatment for Traumatic Brain Injury. Annals of neurology, 87(3), 442–455. https://doi.org/10.1002/ana.25675

162.   Shin, S. S., Grandhi, R., Henchir, J., Yan, H. Q., Badylak, S. F., & Dixon, C. E. (2015). Neuroprotective effects of collagen matrix in rats after traumatic brain injury. Restorative neurology and neuroscience, 33(2), 95–104. https://doi.org/10.3233/RNN-140430

163.   Slovinska, L., Blasko, J., Nagyova, M., Szekiova, E. and Cizkova, D., 2016. In Vitro Models of Spinal Cord Injury. Recovery of Motor Function Following Spinal Cord Injury,. DOI: 10.5772/63459

164.   Sofroniew, M. and Vinters, H.V. 2010. Astrocytes: biology and pathology. Acta Neuropathological, 119(1), pp7–35.

165.   Spira, M., Hai, A. Multi-electrode array technologies for neuroscience and cardiology. Nature Nanotech 8, 83–94 (2013). https://doi.org/10.1038/nnano.2012.265

166.   Stoppini, L., Buchs, P. A., & Muller, D. (1991). A simple method for organotypic cultures of nervous tissue. Journal of neuroscience methods, 37(2), 173–182. https://doi.org/10.1016/0165-0270(91)90128-m

167.   Sünwoldt, J. et al. (2017) 'Neuronal culture microenvironments determine preferences in bioenergetic pathway use', Frontiers in Molecular Neuroscience, 10(September), pp. 1–11. doi: 10.3389/fnmol.2017.00305

168.   Sypecka, J., Koniusz, S., Kawalec, M., & Sarnowska, A. (2015). The organotypic longitudinal spinal cord slice culture for stem cell study. Stem cells international, 2015, 471216. https://doi.org/10.1155/2015/471216

169.   Tabakow P, Raisman G, Fortuna W, et al. Functional Regeneration of Supraspinal Connections in a Patient with Transected Spinal Cord following Transplantation of Bulbar Olfactory Ensheathing Cells with Peripheral Nerve Bridging. Cell Transplantation. December 2014:1631-1655. doi:10.3727/096368914X685131

170.   Tang-Schomer M. D. (2018). 3D axon growth by exogenous electrical stimulus and soluble factors. Brain research, 1678, 288–296. https://doi.org/10.1016/j.brainres.2017.10.032

171.   Tapia, N., & Schöler, H. R. (2016). Molecular Obstacles to Clinical Translation of iPSCs. Cell stem cell, 19(3), 298–309. https://doi.org/10.1016/j.stem.2016.06.017

172.   Trujillo, M., McElroy, T., Brown, T., Simmons, P., Ntagwabira, F., & Allen, A. R. (2021). Combined Mechanical and Enzymatic Dissociation of Mouse Brain Hippocampal Tissue. Journal of visualized experiments : JoVE, (176), 10.3791/63007. https://doi.org/10.3791/63007

173.   Tscherter, A., Heuschkel, M. O., Renaud, P., & Streit, J. (2001). Spatiotemporal characterization of rhythmic activity in rat spinal cord slice cultures. The European journal of neuroscience, 14(2), 179–190. https://doi.org/10.1046/j.0953-816x.2001.01635.x

174.   Ucar B. (2021). Natural biomaterials in brain repair: A focus on collagen. Neurochemistry international, 146, 105033. DOI: 10.1016/j.neuint.2021.105033

175.   Ucar, B., & Humpel, C. (2018). Collagen for brain repair: therapeutic perspectives. Neural regeneration research, 13(4), 595–598. https://doi.org/10.4103/1673-5374.230273

176.   Ucar, B., & Humpel, C. (2019). Therapeutic efficacy of glial cell-derived neurotrophic factor loaded collagen scaffolds in ex vivo organotypic brain slice Parkinson's disease models. Brain research bulletin, 149, 86–95. DOI: 10.1016/j.brainresbull.2019.04.012

177.   Ucar, B., Kajtez, J., Foidl, B. M., Eigel, D., Werner, C., Long, K. R., Emnéus, J., Bizeau, J., Lomora, M., Pandit, A., Newland, B., & Humpel, C. (2021). Biomaterial based strategies to reconstruct the nigrostriatal pathway in organotypic slice co-cultures. Acta biomaterialia, 121, 250–262. DOI: 10.1016/j.actbio.2020.11.035

178.   Udina, E., Furey, M., Busch, S., Silver, J., Gordon, T., & Fouad, K. (2008). Electrical stimulation of intact peripheral sensory axons in rats promotes outgrowth of their central projections. Experimental neurology, 210(1), 238–247. https://doi.org/10.1016/j.expneurol.2007.11.007

179.   Vagaska, B., Gillham, O., & Ferretti, P. (2020). Modelling human CNS injury with human neural stem cells in 2- and 3-Dimensional cultures. Scientific reports, 10(1), 6785. https://doi.org/10.1038/s41598-020-62906-y

180.   Vella, M. A., Crandall, M. L., & Patel, M. B. (2017). Acute Management of Traumatic Brain Injury. The Surgical clinics of North America, 97(5), 1015–1030. https://doi.org/10.1016/j.suc.2017.06.003

181.   Vellis, J. De and Cole, R. (2011) 'Chapter 4 Preparation of Mixed Glial Cultures from Postnatal Rat Brain', 814, pp. 49–59. doi: 10.1007/978-1-61779- 452-0 DOI: 10.1007/978-1-61779-452-0_4

182.   Volovitz, I., Shapira, N., Ezer, H., Gafni, A., Lustgarten, M., Alter, T., Ben-Horin, I., Barzilai, O., Shahar, T., Kanner, A., Fried, I., Veshchev, I., Grossman, R., & Ram, Z. (2016). A non-aggressive, highly efficient, enzymatic method for dissociation of human brain-tumors and brain-tissues to viable single-cells. BMC neuroscience, 17(1), 30. https://doi.org/10.1186/s12868-016-0262-y

183.   von Bartheld, C. S., Bahney, J., & Herculano-Houzel, S. (2016). The search for true numbers of neurons and glial cells in the human brain: A review of 150 years of cell counting. The Journal of comparative neurology, 524(18), 3865–3895. https://doi.org/10.1002/cne.24040

184.   Wagenaar, D. A., Madhavan, R., Pine, J., & Potter, S. M. (2005). Controlling bursting in cortical cultures with closed-loop multi-electrode stimulation. The Journal of neuroscience : the official journal of the Society for Neuroscience, 25(3), 680–688. https://doi.org/10.1523/JNEUROSCI.4209-04.2005

185.   Wagenaar, D.A., Pine, J. & Potter, S.M. Searching for plasticity in dissociated cortical cultures on multi-electrode arrays. J Negat Results BioMed 5, 16 (2006). https://doi.org/10.1186/1477-5751-5-16

186.   Wang H. (2018). Modeling Neurological Diseases With Human Brain Organoids. Frontiers in synaptic neuroscience, 10, 15. https://doi.org/10.3389/fnsyn.2018.00015

187.   Weightman, A. P., Pickard, M. R., Yang, Y., & Chari, D. M. (2014). An in vitro spinal cord injury model to screen neuroregenerative materials. Biomaterials, 35(12), 3756–3765. https://doi.org/10.1016/j.biomaterials.2014.01.022

188.   Williams, A. J., Hartings, J. A., Lu, X. C., Rolli, M. L., Dave, J. R., & Tortella, F. C. (2005). Characterization of a new rat model of penetrating ballistic brain injury. Journal of neurotrauma, 22(2), 313–331. https://doi.org/10.1089/neu.2005.22.313

189.   Wu, Y., Rosset, S., Lee, T., Dragunow, M., Park, T. and Shim, V., 2021. In Vitro Models of Traumatic Brain Injury: A Systematic Review. Journal of Neurotrauma, 38(17), pp.2336-2372.DOI: 10.1089/neu.2020.7402

190.   Xiang, G., Pan, L., Huang, L., Yu, Z., Song, X., Cheng, J., Xing, W., & Zhou, Y. (2007). Microelectrode array-based system for neuropharmacological applications with cortical neurons cultured in vitro. Biosensors & bioelectronics, 22(11), 2478–2484. https://doi.org/10.1016/j.bios.2006.09.026

191.   Xiong, Y., Mahmood, A. and Chopp, M., 2013. Animal models of traumatic brain injury. Nature Reviews Neuroscience, 14(2), pp.128-142. DOI: 10.1038/nrn3407

192.   Yang, C., Wang, L., Weng, W., Wang, S., Ma, Y., Mao, Q., Gao, G., Chen, R., & Feng, J. (2019). Steered migration and changed morphology of human astrocytes by an applied electric field. Experimental cell research, 374(2), 282–289. https://doi.org/10.1016/j.yexcr.2018.11.029

193.   Yang, C., Wang, L., Weng, W., Wang, S., Ma, Y., Mao, Q., Gao, G., Chen, R., & Feng, J. (2019). Steered migration and changed morphology of human astrocytes by an applied electric field. Experimental cell research, 374(2), 282–289. https://doi.org/10.1016/j.yexcr.2018.11.029

194.   Yao, L., Shanley, L., McCaig, C., & Zhao, M. (2008). Small applied electric fields guide migration of hippocampal neurons. Journal of cellular physiology, 216(2), 527–535. https://doi.org/10.1002/jcp.21431

195.   Yeh, J. Z., Wang, D. H., Cherng, J. H., Wang, Y. W., Fan, G. Y., Liou, N. H., Liu, J. C., & Chou, C. H. (2020). A Collagen-Based Scaffold for Promoting Neural Plasticity in a Rat Model of Spinal Cord Injury. Polymers, 12(10), 2245. https://doi.org/10.3390/polym12102245

196.   Zanier, E. R., Fumagalli, S., Perego, C., Pischiutta, F., & De Simoni, M. G. (2015). Shape descriptors of the "never resting" microglia in three different acute brain injury models in mice. Intensive care medicine experimental, 3(1), 39. https://doi.org/10.1186/s40635-015-0039-0

197.   Zhang, B., & Gensel, J. C. (2014). Is neuroinflammation in the injured spinal cord different than in the brain? Examining intrinsic differences between the brain and spinal cord. Experimental neurology, 258, 112–120. https://doi.org/10.1016/j.expneurol.2014.04.007

198.   Zhang, Q., Beirne, S., Shu, K. et al. Electrical Stimulation with a Conductive Polymer Promotes Neurite Outgrowth and Synaptogenesis in Primary Cortical Neurons in 3D. Sci Rep 8, 9855 (2018). https://doi.org/10.1038/s41598-018-27784-5

199.   Zullo, L., Chiappalone, M., Martinoia, S., & Benfenati, F. (2012). A "spike-based" grammar underlies directional modification in network connectivity: effect on bursting activity and implications for bio-hybrids systems. PloS one, 7(11), e49299. https://doi.org/10.1371/journal.pone.0049299